

University of Nottingham
UK | CHINA | MALAYSIA

Development of a Coupled Numerical-Analytical Modelling Approach for Coaxial Direct Energy Deposition

Tomas Richard Walker, MEng

Thesis submitted to the University of Nottingham
for the Degree of Doctor of Philosophy.

July 2020

Dedicated in memory of

Margaret Walker

Abstract

There is increased motivation in industry to extend the service life of high-value components by developing new repair technologies, removing the need for replacement or re-manufacture. Coaxial direct energy deposition is being increasingly used over traditional repair technologies such as electron beam welding and arc welding due to the increased accuracy and the greater material utilisation ratio of the deposition process. The repair strategy can range from applying a thin cladding to the external surface to remedy initial fabrication defects and micro cracks to completely rebuilding the components structure layer by layer. The nature of process also allows in-process changes to be made to the input parameters, therefore increasing the flexibility of the repair scheme.

During the direct energy deposition process, high temperatures and heating/cooling rates are present which have a significant effect on the components microstructure and will also produce high magnitude residual stresses. The combination of these two phenomena will cause the component to no longer exhibit the mechanical properties required to conform to the in service operating conditions, therefore reducing the service life of the repaired component. To assess potential repair schemes for damaged components, a method to predict the thermal and mechanical effects of the deposition process, encompassing the key process parameters, was required.

This work presents a set of design tools to quantify the DED process, based on the sequentially coupled thermo-mechanical finite element approach coupled

with a number of analytical modelling strategies. A method to calibrate the thermal portion of the finite element model is presented based on an automated inverse approach. Methods to predict the geometry of the deposited track and the subsequent thermal/residual stress fields, for a number of processing conditions, has been investigated. In comparison to the simulation methods in the literature, the presented model has a greater flexibility in its modelling approach as it allows different process parameters and deposition techniques to be investigated.

To validate the proposed simulation tools, experimental trials were conducted for a range of operating conditions. Thermal measurements and metallographic weld pool examination was used to validate the thermal models. Residual stress predictions were validated using neutron diffraction at the ENGIN-X facility at the Rutherford Appleton Laboratory.

The developed methods will allow for bespoke repair strategies to be designed for individual components with varying levels of damage, without the need for lengthy and costly experimental trials. Complex parametric studies during the design process can be conducted using the presented tools, allowing an assessment of the proposed repair strategy on the thermal fields, distortion and residual stress formation within the repaired component. Using a parametric study, the simulation tools presented as part of this work, will allow the effect of the process parameters on the subsequent thermo-mechanical fields to be investigated. At this stage of the analysis, the results from the analyses can be used as an input to determine the fatigue life of the repaired component. Optimum tool paths and process parameters can be determined ensuring the optimum repair strategy is adopted, which will ensure the geometry and mechanical properties of the repaired component reflect the original requirements. As a more tailored repair solution can be determined using the proposed tools, a potential reduction in secondary processing of the repaired component maybe possible, which could be advantageous for reducing repair costs.

Acknowledgements

I would like to express my sincere gratitude to my supervisors, Dr Chris Bennett and Professor Adam Clare for their guidance, support and commitment throughout the course of this research. I would also like to thank Mr Stuart Branston, Mr Andrew Plummer and Mr Ken Wilson for their technical contributions to the experimental work for this research, more specifically during the sample preparation and the experimental welds/depositions. My gratitude also extends to my friends and colleagues at the Gas Turbine and Transmissions Research Centre (G2TRC).

I would like to acknowledge the Science and Technology Facilities Council (STFC) for the allocation of beam time at the ENGIN-X instrument, as the data collected enriched the work completed in this thesis. I am thankful to Dr Tung-Lik Lee for his knowledge and support during the residual stress measurements.

Finally, I wish to extend my gratitude to my family for the guidance and motivation they have provided. I would also like to thank my partner for her patience, loyalty and understanding throughout the past three years. My grandfather for his insightful conversations and words of wisdom. Lastly, I am indebted to my mother and father for their continued support and encouragement throughout my life, without them none of this would have been possible.

List of Publications

T. R. Walker, C. J. Bennett, T. L. Lee, and A. T. Clare, "A validated analytical-numerical modelling strategy to predict residual stresses in single-track laser deposited IN718" Int. J. Mech. Sci., vol. 151, no. February 2019, pp. 609–621, 2019 doi:10.1016/j.ijmecsci.2018.12.004.

T. R. Walker and C. J. Bennett, "An automated inverse method to calibrate thermal finite element models for numerical welding applications," J. Manuf. Process., vol. 47, no. July 2019, pp. 263–283, 2019 doi:10.1016/j.jmapro.2019.09.021.

T. R. Walker, C. J. Bennett, T. L. Lee, and A. T. Clare, "A novel numerical method to predict the transient track geometry and thermomechanical effects through in-situ modification of the process parameters in Direct Energy Deposition," Finite Elem. Anal. Des., vol. 169, no. February 2020, pp. 1–20, 2020 doi:10.1016/j.finel.2019.103347.

Contents

Abstract **i**

Acknowledgements **iii**

List of Publications **iv**

Contents **v**

List of Tables **x**

List of Figures **xiii**

Nomenclature **xxix**

1 Introduction **1**

1.1 Background 1

1.2 Research Aims and Objectives 9

1.3 Thesis Outline 10

2 Literature Review **13**

2.1 Introduction 13

2.2 Direct Energy Deposition 13

2.2.1 Laser: Fundamentals and Operation 13

2.2.2 The DED Process 15

2.3 Experimental Investigation to Characterise the Thermal Effects . 17

2.4 Experimental Investigation to Characterise Residual Stresses . . . 18
2.5 Numerical Modelling of AM Processes . . . 20
2.5.1 Thermo-mechanical (Metallurgical) Analysis . . . 25
2.5.2 Heat Source Models . . . 29
2.5.3 Modelling of the Material Deposition . . . 33
2.6 Calibration of FE Heat Source Models . . . 35
2.6.1 Optimisation Methodology . . . 35
2.6.2 Previous Methods to Calibrate Thermal FE Models . . . 36
2.7 Process Modelling of DED . . . 43
2.7.1 Previous Modelling of DED . . . 46
2.7.2 Previous Methods to Predict DED Track Profiles . . . 46
2.7.3 Previous Methods to determine the Thermo-mechanical Effects of DED . . . 56
2.7.4 Knowledge Gap . . . 60

3 Research Methodology 64
3.1 Introduction . . . 64
3.2 Analytical Modelling of DED . . . 65
3.2.1 Powder Flow Distribution . . . 65
3.2.2 Analytical Thermal Field . . . 67
3.2.3 Track Profile Prediction . . . 69
3.3 Numerical Methods to Predict the Thermal and Mechanical Fields of DED . . . 72
3.3.1 Sequentially Coupled Thermo-mechanical Analysis . . . 72
3.3.2 Material Properties of IN718 . . . 76
3.3.3 Numerical Integration . . . 80
3.3.4 Modelling Material Deposition . . . 80
3.4 Experimental Methodology . . . 82
3.4.1 Laser Rig Setup . . . 82

3.4.2 Thermal History Measurements 84
3.4.3 Metallurgical Examination 84
3.4.4 Processing of Metallographic Images 86
3.4.5 Neutron Diffraction Measurements 86

4 Automated Calibration of Thermal Finite Element Models 91
4.1 Introduction 91
4.2 Thermal Model Calibration Method 92
4.2.1 Thermal Model Theory 93
4.2.2 Automated Mesh Refinement 95
4.2.3 Thermal Model Parameter Refinement 99
4.3 Implementation of the Thermal Calibration 103
4.3.1 Experimental Methods 103
4.3.2 Heat Source and Material Model 106
4.3.3 Initiation of the Thermal Calibration 106
4.3.4 Determining Convergence Criteria 110
4.3.5 The effect of w on the Solution 113
4.4 Results and Discussion 119
4.4.1 Mesh Independence Study 119
4.4.2 Calibrated Thermal Model Parameters 123
4.4.3 Accuracy of the Refined Model Parameters 131
4.4.4 Reasons for Error in the Calibration Procedure 137
4.5 Conclusions 140

5 Numerical-Analytical Modelling for Single-Track Depositions 142
5.1 Introduction 142
5.2 Computational Model 143
5.2.1 Analytical Powder Catchment Efficiency 143
5.2.2 Numerical Modelling 148

5.3 Experimental Validation 151
5.3.1 Neutron Diffraction Measurements 152
5.4 Results and Discussion 154
5.4.1 Catchment Efficiency and Track Profile Prediction 154
5.4.2 Thermal Analysis 156
5.4.3 Mechanical Analysis 158
5.4.4 Sources of Error in Residual Stress Prediction 163
5.4.5 Comparison of the Geometrical Representation of the Track Profile 167
5.5 Conclusions 173

6 Transient Numerical Modelling of Adaptive Process Control 174
6.1 Introduction 174
6.2 Numerical Modelling Strategy 175
6.2.1 Track Profile Model 176
6.2.2 Thermo-mechanical Modelling 182
6.3 Validation of the Model 183
6.3.1 Implementation of the Computational Model 184
6.3.2 Experimental Validation 189
6.4 Results 191
6.4.1 Numerical Track Prediction 191
6.4.2 Thermal Analysis 195
6.4.3 Mechanical Analysis 198
6.5 Discussion 206
6.5.1 Track Profile Prediction 206
6.5.2 Thermal History and Melt Pool Profile 208
6.5.3 Residual Stress Predictions 209
6.6 Conclusions 212

7 Numerical-Analytical Modelling of Multi-Track Deposition 214

7.1 Introduction 214

7.2 Multi-Track Geometry Prediction 215

7.2.1 2D Thermal Model 217

7.2.2 Melt Pool Geometry Prediction 220

7.2.3 Overlap Geometry Prediction 223

7.2.4 Validation of the Multi-Track Predictions 231

7.3 Thermo-mechanical Modelling of Multiple Deposits 233

7.3.1 Validation of the Multi-Track Thermo-Mechanical model . 235

7.4 Parametric Investigation into OR and Deposition Strategy 239

7.5 Results and Discussion 242

7.5.1 Multi-Track Profile Predictions 242

7.5.2 Thermo-mechanical Multi-track Validation Case 249

7.5.3 Effect of OR on the Thermo-mechanical Fields 270

7.6 Conclusions 279

8 Conclusions and Future Work 281

8.1 Conclusions 281

8.2 Future Work 285

Bibliography 288

List of Tables

1.1 The advantages and disadvantages of the current advanced manufacturing processes which could be implemented for repair applications. 2

2.1 Examples of modelling methods and the associated literature used to capture the process physics of Powder DED, WAM and PBF. . 21

2.2 A table presenting the most common second generation heat source models and their applications. 32

3.1 Geometrical parameters of the coaxial nozzle used to model the powder flow. 66

3.2 Nominal chemical composition of IN718 in wt%. 77

3.3 Latent heat of fusion properties for IN718 [151]. 79

3.4 Nominal chemical composition of MetcoAdd 718C. 83

4.1 Process parameters used for the experimental validation of the calibration procedure. 104

4.2 Welding and heat source parameters for the parametric study to determine the convergence criteria (Parameter set was designed from the original set 1-9). 110

4.3 Parameters for the test cases used to generate the target solutions to evaluate the use of a SOO or MOO for the optimisation algorithm. (Parameter set was designed from the original set 1-9). . . 114

4.4 Initial element size for the optimisation study. 122
4.5 Optimised heat source parameters for the combined heat source model derived using the experimental cases. 127
4.6 Percentage error between the experimental and predicted peak temperature at 3 mm, 4 mm and 5 mm from the weld centreline. . 132
4.7 Percentage error between the experimental and predicted melt pool surface width (W_s), the throat width at the inflection point (W_t), the total penetration depth (D) and the melt pool area (A_{melt}). . 133
4.8 Systematic error analysis for peak temperature measurements using BS 60584 [177]. 135

5.1 Process Parameters used to investigate the catchment efficiency. . 145
5.2 Calculated catchment efficiencies using the realistic (η_{c_2}) and the modified approach (η_c). 147

6.1 Error and R^2 Values for Experimental and Predicted Track Profiles. 193

7.1 Process parameters used to investigate a modification to the final track height for the spiral deposition strategy. 227
7.2 Process parameters used to fabricate the experimental specimens to validate the multi-track model. 232
7.3 The total number of elements and nodes used for each mesh in the parametric investigation. 242
7.4 Error between the predicted and experimental multi-track profiles for each track height (h_1, h_2 and h_3) and the overall width (W_{total}) for the zig-zag deposition strategy. 245
7.5 Error between the predicted and experimental multi-track profiles for each track height (h_1, h_2 and h_3) and the overall width (W_{total}) for the spiral deposition strategy. 246

7.6 Maximum heating rate and cooling rate at the centre of each gauge volume, 1 mm below each track, for the spiral and zig-zag deposition strategy. 269

List of Figures

1.1 A schematic of the two repair methodologies that can be adopted for the DED process. (a) Repair of an initial fabrication defect and (b) Structural repair using a layer-by-layer approach. 4

1.2 Process flow to determine the use of DED for repair. (a) General information of the repair process. (b) Identifying the process capability using experimental and modelling methods. (c) Methods to assess if the repair using DED is viable. 6

2.1 A schematic of a simple optically pumped laser. 14

2.2 A schematic of the coaxial powder fed DED process using a laser heat source [18]. 16

2.3 The cross-section of the track geometry fabricated by DED. W, H and D is the track height, width and depth respectively [20]. . . . 17

2.4 Stages of AM processing and the associated modelling scale. Modified from [19, 77]. 22

2.5 A flowchart showing the sequentially coupled FE procedure for a commercial code. 23

2.6 The couplings associated with CWM. Modified from [77]. 24

2.7 A schematic of the sub-processes and process variables corresponding to each stage of the DED process [14]. 44

2.8 A schematic of the basic elliptical melt pool used in DED [25]. . . 45

2.9 A schematic of the FOM multi-track geometry model and the associated parameters [126]. Curve face GAD was the initial track profile, ACB was the region of the valley, ECD was the overlap region, h is the track height, w is the track width and l is the offset distance. 51
2.10 A schematic of the TOM for multi-track deposition. BEC defines the region of the valley and AED defines the overlap region [127]. 52
2.11 A schematic of the track profile predicted using the fillet model [128]. 53
2.12 A schematic of an altered melt pool geometry used when a previously deposited track was present [124]. 54
2.13 A schematic of the meshing method implemented to represent a 2D representation of the track [44]. (a) Original mesh with each domain present. (b) Mesh refinement included for the second domain. 55

3.1 Schematic of the coaxial nozzle geometry and the associated parameters to model the powder flow. 66
3.2 A schematic of the melt pool geometry superimposed with the powder mass flux distribution. Modified from [25]. 69
3.3 A schematic of the Gaussian powder flux distribution used in this work. 70
3.4 Nodes for mechanical boundary conditions for both a symmetric and unsymmetrical geometry. 76
3.5 Temperature dependant material properties of IN718 (a) Thermal conductivity, k and density, ρ (b) Specific heat capacity, C_p and thermal expansion coefficient, α (c) Young's modulus, E and yield stress, σ_y. 78
3.6 A schematic of the laser deposition rig. 82
3.7 SEM Image of Gas Atomised MetcoAdd 718C Powder [157]. . . . 83

3.8 A schematic of a metallographic specimen removed from a deposition/weld. 85
3.9 A schematic of a crystalline lattice structure showing the theory of Bragg's Law. 87
3.10 A schematic of the ENGIN-X beamline setup used to obtain ND measurements showing the two plate orientations used, the incident and diffracted beam and the measured strain directions. . . . 89

4.1 Flowchart of the calibration procedure used to determine the optimum element size and the parameters of the thermal model. . . 93
4.2 Schematic of the test specimen geometry and the weld path used for the underlying thermal model. 94
4.3 Flowchart of the process used to determine the optimum element size. 98
4.4 Flowchart of the inverse analysis used to determine the parameters of the thermal model. 99
4.5 Schematic of the inverse approach for (a) Calculating the residual error for the thermal profile (b) Calculating the residual error for the melt pool geometry. 101
4.6 Schematic of the experimental setup showing the weld path, thermocouple locations and the extracted sample location of metallographic examination. 104
4.7 Cross sectional micrographs obtained from the fabricated test specimens. 105
4.8 Schematic of the geometry used to define the initial guess for the heat source parameters for (a) The conductive and keyhole regime where no narrow section of the weld was present (b) The keyhole regime where a narrow weld section was present. 108

4.9 Results from the parametric study showing the change in melt pool area ($1 - \Delta A$) and the coefficient of determination (R^2) for each element size. (a) Set A1-Conductive (b) Set A3-Conductive (c) Set A7-Partial Penetration (d) Set A9-Partial Penetration (e) Set A7-Full Penetration (f) Case A9-Full Penetration. 112

4.10 Cumulative percentage error between the target solution and the optimised parameters for different weight values. (a) Set B1 using Gaussian heat source only (b) Set B1 using combined heat source (c) Parameter Set B8 (d) Parameter Set B9. 115

4.11 A plot comparing the target thermal solutions with the solution for w=0.75 and for w giving the minimum error (a) Set B1 no cylindrical heat source (b) Set B1 with the hybrid heat source (c) Set B7 (d) Set B8. 117

4.12 A plot comparing the target melt pool geometries with the solution for w=0.75 and for w giving the minimum error (a) Set B1 no cylindrical heat source (b) Set B1 with the hybrid heat source (c) Set B7 (d) Set B8. It should be noted for (a) and (b) the optimum was for w=0.75. 118

4.13 Mesh sensitivity results for parameter set 4 for element size (a) 2 mm (b) 1 mm (c) 0.5 mm (d) 0.25 mm. 120

4.14 Example convergence data for the mesh sensitivity study for parameter Set 4. 121

4.15 A comparison between the experimental and predicted thermal histories/melt pool geometries in the conductive regime for (a) Parameter set 1 (b) Parameter set 2 (c) Parameter set 3. 124

4.16 A comparison between the experimental and predicted thermal histories/melt pool geometries in the conductive regime for (a) Parameter set 2 (b) Parameter set 3 (c) Parameter set 4. 125

4.17 A comparison between the experimental and predicted thermal histories/melt pool geometries in the conductive regime for (a) Parameter set 2 (b) Parameter set 3 (c) Parameter set 4. 126
4.18 An example of the iteration history for the heat source radii and the process efficiency for (a) Parameter set 4 (b) Parameter set 5. 130
4.19 A graph showing the effect of the cooling rates through variation of the thermal contact coefficient. The cooling rate was determined for the temperature range governing recrystallization of γ'for IN718 for P=900 W and V=100 mm/min. 136

5.1 A flowchart showing the required inputs for the model and the associated outputs at each stage of the modelling process. 143
5.2 A schematic of the powder flux distribution (q_{pf}) superimposed with the predicted melt pool geometry for (a) Set 1 (b) Set 2 (c) Set 3 (d) Set 4. 144
5.3 Mesh sensitivity study results showing the calculated convergence parameters for each mesh iteration. 148
5.4 A Section of the FE mesh used for the thermo-mechanical models (a) Top surface view (b) Cross sectional view perpendicular to the track. 150
5.5 (a) Schematic of the real life deposition process (b) Adopted FE modelling strategy for element activation to simulate the deposition process. 150
5.6 Schematic of the experimental set up showing the deposition procedure, restraining locations, thermocouple locations and the specimen used for metallographic analysis. 152
5.7 Schematic of Sample B showing the locations of the horizontal line scans (red lines) and the location where the d_0 specimens were extracted (hatched boxes). 153

5.8 Details of the d_0 specimen cross section with the target location of the beam marked with a red circle. 153

5.9 A 3D surface plot of the experimental track deposit upon the substrate generated from surface measurements of Sample A. 154

5.10 A comparison of the experimental and analytical track profile geometries utilising two catchment efficiency approaches, η_c=0.51 and η_{c_2}=0.41. 155

5.11 Comparison of experimental and numerically predicted thermal histories for three thermocouple locations positioned at the mid length of the substrate at; 3 mm, 4 mm and 5 mm from the track centreline. 157

5.12 Comparison of the numerically predicted fusion zone and the metallographic specimen at the centre of the deposition i.e. y=65 mm. 157

5.13 Numerical prediction of the transverse, longitudinal and normal stress components during the deposition process, in the steady-state track region. The nodal point selected was at the mid length of the substrate (y=60 mm) at the track centreline at the centre of the fusion zone (0.375 mm below the substrate surface). 159

5.14 FE contour plots showing the through thickness stress distribution for the transverse stress component, σ_{xx}, at different time intervals through the heating and cooling phase of the process. Cross section taken at the mid length of the substrate i.e. y=60 mm. (a) During the heating phase at t=8.25 s (b) At the peak temperature where t=8.95 s (c) During the cooling phase at t=12.15 s (d) Final residual stress field upon being fully cooled. 161

5.15 FE contour plots showing the through thickness stress distribution for the longitudinal stress component, σ_{yy}, at different time intervals through the heating and cooling phase of the process. Cross section taken at the mid length of the substrate i.e. y=60 mm. (a) During the heating phase at t=8.25 s (b) At the peak temperature where t=8.95 s (c) During the cooling phase at t=12.15 s (d) Final residual stress field upon being fully cooled. 162

5.16 FE contour plots showing the through thickness stress distribution for the normal stress component, σ_{zz}, at different time intervals through the heating and cooling phase of the process. Cross section taken at the mid length of the substrate i.e. y=60 mm. (a) During the heating phase at t=8.25 s (b) At the peak temperature where t=8.95 s (c) During the cooling phase at t=12.15 s (d) Final residual stress field upon being fully cooled. 162

5.17 Comparison of experimentally measured and numerically predicted tri-axial residual stresses at 2 mm below the surface for each line scan position; (a) y=30 mm; (b) y=60 mm; (c) y=90 mm. 164

5.18 Residual stress prediction averaged over the ND gauge volume along the y-direction (transverse stress) directly below the track. . 166

5.19 Comparison of experimentally measured and numerically predicted tri-axial residual stresses at 3 mm below the surface for each line scan position (a) y=30 mm (b) y=60 mm (c) y=90 mm. 168

5.20 Comparison of thermal history profiles at the substrate mid length at x=3,4 and 5 mm for (a) Square track profile with the same geometry, (b) Square track profile with the same height and (c) Square track profile with the same width. 171

5.21 Comparison of the longitudinal, transverse and normal residual stresses at y=60 mm for (a) Square track profile with the same geometry, (b) Square track profile with the same height and (c) Square track profile with the same width. 172

6.1 A flowchart of the modelling strategy used to predict the track profile, thermal histories and residual stress fields. The associated inputs and corresponding outputs are shown at each stage of the modelling process. 175

6.2 Flowchart of the modelling procedure used to determine the transient track geometry. 177

6.3 Schematic of the methodology used to determine a transient track profile. (a) Shows the substrate geometry identifying the two regions of the modelling process. (b) Presents the concept of varying process parameters during the deposition process (c) Schematic of the calculated track profile at each time increment. 178

6.4 Schematic of the power loss function showing the three possible outputs of the model after an iteration during the current time step. 181

6.5 Schematic of the thermo-mechanical modelling process for DED. (a) Realistic representation of the DED manufacturing process. (b) Thermal model showing a thermal contour with the adopted element activation strategy. (c) Mechanical model showing a longitudinal stress distribution and the adopted element activation strategy. 183

6.6 Mesh study results for (a) P=900 W and (b) P=1800 W. Each graph presents the convergence parameters and computational time for each mesh iteration. Convergence criteria is highlighted as a dotted grey line. 185

6.7 Final mesh design utilised for the numerical track prediction mode (a) A section of the mesh used in the traverse direction (b) Through thickness mesh design. For both images, the laser scanning direction is denoted by the red arrow (y-direction). 186

6.8 FE mesh utilised for the thermo-mechanical model showing the through thickness design at (a) y=30 mm (b) y=60 mm (c) y=90 mm. (d) Presents a top view of the mesh design in the transient region. 187

6.9 Schematic of the experimental set up showing the locations of the restraining bolts, thermocouples used to collect thermal histories and the order in which the laser and powder feed were activated/deactivated. 189

6.10 Locations of the specimens used for metallographic examination and the strain-free reference sample. Horizontal line scan locations used for the ND measurements shown in red. 190

6.11 A 3D surface plot of the experimental track deposit upon the substrate generated from surface measurements of Sample A. 191

6.12 A comparison of the experimental and predicted track geometry for two laser powers (a) P=900 W and (b) P=1800 W. 192

6.13 A comparison of the experimental and predicted track geometry at four locations within the transient region. (a) y=55 mm (b) y=60 mm (c) y=65 mm (d) y=70 mm. 192

6.14 Predicted power loss and effective power utilised during the transient portion of the model. 194

6.15 Predicted catchment efficiency used during the transient portion of the deposition. 194

6.16 A comparison of experimental and numerically predicted thermal histories at three locations along the substrate at (a) y=30 mm, (b) y=60 mm and (c) y=90 mm for three thermocouple's positioned at; 3 mm, 4 mm and 5 mm from the track centreline. 196

6.17 A comparison of the numerically predicted fusion zone and the metallographic specimen at three locations (a) y=35 mm (b) y=65 mm and (c) y=95 mm. 197

6.18 Numerical prediction of the transverse, longitudinal and normal stress components during the deposition process, in three region of the track (a) y=30 mm (b) y=60 mm (c) y=90 mm. The nodal point was at the track centreline 0.25 mm below the substrate surface. 199

6.19 FE contour plots at y=30 mm showing the through thickness stress distribution for the transverse stress component, σ_{xx}. (a) During the heating phase at t=8.25 s (b) At the peak temperature where t=8.95 s (c) During the cooling phase at t=12.15 s (d) Final residual stress field upon being fully cooled. 200

6.20 FE contour plots at y=30 mm showing the through thickness stress distribution for the longitudinal stress component, σ_{yy}. (a) During the heating phase at t=8.25 s (b) At the peak temperature where t=8.95 s (c) During the cooling phase at t=12.15 s (d) Final residual stress field upon being fully cooled. 200

6.21 FE contour plots at y=30 mm showing the through thickness stress distribution for the normal stress component, σ_{zz}. (a) During the heating phase at t=8.25 s (b) At the peak temperature where t=8.95 s (c) During the cooling phase at t=12.15 s (d) Final residual stress field upon being fully cooled. 201

6.22 FE contour plots at y=60 mm showing the through thickness stress distribution for the transverse stress component, σ_{xx}. (a) During the heating phase at t=8.25 s (b) At the peak temperature where t=8.95 s (c) During the cooling phase at t=12.15 s (d) Final residual stress field upon being fully cooled. 201

6.23 FE contour plots at y=60 mm showing the through thickness stress distribution for the longitudinal stress component, σ_{yy}. (a) During the heating phase at t=8.25 s (b) At the peak temperature where t=8.95 s (c) During the cooling phase at t=12.15 s (d) Final residual stress field upon being fully cooled. 202

6.24 FE contour plots at y=60 mm showing the through thickness stress distribution for the normal stress component, σ_{zz}. (a) During the heating phase at t=8.25 s (b) At the peak temperature where t=8.95 s (c) During the cooling phase at t=12.15 s (d) Final residual stress field upon being fully cooled. 202

6.25 FE contour plots at y=90 mm showing the through thickness stress distribution for the transverse stress component, σ_{xx}. (a) During the heating phase at t=8.25 s (b) At the peak temperature where t=8.95 s (c) During the cooling phase at t=12.15 s (d) Final residual stress field upon being fully cooled. 203

6.26 FE contour plots at y=90 mm showing the through thickness stress distribution for the longitudinal stress component, σ_{yy}. (a) During the heating phase at t=8.25 s (b) At the peak temperature where t=8.95 s (c) During the cooling phase at t=12.15 s (d) Final residual stress field upon being fully cooled. 203

6.27 FE contour plots at y=90 mm showing the through thickness stress distribution for the normal stress component, σ_{zz}. (a) During the heating phase at t=8.25 s (b) At the peak temperature where t=8.95 s (c) During the cooling phase at t=12.15 s (d) Final residual stress field upon being fully cooled. 204

6.28 Comparison of experimentally measured and numerically predicted tri-axial residual stresses at 2 mm below the surface for each line scan position (a) y=30 mm (b) y=60 mm (c) y=90 mm. 205

6.29 Schematic of the estimated HAZ and the ND gauge volume for (a) y=30 mm and (b) y=90 mm. 211

7.1 A schematic of two common DED tool paths. (a) Spiral strategy (b) Zig-zag strategy. 215

7.2 A flowchart of the process used to determine the geometry of a multi-track deposition. 216

7.3 An example of the 2D FE mesh used for the multi-track model with the seeding constraints highlighted for each geometrical section. 219

7.4 A schematic of the heat flux distribution for a three track deposition using the zig-zag strategy. (a) Initial heat source pass. (b) Heat flux definition after a single track deposition. (c) Heat flux definition after a double track deposition. (d) Final geometry for a three track deposition. 219

7.5 A schematic of the multi-track melt pool geometry and the associated coordinate systems and geometrical parameters. 221

7.6 An example of the experimentally determined track profile for (a) Spiral deposition strategy and (b) Zig-zag deposition strategy. . . 223

7.7 A schematic of two overlapped tracks and the geometrical parameters used to define the geometry. 224

7.8 A schematic of the fillet overlap model denoted with the associated variables and geometrical features. The schematic is presented for two track profiles with the second track having a greater maximum height. 227

7.9 Results of a study depicting the through thickness melt pool geometry for (a) No previous deposition (b) Subsequent track using the zig-zag strategy (c) Final track using the spiral strategy. . . . 228

7.10 A schematic of a track positioned between two previous deposits and the associated parameters used to define the geometry. 230

7.11 A schematic of the experimental set up which was used to obtain the metallographic specimens used to analyse the multi-track profile. 231

7.12 Mesh design used for the multi-track thermo-mechanical models for both the spiral and zig-zag deposition strategy. (a) x-z cross sectional planar view and (b) y-x cross sectional planar view. . . . 235

7.13 A schematic of the experimental set up used to validate the multi-track deposition model. 236

7.14 Locations of the ND horizontal line scans and the d_0 specimen. . . 236

7.15 Details of the d_0 specimen cross section used for the multi-track ND measurements. The beam target is marked with a red circle. . 237

7.16 A comparison between the ND line scan used for (a) Single track deposition (b) Multi-track deposition. Line scan for each specimen marked with a red cross line. 239

7.18 Mesh design used for the zig-zag deposition strategy for (a) 10% OR (b) 20% OR and (c) 40% OR. 240

7.17 Mesh design used for the spiral deposition strategy for (a) 10% OR (b) 20% OR and (c) 40% OR. 241

7.19 A 3D surface plot of the experimental multi-track deposit generated from the ENGIN-X laser scan data from Sample S. 243

7.20 Comparison between the predicted multi-track profile (red line) and the experimental profile (black and white image) for the zig-zag deposition strategy. (a) 10% overlap ratio (b) 20% overlap ratio and (c) 40% overlap ratio. 244

7.21 Comparison between the predicted multi-track profile (red line) and the experimental profile (black and white image) for the spiral deposition strategy. (a) 10% overlap ratio (b) 20% overlap ratio and (c) 40% overlap ratio. 245

7.22 Comparison of the experimental and numerically predicted thermal histories for the spiral deposition strategy for thermocouple position (a) x=6 mm (b) x=7 mm and (c) x=8 mm. All thermocouples positioned at the substrate mid-length. 250

7.23 Comparison of the experimental and numerically predicted thermal histories for the zig-zag deposition strategy for thermocouple position (a) x=6 mm (b) x=7 mm and (c) x=8 mm. All thermocouples positioned at the substrate mid-length. 251

7.24 Numerical prediction of the longitudinal, transverse and normal stress components, during the multi-track deposition process, under each track, for the spiral deposition strategy. (a) Stress evolution at x=-3 mm (b) Stress evolution at x=3 mm and (c) Stress evolution at x=0 mm. 254

7.25 Numerical prediction of the longitudinal, transverse and normal stress components, during the multi-track deposition process, under each track, for the zig-zag deposition strategy (a) Stress evolution at x=-3 mm (b) Stress evolution at x=0 mm and (c) Stress evolution at x=3 mm. 255

7.26 Comparison of the experimental and numerically predicted residual stress profiles for the spiral deposition strategy at y=30 mm for (a) Longitudinal Stress (σ_{yy}) (b) Transverse Stress (σ_{xx}) (c) Normal Stress (σ_{zz}). 258

7.27 Comparison of the experimental and numerically predicted residual stress profiles for the spiral deposition strategy at y=60 mm for (a) Longitudinal Stress (σ_{yy}) (b) Transverse Stress (σ_{xx}) (c) Normal Stress (σ_{zz}). 259

7.28 Comparison of the experimental and numerically predicted residual stress profiles for the spiral deposition strategy at y=90 mm for (a) Longitudinal Stress (σ_{yy}) (b) Transverse Stress (σ_{xx}) (c) Normal Stress (σ_{zz}). 260

7.29 Comparison of the experimental and numerically predicted residual stress profiles for the zig-zag deposition strategy at y=30 mm for (a) Longitudinal Stress (σ_{yy}) (b) Transverse Stress (σ_{xx}) (c) Normal Stress (σ_{zz}). 263

7.30 Comparison of the experimental and numerically predicted residual stress profiles for the zig-zag deposition strategy at y=60 mm for (a) Longitudinal Stress (σ_{yy}) (b) Transverse Stress (σ_{xx}) (c) Normal Stress (σ_{zz}). 264

7.31 Comparison of the experimental and numerically predicted residual stress profiles for the zig-zag deposition strategy at y=60 mm for (a) Longitudinal Stress (σ_{yy}) (b) Transverse Stress (σ_{xx}) (c) Normal Stress (σ_{zz}). 265

7.32 Comparison of the experimental and numerically predicted residual stress profiles for each bead for (a)Spiral deposition strategy and (b) Zig-zag deposition strategy. Both locations are at y=60 mm. . 267

7.33 A comparison between the thermal history predictions, for an OR of 10%, 20% and 40% for (a) Spiral deposition strategy and (b) Zig-zag deposition strategy. 271

7.34 A comparison between the numerical predictions, for an OR of 10%, 20% and 40% for the spiral deposition strategy for (a) Longitudinal stress (σ_{yy}) (b) Transverse stress (σ_{xx}) and (c) Normal stress (σ_{zz}). 273

7.35 A comparison between the numerical predictions, for an OR of 10%, 20% and 40% for the zig-zag deposition strategy for (a) Longitudinal stress (σ_{yy}) (b) Transverse stress (σ_{xx}) and (c) Normal stress (σ_{zz}). 274

7.36 A comparison between the numerical predictions, for an OR of 10%, 20% and 40% for the spiral deposition strategy, at the track centre, at y=60 mm for (a) Longitudinal stress (σ_{yy}) (b) Transverse stress (σ_{xx}) and (c) Normal stress (σ_{zz}). 277

7.37 A comparison between the numerical predictions, for an OR of 10%, 20% and 40% for the zig-zag deposition strategy, at the track centre, at y=60 mm for (a) Longitudinal stress (σ_{yy}) (b) Transverse stress (σ_{xx}) and (c) Normal stress (σ_{zz}). 278

8.1 Process flow to identify the process capability of DED using experimental and modelling methods. The work as presented in Chapter 4-7 is highlighted in grey. 285

Nomenclature

Abbreviations

2D Two-Dimensional

3D Three-Dimensional

AM Additive Manufacture

CFD Computational Fluid Dynamics

CMM Coordinate Measurement Machine

CNC Computer Numerically Controlled

CWM Computational Welding Mechanics

DED Direct Energy Deposition

EDM Electro Discharge Machining

FEM Finite Element Method

FE Finite Element

FOM Flat Top Overlap Model

FZ Fusion Zone

GSAS General Structure and Analysis System

HAZ Heat Affected Zone

IN718 Inconel 718

LBW Laser Beam Welding

MOO Multi-Objective Optimisation

ND Neutron Diffraction

OR Overlap Ratio

SOO Single-Objective Optimisation

TOM Tangent Overlap Model

UTS Ultimate Tensile Strength

XRD X-ray Diffraction

YAG Ytterbium Aluminium Garnet

Variables

α Thermal Expansion Coefficient

$\dot{m}$ Powder Mass Flow Rate

$\dot{V}$ Volumetric Flow Rate

ϵ Emissivity

η Process Efficiency

η_c Powder Catchment Efficiency

ρ Density

σ Stefan-Boltzmann Constant

σ_y	Yield Stress
σ_{ij}	Stress Tensor
σ_p	Plastic Stress
τ	Substrate Thickness
θ	Initial Powder Stream Angle
Υ	Skewness Factor
ε	Total Strain
ε^e	Elastic Strain
ε^p	Plastic Strain
ε^{th}	Thermal Strain
$\vec{q}$	Heat Flux Vector
C_p	Specific Heat Capacity
C_{flux}	Centre of the Heat Flux Distribution
D	Melt Pool Depth
d_0	Strain-free Lattice Spacing
d_{hkl}	Lattice Spacing
d_p	Penetration Depth
E	Young's Modulus
f	Heat Flux Partition Factor
h	Convective Film Coefficient

h_c	Height of Cylindrical Heat Source
h_v	Latent Heat of Vaporisation
$h_z(x)$	Track Height
k	Thermal Conductivity
L	Melt Pool Length
L^f	Length of Front Melt Pool
L^r	Length of Rear Melt Pool
L_m	Latent Heat of Melting
L_e	Element Length
P	Laser Power
P_{eff}	Effective Laser Power
P_{loss}	Laser Power Loss
P_{ss}	Steady-state Power
q_{pf}	Powder Flux Distribution
R	Laser Spot Radius
r_0	Gaussian Radius
r_c	Cylindrical Heat Source Radius
r_i	Inner Nozzle Radius
r_o	Outer Nozzle Radius
r_p	Gaussian Feed Radius

r_s	Gaussian Surface Radius
T	Temperature
t	Time
T^{exp}	Experimental Temperature
T^{pre}	Predicted Temperature
T_m	Melting Temperature
T_p	Peak Melt Pool Temperature
T_{abs}	Absolute Zero Temperature
T_{amb}	Ambient Temperature
t_i	Integration Time Step
T_{mean}	Mean Melt Pool Temperature
t_{ss}	Steady-state Time
V	Traverse Velocity
W	Melt Pool Width
w	Weight Parameter
W^{exp}	Experimental Melt Pool Width
W^{pre}	Predicted Melt Pool Width
x, y, z	Cartesian Coordinates
x_{off}	Centre Distance between Deposits
y_f	Front Melt Pool Boundary

y_r	Rear Melt Pool Boundary
y_0	Initial Centre of the Heat Flux
z_l	Lower Radius of the Cylindrical Heat Source
z_s	Stand-off Distance
z_u	Upper Radius of the Cylindrical Heat Source

Chapter 1

Introduction

1.1 Background

Additive Manufacturing (AM) techniques are being increasingly used to repair high value components. Previously, traditional fusion welding processes were used for repair in many industrial fields; however, AM methods are becoming more prevalent due to their improved accuracy, higher material utilisation ratio and increased flexibility of the implemented repair strategy. During maintenance inspections, components that have been damaged in-service are often removed and discarded as the component contains significant defects and/or damage which would compromise the structural integrity and safe operation of the system. Therefore, to increase the service life of the component and to reduce the operational costs, repair of the component is beneficial. A number of different advanced manufacturing technologies, which include Direct Energy Deposition (DED), Wire Arc Additive Manufacturing (WAAM), Laser Beam Welding (LBW) plus wire, Electron Beam Powder Bed Fusion (E-PBF) and Laser Powder Bed Fusion (L-PBF) could be used to repair components. Table 1.1 identifies the advantages and disadvantages of each technology with regards to implementing them for repair applications.

Table 1.1: The advantages and disadvantages of the current advanced manufacturing processes which could be implemented for repair applications.

Advanced Manufacturing Process	**Advantages**	**Disadvantages**
DED - Powder [1]	- Reduced oxidation rates - Mixture of materials to tailor properties - Greater build rates than PBF - No support structures required during deposition - Can deposit onto pre-existing structure with ease - Small bead geometry suitable for a range of repair methodologies	- Low deposition efficiency - Poor build surface requiring secondary machining - High energy density system leading to distortion and residual stress formation
WAAM [2], [3]	- High deposition efficiency and build rates - Large bead geometry suitable for producing large-scale metal structures - Cheaper than other AM processes due to similarity with existing welding technologies - Can deposit onto pre-existing structure with ease	- Susceptible to porosity, cracking and delamination of layers - Mechanical strength is less than wrought products - High surface roughness when compared to powder based processes - Applications restricted to the production of low or medium part complexity - High magnitude residual stress and distortion is present, greater than for DED and PBF

continued on the next page

LBW - Wire [4], [5]	- Localised heating effects - Produces parts comparable to wrought materials - Medium to large track size typically used to fabricate simple components - Can be mixed with powder stream to generate graded coatings	- Material limitations due to wire production - Waviness generated in deposited track requiring secondary machining - High energy density process leading to high magnitude residual stress and distortion - High oxidation rates
E-PBF [1], [6]	- Low oxidation and high purity of fabricated components - Can process highly reactive materials such as titanium alloys due to oxygen-free environment - Minimum material waste - Residual stress reduction due to increase process temperature - Production of fully dense parts with minimal porosity	- Requires a vacuum chamber leading to high associated costs - Build height is limited by the powder size - Difficult to deposit powder on pre-existing structure - Recasting and metal splash occurs on each layer which has to be removed using abrasive cleaning
L-PBF [1], [7]	- High purity of the fabricated component - Can generate fully dense components - Good mechanical properties when compared to wrought materials	- Build height is limited by the powder size - Slow build rates - Requires support structure for large structures - Near impossible to deposit powder onto pre-existing component - Very high cost for machines and materials

Both powder bed fusion technologies (Table 1.1) provide a fully dense repair solution with optimum mechanical properties; however, due to the difficulty in

supplying powder to a pre-existing structure, it would not be a valid repair technology. Although, the wire additive manufacturing methods can deposit directly onto a pre-existing structure, the use of the wire feed results in a deposition geometry which would be too large for repair applications.This is because WAAM technology is more prevalent for component fabrication. Also, due to the high energy density processing required, the generated residual stresses are greater than for the DED and PBF process; therefore, further limiting their use for repair applications. Due to the use of a powder feed for the DED process, a smaller bead geometry is generated, therefore it is suitable for a range of repair strategies, increasing the flexibility of the approach. Similar to WAAM, the deposition can be applied directly to the damaged component and although high magnitude residual stresses are presented, these are less when compared to the other technologies, making it an ideal candidate for repair applications.

The repair process utilising DED can range from applying a thin cladding to the external surface to remedy material defects, such as fatigue cracks, to a structural repair of the component utilising a layer-by-layer deposition approach. A schematic of these two types of repair methodologies are presented in Figure 1.1.

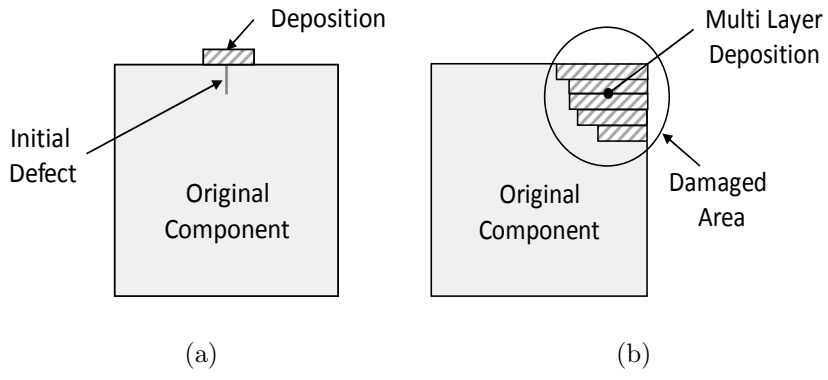

Figure 1.1: A schematic of the two repair methodologies that can be adopted for the DED process. (a) Repair of an initial fabrication defect and (b) Structural repair using a layer-by-layer approach.

The use of DED is prevalent within the aerospace industry to repair components such as compressor and turbine blades [8]. However, it should be noted that the DED technology is not restricted to only the aerospace engineering sector. Applications could range from repairing worn shaft seals or dies within the automotive sector [9], to applying a corrosion resistant surface finish to components within the nuclear industry [10]. The DED process consists of various operating parameters, which are chosen and monitored to ensure a successful repair is achieved. As the process requires a high magnitude of thermal energy to melt the substrate and due to previously deposited layers being reheated, a significant amount of distortion and residual stress can be present within the final component. The use of experimental investigations to quantify the process would be time consuming and costly, due to the infinite number of process parameter combinations. A method is therefore required to model the process, to enable multiple parameter studies to be conducted and thus allow a bespoke repair strategy to be determined for the component.

A generalised flowchart to determine if a component can be repaired using DED is presented in Figure 1.2. The flowchart consists of three successive parts that gather information to build a business case to assess the viability of DED for the current component. This is based on simulation/experimental investigations and costing of the repair. Firstly, it is determined if a repair is feasible through assessing the components conformity to its original specifications. Non-conformance could be to drawing requirements, design intent, structural integrity and/or component life. The specific nature of the damage has to be assessed which may include details such as the size of a crack/dent or the geometrical deviation to the original design. The damage can be used to assess the remaining life of the component and, if this satisfies the number of cycles to the next inspection, then a repair is not required.

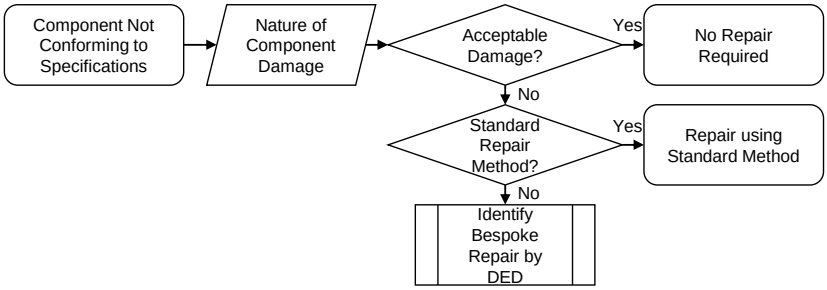

(a)

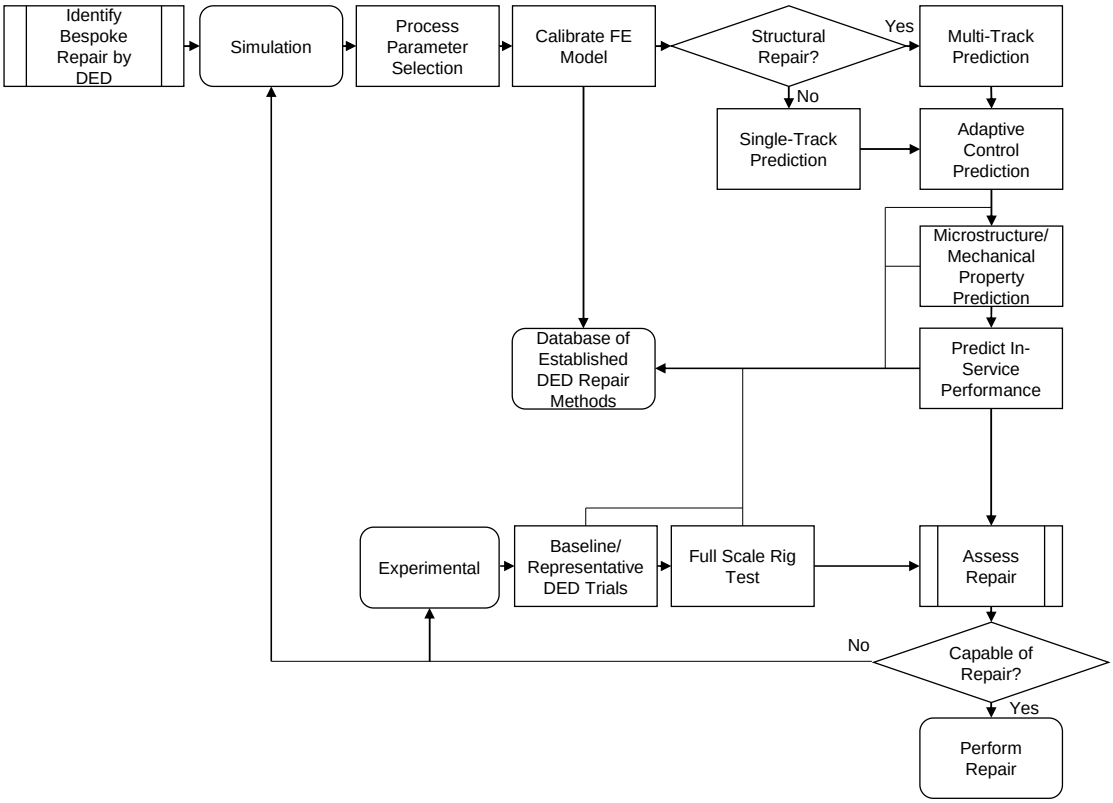

(b)

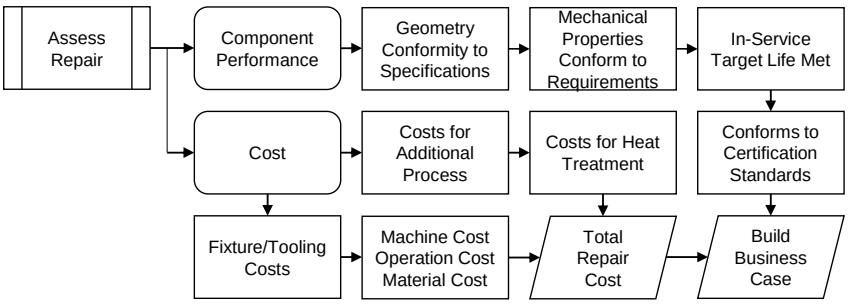

(c)

Figure 1.2: Process flow to determine the use of DED for repair. (a) General information of the repair process. (b) Identifying the process capability using experimental and modelling methods. (c) Methods to assess if the repair using DED is viable.

If the part shows non-conformity and would sacrifice the safety of operation, then a repair scheme would be identified. If traditional methods were not suitable for repair then the process of evaluating DED would continue.

The process used to evaluate DED could involve both an experimental and a simulation testing program. The simulation method would involve process parameter selection to calibrate the FE model which can then be used to assess a potential repair scheme. If a structural repair was required (Figure 1.1), a multi-track prediction would be implemented; however, if this was not required, a single-track prediction should be used. In conjunction with these two methods, an adaptive control model could be used to identify if less material was required or if tailored material properties could be attained through variation of the process parameters. Finally, microstructure and mechanical property predictions will be required to enable a representative in-service simulation to be completed, enabling a true assessment of the proposed repair scheme. To enable validation of the proposed repair scheme, experimental trials may have to be completed in parallel to the simulations. This could include representative small scale DED trials which could be scaled up to complete a full scale rig test of the repaired component. Experimental validation, although costly, would provide greater confidence in the repair method allowing a greater assessment of whether DED would be suitable. All of the data generated through the simulation and experimental studies should be entered into a database for established repairs. This would allow other repairs to be more easily identified, as a baseline study could be performed based on existing data and then refined using the proposed methodology in Figure 1.2(b).

The final stage is to assess the proposed repair based on both component performance and cost. With regards to component performance, the final geometry will have to conform to the original design and drawing specifications, this may require secondary manufacturing methods to machine the repaired section. Upon inspection of the microstructure, or from the predictions, the mechanical prop-

erties must also conform to the original design intent. This will ensure that the structural integrity of the component is maintained in service and the operational life has been extended. Finally, the repair methodology and its performance have to comply with the certification standards of the regulatory body that governs where the component will be used in service. For costing, many factors have to be taken into consideration, this may include costs from secondary manufacturing or heat treatments to ensure the component conforms to geometrical function and also mechanical performance. To enable the repair to be completed, tooling and fixtures may have to be designed and manufactured, therefore increasing the overall costs. Other expenses will include; the machine, operational and material costs. If the total repair costs are less than the re-manufacture, and a viable repair is generated which conforms to the in-service requirements, then DED should be used. If these conditions are not satisfied then further iterations should be included following the methodology outlined in Figure 1.2(b) and Figure 1.2(c).

Modelling methodologies to represent the DED process have evolved from experimental empirical models to numerical models, allowing key parts of the process to be modelled efficiently. However, limited modelling methods exist which allow the thermo-mechanical effects of the process to be predicted based on the process parameters of DED. Currently, the modelling methods are segregated to allow for sub-sections of the process to be predicted, which include; the powder stream, melt pool process, track formation and the thermo-mechanical effects. Due to the similarity between traditional welding and DED, the theory of Computational Welding Mechanics (CWM) is often applied in conjunction with the Finite Element Method (FEM), to model the thermal and mechanical effects of the process.

Currently, the research in this area involves quantifying the process in distinct stages with a large amount of understanding being determined through experimental investigation. No attempt has been made to model the process as a single

entity to predict both the thermal and mechanical effects of the process. It is also apparent that if the existing modelling strategies are implemented, the flexibility of the DED process would be neglected and in turn, the complex repair strategies that could possibly be implemented. Therefore, a numerical approach which allows the whole process to be simulated is required.

1.2 Research Aims and Objectives

The aim of the present study was to develop generalised numerical tools which modelled the coaxial laser deposition process with accuracy. The chosen alloy system used for the whole study was Inconel 718 (IN718) due to its current widespread use in high value aerospace components, which benefit from repair and overhaul. The objectives for this research were as follows:

- An automated method to calibrate thermal Finite Element (FE) models, based on experimental data was developed to ensure accurate prediction of the thermal fields. The model was based on a multi-objective optimisation to determine the optimum element size, process efficiency and the parameters of the heat source for prescribed process parameters. The developed method was used to calibrate the entire process window for depositing IN718, allowing the optimised parameters to be used for subsequent thermo-mechanical models.

- A method to predict and implement a realistic single-track profile, to determine the thermal and mechanical effects of the process, was developed. The proposed methodology was experimentally validated at each stage of the modelling process for a single-track deposition. To encompass the flexibility of the DED process, the methodology was extended to allow in-situ process parameter variations to be considered. A corresponding experimental trial was conducted to evaluate the thermo-mechanical effects, utilising

an in-situ parameter change.

- A validated method to predict the track profile, thermal fields and the subsequent melt pool geometry arising from multiple overlapping tracks was developed. Based on the single-track deposition models, the approach was extended to determine the mechanical effects of multi-track depositions. An experimental programme to assess the effect of the tool path and overlap ratio on the final deposition geometry was devised, with the corresponding numerical predictions being completed. Using the proposed methodology, a parametric study was conducted to evaluate the effects of deposition strategy and overlap ratio on the subsequent thermal and residual stress fields.

1.3 Thesis Outline

Chapter 2, the literature review, presents the key principles of DED, more specifically discussing the process of coaxial laser deposition. The theory of CWM and the use of Heat Source models were discussed, together with how they are utilised to model the DED process using a numerical approach. Previous methods to calibrate the thermal portion of the FE modelling approach were critically reviewed. Empirical formulations, analytical and numerical models were reviewed for three key research areas of DED which included; single-track deposition, adaptive process control and multi-track deposition. A review of all the previous methodologies was presented and knowledge gaps were identified to justify the proposed research work.

Chapter 3 discusses the underlying methodologies used to model the DED process for this work. An analytical model used to represent the behaviour of the powder stream for the process was presented in conjunction with an approach to calculate the powder catchment efficiency. The associated theory and

modelling strategy to represent the DED process using a sequentially coupled thermo-mechanical FE model was discussed in detail. The heat source model used throughout this work, and the associated material properties for the alloy system (IN718), was presented. The second section of this chapter discusses the experimental methods used to validate the modelling methods derived in this work. The experimental methods include; the deposition process, metallographic analysis of deposition specimens, thermocouple measurements and the use of Neutron Diffraction (ND) to predict residual stress.

Chapter 4 presents an automated numerical model which calibrated the entire thermal model for DED. As part of this modelling method, an optimum element size was derived, which can be used in subsequent mesh designs required to model the DED process. The multi-objective optimisation algorithm was evaluated to determine the parameters required to produce a unique solution. Numerical and experimental data is presented to calibrate the laser deposition rig across the entire process parameter window.

Chapter 5 implements an analytical-numerical modelling strategy to predict the thermo-mechanical effects in a single-track deposition. A realistic track profile was implemented into the FE model, derived from an analytical representation of the powder stream and its interaction with a moving melt pool. The process was simulated for a constant set of process parameters. A corresponding experimental investigation was conducted to validate the proposed modelling methodology through the use of in-situ temperature measurements and ND measurements. A study was conducted to determine the effects of utilising a simplified deposition geometry upon the predicted thermal histories and residual stress profiles.

Chapter 6 introduces the concept of adaptive process control for DED. The

chapter presents a general modelling methodology to predict the deposition track profile arising from in-situ modifications to the process parameters. The modelling method was validated using an experimental trial, with an in-situ modification generated by varying the laser power. For this case, the thermo-mechanical effects are predicted and validated through in-situ temperature measurements and ND measurements.

Chapter 7 presents a method to predict the thermal fields and melt pool geometry for overlapping deposition tracks. Based on this approach, and with the use of analytical models within the literature, a method to predict the geometry of a multi-track profile was developed. An experimentally validated FE model, which predicted the thermo-mechanical effects for two common deposition strategies ,was also presented. A parametric study to determine the effects of track overlap ratio and deposition strategy on the residual stress formation concludes the chapter.

The conclusions of this work were detailed in **Chapter 8** and suggestions for future work were also discussed.

Chapter 2

Literature Review

2.1 Introduction

In this chapter, the basics of Direct Energy Deposition (DED) utilising a laser heat source is presented, more specifically focused on the coaxial deposition process. Methods used to characterise the thermal and mechanical effects of the process are introduced. A review of the key modelling methods, which include: empirical, analytical and numerical models, are discussed. The use of Computational Welding Mechanics (CWM) and numerical modelling strategies used to predict the thermo-mechanical effects induced by the DED process are then critically reviewed.

2.2 Direct Energy Deposition

2.2.1 Laser: Fundamentals and Operation

Laser is an acronym of 'Light Amplification by Stimulated Emission of Radiation' and are devices which produce an intense beam of light. The wavelength of a laser source is narrow and is highly monochromatic when compared to other light sources . The wave formation generated in the laser spectrum are in phase

and are therefore coherent with one another. This results in low divergence of the beam, allowing it to be focused to a very small spot. The fundamentals of laser operation relies on the excitation of an electron using an external medium [11]. When an electron has a higher energy, it must decay to a lower energy state and when doing so, a photon of radiation is released through spontaneous emission. When this occurs the emitted photon has both random direction and phase. However, if the energy of an electron does not spontaneously decay, and an incoming photon passes within the stimulation range of the electron, emission of a photon with an identical wavelength, direction and polarisation occurs. This process is called stimulated emission, which adds to the amplitude of the wave, therefore amplifying the initial stimulating photon [11].

Every laser system contains an active/gain medium situated within an optical resonator as shown in Figure 2.1. The gain medium can be in the form of a solid, liquid or gas and will have the required properties to increase the amplitude of the light passing through it by stimulated emission [12]. To allow the laser source to be used for industrial applications, the beam of light is passed through various optical arrangements, including a collimator and focusing lens.

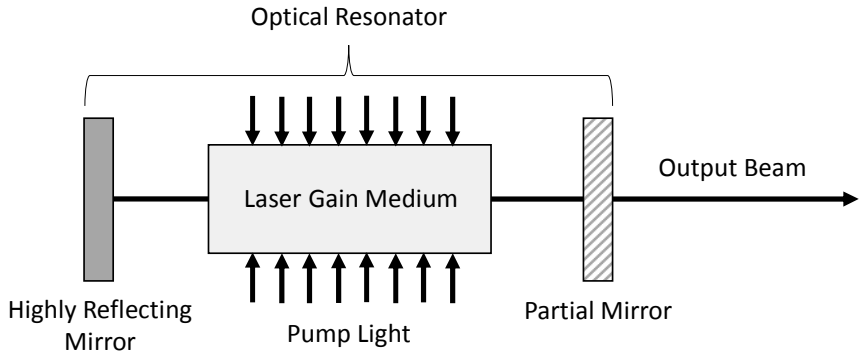

Figure 2.1: A schematic of a simple optically pumped laser.

Industrial lasers are classified into three main categories; solid, liquid and gas, with the classification being dependant upon the nature of the gain media utilised. It is common for industrial lasers to use either fibre, diode or CO_2 as the gain

media [12]. As the current research study utilises a Nd:YAG fibre laser system, only this type of laser will be considered here. Most fibre lasers are pumped using laser diodes, allowing them to operate at a higher gain. This results in a high powered laser output [13]. Amongst this classification of laser, ytterbium doped fibre lasers are the most powerful. The Nd:YAG laser type is often a neodymium doped Yttrium Aluminium Garnet (YAG)($Y_3Al_5O_{12}$), which is a synthetic laser crystal medium [13]. YAG is a gain medium with favourable properties, particularly for high-power laser applications, and offers substantial laser gain for moderate pump intensities. The emission of laser light from a fibre can either be pulsed or continuous and is in the range of kilo-watts (kW). The main advantage of fibre lasers over other commercial laser types is that a very high quality beam with a small spot size is produced, as a small diameter fibre core is utilised. Since the beam can be focused to a small diameter, fibre lasers are very efficient. This is because a high powered beam can be produced from a small power input by the pump source. It should also be noted that unlike any other commercial laser, the laser beam is generated within a single system, therefore, fibre laser is stable and can be used for a wide range of applications.

2.2.2 The DED Process

DED is being increasingly used within the advanced manufacturing sector for rapid repair applications [14]. This processing technology provides increased flexibility in the repair strategy that can be implemented when compared to other Additive Manufacturing (AM) techniques [15]. A schematic of the DED process is presented in Figure 2.2.

The DED process involves a laser source irradiating a metallic substrate to generate a moving melt pool. The feedstock material may be delivered in powder, wire or strip form and conveyed to the work area using a nozzle and an inert gas stream [16]. Unlike many other processes, DED combines the material and energy

delivery process into a single system (Figure 2.2). This allows inert gas to be fed around the deposition to minimise high oxidation rates [17] that arise from high temperature metal processing.

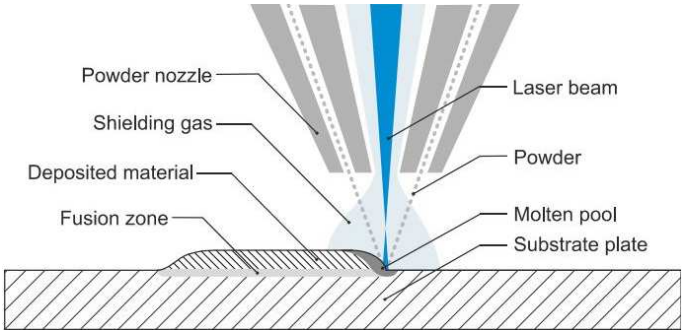

Figure 2.2: A schematic of the coaxial powder fed DED process using a laser heat source [18].

The moving melt pool is generated from the deposition head moving relative to the substrate surface [16]. A substrate is fixed to a CNC table and has a similar material composition to the material feedstock [19]. The feed material in the process is directly fed to the substrate using a single or coaxial nozzle geometry [16]. When the feed material impacts the substrate, it will become molten. As the melt pool is moving, a pool of molten metal will travel in time and space, thus creating a three dimensional deposition track [19]. The track will always form directly below the centre of the deposition nozzle as observed in Figure 2.2. The cross-section of the track geometry produced through DED and the associated variables used to define its geometry is presented in Figure 2.3. Upon completion of a single track, the substrate will move via the CNC table relative to the deposition head along a defined tool path. The process is repeated for each required track to be fabricated, enabling the component to be repaired.

The DED process consists of various operating parameters which are monitored and controlled to obtain a successful build with good part quality. The prominent operating parameters used within the process are: traverse velocity (V), laser tool path, laser power (P), spot radius (R) and material feed rate ($\dot{m}$)

[19]. Due to the high magnitudes of temperature present during the process, and the re-melting of subsequent deposition tracks, a high thermal gradient will be present within the Heat Affected Zone (HAZ). Due to the rapid cooling rates present in the process, in-situ deformations and residual stresses will be present within the component.

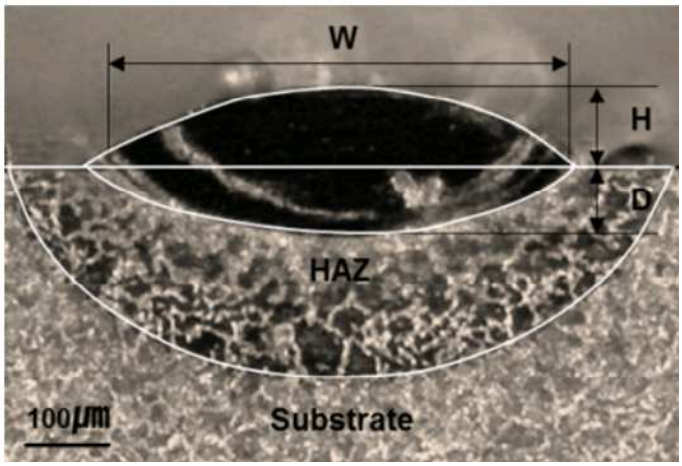

Figure 2.3: The cross-section of the track geometry fabricated by DED. W, H and D is the track height, width and depth respectively [20].

2.3 Experimental Investigation to Characterise the Thermal Effects

For the DED process, thermal energy is transferred to the substrate and any previously deposited tracks to cause the material to melt. To quantify this phenomena experimentally, two experimental methodologies exist which include analysis of the Fusion Zone (FZ) from a metallographic specimen and in-situ thermal history measurements of the process. For analysis of the fusion zone, a two-dimensional (2D) specimen perpendicular to the traverse direction of the laser is often used [21–25]. The use of the metallographic specimen allows the shape and the geometrical parameters of the melt pool geometry, to be determined, allowing the validation of numerical models of the process. This type of experimental characterisation can also be used for microstructural characterisation in the region of

the track, fusion zone, HAZ and the substrate material; however, this was beyond the scope for the current work. It should be noted that the variation in the microstructure, between each of the zones, allows the shape of the fusion zone to be identified.

To measure the in-situ thermal histories of the process, thermocouples are often used due to their high temperature range and low cost. Often, a number of thermocouples are spot welded to the upper surface of the work piece, allowing a number of thermal histories to be measured at different locations. However, due to the high magnitude peak temperatures during the process, each thermocouple has to be sufficiently insulated, or be a suitable distance away from the peak temperature location. Although many factors affect the thermal histories of the process, the thermocouple measurements allow the heating rate, peak temperature and the cooling rate to be determined.

2.4 Experimental Investigation to Characterise Residual Stresses

During the DED process, extremely high temperatures are exhibited within the material. Due to the cooling of the component, high magnitude residual stresses are present. These stresses are undesirable as they can affect the components in service performance through reduction of the fatigue life. Prediction of the residual stress fields within repaired components is imperative to try and control this phenomena to prevent in-service failures. The thermal field during the deposition process is non-uniform due to the adopted tool paths and associated heating and cooling rates. The rapidly changing temperature gradients within the material will induce thermal strain. During the heating and cooling portions of the process, the HAZ and fusion zone will expand and contract respectively; however, this motion is restricted by the substrate and previously deposited material. As

the component cools to room temperature, the molten material attempts to contract back to its original volume, however, the remaining material prevents this from occurring, resulting in the formation of residual stresses. Often, a high tensile region is present around the fusion zone and the HAZ, which is compensated by a compressive stress away from this area.

To measure residual stresses within components, two common methods are implemented for engineering materials, including destructive and non-destructive techniques. The destructive methods rely on strain relaxation by removing a portion of the material from the component. From removing material, the component will alter its shape which is measured using strain-gauges or a Coordinate Measurement Machine (CMM). The stress is then calculated from the change in strain and through using a constitutive material law. The major benefit of using destructive testing is the simplicity of the approach and the results are not affected by the microstructure arrangement within the material. However, the approach is sometimes limited to a specific geometry and a major disadvantage is the permanent damage caused to the component. Common non-destructive techniques include:

- **Hole-drilling**: A blind hole is drilled with a diameter ranging from 0.5 to 4 mm at the centre of the strain gauge [26]. The residual stresses are reduced in the location of the hole and the associated strain is measured by the strain gauge. The residual stress is calculated by a mathematical model; however, the method is not sensitive to steep stress gradients.

- **Compliance method**: Many strain gauges are attached to the component and a small slot is cut using Electric Discharge Machining (EDM) [27]. The depth of the slot is increased and the associated difference in strain is measured using the strain gauges. The depth of the slot versus the difference in strain is recorded. This method is suited for thick materials.

- **Contour method**: The component is cut into two pieces using EDM and the exposed surface is measured using surface microscopy. The deformed surface is modelled using the Finite Element (FE) method and the stress required to return the surface back to a flat condition is calculated [28]. The method allows a full tri-axial stress state to be predicted, however, the accuracy is highly dependant upon the quality of the EDM cut.

Non-destructive techniques allows for multiple stress components to be evaluated without permanently damaging the component. However, the results are often highly dependant upon the grain orientation, size and chemical composition of the component. Another drawback is that this methodology has a greater associated cost than for the destructive techniques. The two main techniques include:

- **Ultrasound**: The ultrasound method applies a polarised ultrasonic wave to the external surface and is allowed to penetrate through the depth of the component. The velocity of the wave is related to the stress magnitude [29]. A comparison between the stress free material and the stressed material is completed to calculate the resultant residual stress in the component.

- **Diffraction**: The method works by the diffraction of radiation from a crystalline structure [29]. The lattice strain of the measured component is determined by calculating the difference between the lattice spacing of the component and a strain free reference sample. The two most common diffraction methods include X-ray diffraction (XRD) and neutron diffraction (ND). A major disadvantage of the method is the high associated costs.

2.5 Numerical Modelling of AM Processes

Various techniques within AM fabricate or repair three-dimensional (3D) parts layer by layer. The energy sources used in many AM processes replicate those used

in traditional welding processes, therefore a number of modelling methodologies are shared between the two manufacturing processes. Common methodologies exist which can be used for process modelling of the AM processes outlined in Table 1.1. A comparison of the AM processes tailored for repair and the associated modelling methods for key outputs of the process are presented in Table 2.1.

Table 2.1: Examples of modelling methods and the associated literature used to capture the process physics of Powder DED, WAM and PBF.

	Powder Direct Energy Deposition (DED)			
	Process Physics			
Modelling Methods	Deposit Properties	Heat Transfer	Melt Pool Physics	Mechanical Properties
Empirical	[30–34]			
Analytical	[25, 35, 36]	[16, 25, 37]	[16, 38]	
CFD	[39, 40]	[39, 41]	[39, 42]	
FE Method	[43]	[16, 43–46]	[41, 47]	[45, 46, 48, 49]
	Wire Additive Manufacture (WAM)			
Empirical	[50, 51]			
Analytical	[52]	[52]		
CFD	[53]	[53–55]	[53–55]	
FE Method	[56]	[56–59]	[56–58]	[56–59]
	Powder Bed Fusion (PBF)			
Empirical	[60, 61]	[60]		
Analytical	[62]	[63, 64]		
CFD	[65, 66]	[65–67]	[65, 67]	
FE Method	[68]	[69–73]	[72, 74, 75]	[68, 73, 75, 76]

From Table 2.1, it is clear that there are similarities between the modelling methodologies and the associated physics of the AM processes. Across all three technologies, it is apparent that empirical modelling approaches are only viable to determine the properties of the deposit, such as the width and height. This is due to the complex physics and the high number of process variables associated

with AM, especially when predictions of the thermal and mechanical effects of the process is required. Similarly, analytical and CFD models are restricted to predict the process physics for the deposit, heat transfer and the melt pool physics; however, these approaches cannot be extended to predict the mechanical effects of the AM processes. To enable all of the key physics and stages of the AM processes to be captured, from the literature, it is clear that a combination of thermal and mechanical FE methods should be used. This is similar across all of the presented AM processes in Table 2.1, therefore further identifying the shared process physics between different AM processes.

For AM processes, electron or laser beam heat sources are commonly used [77]. However, the major difference to traditional welding is the number of process parameters present, therefore increasing the complexity of the process physics and the modelling approach required. Generally the modelling of AM is divided into two sub-scale models, mesoscale and macroscale modelling. Mesoscale models focus on quantifying the characteristics of the melt pool and/or the solidification of the material feed [78]. Macroscale models aim to predict the effect the process has on the final fabricated part, such as; microstructure formation, thermal deformations and residual stresses [19]. Figure 2.4 provides a visual representation of each stage of AM processing and the branch of modelling which is applicable.

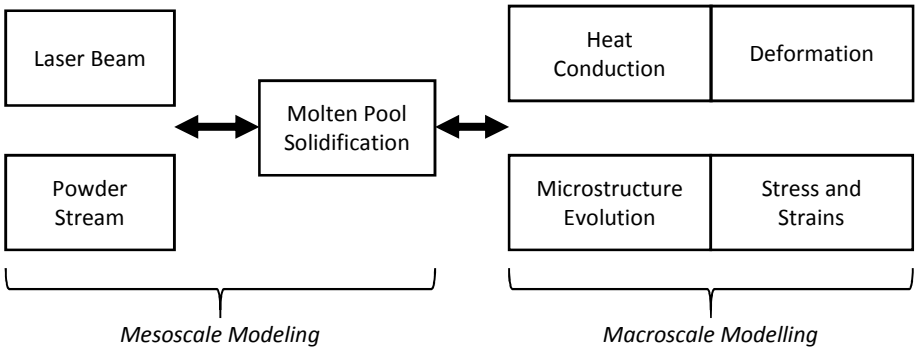

Figure 2.4: Stages of AM processing and the associated modelling scale. Modified from [19, 77].

For all of the couplings of CWM to be implemented, the thermal and mechanical fields should be solved simultaneously using a fully coupled thermo-mechanical FE model. However, this can lead to a large un-symmetric system of equations that must be solved. This is computationally demanding and can lead to long analysis times. When conducting a welding analysis, couplings two and five are often neglected due to their negligible effects [79]. Often, coupling four and six can be predicted before the analysis, therefore, it is possible to preform a weakly coupled analysis. This allows a modular approach to be used, in which the remaining coupled fields are solved using a staggered solution procedure [80]. The most common approach is to complete a thermal analysis followed by a mechanical analysis, leading to a sequentially coupled thermo-mechanical FE model. The temperature field is predicted first, which are applied to the mechanical model as thermal strains. A flowchart of the sequentially coupled procedure, implemented in a commercial FE code, is presented in Figure 2.5.

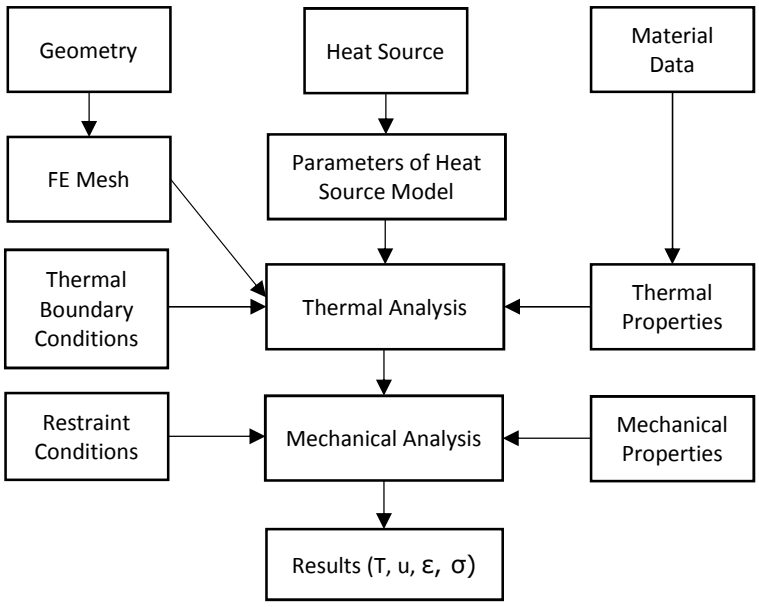

Figure 2.5: A flowchart showing the sequentially coupled FE procedure for a commercial code.

It is apparent that from Figure 2.4 that the modelling of the melt pool and solidification of the feedstock material is what links the two scales of the mod-

elling approaches. To model the thermal field and mechanical effects of AM processes, CWM is often implemented. CWM considers the couplings between three different fundamentals of the process; the thermal cycles, mechanical response and microstructure evolution. Early formulations of CWM were based on analytical solutions or simplified models, however, it is now common to use the Finite Element Method (FEM). CWM primarily focuses on the macroscale of the process and treats the molten material as a soft solid, with the heat source being represented as an analytical distribution of heat flux [77]. Therefore, the fluid flow is neglected as very different spatial resolutions and material properties are required [79]. Therefore, the physics of the melt pool are considerably simplified. The couplings of CWM are presented in Figure 2.6.

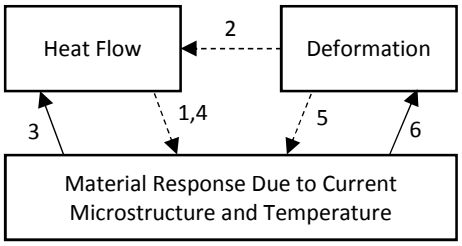

Arrow	Definition
1	Temperature changes drive deformation via thermal expansion
2	Deformation generates heat and affects the thermal boundary conditions
3	Thermal properties depend upon microstructure and phase changes depend on latent heats
4	Thermal driven phase change
5	Deformation drives phase change
6	Materials mechanical properties depend on the current microstructure and temperature

Figure 2.6: The couplings associated with CWM. Modified from [77].

2.5.1 Thermo-mechanical (Metallurgical) Analysis

The thermal analysis of a sequentially coupled model is governed by the non-linear transient heat conduction equation. In a stationary medium, the governing equation has the form [81]:

$$\frac{\partial}{\partial x}\left(k(T)\frac{\partial T}{\partial x}\right)+\frac{\partial}{\partial y}\left(k(T)\frac{\partial T}{\partial y}\right)+\frac{\partial}{\partial z}\left(k(T)\frac{\partial T}{\partial z}\right)+Q=\rho C_p\frac{\partial T}{\partial t} \tag{2.1}$$

where $k(T)$ is the temperature dependant thermal conductivity, T is temperature, Q is the heat generation per unit volume, ρ is density of the material, C_p is specific heat capacity of the material, t is time and x, y and z are the Cartesian coordinates of the domain. Re-writing the governing equation (Equation 2.1), in terms of and enthalpy balance, allows the second order equations to be discretised using the FEM [79, 81]:

$$\frac{\partial}{\partial x}\left(\frac{k(T)}{\rho C_p}\frac{\partial H}{\partial x}\right)+\frac{\partial}{\partial y}\left(\frac{k(T)}{\rho C_p}\frac{\partial H}{\partial y}\right)+\frac{\partial}{\partial z}\left(\frac{k(T)}{\rho C_p}\frac{\partial H}{\partial z}\right)+F=\frac{\partial H}{\partial t} \tag{2.2}$$

where $H=\int_{T_n}^{T_{n+1}}\rho C_p\ dT+(Latent\ Heats)$ and F is equal to the heat source model, which represents the heat flux of the process. It should be noted that Equation 2.2 can be modified to include the latent heat of fusion/solidification and possible phase transformations. The discretised form of Equation 2.1 and 2.2 becomes:

$$\begin{aligned}\mathbf{M}\dot{\mathbf{H}}&=\mathbf{F}_{ext}-\mathbf{F}_{int}\\ \mathbf{C}\dot{\mathbf{T}}&=\mathbf{F}_{ext}-\mathbf{F}_{int}\end{aligned} \tag{2.3}$$

where $\mathbf{M}$ is the mass matrix, $\mathbf{C}$ is the capacity matrix, $\mathbf{F}_{ext}$ and $\mathbf{F}_{int}$ are the external flux and internal flux generation vector. The discretised domain is represented using a series of geometrical elements for the FEM, consisting of nodes (discrete points) at the corners of the geometrical entity. For the temperature

field, discrete values are computed at the nodes. Each element is represented by a shape function, usually in the form of a low order polynomial. This is used to interpolate the solution between the discrete solutions. Therefore, the temperature field within each element and the corresponding temperature gradient can be expressed as:

$$T(\mathbf{x}, t) = \mathbf{N}(\mathbf{x})\mathbf{T}^e(t) \tag{2.4}$$

$$\mathbf{g} = \nabla\mathbf{T} = \nabla\mathbf{N}(\mathbf{x})\mathbf{T}^e(t) = \mathbf{B}(\mathbf{x})\mathbf{T}^e(t) \tag{2.5}$$

where $\mathbf{N}(\mathbf{x})$ is a matrix containing the element shape functions, $\mathbf{T}^e(t)$ is a matrix containing the element temperatures and $\mathbf{B}(\mathbf{x})$ is a matrix which contains the first derivative of the shape functions. The contribution of each element to Equation 2.3 is then calculated from [79]:

$$\begin{aligned} \mathbf{C} &= \int_{v_e} \rho c(T)\mathbf{N}^T\mathbf{N}dv \\ \mathbf{F}_{int} &= -\int_{v_e} \mathbf{B}^T\mathbf{K}\mathbf{B}dv\mathbf{T}^e = \mathbf{k}^e\mathbf{T}^e \end{aligned} \tag{2.6}$$

where $c(T)$ is the temperature dependant specific heat, $\mathbf{K}$ is the thermal conductivity, v_e is the element volume and $\mathbf{k}_e$ is the elements material matrix. These equations are solved using a computationally efficient integration scheme. Often the Newton-Raphson method is implemented.

Upon solving the temperature field, the mechanical model can be defined using a discretised method. As the melt pool physics are replaced with a heat source model, the inertia effects in the mechanical response are negligible; therefore, the mechanical analysis is quasi-static having the following form [82]:

$$\mathbf{M}\ddot{\mathbf{U}} \approx 0 = \mathbf{F}_{ext} - \mathbf{F}_{int} \tag{2.7}$$

where $\mathbf{M}$ is the mass matrix, $\ddot{\mathbf{U}}$ is the acceleration matrix, $\mathbf{F}_{int}$ is the internal force due to stress and $\mathbf{F}_{ext}$ is the external load vector. The external load vector for

this case will arise from the boundary conditions. This includes the displacements arising from the thermal strain. The thermal strains are computed from the thermal expansion coefficient of the material and the temperatures determined from the thermal analysis. Therefore, to successfully couple the two models, the FE mesh used for each model must be identical. As the solution procedure for the mechanical model is non-linear, an incremental solution procedure is required [83]. To solve the displacement matrix ($\mathbf{u}$), for each time step used for the thermal analysis, the following equation is used:

$$\mathbf{u}(\mathbf{x}_i^{n+1}, t) = \mathbf{N}(\mathbf{x}_i^{n+1}, t)_i^{n+1}\mathbf{u}(t) \tag{2.8}$$

where $\mathbf{x}_i^{n+1}$ is the estimated position of the nodal coordinate at the end of the time step, n is the current node number and i is the iterative count. The iteration will progress until a equilibrium convergence criteria is met. As the material properties are temperature dependant, the elements stiffness (k^e) will also be dependant upon temperature. Therefore, the stiffness matrix is also solved for each time step of the analysis. The contribution of each element to the global matrix of equations is therefore:

$$\begin{aligned} \mathbf{F}_{ext(i)}^{n+1} &= \mathbf{K}_i^{n+1}\mathbf{U}_i^{n+1} \\ \mathbf{K}_i^{n+1} &\approx \frac{\partial_i^{n+1}\mathbf{F}_{int}}{\partial \mathbf{u}} \\ \mathbf{f}_{int(i)}^{n+1} &= \int_{v_i^{n+1}} \mathbf{B}_i^{T(n+1}\sigma_i^{n+1} dv \end{aligned} \tag{2.9}$$

The integration is solved through the Newton-Raphson scheme and through inversion of the global stiffness matrix, the nodal displacements are calculated. From interpolation of the nodal displacements and the use of a material constitutive equation, the stress and strain across each element can be predicted.

To account for the metallurgical effects of the process, three common methods

are adopted, which include utilising a thermal-metallurgical-mechanical (TMM) analysis, accounting for microstructure changes using simplified expressions or neglecting them. The TMM approach was devised and used by Ronda *et al.* [84]. Microstructure evolution is predicted by determining the main phase fractions present during the process. The formulation generates a large system of asymmetric equations and often requires prior assumption of the characteristics of the metallurgical behaviour of the material. Therefore, there is limited usage of this approach. The second method neglects the third coupling from the process (Figure 2.6) and therefore assumes that the thermal field is the only driving force for the microstructure changes. To include this effect, two possible equations can be coupled with the second order conduction equations (Equation 2.1). These include the Johnson-Mehl-Avrami-Kolmogrov equation (JMAK) or the Koistinen-marburger relationship. These approaches are commonly used for materials where the metallurgy of the alloy system is well developed. The JMAK equation simulates the diffusive phase transformations during the heating phase of the process [85–87]. The Koistinen-Marburger relationship allows the inclusion of the non-diffusive transformations during the cooling phase [88]. However, with these relationships, an element of experimental calibration is required to derive coefficients of the equations. A major disadvantage of these methods is that they can only determine a percentage of the material phase present. Therefore, no information about microstructural growth, phase boundaries or dislocation density can be determined. For some alloy systems, it is often acceptable to neglect the miscrostructural changes of the process; therefore, this is the most common approach. It is applicable when analysing a location outside of the melt pool which remains as a single phase.

2.5.2 Heat Source Models

Temperature field prediction of the DED process is predominantly driven by the heat source, therefore, this has to be modelled with accuracy. To reduce the complexity of the model, often the physics of the melt pool are simplified and represented as heat source models within the FE solution. Heat source models are classified into four generations, with the first generation being the oldest [79]. Heat source models are usually quantified by their geometrical shape, with the generation and shape selected based on the manufacturing process being modelled.

First generation models consist of analytical equations which can be solved efficiently due to having known solutions for specific types of geometries. The geometry is often considered as an infinite cuboidal plate, with either a thin or thick cross sectional depth. The solution for the thermal field is quasi-stationary, therefore, the temperature distribution is constant in time as it is observed from the coordinate system moving with the heat source. The most common first generation models include the point heat source and line heat source developed by Rosenthal [89] and Rykalin [90] respectively. The point model is generally used for thick plates that generate a shallow melt pool [79]. The line heat source distributes the heat input uniformly over a line segment, with the model typically being used for thick plates with overlaying welds [79]. Rosenthal obtained a solution to the generalised heat flow equation to determine the temperature distribution for a quasi-steady state solution implementing the two different heat source models. This allowed predictions of the thermal field in both thin and thick plates where the heat flow operates in a 2D and 3D regime respectively. For thin plates:

$$T - T_0 = \frac{q}{2\pi kd} exp\left(\frac{-v\zeta}{2\alpha}\right) K_0\left(\frac{vr'}{2\alpha}\right) \tag{2.10}$$

For thick plates:

$$T - T_0 = \frac{q}{2\pi kR} exp\left[\left(\frac{-v}{2\alpha}\right)(\zeta + R)\right] \tag{2.11}$$

where q is the effective heat source power, k is the thermal conductivity, α is the thermal diffusivity, d is the sheet thickness, R is the distance from the point heat source, r' is the distance from the line heat source and ζ is the distance in the traverse direction of the heat source. The approach is effective for computing the thermal field far from the weld pool as infinite temperatures are predicted in the vicinity of the heat source. This is due to the localised application of the heat flux at a definitive point.

The use of second generation models replaced simple geometrical shapes to represent the heat flux with distribution functions, allowing the temperature field to be computed for any geometry. However, due to the nature of the heat flux distribution, the temperature field is often solved using numerical methods, such as the FEM. When solving the temperature field using a second generation model, the accuracy of the temperature distribution in the HAZ and the melt pool is increased in comparison to the point and line model [91]. This generation of heat source model can be divided into two sub categories; surface and volumetric models. This designates the distribution of heat flux which ranges from 2D for the surface flux and 3D for the volumetric flux, where the units are W/m^2 and W/m^3 respectively. A table of common second generation heat source models is presented in Table 2.2. The formulation of the second generation heat source models presented in Table 2.2 are as follows:

Circular Disc:

$$q(x, y, z) = Qexp\left(-\frac{x^2 + y^2}{r_0^2}\right) \tag{2.12}$$

where q is the heat flux distribution in Cartesian coordinates, Q is the effective power input, r_0 is the Gaussian radius of the distribution.

Double Ellipsoid:

$$\begin{aligned} q_f(x,y,z) &= \frac{6\sqrt{3}f_f Q}{abc_1\pi\sqrt{\pi}} exp\left(-\frac{3x^2}{a^2}\right) exp\left(-\frac{3y^2}{b^2}\right) exp\left(-\frac{3z^2}{c_1^2}\right) \\ q_r(x,y,z) &= \frac{6\sqrt{3}f_r Q}{abc_1\pi\sqrt{\pi}} exp\left(-\frac{3x^2}{a^2}\right) exp\left(-\frac{3y^2}{b^2}\right) exp\left(-\frac{3z^2}{c_2^2}\right) \end{aligned} \tag{2.13}$$

where a, b, c_1 and c_2 are the parameters used to define the geometry of the ellipsoid.

Truncated Conical:

$$\begin{aligned} q(x,y,z) &= Qexp\left(-\frac{3r^2}{r(z)^2}\right) \\ r(z) &= r_u + \frac{(r_l - r_u)(z - z_u)}{(z_l - z_u)} \end{aligned} \tag{2.14}$$

where $r = x^2 + y^2$, r_u is the radius of the upper circle, r_l is the radius of the lower circle, z_u and z_l is the upper and lower limit of the conical distribution.

Gaussian Disc and Cylindrical:

$$\begin{aligned} Q_{total} &= fQ_{disc} + (1-f)Q_{cylindrical} \\ Q_{disc} &= Qexp\left(-\frac{x^2+y^2}{r_0^2}\right) \\ Q_{cylindrical} &= Qexp\left(-\frac{3(x^2+y^2)}{r(z)^2}\right) \\ r(z) &= r_c + \frac{z}{h_c} \end{aligned} \tag{2.15}$$

where r_c is the radius of the cylinder and $h_c = z_u - z_l$.

Table 2.2: A table presenting the most common second generation heat source models and their applications.

Heat Source Model	**Flux Distribution**	**Schematic**	**Application**
Circular Disc [92] (Surface $[W/m^2]$)	Gaussian	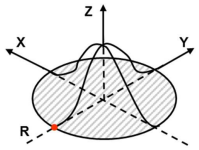	Laser Welding Arc Welding
Double Ellipsoid [91] (Volumetric $[W/m^3]$)	Two elliptical Gaussian regions	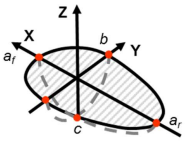	Gas Tungsten Arc Welding Metal Inert Gas Welding Laser Beam Welding
Truncated Conical [93] (Volumetric $[W/m^3]$)	Conical distribution through the thickness	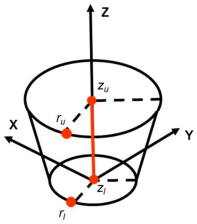	Electron Beam Welding Laser Beam Welding
Disc + Cylindrical [94] (Surface $[W/m^2]$ and Volumetric $[W/m^3]$)	Gaussian with linear distribution through thickness	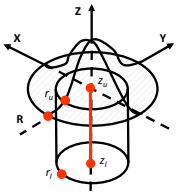	Key Hole Regime: Laser Beam Welding Electron Beam Welding

Third generation models begin to analyse the liquid phase present within the melt pool to predict the shape of the liquid melt region. This was made possible by solving the Stefan problem for the weld pool at the liquid-solid boundary [95]. This allows the heat conduction problem to be solved with the inclusion of phase changes. Through the inclusion of the Stefan problem, it was determined that the rate at which grain growth occured was very different from only solving a linear heat conduction equation [95]. This generation of model can also include the following phenomena; hydrostatic stresses in the melt pool and the surface tension between the liquid and solid interface [79]. Fourth generation models

implement fluid dynamics to investigate the characteristics of the fluid flow within the melt pool. The heat conduction equation is coupled with the Navier-Stokes equations, therefore, forces such as; Buoyancy, Lorentz and Marangoni forces, that act on the fluid phase, can be investigated [79]. Difficulties in implementing and solving the final two generations of heat source models impede their use in commercial FE codes. If an accurate representation of the fluid flow is required, a Computational Fluid Dynamic (CFD) model is often used to explicitly replicate the domain [96–98].

2.5.3 Modelling of the Material Deposition

Within the DED process, material is deposited upon a metallic substrate, which must be incorporated within the modelling strategy. Currently within the literature, there are two common methodologies that can imitate material addition through the reactivation of elements. The two methods are referred to as the quiet and inactive element approach.

Quiet elements are present throughout the entire analysis and are applied to the deposition material only. Before the addition of material is required in the analysis, the elements are made passive by being assigned a low stiffness or thermal conductivity, therefore having negligible effect on the rest of the model [99]. However, a degree of trial and error is required to ensure that the material property values are not too low, therefore, generating an ill-conditioned material matrix. Also, if the selected values are too high, the elements will no longer be passive, causing thermal energy to represented in that part of the domain before the deposition has occurred. When the addition of material has been added, the true material properties are applied as the heat source passes over them. This is achieved by ramping the material properties from the scaled value to the absolute value over the current time step of the analysis. The advantage of this approach is the ease in which it can be implemented within commercial FE codes using user

subroutines [69]. It also allows the nodes of the deposition to move to their new respective locations during the mechanical analysis, therefore limiting the issue of poor element aspect ratios, which can lead to numerical instabilities. With large scale AM models, using the quiet element approach, all of the elements for the build geometry will exist at the beginning of the analysis, therefore increasing the computational cost of the approach.

With the inactive element approach, the elements are not present at the start of the analysis, therefore, they are not included within the global stiffness matrix [99]. When implementing this method, no scaling of material properties is required, mitigating the issue of an ill-conditioned material matrix occurring. As the heat source passes over the element representing the material addition it will be reactivated, i.e. included within the global stiffness matrix. Therefore, as each element is reactivated, the number of equations that is solved per time step increases, making it computationally more efficient. However, as the stiffness matrix has to be reassembled at each time step, for some computing techniques e.g parallelisation of the solver, this method could become computationally demanding. The inactive element approach is commonly adopted for modelling AM processes [77] because of two reasons. The first is that commercial FE codes, such as ABAQUS and ANSYS now contain methods to activate/deactivate sets of elements. This is completed using the *Model Change* function within ABAQUS [100] and using *Birth/Death* element types within ANSYS [101]. The second benefit is that there is a known modelling methodology to implement inactive elements for DED as outlined by Lundbäck *et al.* [102]. A study by Michaleris [103] compared the effects on the temperature field when using either the quiet or inactive element approach to model powder fed deposition. The numerical model represented the deposition of a thin walled structure upon a thick substrate. For the quiet element approach, the thermal conductivity and specific heat capacity were scaled by $1e-6$ and $1e-2$ respectively. When analysing the temperature history

for each approach, the results were identical. However, the inactive approach led to an increase in computational time.

2.6 Calibration of FE Heat Source Models

To implement any heat source model into a FE domain, calibration of the heat source parameters are required to accurately determine the temperature field and the melt pool profile. Accurate predictions of the thermally induced residual stresses and the associated distortions of the process are highly dependant upon the accuracy of the simulated thermal fields [104]. A common approach to heat source calibration is to estimate each parameter of the heat source based on physical measurements of the melt pool geometry. A manual trial and error approach is then completed until a satisfactory representation of the experimentally determined thermal fields/melt pool geometries are achieved. Although this method is simple, it can often be time consuming and due to the trial and error approach, there is no measure of the accuracy of the final calibrated model and therefore is inherently inaccurate. Optimisation methods to calibrate thermal models is becoming more prevalent within the literature.

2.6.1 Optimisation Methodology

Optimisation is an important tool which allows a function to be minimised or maximised until a termination criteria has been satisfied. An optimisation model has to be constructed which identifies an objective which provides a quantitative measure of the system. The objective is dependant upon variables of the system. These are systematically evaluated to determine an optimum set which minimise/maximise the objective. Often the variables are constrained by physical demands of the system being evaluated. The solution of the optimisation model is determined through the use of an optimisation algorithm. This aims

to determine the optimum variables of the objective which are often referred to as the Pareto optimal set [105]. When deciding on an optimisation algorithm, there are no governing rules or any one particular algorithm which will satisfy the problem. Therefore, a choice must be made on which algorithm is tailored to the current system and objective [106].

Optimisation algorithms can be divided into two categories, depending upon the solution which is obtainable. Local optimisation algorithms will attempt to find the minimum solution to the objective function which is smaller than all other feasible points in the local vicinity. However, the solution that is determined as the optimum may not be the absolute minima of the entire system. Global algorithms attempt to determine the absolute minimum solution to the objective function; however, a solution of this type is more difficult to identify and even locate [106]. Optimisation algorithms are an iterative solution procedure, where an initial guess of the optimum variables is used as a basis to generate a series of better estimates of the variables until a solution is reached. The method in which the next iteration is generated often defines the type and methodology of the algorithm used. Most methods will use the values evaluated from the objective function, possibly in conjunction with information from previous iterations to determine the direction of the next function evaluation.

2.6.2 Previous Methods to Calibrate Thermal FE Models

A study presented by Azar *et al.* [107] determined the parameters of a double ellipsoid heat source, utilising an analytical approach to model the temperature field for an arc welding process. The analytical model was based on the work by Myhr and Grong [108]. This allowed the heat source to be represented as a series of discrete point sources, which were evenly distributed throughout the domain. Each heat source contributes to the total heat flux, with this value being determined from; the arc current (I), velocity (v) and efficiency (η). The

effect the heat flux had on the temperature field was determined by analysing the contribution of the heat source in both the transverse ($T(q_t)$) and perpendicular ($T(q_p)$) direction:

$$T - T_0 = \sum_i [T(q_t)_i + T(q_p)_i]$$

$$T(q_t) = \frac{q_t}{2\pi\lambda} exp\left(-\frac{vx}{2\alpha}\right)\left[\sum_{i=-\infty}^{+\infty} \frac{1}{R_i} exp\left(-\frac{v}{2a}R_i\right)\right]$$

$$T(q_p) = \frac{q_p}{4\pi\lambda} exp\left(-\frac{vx}{2\alpha}\right)\left[\sum_{j=-\infty}^{+\infty} \frac{1}{R_j} exp\left(-\frac{v}{2a}R_j\right) + \sum_{k=-\infty}^{+\infty} \frac{1}{R_k} exp\left(-\frac{v}{2a}R_k\right)\right] \tag{2.16}$$

where q_t and q_p are the transverse and perpendicular fluxes respectively, α is the thermal diffusivity, λ is the thermal conductivity and R_i, R_j and R_k are the radial distances from the sources in the i, j and k direction respectively. Isotherms from the analytical model can be determined from Equation 2.16, from this, the geometry of the fusion zone was determined. The dimensions of the analytical melt pool geometry were used to determine the parameters of the heat source model. To test the validity of the approach, a numerical FE model was formulated from the calibrated parameters and the fusion zone geometries from the numerical and analytical approaches were compared. A good agreement was attained with a maximum error of 16.44% and 0.87% for the width and length of the melt pool respectively. It should be noted that no attempt was made to quantify the heat source parameters from an experimental weld. The current methodology was also restricted to the double ellipsoid heat source only. Fu *et al.* [109] also used an analytical approach to define the parameters of a double ellipsoid heat source model for an arc welding process. An analytical solution of the thermal field was derived for a semi-infinite body, using a quasi-static solution for the heat source model. The thermal field was solved using MATLAB to capture the maximum size of the melt pool along with the corresponding ge-

ometrical parameters of the 3D heat source model. These parameters became input data for a neural network to increase the computational efficiency of the calibration procedure. The Levenberg-Marquardt algorithm was used as the basis for the neural network, which was trained using 128 data sets derived from the analytical model. For calibration of the neural network, a further 10 data sets were required. The associated inputs for the neural network included the voltage, current and traverse velocity of the arc, with the geometry of the melt pool and heat source parameters being generated as an output. To evaluate the accuracy of the devised methodology, a transient thermal FE model was used to predict a series of melt pool geometries which were used to compare the results obtained by the neural network. A good agreement was attained between the predicted and experimental temperature profiles, with a maximum error for the peak temperature equating 5%; however, the predicted cooling rate was underestimated by the FE model. The reason for this was that no conductive or radiative losses to the surrounding or CNC bed were included within the thermal field approximation. It should be noted that as the neural network was only evaluated using numerically obtained data, the model may have been inadequate to calibrate experimentally obtained melt pool geometries. Another calibration approach, using the Levenberg-Marquardt algorithm, was presented by Rouquette *et al.* [110]. The method aimed to quantify the effective power, beam diameter and the source position of a Gaussian energy distribution, representing an electron beam heat source. A 2D quasi-steady state model, utilising the commercial code SYSWELD was used to predict the thermal fields of the process and the subsequent melt pool geoemtry. The parameters of the heat source were determined using an inverse problem based on the Levenberg-Marquardt method. The inverse problem consisted of minimising a quadratic function ($S(P)$) for an unknown set of parameters (P). The solution of the inverse problem was obtained when the minimisation of the difference between the calculated and measured

temperatures was achieved, using the least squares method. The expression of the quadratic function had the following form:

$$S(P) = [Y_i - T_i]^T [Y_i - T_i] \tag{2.17}$$

where Y_i was the measured temperatures and T_i were the calculated temperatures determined from the numerical model. As the number of parameters of the function were low, the Levenberg-Marquardt was used to increase computational efficiency. However, the methodology was extensive as a sensitivity analysis was required to determine the effect of each parameter on the final temperature field. The profile of the fusion zone was not included in the validation of the calibration method, nor was it used to determine the heat source parameters. It was also determined that the temperature measurements alone do not allow for the beam diameter to be derived. From comparing the experimental and predicted thermal field, the maximum error for the peak temperatures was 6.97% and for some cases, the cooling rate was again overestimated. Similar to Rouquette *et al.* [110], secondary heat losses were not calibrated within the model.

An automated solution procedure was presented by Belitzki et al. [111], which utilised optimisation algorithms to define the geometrical parameters of a double ellipsoid heat source. The optimisation methodology was based on a least squares regression algorithm to reduce the error between the experimental and numerically predicted weld geometry. The objective function for the optimisation had the following form:

$$\mathbf{u} = \sqrt{\Sigma_{n=1}^{q} (\mathbf{p}_n^{pre} - \mathbf{p}_n^{exp})^2} \tag{2.18}$$

where q is the number of data points, $\mathbf{p}_n^{pre}$ is the predicted melt pool and $\mathbf{p}_n^{exp}$ is the experimental melt pool. The welding process was modelled as a quasi-stationary process using a FE thermal model. Unlike the other calibration methods previously outlined, the temperature histories were neglected from the optimisation

procedure; therefore, a single objective optimisation based on the fusion zone was used. It should be noted that the inclusion of the secondary heat loss effects were neglected from the modelling approach and the calibration procedure. To further refine the calibration procedure, two optimisation techniques were used. Firstly, a global Genetic Algorithm (GA) was used to define the local solution space. The least squares method was then implemented to find the local minimum of the objective function. Overall, a good agreement between the experimental and predicted fusion zone was achieved from the optimisation. A maximum error of 8.9% and 4.4% was achieved for the width and depth of the melt pool respectively; however, due to the requirement of multiple optimisation algorithms, the approach was computationally intensive. To ensure the thermal model was fully calibrated, a sufficient element size should be used which provides a solution independent of the mesh for both the temperature field and subsequent melt pool geometry. Belitzki *et al.* [111] conducted a brief mesh independence study for a single heat source model based on an initial guess of the parameters; however, the final element size was used for the subsequent optimisations. Further to this, no attempt was made to verify the initial element size when using the optimised results for the heat source parameters, therefore, a unique solution may not have been obtained. To address the issue of determining the optimum element size, an automated mesh refinement model for a 3D FE welding model was presented by Lindgren *et al.* [77]. The model refined the mesh in the area of the HAZ to model the non-linear thermal effects at the heat source. The refinement was based on a graded hexahedral element using the h-adaptive method, which is typically used for where the solution has steep gradients present in the independent data set. The refinement methodology firstly used eight node elements across the entire domain, with a further nine to twenty nodes being reserved per element. For each remesh, the number of nodes were increased to a value which allows adequate connectivity between the elements. Secondary to this, the elements

were subdivided to increase the total element count. It should be noted that no attempt was made to measure the error of the solution based on physical quantities, such as the temperature or melt pool area. Instead, the element size was determined based on a simple geometric parameter. This involved calculating the ratio between the current element size and the shortest distance from an element to the heat source path, with the user choosing the combination of this parameter to drive the refinement process. As there were no physical measurements of the error associated with the element size and due to the refinement not being driven by this associated error, a truly independent solution would not have been obtained. Also, as a user input was required to drive the refinement process, a consistent approach would not have been attained between FE models using different processing conditions.

Other than the parameters of the heat source model, the thermal FE analysis also required the process efficiency and the heat transfer coefficients of the secondary losses to be included. This would ensure that an accurate representation of the process was attained. For welding and DED processes, through using numerical and experimental investigations, quantifying these two parameters has received some attention in the literature. Often, to represent the secondary heat losses, a thermal contact conductance coefficient is included on the surface in contact with welding apparatus. Some authors [112, 113] determined both of these parameters through trial and error until the thermal field and melt pool geometry match experimental data; however, this is an inefficient method. Ganser *et al.* [114] used a numerical Computational Fluid Dynamic (CFD) model to determine the process efficiency for a deep penetration weld. The numerical model was calibrated until the isotherm representing the melt pool geometry was equal to the experimental case. This part of the process was completed manually, using a stepwise approach, until a best fit was achieved between the experimental and numerical data sets. A numerical model was used to obtain the predicted melt

pool geometry, however, similar to Belitzki *et al.* [111], a single element size was used for the calibration of the process efficiency, therefore, the validity of the approach was compromised through neglecting this step. To determine the process efficiency, the absorbed power within the melt pool was calculated through integrating the heat flow across the surface of the melt pool. This was then compared to the original input power of the heat source, with the ratio between the two giving the process efficiency. Although the method to determine the process efficiency based on an inverse approach was valid, the accuracy of this parameter was dependent upon the heat source parameters, which were determined through a trial and error. It should also be noted that the predicted thermal histories were not compared to experimental thermal data, therefore, the effect of the process efficiency on the peak temperature was not evaluated. Salerno *et al.* [115] combined an experimental and numerical approach to determine the process efficiency for Tungsten Inert Gas (TIG) welding. The parameters of the heat source model and the element size were not determined as part of this study. The parameters were defined based on measurements of the experimental melt pool geometry and the element size based on previous works by Salerno *et al.* [100]. Two variants of experimental samples were fabricated which involved the substrate being either isolated or in contact with the welding apparatus. Experimental micrographs of the fusion zone and thermocouple measurements were used to determine the process efficiency through a trial and error approach. To quantify the affects of the secondary thermal losses to the welding apparatus, a reduction in the process efficiency was required. This phenomena was not present for the isolated samples, therefore highlighting the importance of including the secondary heat losses to accurately represent the process. Although a relatively simple method to determine both the process efficiency and secondary heat losses were presented, the approach was limited as some key physics were neglected from the initial model and the calibration of the thermal FE model was based on trial and error.

A method to determine the secondary heat losses due to conduction through the thickness of the substrate was presented by Ayoola *et al.* [116]. The method was based on a 3D analytical representation of the thermal field presented by Ashby and Easterling [117], which implemented a surface heat flux distribution representing a laser heat source. A 2D isotherm was used to predict both the energy required to cause melting and the energy required to heat the remainder of the material. To reduce the complexity of the calculated energy losses, it was assumed that only a 2D hemispherical melt pool was achieved. The energy associated with melting (E_{melt}) was calculated as follows:

$$E_{melt} = \left[\frac{1}{2}\pi\left(z_{melt}^2\right)l\right]\left[C_p\left(T_M - T_0\right) + H_m\right] \tag{2.19}$$

where z_{melt} was the depth of the melt pool, C_p was the specific heat capacity, H_m was the latent heat of melting, T_M was the material melting temperature and T_0 was the ambient temperature. The energy required to heat the remaining material was calculated in the same way, however the area was formulated through integrating between each hemispherical temperature interval, from ambient to the melting temperature. This method gave an indication of the energy losses through conduction; however, it would be difficult to determine the percentage of the conduction losses which occurred at the interface of the welding apparatus.

2.7 Process Modelling of DED

A combination of experimental, analytical and numerical methods have been used to model the DED process. The implementation of these methods have only allowed the DED proces to be modelled in sub-sections, as outlined in Figure 2.7. The sub-processes outlined in Figure 2.7 in reality are coupled and govern the entire DED process. However, to date, the modelling methods do not encompass all of the phenomena into a single strategy. Instead, each model captures a

certain part of the process. For example, the physics of the powder stream and laser characteristics will dictate the geometry of the track. Also, the tool path and heat input from the laser will affect the melt pool physics and subsequently, the track formation. A combination of these two phenomena will dictate both the microstructure and residual stress fields exhibited within the component. Therefore, it is important to capture all of these physics in a single approach to ensure an accurate prediction of the process is achieved.

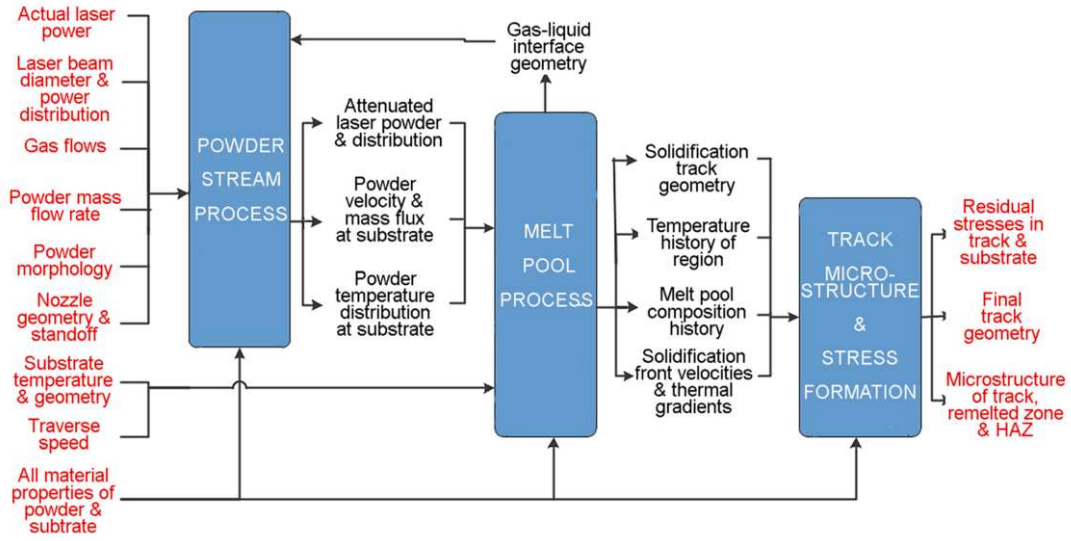

Figure 2.7: A schematic of the sub-processes and process variables corresponding to each stage of the DED process [14].

Often, an analytical model was used to capture the fluid effects of both the powder stream and the melt pool geometry, which could also be determined using complex CFD models of the process as outlined in [114, 118, 119]. It is now well documented that the powder stream distribution for the coaxial nozzle has a Gaussian distribution. This phenomena was determined from the work presented by Pinkerton and Li [120], in which optical images of the powder stream were generated for a series of stand-off distances, utilising a coaxial deposition head. It was established that along the axis of the nozzle, the powder concentration rose exponentially to a peak where the powder outlet passages cross. After this point, the concentration decreases as a reciprocal function of the stand-off distance. It

was also found that when the laser was in focus, a Gaussian distribution was obtained across the stream width. The melt pool physics are often simplified using either an analytical representation of the temperature distribution, or implementing a FE heat source model and solving for the transient thermal field. Melt pools in the DED process are geometrically simple, usually defined by two half ellipses (Figure 2.8).

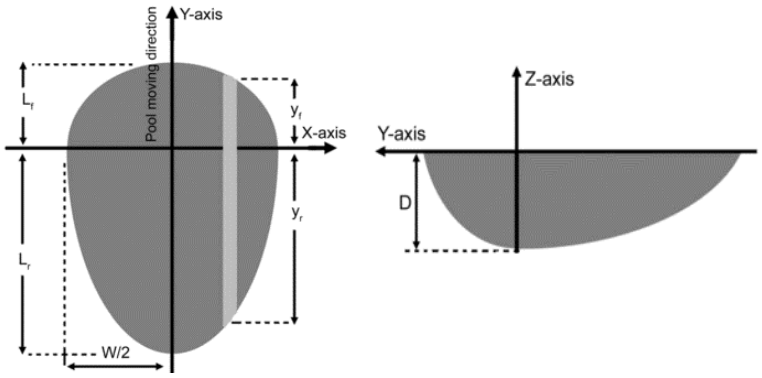

Figure 2.8: A schematic of the basic elliptical melt pool used in DED [25].

At a constant transverse velocity, the temperature behind the heat source decays until ambient temperature is reached [37]. Therefore, the varying aspect ratio arises from the movement of the substrate, generating a thermal lag. To represent the melt pool, it is divided into a front (L_f) and rear length (L_r). The ellipses can be defined using the following equations:

$$\begin{aligned} \frac{y^2}{L_f^2} + \frac{4x^2}{W^2} + \frac{z^2}{D^2} = 1 \\ \frac{y^2}{L_r^2} + \frac{4x^2}{W^2} + \frac{z^2}{D^2} = 1 \end{aligned} \tag{2.20}$$

where W is the melt pool width, D is the melt pool depth and x, y, z are spatial coordinates in the Cartesian system.

2.7.1 Previous Modelling of DED

Typical applications of DED include the repair of initial fabrication defects using single-track depositions. Due to the nature of the DED process in-situ modifications to the process parameters can be included, which could allow a greater control of the track geometry, cooling rates and subsequently the mechanical properties of the component. When the structural repair of a damaged component is required, multiple depositions to fill the geometry are used. Previous modelling of the DED process has included track profile prediction and prediction of the thermal histories. These approaches have been extended to predict residual stress formation, however, these types of models are limited. Modelling of DED has evolved from simple empirical models to the use of numerical models. The most extensive investigations into DED were through experimental testing to derive empirical-statistical models. In recent years, there has been an increase in the number of analytical and numerical models used to represent the DED process [14], with analytical models being prevalent to predict the melt pool and/or the track geometry. Numerical models of DED are commonly used to predict the thermo-mechanical effects of the process.

2.7.2 Previous Methods to Predict DED Track Profiles

Early models to determine track profiles were derived empirically across a range of process parameters, often neglecting the physical complexities of the process, such as the interaction of the powder feed distribution and the melt pool [14]. An empirical model, presented by Kumar *et al.* [30], allowed the track height to be derived based on the laser power and the material mass flow rate. Although the time required to predict the track height was minimal, experimental data was required to calibrate the model. This was required to reduce the maximum error between the predicted and experimental height from 50% to 13%. Davim *et al.* [33], utilised a similar method, with the final equation being derived using

a Multiple Regression Analysis (MRA). The track height and width were determined with an error of 7.6% and 6% respectively. Despite the volume of data collected to inform the model, the percentage error for the predicted melt pool depth was 20.1%, showing a level of inaccuracy with this approach. The main issue with using empirical/statistical models is the experimental data needed to derive the model. This would not be feasible to design repair strategies, as each repair would be bespoke. In addition to this, the empirical approach is limited in providing accurate predictions within the bounds of the process parameters used to define the model. Therefore, to enable the effects of in-situ modifications to be evaluated for bespoke repair applications, a high number of experiments would be required. As this lead to a costly design process, a generalised modelling method allowing the process to be simulated is therefore required.

Picasso *et al.* [43], predicted the track height of a single deposit, using three sub-modelling strategies. This involved solving the power attenuated by the powder particles, the absorption of power into the substrate and the geometry of the elliptical melt region. A 3D analytical model was used to determine the temperature field, allowing efficient prediction of the melt pool geometry, with the track height equalling the melt pool depth. Experimental validation of the analytical model was presented, with a maximum error of 92.7% for the track height. It was noted that the error occurred due to an inaccurate representation of the melt pool geometry derived from the 3D thermal field. As the physics of the DED process are interdependent a more representative analytical model was derived by Ahsan *et al.* [25] to predict the profiel of a single-track. The use of a 3D temperature distribution determined for a moving Gaussian heat source was used to predict the elliptical melt pool geometry. A fully-coupled mass-enthalpy balance was used to ensure a stable melt pool geometry was attained from the thermal field. Similar to Picasso *et al.* [43], power loss attenuated by the powder particles and substrate were included. Furthermore, a physical representation of the pow-

der stream was included through implementing an analytical representation (q_{pf}) determined by Pinkerton and Li [120]. The track profile ($h_z(x)$) was predicted through integration of the powder distribution between the melt pool limits (y_f and y_r):

$$h_z(x) = \frac{1}{\rho V} \int_{y_r}^{y_f} q_{pf} dy \tag{2.21}$$

where ρ and V were the material density and laser traverse velocity respectively. A good agreement for both the thermal fields and track dimensions was attained. As no discretisation of the domain was required, a more computationally efficient model was achieved.

Peyre *et al.* [16] proposed a three step numerical-analytical model to predict the track geometry and thermal histories. The first step required calculation of the temperature profile in the powder stream, this was overestimated by a factor of two. The track height was predicted from obtaining the elliptical melt pool boundaries from the thermal model. This was further discretised to calculate the cell by cell interaction between the powder particles and each melt pool cell to calculate the elemental contribution to the layer growth:

$$\Delta h_{ij} = \frac{D_m^* \Delta l}{\rho V} \tag{2.22}$$

with D_m^* equating the local surface powder feeding parameter, Δl is the cell length, ρ is the material density and V is the laser scanning speed. The track width equated the melt pool width. The track height and width were predicted to within 13% and 10% of the experimental findings. No track profile was derived from the model, with the track being represented as square elements in the subsequent thermal models. It should also be noted that as no moving heat source was used within the thermal model, a transient history of the process could not be predicted. A more advanced model, presented by Alimardani *et al.* [47], determined the transient formation of a 3D track geometry for the entire

deposition process; however this was only developed for a constant set of process parameters. A 3D numerical heat transfer model was utilised to determine the boundary of a moving melt pool. At each time step of the analysis, the mesh was altered to introduce the addition of material into the domain. The height (h) of the track was determined from the powder feed rate ($\dot{m}$), elapsed time (t) and the interaction between the melt pool and powder stream:

$$\Delta h = \frac{\dot{m}\Delta t}{A^{melt}\rho_p} \tag{2.23}$$

where Δt is each time step of the analysis, A^{melt} is the area of the melt pool and ρ_p is the density of the powder. A second order polynomial was used to represent the track geometry; therefore, an idealised representation of the geometry was used for the model. The model allowed a transient representation of the track profile to be determined and the subsequent thermal fields during the process. The peak temperatures were overestimated by the model with a maximum error of 8%. Experimental validation of the average track height was completed with a maximum error of 19.35%.

A 2D numerical model, presented by Ya *et al.* [44], predicted the track geometry based on a mass-energy balance. A Gaussian disc heat source was used to model the external heat flux, with the absorbed energy from the laser equalling the required energy to produce a track. The attentuation power was determined from previous work by Ya *et al.*, as outlined in [121]. From predicting the thermal fields and the associated melt pool, the change in track height during the process for a 2D isotherm was described using the function, $F_0(y, z, t)$. The derivative of F_0 equated a speed term, V_m equal to:

$$V_m = \frac{F_0(y, z, t)}{dt} = \frac{2\dot{m}\eta}{D\rho V_c} exp\left[\frac{-y^2}{r_b^2}\right] \tag{2.24}$$

where $\dot{m}$ is the powder mass flow rate, η is the powder catchment efficiency, D is

the particle diameter, V_c is the velocity of the carrier gas and r_b is radius of the laser beam. Unlike Ahsan *et al.* [25], the track profile was not predicted based on the interaction between the melt pool and powder stream. Instead, a parabolic representation was used to define the profile:

$$F_0(z) = a_0 y^2 + b_0 y + c_0 \tag{2.25}$$

where a_0, b_0 and c_0 are the coefficients of the parabola. Although a physcial representation of the track was neglected, the predictions were in a good agreement with the experimentally obtained optical micrographs, with a maximum error of 5.1% and 5.4% for the track height and width respectively. Pirch *et al.* [122] used a moving mesh technique to simulate the addition of a single track to a discretised domain. A in-house simulation tool (StrucSol) was developed for the rapid solution of the thermal equations, as the solver used a sparse iterative solver. The material addition was accounted for using a Gaussian powder density function similar to the one derived by Pinkerton and Li [120]. The interaction between the powder density function and the predicted melt pool geometry dictated the addition of material and was added to the domain using a time-resolved adaptive re-meshing technique. It should be noted that for the proposed methodology, only the powder density function was experimentally verified; therefore, the validity of the thermal and track profile predictions cannot be confirmed. Although there was merit in the devised approach, the numerical complexity of the model and the use of an in house solver reduces the accessibility of the approach.

For multi-track deposition, each track can be deposited using a different tool path; the most common for DED being the zig-zag and spiral strategy [123]. Each sequential track is overlapped with the previous, utilsing typical overlap ratios (OR's) ranging between 10% and 50% [124, 125]. Limited modelling methods currently exist to predict the profile for sequential overlapping of multiple tracks.

Most commonly, a geometrical based model is utilised, which requires approximation of the track parameters measured from experimental data. A curve fitting approach, derived by Cao *et al.* [126], was used to determine the shape of a multi-track profile. To predict the geometry of the track profile, various mathematical functions were used to represent the experimental data. It should be noted that it was assumed that each subsequent deposition had an identical profile to the initial track. The mathematical functions included, a Gaussian, logistic, parabola and sine function. It was found that the sine function provided the best fit with a maximum error of 0.2%. The most inaccurate fit was derived from the Gaussian function presenting a maximum error of 2.8%. Four geometrical models are used to predict the overlap geometry for multi-track deposits. A method presented by Cao *et al.* [126] determined that the overlap region could be represented by a flat top overlap model (FOM)(Figure 2.9).

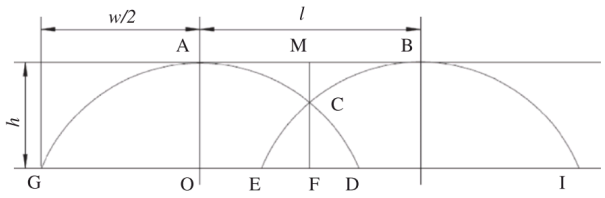

Figure 2.9: A schematic of the FOM multi-track geometry model and the associated parameters [126]. Curve face GAD was the initial track profile, ACB was the region of the valley, ECD was the overlap region, h is the track height, w is the track width and l is the offset distance.

The author assumed that superfluous liquid fills the valley region between two adjacent beads; therefore, the two peaks of the track were joined with a flat plane. The model was used to investigate the optimum overlap ratio to provide a flat surface for subsequent depositions, which equated 36% for this study. The FOM was extended by Ding *et al.* [127] to a Tangent Overlap Model (TOM). A schematic of the TOM is presented in Figure 2.10. Similar to the FOM [126], the initial track was defined based on experiemental data, however, a parabolic fit was used to define the initial track profile. Unlike the FOM model [126],

the relationship between the area of the overlap and valley region are taken into consideration to derive the geometry of the overlap region. The ratio between the two areas dictated the position of intersection for the tangent line between the previous and subsequent track.

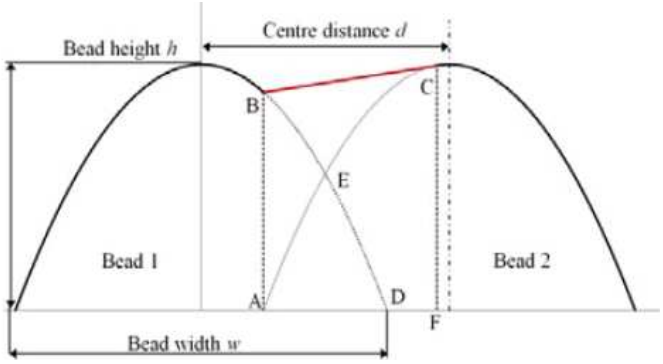

Figure 2.10: A schematic of the TOM for multi-track deposition. BEC defines the region of the valley and AED defines the overlap region [127].

The model was used to determine the optimum OR to obtain a flat surface for susbequent layers, this equated 26%; therefore, the FOM, presented by Cao *et al.* [126], potentially overestimated this parameter. The geometric model was validated for three overlap ratios, with a maximum error of 8% between the experimental and predicted track profile. Another geometrical based model presented by Suryakumar *et al.* [128], represents the geometry of the overlap region using a fillet radii. Similar to the model presented by Ding *et al.* [127], an original bead profile was represented using a parabolic function, with an identical profile assumed for each subsequent track. A schematic of the track profile predicted from the fillet model is presented in Figure 2.11.

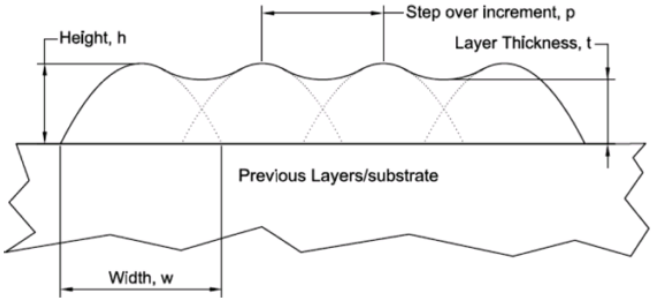

Figure 2.11: A schematic of the track profile predicted using the fillet model [128].

The solution procedure determined the radius of the circle and the two intersection points between the fillet and the first and second track respectively. The two parameters are determined from the roots of two linear equations which were derived through analysing the area of the valley and overlap region. Therefore, the method adopted by Suryakumar *et al.* [128] was similar to that of both Cao *et al.* [126] and Ding *et al.* [127]. A major disadvantage with this approach was the time required for convergence to be met due to a stepwise method being used to solve the system of linear equations. The model was validated for a single experimental deposition at an OR of 20%. The maximum error between the predicted and experimental track profile region equated 7% for the overlap region. A major issue with the geometrical models presented was the prediction of the first track profile, as using experimental data reduced the flexibility of the approach. Also, as no physics of the process were included, a large amount of experimental trials would be required to use the modelling methodologies.

Ahsan *et al.* [124] developed a nuemrical-analytical method to predict the geometry of multi-track depositions. The method was based on the single-track method as presented by Ahsan and Pinkerton [25]. The melt pool physics were included by predicting the thermal distribution of the process on a virgin substrate using the Cline and Anthony distribution [37]. The standard elliptical melt pool geometry was altered to take into consideration a previously deposited track. Due to the inclination angle between the track and substrate, the bound-

ary of the melt pool was assumed to be triangular in the region of the overlap, as presented in Figure 2.12. The multi-track profile was determined through integrating a Gaussian surface representing the powder distribution between the limits of the melt pool geometry. The model was validated experimentally for three overlap ratios with a maximum error of 15.8% for the track height. An inaccurate representation of the multi-track profiles were determined when compared to the experimental data, as an unrealistic waviness on the surface of the track profile was predicted. This could not occur due to the melt pool surface tension as detailed by [129]. It should be noted that from analysing the experimental micrographs presented by Ahsan *et al.* [124], for the presented OR's, a concave semi-circular geometry was present in the overlap region. Therefore, this agreed with the work presented by Suryakumar *et al.* [128].

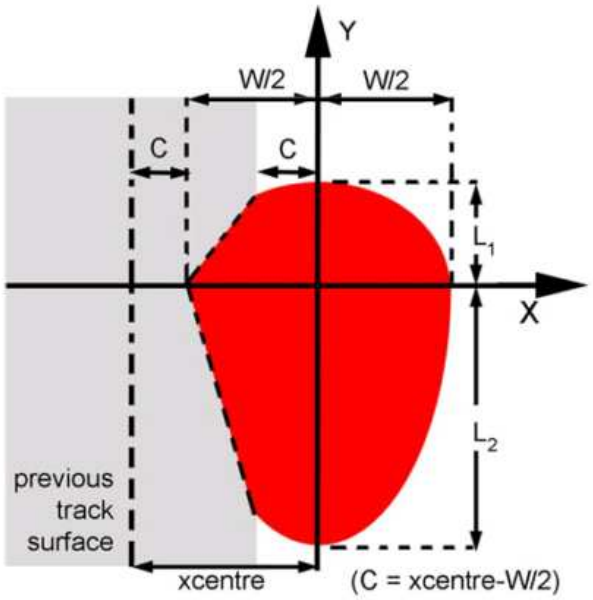

Figure 2.12: A schematic of an altered melt pool geometry used when a previously deposited track was present [124].

A 2D numerical model, presented by Ya *et al.* [44], determined the multi-track profile using a moving mesh method. A 2D planar section, parallel to the laser traverse direction was used. The model evaluated the mass and energy equations for a moving Gaussian heat source, with the incoming powder modelled

using a Gaussian powder density function. An original mesh consisting of two domains was implemented, with domain one being equal to the length and depth of the substrate. The second domain was used to represent the track height, with an initial height and width equalling $10\mu m$ and the length of the substrate respectively. The height of the deposit was evaluated for the current time step, with the mesh in the second domain being refined to equate the height of the moving boundary. The mesh refinement was controlled by the auto meshing solver within the commercial software COMSOL. A schematic of this process is presented in Figure 2.13.

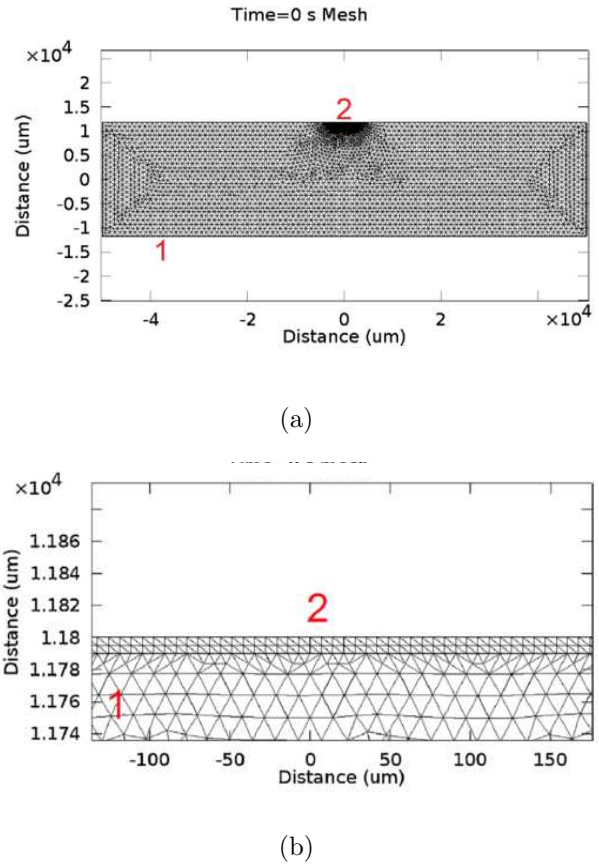

Figure 2.13: A schematic of the meshing method implemented to represent a 2D representation of the track [44]. (a) Original mesh with each domain present. (b) Mesh refinement included for the second domain.

As only the track height was predicted, it was assumed that each track geometry could be represented as a parabola. The powder catchment efficiency was derived

based on experimental data, therefore limiting the flexibility of the approach. The model was validated using thermocouple measurements and measurements of the track height, with a maximum error of 5% and 4.8% respectively. An issue with this modelling approach was that the previous track geometry was not included in the 2D thermal model, therefore, the heat flux was assumed to be identical for each track. Also, it should be noted that no attempt was made to determine the geometry of the overlap region. Another numerical method to predict multi-track deposition profiles was presented by Wen and Shin [130]. A 3D model was used to include; the laser powder interaction, mass addition and fluid flow motion. The governing conduction equations were solved using the finite volume approach, with a transient solution being formulated using an implicit solving scheme. Validation of the model was conducted for a zig-zag tool path, with measurements of the track height and width being compared to the predicted track profile. It was found that the model predicted the track width with negligible error and the track height was predicted with a maximum error of 16%.

2.7.3 Previous Methods to determine the Thermo-mechanical Effects of DED

As outlined in Section 2.5, a sequentially coupled thermo-mechanical approach can be used to assess the thermal and mechanical effects of the DED process; however, to date, modelling the development of residual stresses within laser deposited parts has received little attention, due to the high computational complexity and associated cost [14]. Shah *et al.* [45] and Chew *et al.* [48] both implemented a thermo-mechanical model to evaluate the residual stress field of a single-track deposition. The track geometry was represented using square elements for both studies. Validation was conducted through the use of XRD measurements. Shah *et al.* [45] compared the predictions with experimental measurements for two

components of residual stress along the build direction. Both pulsed and continuous laser sources were used in the study, with models showing a good agreement with the experimentally obtained residual stress data. Chew *et al.* [48] quantified two residual stress components across the mid plane of the substrate. Again, a good agreement with the experimental residual stress profiles was presented, with the longitudinal stress profile following the same trend as a traditional single weld pass. The in-situ temperature histories agreed well with the FE models for both studies. The use of XRD data was a limitation for the validation of the modelling approaches, presented by Shah *et al.* [45] and Chew *et al.* [48], as the limited penetration depth of X-ray does not allow for a tri-axial stress comparison. Also, as the track profile was approximated as rectangular elements, the true track geometry and its effect on the thermo-mechanical fields was not investigated.

Mukherjee *et al.* [49] included the fluid flow of the melt pool in the thermal analysis by solving the mass, energy and momentum equations in a 3D discretised domain. The domain consisted of a square substrate with a rectangular geometry used to represent the deposit. The predicted thermal histories agreed well with the experimental data with a maximum error of 2.1%. Validation of the mechanical model was conducted through comparison of the predicted longitudinal and through thickness stress components with XRD data. Due to the aforementioned reasons, the validation of the model was limited. Despite the inclusion of a more accurate representation of the weld pool, a maximum error of 62% and 40% for each stress component was observed respectively, with the predicted data set falling outside the confidence limits for the experimental data. A 3D model for DED, utilising both an analytical and numerical approach, was derived by Labudovic and Kovacevic [22]. An analytical model, based on Green's function, was used to solve the thermal field for a moving heat source, with the analytical solution being compared to the FE simulation. A numerical model to determine the residual stress field was also presented, this was developed in an

attempt to generate a feedback control system to reduce residual stresses during the deposition based on the process inputs. Experimental data for both the thermal and mechanical portions of the model were used to validate the approach, with the use of a high speed camera and XRD data. Although a good agreement was present between the experimental data and the modelling method, a square track geometry was used for the FE model. The interaction between the powder feed and melt pool were not included; therefore, a prediction of the track profile was not possible. Utilising this methodology, the residual stress was controlled using the feedback control in combination with the process parameters. However, a bespoke repair solution could not be designed, as a true representation of the track geometry was not included in the model; also, as the powder feed was not included, in-situ variation of this process parameter could not be incorporated with this approach. A model was presented by Farahmand and Kovacevic [131] which included a more accurate representation of the track geometry and was used to predict the thermo-mechanical effects due to variation in the traverse velocity. The track geometry was not determined through a numerical method and was implemented into the model through geometrical measurements of the experimental tracks. A good agreement was attained between the experimental and predicted melt pool geometry with a maximum error of 3.8%; therefore validating the approach. The residual stresses were determined for a planar section and compared to XRD data. A maximum error of 10% was reported for the peak stress. Although the presented methodology for the thermo-mechanical portion of the model was accurate when compared to experimental data, the flexibility of the approach was reduced as no track profile could be determined without prior measurement of the experimental geometry. Zhang and Kovacevic [46], evalauted the effects of depositing dissimilar materials on the thermo-mechanical effects of the process. A heat source model was used to represent the heat flux addition to the domain, with the interaction between the laser and powder being introduced

through modification of the power attenuation. Element birth and death was utilised to include the effect of material addition during the process; however, the cross-section of the track was uniform and was determined through experimental measurements. Validation of the thermal model was completed through thermocouple measurements and the maximum error between the peak temperatures was 5.8%. No experimental validation for the mechanical model was presented as part of this study.

Bailey *et al.* [132] predicted the thermo-mechanical effects of the process, through implementing multi-track geometries predicted by Wen and Shin [130]. The thermal field evaluated by Wen and Shin [130] was used to calculate the thermal strain and the strain arising from solid state phase transformations. All of the solid state transformations were predicted using the Johnson-Mehl-Avrami model. Both strain components were applied as boundary conditions to an ABAQUS mechanical FE model. The thermal field from the previous model and the associated phase changes during the process were calculated using an ABAQUS user subroutine. The resultant stress distribution, was validated against microhardness and XRD data, across the depth of the deposition and the substrate. A maximum error of 6.36% and 38% was achieved respectively. It should be noted that for this study, only a single stress component was validated using XRD due to the limitation in the experimental apparatus. A numerical and experimental study, presented by Foroozmehr *et al.* [133], analysed the effect of two common multi-track deposition strategies, the spiral and zig-zag, on the thermal and residual stresses induced by the process. It was found that both strategies alter the thermal history of the process (maximum differenct 9.8%), with the zig-zag strategy exhibiting the largest peak temperature. No validation of the thermal cycles was presented, however the residual stress was validated across the width of the deposited surface at the centre of the substrate, using XRD. Two stress components were validated with a maximum error of 50% and

37.5%, for zig-zag and spiral strategy respectively. The highest stress magnitude was present in the zig-zag strategy for the longitudinal stress component. A numerical investigation, presented by Nazemi *et al.* [134], utilised a fully coupled thermo-metallurgical FE model to determine the effect of the OR (40%, 50% and 60%) on the residual stress distribution. Through the use of experimental data, a simplified track profile was implemented in the model, therefore reducing the flexibility of the modelling approach. A lower residual stress was observed at the end of the track for all of the depositions due to the transient end effects. It was observed that a lower magnitude residual stress was present within the overlap region for high OR's, due to the increased localised heating effects. Through a parametric study, it was apparent that no correlation was present between the maximum longitudinal stress and the overlap ratio for both deposition strategies. It should be noted that there was no experimental validation of the thermal cycles or residual stress distributions for this study.

2.7.4 Knowledge Gap

The current calibration methods only use the thermal history or melt pool geometry to calibrate the parameters of the thermal model. Also, no attempt was made to determine the process efficiency, heat source parameters and the effect of secondary heat losses from the domain; therefore, a complete calibration of the thermal model was not achieved. The previous approaches are also limited as they are restricted to a single heat source model; therefore, if the process required a high magnitude thermal flux, a calibration of the model could not be completed with the current approaches. For the previous numerical calibrations, mesh independence was not addressed, as this would be a factor in the accuracy of the predicted thermal fields, it should be included in the thermal calibration. In response, a fully automated calibration procedure which determines: the optimum element size for the HAZ, the parameters of the FE heat source model, the pro-

cess efficiency and the thermal losses associated between the work piece and the welding apparatus, is required. The proposed calibration procedure is required to allow automation of a key step in the thermal modelling of DED processes; therefore, increasing the efficiency of the sequentially coupled FE approach for industrial application.

Currently, modelling of the DED process has received interest in three main areas which include; single-track deposition, in-situ parameter variation and multi-track deposition. The use of empirical models allowed the track geometries to be predicted; however, these methods are not cost effective due to the large amounts of experimental data required. Analytical models, which include the physics of the process allow a more accurate representation of the process to be completed. This type of modelling methodology allows for a more generic approach to be implemented. A limited number of models exist which predict the thermo-mechanical effects of single-track DED using a true representation of the track profile. Often a square representation of the track is used to assess the thermo-mechanical effects of the process. Although previous models were validated experimentally, a tri-axial stress comparison between experimental data was not completed due to the use of XRD. A modelling methodology which encompasses the key physics of the process and a true representation of the single-track geometry was required to predict the thermo-mechanical effects. This would provide superior fidelity in modelling of the single-track deposition process, allowing parametric studies to be completed to asses optimum repair strategies.

The current uptake of in-situ parameter variation for repair processes is restricted by the modelling approaches not incorporating these phenomena; therefore, the only method to quantify the effect of process variations would be through the use of costly experimental trials. Although methodologies exist to predict the track formation within DED using analytical approaches only a constant set of process parameters can be implemented. Also, as a quasi-static solution of

the thermal field was calculated, the time dependent history of the process was neglected; therefore, the effect of in-situ parameter modifications cannot be evaluated. Therefore, to allow the inherent manufacturing flexibility of the DED process to be encapsulated in a modelling approach, a method which can incorporate variation of the process parameters during the deposition is required. Numerical models can be used to predict the track geometry, however, the physics are often simplified or the track geometry is represented using a simplified square geometry. Also, similar to the analytical models, only a constant set of parameters can be used. It should be noted that to date, the geometry, thermal and mechanical effects induced through adaptive process control has not been reported in the literature. With the use of a transient numerical approach, a time history of the input/outputs of the process using adaptive process control can be implemented/determined. An assessment of the repair methodology could then be completed to allow a bespoke repair strategy to be designed, without the need for lengthy and costly experimental trials.

The geometrical models that currently exist to predict the track profile for multi-track DED are limited, as experimental data was required to define the initial geometry. Also, it should be noted that no physics of the DED process were included; therefore, the flexibility of these modelling approaches were compromised. A limited number of validated models exist to predict the thermo-mechanical effects of multi-track DED. In response, a numerical model which predicts the multi-track geometry, implementing the physics of the process, should be devised. As multiple models (FOM, TOM and Fillet) exist to predict the geometry of the overlap region, a single method which can be applied to coaxial deposition needs to be addressed. From the literature, there was no attempt made at predicting track profiles for different tool paths and OR's. There is also a lack of knowledge in predicting the thermo-mechanical effects induced by multi-track DED when varying the tool path and OR. This should be investigated in

an attempt to identify potential methods to control residual stress formation. It should also be noted that experimental data to validate the tri-axial stress state of the mechanical portion of the model has is limited.

Chapter 3

Research Methodology

3.1 Introduction

This chapter presents the numerical, analytical and experimental methods utilised for this work. The chapter is divided into three sections:

1. Analytical methods to simulate the powder flow and track formation in Direct Energy Deposition (DED).

2. Numerical methods to predict the thermal and mechanical fields of DED.

3. Experimental methods used to validate the numerical and analytical approaches.

The first part describes the analytical models required to simulate the powder flow of the DED process and its interaction with the molten pool to fabricate a deposition track. The second presents the method used to predict the thermal and mechanical effects of the process, based on the the sequentially coupled thermo-mechanical Finite Element (FE) analysis. The third part documents the experimental methods used to validate the modelling processes adopted to simulate the DED process.

3.2 Analytical Modelling of DED

To model all key stages of the DED process, the interaction of the powder stream and the molten region to generate a track, must be considered. Including these interactions into the current modelling strategy, using a numerical approach, would be computationally more complex and time consuming. Although numerical models for this part of the DED process exist [44, 118, 130, 135–137], this was included in the current modelling methodology using an analytical approach. The analytical approach included:

- **Powder Flow**: Modelling of the powder flow concentration and distribution at the exit of the coaxial nozzle.
- **Thermal Field**: An analytical model of the thermal field arising from a laser heat source, used to determine an analytical approximation of the melt pool width and length.
- **Track Profile**: Models the interaction of the powder distribution and melt pool geometry to predict a 2D track profile for a single deposition.

3.2.1 Powder Flow Distribution

The powder flow and its distribution upon the substrate are fundamental to modelling the process to encompass all of the key process variables in the modelling approach. An analytical representation of the powder flow was utilised throughout this work. The nozzle delivery system for the experimental depositions was coaxial in design, with a schematic of the geometry and the associated parameters presented in Figure 3.1 and Table 3.1 respectively.

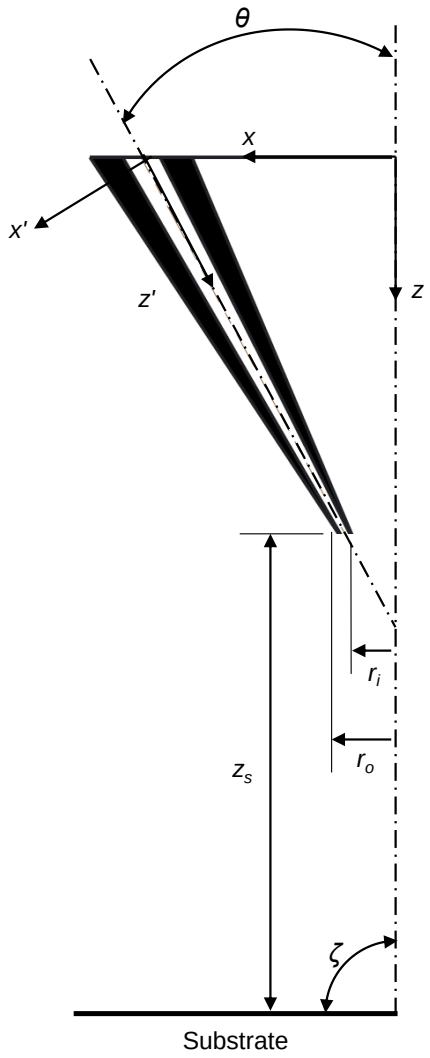

Figure 3.1: Schematic of the coaxial nozzle geometry and the associated parameters to model the powder flow.

Table 3.1: Geometrical parameters of the coaxial nozzle used to model the powder flow.

Parameter	**Dimension**
Nozzle stand-off distance (z_s)	12 mm
Nozzle inclination angle (ζ)	90°
Annulus distance ($r_o - r_i$)	0.25 mm
Initial powder stream angle (θ)	60°
Powder stream divergence angle (ϕ)[138]	8°

It was assumed that the distribution of the powder flux across the stream

width was Gaussian [120, 139, 140]. To obtain the powder distribution at the substrate, the radius which defined the spread of the Gaussian distribution had to be determined. From Pinkerton and Li [120] it was determined that the Gaussian radius (r_p) equated where the powder concentration was equal to 1% of the peak concentration. The powder concentration, as a function of the stand-off distance, had the following form, with the peak value equating C^* [120]:

$$\begin{aligned} C(x,y,z) &= C^* exp\left[\frac{x^2+y^2}{w^2}\right] \\ C^* &= \frac{2\left[r_i+r_o\right]\dot{m}}{\sqrt{\pi}0.843\dot{V}z_s(\theta)} \end{aligned} \tag{3.1}$$

The width of the powder stream was equal to:

$$w = \frac{2(r_o-r_i)tan(\theta)}{(r_o+r_i)}z_s \tag{3.2}$$

where r_i and r_o is the inner and outer radius of the nozzle outlet respectively, $\dot{m}$ is the mass flow rate of powder, $\dot{V}$ is the volumetric flow rate of the carrier gas, z_s is the stand-off distance and θ is the initial powder stream angle.

3.2.2 Analytical Thermal Field

To determine the interaction between the powder flow distribution and the molten geometry at the substrate, an analytical thermal field was used to predict the melt pool geometry. An analytical thermal analysis for laser heating presented by Cline and Anthony [37] was utilised. The heat flow for a rapidly moving, high powered laser heat source is dominated by conduction in the solid. Therefore, the temperature distribution in the material was related to the power density by the diffusion equation:

$$\frac{\partial T}{\partial t} - D\nabla^2 T = \frac{Q}{C_p} \tag{3.3}$$

where T is the temperature of the material, t is the time, Q is the heat flux, C_P is the specific heat capacity and D is the thermal diffusivity of the material. To represent the heat flux, Cline and Anthony [37] used a more realistic Gaussian intensity distribution, similiar to the Gaussian disc FE heat source model presented by Pavelic [92]. The analytical heat flux distribution for a moving heat source had the following form:

$$Q = \frac{P}{2\pi R} exp\left[-\frac{x^2 - (y^2 - Vt)}{2R^2}\right] \tag{3.4}$$

where P is the laser power, R is the laser spot radius, V is the traverse velocity and x, y are the Cartesian coordinates of the domain. To solve Equation 3.3, the known solution for the thermal distribution of a unit point source, G, located at reference coordinates x', y', at time t' on the surface was used [141]. Therefore, the heat flow from the laser at the reference coordinate system influences the temperature at the global coordinate system (x, y, z) for an infinite rectangular geometry, as follows:

$$\begin{aligned} T &= \int_{-\infty}^{t} \int_{-\infty}^{+\infty} \int_{-\infty}^{+\infty} \int_{-\infty}^{+\infty} \left(\frac{Q}{C_p}\right) G dz' dy' dx' dt' \\ G &= \frac{exp\left[-R^2 \left[4D\left(t - t'\right)\right]^{-1}\right]}{4\left[\pi D\left(t - t'\right)\right]^{\frac{3}{2}}} \end{aligned} \tag{3.5}$$

To reduce the complexity of solving the analytical expression, Equation 3.5 was non dimensionalised to give:

$$\begin{aligned} T(x, y, z) &= P_{eff}\left(C_p D R\right)^{-1} f(x, y, z, V) \\ f &= \int_0^{\infty} \frac{exp(-H)}{\left(2\pi^3\right)^{0.5}\left(1 + \mu^2\right)} d\mu \\ H &= \frac{\left(X + \zeta/2\mu^2\right)^2 + Y^2}{2\left(1 + \mu^2\right)} + \frac{Z^2}{2\mu^2} \end{aligned} \tag{3.6}$$

where P_{eff} is the effective power of the laser, f is the function distribution, $\mu^2 = 2Dt'/R$, $\zeta = R/DV$, $X = x/R$, $Y = y/R$, $Z = z/R$. This new form was evaluated numerically using the integration function within MATLAB.

3.2.3 Track Profile Prediction

To determine the deposition profile, an analytical model was used to integrate the powder mass flux distribution over the bounds of the melt pool geometry. A schematic of the melt pool geometry, superimposed with the powder mass flux distribution, is presented in Figure 3.2.

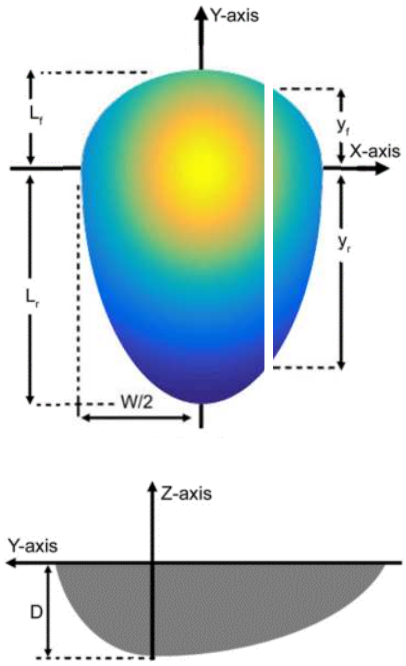

Figure 3.2: A schematic of the melt pool geometry superimposed with the powder mass flux distribution. Modified from [25].

The limits of the melt pool were defined as follows:

$$y_f = L_f \sqrt{1 - \frac{4x^2}{W^2}} \tag{3.7}$$

$$y_r = L_r \sqrt{1 - \frac{4x^2}{W^2}} \tag{3.8}$$

where the Width (W), front length (L_f) and the rear length (L_r) are defined from the thermal field (Equation 3.6) using the following criteria:

$$\begin{aligned} T\left(\pm\frac{W}{2}, 0, 0\right) &= T_m \\ T\left(0, L_f, 0\right) &= T_m \\ T\left(0, L_r, 0\right) &= T_m \end{aligned} \tag{3.9}$$

The powder mass flux distribution (Figure 3.3) for coaxial laser deposition has been determined to be Gaussian [120]; therefore, the distribution at any point (x, y), with the laser centred at the origin, has the following form:

$$q_{pf} = \frac{2\dot{m}}{\pi r_p^2} exp\left[-2\frac{x^2+y^2}{r_p^2}\right] \tag{3.10}$$

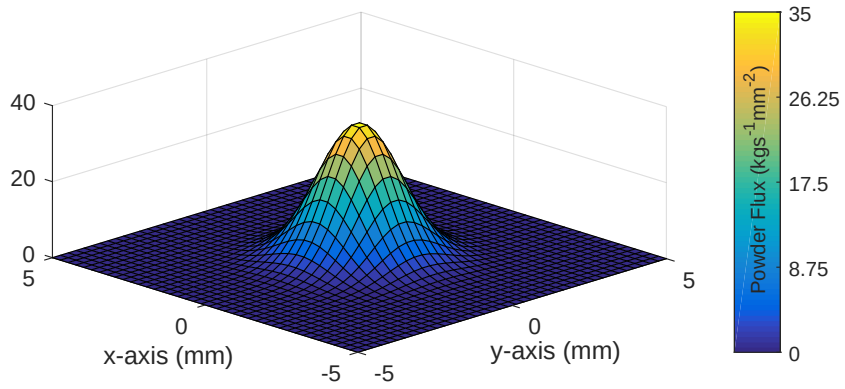

Figure 3.3: A schematic of the Gaussian powder flux distribution used in this work.

The variation in the track height over the width of the melt pool was determined as follows:

$$h_z(x) = \frac{\eta_c}{\rho V}\int_{y_r}^{y_f} q_{pf} dy \tag{3.11}$$

where η_c is the powder catchment efficiency, ρ is the material density. Due to the use of a mathematical expression to determine the track geometry, there will be limitations in the predicted shape of the profile. As the track profile was determined based on Equation 3.10 only, the track profile will always resemble a

2D planar section of the distribution presented in Figure 3.3. Therefore, if the true powder distribution is not Gaussian, errors in the prediction of the profile will be present.

To ensure that the mass and enthalpy balance was stable within the system, the power required to sustain mass addition and the power loss associated with the evaporation heat flux were, considered. Through mass addition, the melt pool geometry size often reduces, therefore, the power required to melt the incoming powder was calculated as follows [25]:

$$P_m = \rho V \left[C_p \left(T_m - T_{amb}\right) + L_m\right] \int_{-W/2}^{W/2} h_z(x)\, dx \tag{3.12}$$

where T_m is the melting temperature, T_{amb} is the ambient temperature and L_m is the latent heat of melting. For the evaporation losses from the melt pool, the overall evaporation model determined, by Choi *et al.* [142] was implemented:

$$P_{evap} = \frac{\pi}{4} W \left(L_f + L_r\right) \left(\frac{455.32 Exp\left[4.834 - (18836/T_{mean})\right]}{\sqrt{T_{mean}}}\right) h_v \tag{3.13}$$

where h_v is the latent heat of vaporization. The mean melt pool temperature (T_{mean}) was determined from dividing the the melt pool region into two sections, this included the upper region (deposition region) and the lower portion (molten region below the substrate) [25]. The two volumes of the upper (V_u) and the lower (V_l) molten regions were determined as follows:

$$\begin{aligned} V_u &= \frac{1}{\rho V} \int_{y_r}^{y_f} \int_{y_r}^{y_f} q_{pf} \\ V_l &= \frac{1}{2}\left[\frac{4}{3}\pi \left(\frac{W}{2}\right)^2 \left(\frac{L_f}{2} + \frac{L_r}{2}\right)\right] \end{aligned} \tag{3.14}$$

Through maintaining an enthalpy balance across the entire melt pool, the mean

melt temperature was calculated as:

$$T_{mean} = \frac{V_u T_m + V_l T_p}{V_u + V_l} \tag{3.15}$$

where T_p is the peak melt pool temperature. The effective power of the laser (P_{eff}) was determined through subtracting both losses from the initial laser power. To ensure a stable mass/enthalpy balance was achieved, an iterative solution procedure was used. The thermal field was reassessed through updating the associated losses and the solver was terminated upon a stable melt pool being achieved. This occurred when the following criteria was met:

$$\begin{aligned} W_n &= W_{n-1} \pm 0.5\% \\ L_n &= L_{n-1} \pm 0.5\% \end{aligned} \tag{3.16}$$

where W_n and L_n are the current width and length of the melt pool, respectively.

3.3 Numerical Methods to Predict the Thermal and Mechanical Fields of DED

3.3.1 Sequentially Coupled Thermo-mechanical Analysis

The numerical methodology used to determine both the thermal and mechanical effects of the DED process, was a sequentially coupled thermo-mechanical model, solved using the Finite Element Method (FEM). This method is commonly adopted in Computationally Welding Mechanics (CWM) to predict thermal strains and the associated deformations of the process. As DED is very similar to conventional welding processes, the theory of CWM can be implemented. Sequentially coupled models can be used as the heat generation from the mechanical deformations have a negligible effect on the associated thermal field.

For all numerical models in this work, the commerical code ABAQUS was used. Firstly, a thermal analysis was completed which solves the governing transient heat transfer equation for a stationary medium [143]:

$$\rho C_p \frac{\partial T}{\partial t}(x, y, z, t) = -\nabla.\vec{q}(x, y, z, t) + Q(x, y, z, t) \tag{3.17}$$

where T is the current temperature, Q is the internal heat generation rate, ∇ is the spatial gradient operator and $\vec{q}$ is the heat flux vector equalling the non-linear Fourier heat flux constituitive equation [144]:

$$\vec{q} = -k\nabla T \tag{3.18}$$

where k is the thermal conductivity of the material. The governing equation (Equation 3.17) was integrated by the FEM. However, to solve the equation and obtain a closed solution, the system of equations are subject to boundary conditions. For the thermal analyses in this work, all of the sink and ambient temperatures were set to 20°C. Convection and radiation boundary conditions were applied to the free surfaces exposed to the surrounding atmosphere, by using the Newton (Equation 3.19) and Stefan-Boltzmann (Equation 3.20) laws respectively:

$$\dot{q} = -h(T - T_{amb}) \tag{3.19}$$

$$\dot{q} = \sigma\epsilon\left[(T - T_{abs})^4 - (T_{amb} - T)^4\right] \tag{3.20}$$

where $\dot{q}$ is the heat flux generated across the surface, T is the temperature at a point on the surface, ϵ is the emissivity of the material equating 0.8 [145], T_{abs} is the absolute zero temperature, σ is the Stefan-Boltzmann constant equal to $5.67 \times 10^{-8}\ W/m^2K^4$ and h is the convective heat transfer coefficient which equated the free surface value of $25\ W/m^2K$ [145], unless otherwise stated. During the DED process, the substrate was in contact with the machine apparatus during

the process; therefore, an artificial convective boundary condition, using Equation 3.19, was used to simulate the heat sink effect at this location.

The application of thermal flux, which drives the thermal field, was assumed to be driven by a second generation heat source model. A user subroutine (*DFLUX* within ABAQUS) was used to implement the heat source distribution. The heat source replaces the physical phenomena of the melt pool physics, therefore Marangoni, Buoyancy and surface tension effects were neglected from this work. In order to capture the melt pool geometry with accuracy and correctly replicate the conduction from the Fusion Zone (FZ) to the Heat Affected Zone (HAZ), a correct representation of the heat flux distribution was required. For the current study, the laser heat source was operated predominantly in the conductive regime; therefore, a Gaussian disc heat source model was utilised [102, 146], unless otherwise stated. The heat source model had the following form:

$$Q_{disc} = \frac{\eta P}{\pi r_0} exp\left(-\frac{r^2}{r_0^2}\right) \tag{3.21}$$

where η is the process efficiency, r_0 is the Gaussian surface radius and $r = \sqrt{x^2 + y^2}$.

To solve the thermal problem, Equation 3.17 was solved using a numerical integration scheme, often using the full Newton-Raphson scheme. The second step of the analysis requires the predicted thermal histories to be converted to thermal strain and then applied to the mechanical model as a boundary condition. As the thermal field was solved for a stationary medium, the process was assumed to be quasi-static; therefore, the equilibrium conditions can be formulated as [147]

$$\{\sigma_{ij}\} + \{b_i\} = \{0\} \tag{3.22}$$

where σ_{ij} is the stress tensor and b_i is the body force. It is assumed that the stress tensor is symmetrical i.e. $\sigma_{ij} = \sigma_{ji}$. The thermal elasto-plastic material

model, based on the von Mises yield criterion , gives the following stress-strain relationship [148]:

$$\{d\sigma\} = \{D^{ep}\}\{d\varepsilon\} - \left\{C^{th}\right\} dT \tag{3.23}$$

$$\{D^{ep}\} = \{D^{e}\} + \{D^{p}\} \tag{3.24}$$

where $\{D^e\}$ is the elastic stiffness matrix, $\{D^p\}$ is the plastic stiffness matrix, $\left\{C^{th}\right\}$ is the thermal stiffness matrix, $d\sigma$ and $d\varepsilon$ are the stress and strain increments respectively and dT is the temperature increment. Since the thermal elasto-plastic analysis was non-linear, an incremental solution procedure was required. Again, the full Newton-Raphson integration scheme was required to solve for the incremental stress. To solve the mechanical fields, the FE mesh used for the thermal analysis have to be identical for the two models to be coupled. As there are no solid state transformations occurring in Inconel 718 (IN718) from room temperature to the melting temperature of the material, the strain components can be divided into three components [144]:

$$\varepsilon = \varepsilon^{e} + \varepsilon^{p} + \varepsilon^{th} \tag{3.25}$$

where the components of strain are elastic (ε^e), plastic (ε^p) and thermal (ε^{th}). The elastic strain component was modelled as isotropic using Hooke's law and the plastic strain was determined using the von Mises yield criterion. The thermal strain was evaluated using the thermal history of the heating and cooling phase of the process in conjunction with the materials thermal expansion coefficient.

To solve the system of equations representing the mechanical formulation, the relevant boundary conditions must be applied. In conjunction with the thermal loading, the clamping conditions of the work piece must be considered to predict accurate deformations and stress in the component. For all of the cases considered for this work, no fixed clamps were used. Therefore, the mechanical boundary conditions applied were artificial to prevent rigid body motion occurring. For

some models, only half of the geometry was considered due to the symmetric thermal and mechanical fields which were present. For this case, the following boundary conditions were applied (Figure 3.4):

- A: Displacement constrained in Y and Z direction
- D: Displacement constrained in Z direction
- Plane A', B', C', D': Displacement constrained in X direction. Rotation constrained in Y and Z axis.

For the case where the full geometry was modelled, i.e. no symmetry was present, the following boundary conditions were applied (Figure 3.4):

- A: Displacement constrained in X, Y and Z direction
- B: Displacement constrained in Y and Z direction
- C: Displacement constrained in Y direction.

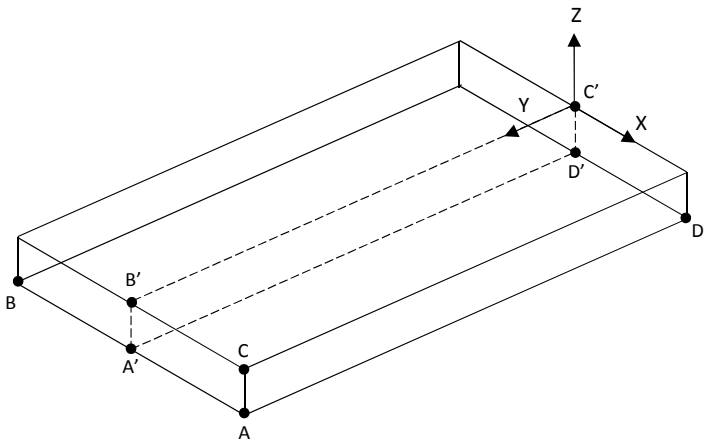

Figure 3.4: Nodes for mechanical boundary conditions for both a symmetric and unsymmetrical geometry.

3.3.2 Material Properties of IN718

All of the experimental and numerical investigations for this work were conducted using the alloy IN718. The material was supplied by Haynes International

(Manchester, UK.) in the solution heat treated state. The nominal composition of IN718 is presented in Table 3.2.

Table 3.2: Nominal chemical composition of IN718 in wt%.

Ni	**Co**	**Fe**	**Cr**	**Co+Ta**	**Mo**	**Mn**	**Si**	**Ti**	**Al**	**C**	**B**
52	1	19	18	5	3	0.35	0.35	0.9	0.5	0.05	0.004

For all numerical models, to ensure that an accurate representation of the process was simulated, material property definition was required between the ambient and melting point of the material. A tabular approach was used to define the thermal and mechanical material property data. The commercial code, ABAQUS, uses linear interpolation to determine material properties between the specified data. The temperature dependant material properties are presented in Figure 3.5 [145]. Poisson's ratio was assumed to be constant, equating a value of 0.33 [145]. The DED process causes material melting and solidification of the track and substrate, therefore leading to dissolution of powder and recrystalisation in the deposited track and in the HAZ. This will cause metallurgical differences in the grain size and orientation, therefore altering the mechanical properties in these regions. However, both of these regions were assigned identical material properties as outlined in Figure 3.5 as it was determined by Deshpande *et al.* [149], that modifications to the material properties, to match that of the molten region, had a negligible effect on the final residual stress field.

To include the effects of heat transfer due to fluid flow within the melt pool, two additional material properties were defined. Firstly, the thermal conductivity was artificially increased for temperatures above the solidus temperature [150]. Secondly, the latent heat of fusion was considered (Table 3.3) for the respective solidus and liquidus temperature of the material. The phase change was bound by these upper and lower temperature values, with the latent heat modifying the specific heat capacity within the relevant temperature range, ensuring that the area underneath the modified portion of the curve equalled the latent heat.

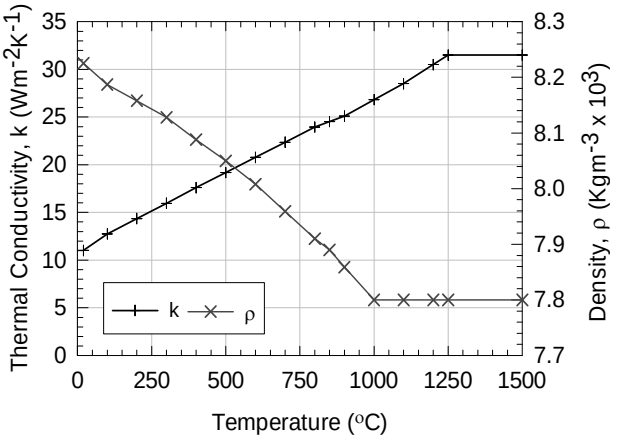

(a)

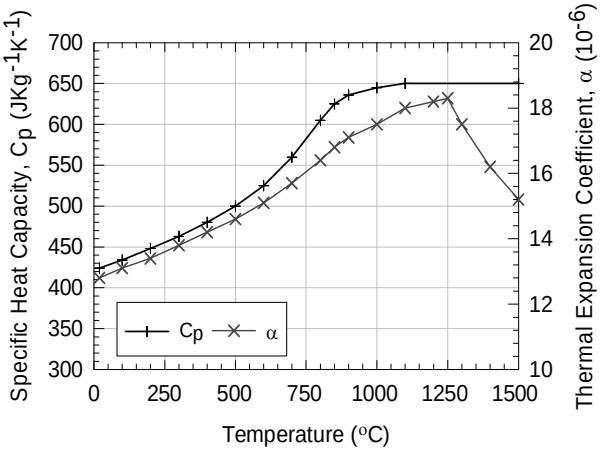

(b)

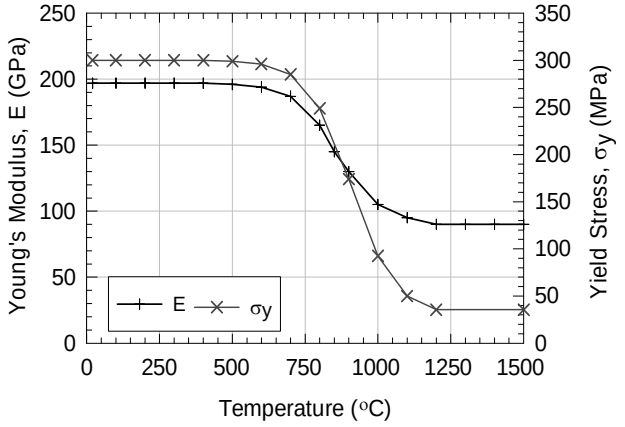

(c)

Figure 3.5: Temperature dependant material properties of IN718 (a) Thermal conductivity, k and density, ρ (b) Specific heat capacity, C_p and thermal expansion coefficient, α (c) Young's modulus, E and yield stress, σ_y.

It should be noted that the release of latent heat during solidification was not considered in this work.

Table 3.3: Latent heat of fusion properties for IN718 [151].

Solidus Temperature (°C)	1260
Liquidus Temperature (°C)	1336
Latent Heat of Fusion (J/Kg)	210

With regards to the mechanical properties, the plastic behaviour of the material was defined using a material hardening law. The two most common hardening laws applied to FE welding models are the isotropic and kinematic laws. Often, when there is minimal cyclic loading behaviour present within the model, the isotropic hardening model is used; however, for cases where several thermo-mechanical loading cycles are present, the kinematic law is used. For single-track depositions, it is acceptable to use an isotropic hardening model to define the plastic behaviour as a limited amount of cyclic loading is present [152]. For cases where multi-track deposition were present, using an isotropic hardening model may lead to the underestimate of plastic strains, as no translation of the yield surface can occur. For multi-track deposition, Mullins *et al.* [153] implemented an isotropic hardening and kinematic hardening. It was determined that the isotropic model gave the best comparison with the kinematic model providing an underestimate for all stress directions. From the conclusions of the two studies, the isotropic hardening model was used for all mechanical analyses having the following form [152]

$$\frac{\sigma_p}{\varepsilon_p} = 0.01E \tag{3.26}$$

where σ_p and ε_p are the plastic stress and plastic strain respectively. As the feedstock material and substrate enters a molten state during deposition, this phenomena was included through using the annealing fucntion within ABAQUS. This function allows the effects of melting and resolidification in metals to be accounted for during high temperature material processing [154]. This function

causes the accumulated plastic strain, due to work hardening, to be reset to its initial condition if the melting temperature of the material was exceeded. If the temperature falls below the melting temperature, then plastic strain can be accumulated again. The annealing temperature was set to the solidus temperature for IN718. It should be noted that volume change due to phase transformations upon solidification were neglected.

3.3.3 Numerical Integration

To solve both thermal and mechanical non-linear FE problems, a numerical integration scheme was required. The full Newton-Raphson integration scheme was used in ABAQUS. The integration time step for the heating phase of the thermal model was selected so that the heat source traversed one element length per time step. This was chosen to ensure convergence and so that a stable thermal field was predicted. For the cooling phase, an automatic integration time step was used to reduce the time for the computation. For the mechanical model, to mitigate convergence issues, the time incrementation was set to automatic. The minimum time step was set as the integration time step from the thermal model. This was utilised across both the heating and cooling step for the mechanical analysis.

3.3.4 Modelling Material Deposition

The method used to model material deposition within both the thermal and mechanical models was the active/inactive element approach. This was implemented in ABAQUS using the *MODEL CHANGE* module [154]. At the start of the analysis, all of the elements which represented the material deposition were set to an inactive state (*MODEL CHANGE* $\rightarrow$*Remove*). When the elements are set to inactive, any previous loading conditions are ramped down to zero. This was completed in a single analysis step to ensure that a new equilibrium condition

was achieved and convergence was met for the initial boundary conditions of the model. The elements remained inactive unless they were reactivated (*MODEL CHANGE* $\rightarrow$*Add*) in the analysis step. This method has a computational advantage, as the material stiffness matrix is reduced for early stages of the model, reducing the computational time of the analysis. In some cases where large element volumes are reactivated, the convergence criteria cannot be met due to the redistribution of the thermal and/or mechanical field. When reactivating element sets within the thermal model, the thermal conductivity is ramped from a value of zero up to the true value. When reactivating element sets within the melt pool, care has to be taken to ensure that the peak temperature within the model does not fluctuate due to the ramping of material properties. Therefore, to maintain an energy balance within the molten region, the elements were reactivated at the melting point of the material and at one element width ahead of the centre of the heat source. For consistency, the same reactivation method was used in the mechanical analysis. Elements were reactivated in a sequential order, using pre-defined element sets, the setup process was automated using the Python scripting functionality within *ABAQUS*. For each element reactivation, a new analysis step was defined. This ensured that for the mechanical model, the elements were reactivated when melting occurred; therefore, stress free elements were assigned the correct strain value upon cooling below the annealing temperature. The definition of a new step also mitigated set up errors when using the pre-determined thermal field as a boundary condition of the mechanical model. This process was also automated using Python Scripting.

3.4 Experimental Methodology

3.4.1 Laser Rig Setup

Experimental laser deposition and Laser Beam Welding (LBW) were completed using a deposition system at the University of Nottingham, as presented in Figure 3.6. The experiments were conducted using a 2 kW Ytterbium-doped, continuous wave, fibre laser manufactured by IPG Photonics. The laser operates at a wavelength of 1070 nm, utilising a 125 mm collimating lens and a 200 mm focusing lens in the beam-optic delivery system. The laser system was coupled with a four feed, coaxial fed, YC50 cladding head. The delivered laser beam has a Gaussian profile when using a 600 μm diameter fibre to convey the laser to the cladding head. It is common to operate the laser out of focus (increase the stand-off distance from the nominal value) to accommodate the feed material in the melt pool. The laser was operated at a defocus distance of 12 mm which gave a laser spot diameter of approximately 2.5 mm. This remained constant for all of the experiments in this work. The laser system was mounted to a 4-axis CNC bed which allowed the substrate to traverse linearly in the x, y and z direction and rotate about the z axis, relative to the stationary laser. For all of the experiments, the substrate was traversed in the y-direction only, all other directions remained stationary.

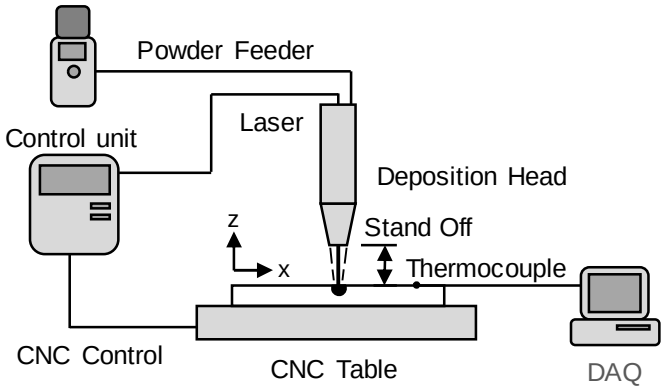

Figure 3.6: A schematic of the laser deposition rig.

The feed material selected for this study was gas atomised IN718, supplied

by Oerlikon (MetcoAdd 718C). The nominal chemical composition of MetcoAdd 718C is presented in Table 3.4 with a Scanning Electron Microscope (SEM) image of the gas atomsied powder shown in 3.7. MetcoAdd 718C has a nominal particle size ranging from -45 to +15 μm. This was determined by the manufacturer through particle sieving and laser diffraction, in compliance with ASTM B214 [155] and ASTM C 1070 [156]. The powder delivery system was a Praxair (Model 1264) powder feeder which supplied the coaxial cladding head. In order to obtain a mass flow rate, calibration of the powder feed was conducted by measuring the mass of powder over a duration of one minute. An inert gas supply of argon was used as the carrier gas and was set to 10 l/min for all experimental set ups. It should be noted that the deposition process was not isolated from atmospheric conditions, i.e. no chamber was used around the substrate.

Table 3.4: Nominal chemical composition of MetcoAdd 718C.

Ni	**Cr**	**Fe**	**Nb+Ta**	**Mo**	**Al**	**Ti**	**Other**
Balance	18	18	5	3	0.6	1	<0.5

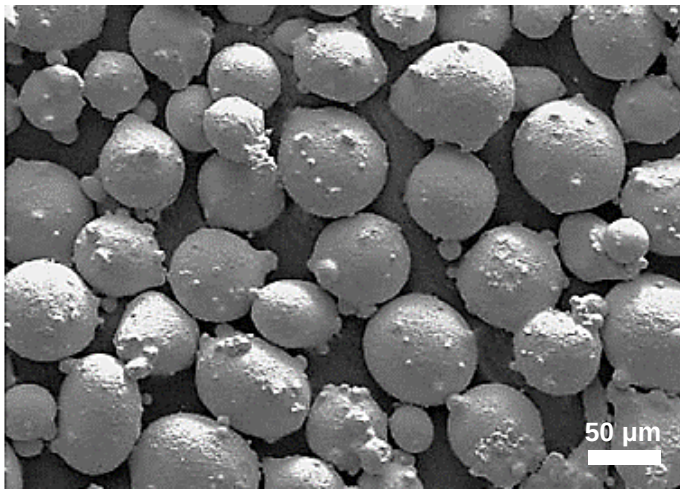

Figure 3.7: SEM Image of Gas Atomised MetcoAdd 718C Powder [157].

Prior to completing deposition trials, it should be noted that all substrates were grit blasted using alumina garnet powder to reduce the reflectivity of the material. Each rectangular substrate was mounted on the table of the CNC bed.

No clamps or bolts were used to fully restrain the substrate unless otherwise mentioned; therefore, the substrate was free to deform.

3.4.2 Thermal History Measurements

To validate the thermal FE modelling, in-situ temperature histories were measured using K-type thermocouples. Each thermocouple was insulated with fibre glass (401-900) in conjunction with a ceramic sheath to further insulate the thermocouple junction. The thermocouples and ceramic sheath were supplied by TC Direct (Uxbridge, UK.) and Omega Engineering Limited (Manchester, UK.) respectively. To ensure suitable measurements were taken, each thermocouple had to be mounted as close to the HAZ as possible due to the localised heating effects of the DED process. For the trials conducted for this work, the distance of the the thermocouple relative to the heat source is presented in the relevant section. To ensure a good contact between the thermocouple and the substrate, each junction was spot welded to the substrate surface in an open junction arrangement. Data was captured using a National Instruments SCXI-1000 chassis in conjunction with a SCXI-1102B voltage input module. The data was logged using LabVIEW, where the data was processed and analysed.

3.4.3 Metallurgical Examination

To generate 3D data of the deposition surface, focus variation microscopy was used. A scan of the top surface was completed using an Alicona Infinite Focus, between the limits of -20 mm and +20 mm from the substrate mid-length. A total of 26 2D cross sectional profiles were generated from the data. This was used to generate a surface plot of the track and substrate using MATLAB.

To further validate the thermal section of the modelling strategy, metallographic analysis of a specimen removed from the deposition or weld was conducted. All specimens were prepared in compliance with ASTM E3 [158]. To

fabricate a specimen, a small rectangular section was removed from the required area (Figure 3.8). This was completed using water-jet cutting to ensure any secondary manufacturing effects were neglected. This ensured that minimal heat input was induced into the specimens after processing. Sizes of the removed specimens are documented for each specific case. After removing the specimen, it was mounted in conductive resin using a 30 mm press. Grinding of the exposed surface was completed using silicon carbide (SiC) abrasive paper, with a grit size ranging from 240 to 1200. This process was then followed by polishing using a 6 and 1μm diamond wheel with lubricant.

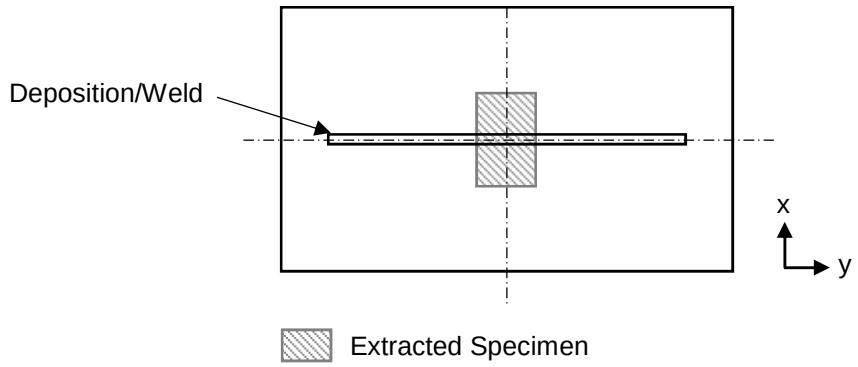

Figure 3.8: A schematic of a metallographic specimen removed from a deposition/weld.

Acid etching of the specimens were completed using two different types of chemical etchant depending on the application and the method in which the results were to be processed. For metallographic analysis of the deposition and substrate interaction, Marble's Reagent (10 g C_uSO_4, 50 ml HCL and 50 ml H_2O) was used, this effectively highlighted the three regions of interest (Deposition Geometry, FZ and unmelted powder) in the specimen. For any application which required image processing of the specimen, Beraha's tint (100 ml HCL, 50 ml H_2O, 1 g potassium metabisulphate and 1 g ferric chloride) was used. This etch highlighted the melt pool region, with the substrate remaining a dark colour, therefore allowing image processing tools to distinguish between each region. All specimens were examined through a digital optical microscope to produce metal-

lographic images of the specimen.

3.4.4 Processing of Metallographic Images

To validate the methods used to predict the geometry of the track profile, a metallographic specimen was removed from the centre of the track as depicted in Figure 3.8. The specimen was mounted in conductive resin and the sample was then polished to a 1 μm surface finish using an abrasive diamond wheel. An optical image of the exposed cross section of the track was obtained. To determine the track profile, image analysis was completed using the Image Processing Toolbox^{TM} within MATLAB. The optical image was converted to a binary image using the in-built MATLAB function *im2bw*, using the default threshold value determined by *greythresh*. The boundaries in the image were traced using the Moore-Neighbour tracing algorithm, presented by Gonzalez *et al.* [159]. The algorithm was implemented using the in-built function *bwboundaries* using the default settings.

3.4.5 Neutron Diffraction Measurements

Neutron Diffraction (ND) measurements were conducted at the ENGIN-X facility, using the ISIS neutron source located at the Rutherford Appleton Laboratory, UK [160]. The ISIS neutron source is a pulsed spallation source, which produces neutrons through accelerating protons at a heavy metal tungsten target. The process is repeated every 20-60 Hz leading to a generation of low flux neutrons. The ENGIN-X facility works on the time-of-flight (TOF) theory for ND. A short pulse of neutrons allows the time of arrival at the detector to be determined

through the use of De Broglie's law:

$$\begin{aligned} p = m_n v = \frac{h}{\lambda} \\ t = \frac{L}{v} = \lambda \left(\frac{m_n L}{h} \right) \end{aligned} \tag{3.27}$$

where p is momentum, m_n is the mass of a neutron, v is the particle velocity, h is Planck's constant, λ is the wavelength, L is the length of the flight path and t is the time of flight. Detector banks are used to measure the intensity of neutrons as a function of time. Two directly opposing detector banks are used at a scattering angle of $2\theta = \pm 90°$ to the workpiece. In a crystalline material, a regular pattern of atoms exist which defines the material structure. These can be considered as a series of lattice points in real space, which have a prescribed lattice spacing (Figure 3.9).

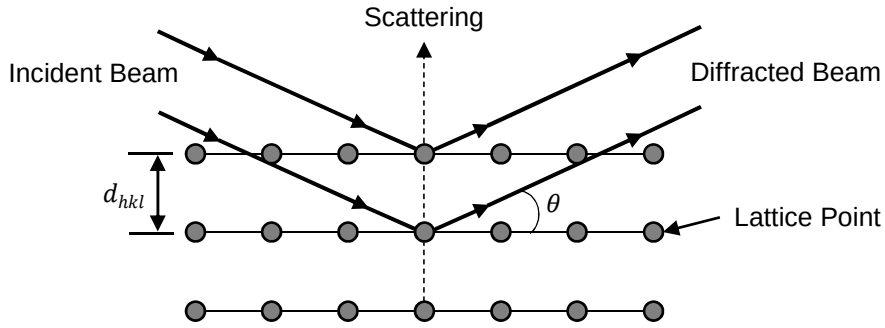

Figure 3.9: A schematic of a crystalline lattice structure showing the theory of Bragg's Law.

This arrangement of atoms can be used as an atomic strain gauge. Diffraction peaks exist for a known lattice spacing (d_{hkl}) using Bragg's law:

$$\lambda = 2d_{hkl} \sin(2\theta) \tag{3.28}$$

where d_{hkl} is the lattice spacing and 2θ is the angle between the incident and diffracted beam. Therefore, the diffraction peaks measured at each time after the

initial pulse was given by:

$$t = d_{hkl}\left(\frac{2m_n L \sin\theta}{h}\right) \tag{3.29}$$

To obtain diffraction spectra, from the scattering of neutrons, a gauge volume was used to define the spatial resolution of the measurements. With the use of collimators and choppers, the gauge volume can range in size from $4 \times 4 \times 4$ mm^3 to $1 \times 1 \times 1$ mm^3. To ensure pseudo-strain correction methods do not have to be used after completing ND measurements, the sample was positioned so the gauge volume was fully filled. With most ND experiments, the gauge volume remains stationary, with the sample being positioned relative to the incident beam with the use of a 4-axis CNC table. To obtain the lattice strain, the strain-free lattice spacing (d^0_{hkl}) was required, i.e. the lattice spacing of the original crystal structure before processing. For this work, a combed specimen was selected to obtain the strain free lattice spacing. Firstly, it ensured that the lattice spacing at the chosen measurement locations and the strain free value were taken at near identical positions. Secondly, it allowed more efficient use of the beam time as the strain free reference sample could be mounted to the measurement sample, allowing all of the measurements to be taken without multiple experimental set ups. For all of the neutron diffraction experiments conducted for this work, the experimental setup, outlined in Figure 3.10, was used. During the experiment, two strain components were collected simultaneously with the use of the two opposing detector banks. Through rotation of the sample, a full tri-axial stress measurements was completed. With the sample mounted in the first orientation, i.e. the deposition direction parallel to the CNC table, the longitudinal (d_{010}) and normal strain components (d_{001}) were measured. Through rotation of the sample by 90°, the transverse (d_{100}) and the normal (d_{001}) were measured. To obtain the lattice parameters from the diffraction data, the Reitveld analysis was used.

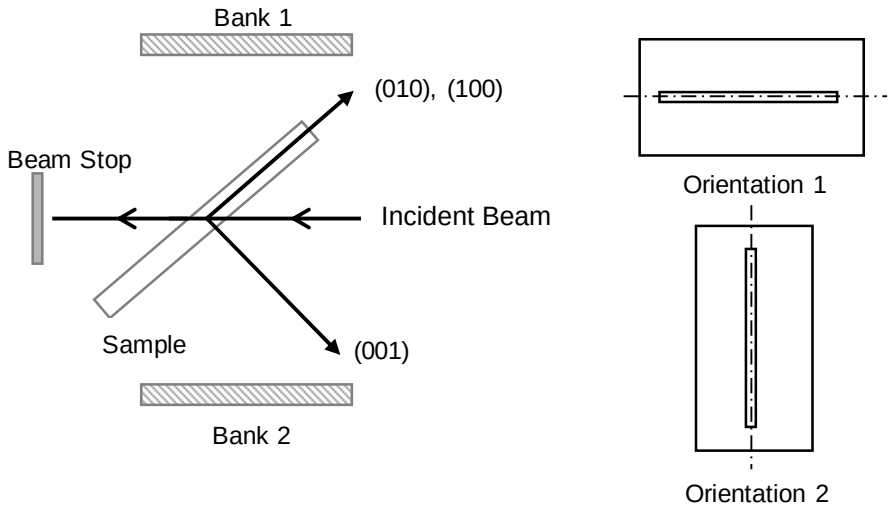

Figure 3.10: A schematic of the ENGIN-X beamline setup used to obtain ND measurements showing the two plate orientations used, the incident and diffracted beam and the measured strain directions.

This analysis is a refinement technique which minimises the error between an experimentally determined diffraction profile and a predicted profile, using a least squares regression. The analysis of the collected data was completed using the General Structure and Analysis System (GSAS), which is a bespoke program used to process and analyse signal data from x-ray or ND data [161]. Upon determining the lattice parameters, the elastic strain was calculated as follows:

$$\varepsilon_i = \frac{d^i_{hkl} - d^0_{hkl}}{d^0_{hkl}} \tag{3.30}$$

where ε_i is the elastic strain in the i direction and d^i_{hkl} is the lattice spacing corresponding to the i direction. As the lattice spacing was measured for each principle direction of the sample, the macroscopic stress in the i direction was obtained from Hooke's law, utilising the following formulae:

$$\sigma_{ii} = \frac{E}{1+\nu}\left[\varepsilon_{ij} + \frac{\nu}{1-2\nu}\left(\varepsilon_{11} + \varepsilon_{22} + \varepsilon_{33}\right)\right] \tag{3.31}$$

where the numerical subscripts denote the direction in the sample, E is the

Young's Modulus and ν is the Poisson's ratio of the material, having values of 209 GPa and 0.29 respectively [162]. Through using GSAS, the uncertainty from fitting the nominal diffraction peaks to the measured diffraction spectra were calculated for both the strain-free lattice parameter (d_0^{hkl}) and the lattice spacing of interest (d_{hkl}^i). Through propagation of uncertainty, a combined error analysis, using Equation 3.30 and 3.31, can be conducted to determine the uncertainty in the experimental stress for all three macroscopic stress components.

Chapter 4

Automated Calibration of Thermal Finite Element Models

4.1 Introduction

The accurate prediction of thermally induced residual stresses and the associated distortions are highly dependant on the accuracy of the predicted thermal field. As outlined in Chapter 2, a number of Finite Element (FE) heat source models are available to represent heat flux distributions. Although utilising FE heat source models neglects the complexity of the melt pool physics, often a number of geometrical parameters have to be calibrated before they can be implemented. Often the heat source model is selected based on the welding process and for some cases two or more have to be superimposed to represent complex flux distributions. To date the most common method to calibrate the thermal model is through a trial and error approach. An initial guess of the heat source parameters based on experimental measurements is used and theses parameters are refined until the predicted thermal profile and fusion zone represent the experimental data with accuracy. Although this method is simple, it can be time consuming and inherently inaccurate.

This chapter presents a fully automated calibration methodology, which determined the parameters of the thermal FE model, based on an inverse approach. The calibration procedure was designed to include any combination of heat source model, thus allowing the calibration to be applied to common processes which require a heat source model, such as welding and deposition processes. The procedure determined the optimum element size and refines the parameters of the thermal model to determine a calibrated set of results. The thermal parameters included the process efficiency, the heat source parameters and the secondary losses to the welding apparatus.

4.2 Thermal Model Calibration Method

The calibration procedure, presented in Figure 4.1 can be divided into two sections; the first determined the optimum element size for the thermal solution, based on an initial guess for the parameters of the thermal model. The second refined the parameters using an iterative optimisation algorithm. To initiate the calibration, an initial guess for the thermal model parameters was required. These parameters were stored in the initial guess vector, $\mathbf{x}_0$, and were used to determine the optimum element size for the optimisation model. The ideal element size was determined through the use of a fully automated mesh sensitivity study and converged when the thermal history and melt pool area satisfied a predefined convergence criteria. The heat source parameters were then refined using a non-linear optimisation, based on the trust-region reflective algorithm. To ensure that the final optimised solution was mesh independent, the accuracy of the thermal history and melt pool profile were reassessed. If the convergence criteria was not achieved, the optimisation was repeated utilising the new element size and the current optimised parameters. The calibration procedure was terminated when either mesh independence was achieved, or when the current and previously

optimised heat source parameters were within an acceptable tolerance.

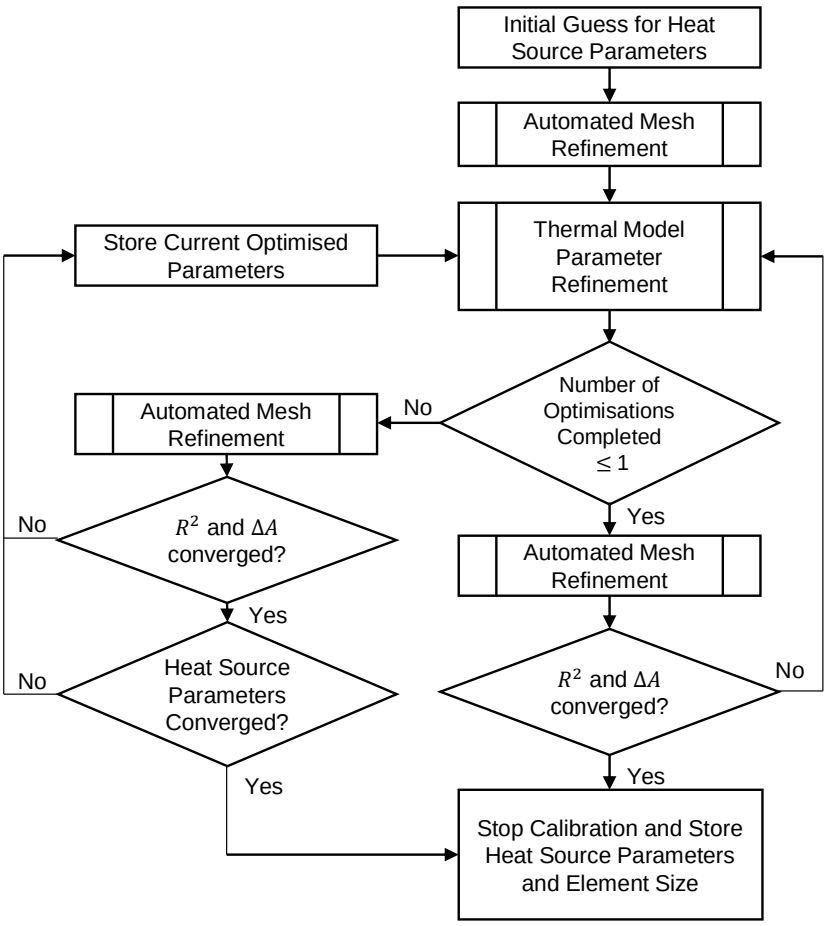

Figure 4.1: Flowchart of the calibration procedure used to determine the optimum element size and the parameters of the thermal model.

4.2.1 Thermal Model Theory

To determine the thermal history and melt pool profile required for the calibration, an underlying numerical model was required. A thermal FE heat transfer analysis was used to solve the transient heat conduction equation (Section 3.3.1). The commercial FE code ABAQUS was used to solve the transient thermal fields for all of the presented models in this chapter. The integration time step was set to the time increment for the heat source to move one element length for all cases [100]. The geometry and the associated weld path used as the test specimen for the calibration is presented in Figure 4.2.

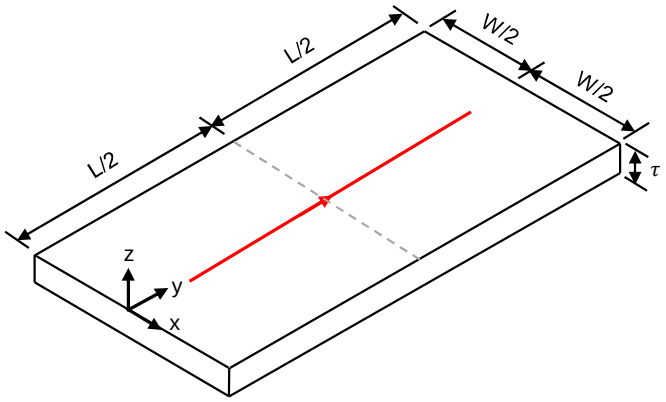

Figure 4.2: Schematic of the test specimen geometry and the weld path used for the underlying thermal model.

For the numerical model only the heating phase of the process was considered; therefore a fixed time increment was used for the entire analysis. Due to the symmetric geometry about the weld centreline and the associated temperature field, only half of the work piece was modelled. Convective and radiative losses were applied to all the free surfaces of the geometry using the methodology outlined in Section 3.3.1. The secondary losses were modelled using an artificial convective loss on the surface which would be in contact with the welding apparatus. This value equalled the free surface value unless otherwise stated. It should be noted that to determine the value of the thermal contact coefficient, cooling data from the process was required. To generate this data, the thermal history was extracted at the mid plane of the weld path (y=50 mm); therefore, allowing the cooling phenomena to be represented.

The domain was meshed with 8 node linear brick elements (DC3D8), with the mesh consisting of square elements throughout the domain. Due to the high thermal gradients in the vicinity of the Heat Affected Zone (HAZ), finer elements were used in this region ($0 \leq x \leq 10$ mm). Through the use of mesh biasing the element size in the far region ($x \geq 10$ mm), the element size was ten times that of the HAZ. The through thickness size equated the finer element size. Temperature dependant material properties were defined for the thermal FE model. Effects

due to solidification were also included by specifying the latent heat of melting at the respective solidus and liquidus temperatures.

4.2.2 Automated Mesh Refinement

An initial element size was determined for where mesh independence was achieved, from the thermal solution, using the initial guess vector. The flowchart of the process used to determine the optimum element size is presented in Figure 4.3. The initial element size was chosen as 2 mm in the HAZ, this was equal to the maximum experimentally measured melt pool width. The thermal model was solved for one time step to determine the current thermal profile and the through thickness melt pool geometry. Each sequential time step was then evaluated using the *Restart* function within ABAQUS. The iterative FE model was implemented to reduce the computational time of the analysis, as only the number of time steps required to achieve a steady-state melt pool were evaluated. For each time step of the analysis, the through thickness isotherm (x-z plane) was used to determine the coordinates of the melt pool as follows:

$$\begin{aligned} T(W, 0, 0) &= T_m \\ T(0, 0, D) &= T_m \end{aligned} \tag{4.1}$$

If no melting occurred for the current time step, the width of the melt pool was set to zero for the entire depth of the work piece. A steady-state melt pool was achieved when the following criteria was met:

$$\begin{aligned} \left(\frac{W_i - W_{i-1}}{W_i}\right) \times 100\% \leq 0.5\% \\ \left(\frac{D_i - D_{i-1}}{D_i}\right) \times 100\% \leq 0.5\% \end{aligned} \tag{4.2}$$

where W is the melt pool width, D is the depth of the melt pool and i is the current time step of the analysis, with the selected convergence value based on the work by Ahsan *et al.* [25]. The steady-state melt pool geometry was then stored for the current element size, in conjunction with a thermal profile determined from a pre-defined path. The coordinates for the start and end of the path equated $(0, 0, 0)$ and $(0, 100, 0)$ respectively. For the next iteration of the model, the element size was reduced by 50% to determine a second melt pool geometry and temperature profile.

To determine the accuracy between the derived melt pool geometries and thermal profiles, the coefficient of determination (R^2) between the temperature profiles and the change in melt pool area were used. The coefficient of determination (R^2) was calculated as follows:

$$R^2 = \frac{\sum_{j=1}^{n} \left(T_j^{e_1} - T_j^{e_2}\right)^2}{\sum_{j=1}^{n} \left(T_j^{e_1} - \frac{1}{n}\sum_{j=1}^{n} T_j^{e_1}\right)^2} \tag{4.3}$$

where n is the total number of data points and $T_j^{e_1}$ and $T_j^{e_2}$ are discrete temperatures within the temperature profile for each element size e_1 and e_2 respectively. The melt pool area was determined using the trapezoidal integration scheme as follows:

$$A_{melt} = W_{max}\tau - \frac{1}{2}\sum_{j=1}^{n-1} \left[x_{j+1} - x_j\right]\left[z_j - z_{j+1}\right] \tag{4.4}$$

where W_{max} is the maximum melt pool width, τ is the thickness of the substrate, x_j is the x coordinate at the jth data point and z_j is the z coordinate at the corresponding j^{th} data point. To allow a consistent comparison to be made for each element size, the number of discrete data points in each profile had to be equal. To achieve this, the data set containing the fewer data points was linearly interpolated, therefore, only one data point was predicted between two data points. Upon the convergence criteria being met, the optimum element size was stored in conjunction with the meshed FE domain which was used for the

optimisation analysis.

During the optimisation, the element size was not changed from the initial determined value. This was due to the formulation of the optimisation algorithm, as a mesh independence check could not be performed between each iteration of the algorithm. Also, if this was possible, the overall computational deficit would be costly due to the number of thermal analyses required. Therefore, it was assumed that the initial mesh size was satisfactory for all of the subsequent iterations of the optimisation. After an optimised set of parameters was determined, mesh independence for the solution was checked. This was completed by meshing the geometry using an element size 50% less than the initial value. The process outlined in Figure 4.3 was then utilised, using the same convergence criteria as the initial model. If the convergence criteria was met for the current optimised parameters, the calibration procedure was terminated; however, if the convergence criteria was not met, the optimisation was repeated for the new element size which achieved mesh independence. Upon determining another set of optimised parameters, the percentage difference between each heat source parameter was calculated. If the value was less than the prescribed convergence criteria, the calibration process was terminated; however, if the criteria was not achieved, the mesh refinement and optimisation model were repeated.

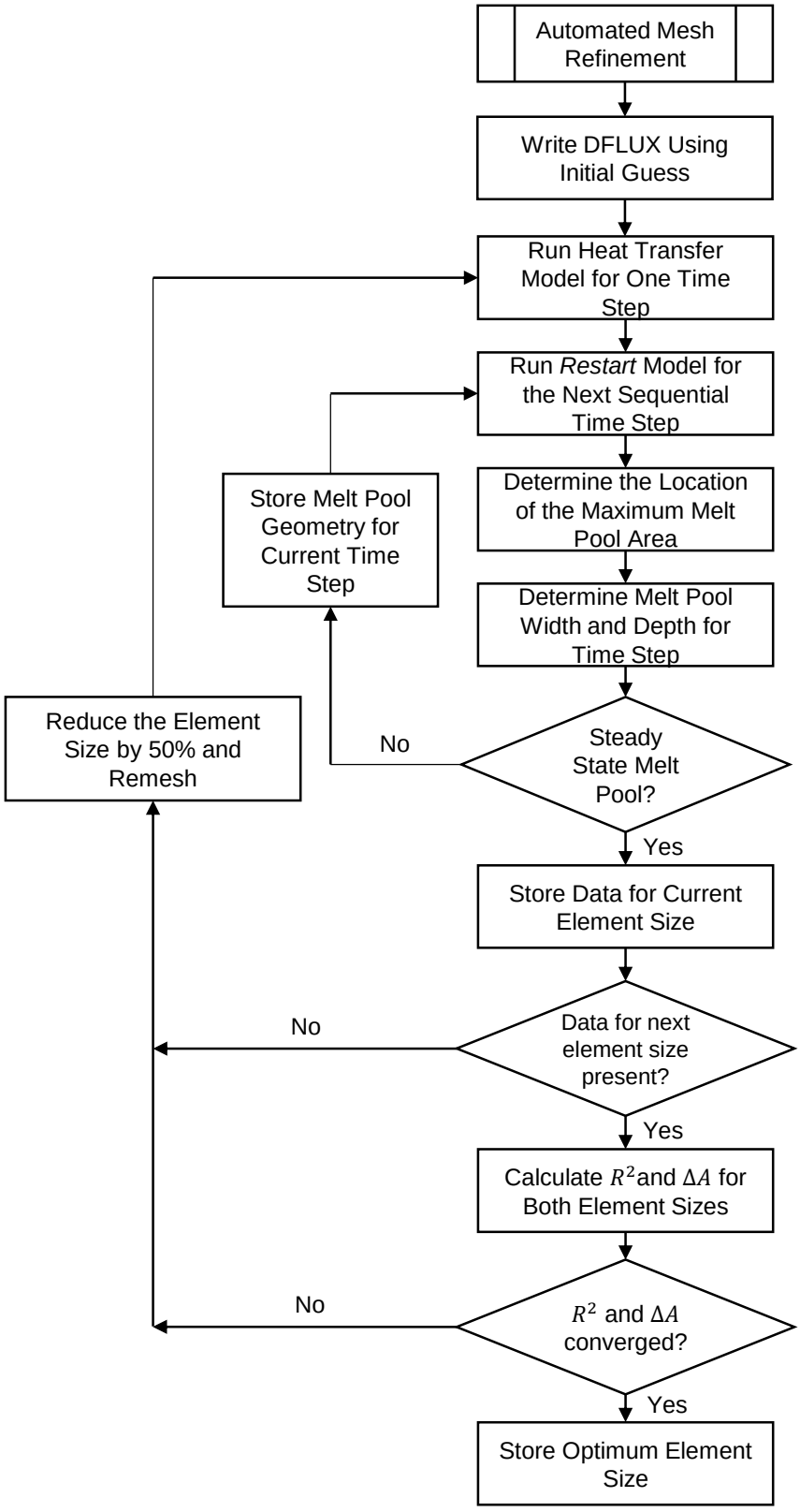

Figure 4.3: Flowchart of the process used to determine the optimum element size.

4.2.3 Thermal Model Parameter Refinement

The parameters of the thermal model were determined using an inverse analysis approach, with the process outlined in Figure 4.4. The inverse approach minimised the error between the experimental and predicted numerical data. A schematic of the inverse approach is presented in Figure 4.5.

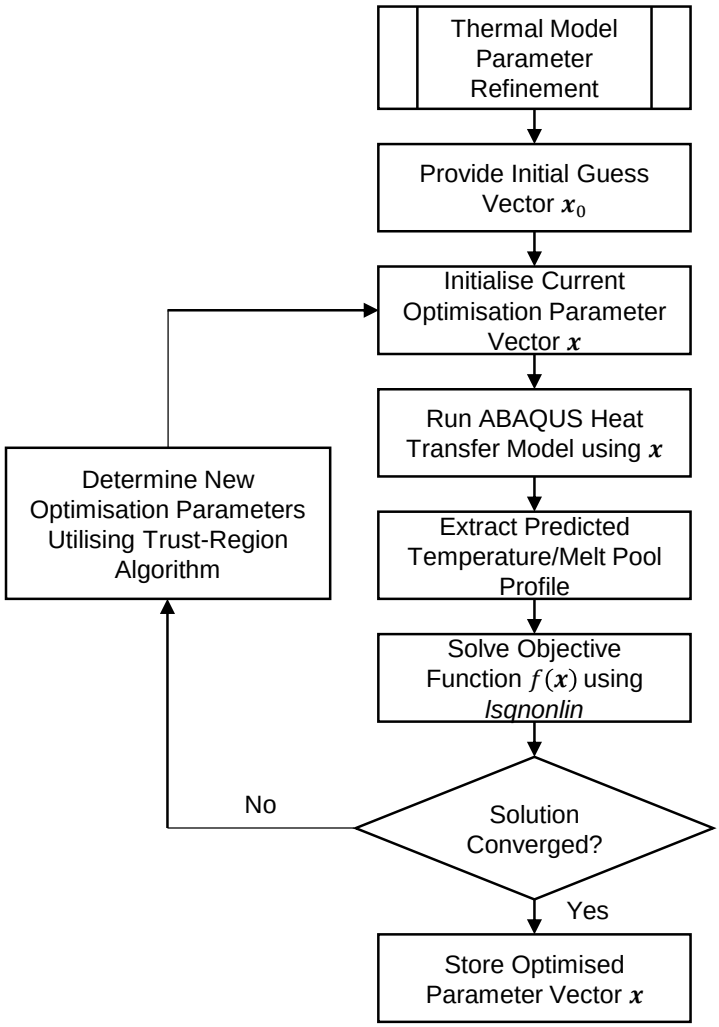

Figure 4.4: Flowchart of the inverse analysis used to determine the parameters of the thermal model.

The data used for the optimisation was the through thickness steady-state melt pool geometry and a thermal history profile. To minimise the error between the two data sets, a non-linear optimisation using the trust-region reflective algorithm, based on the work by Coleman and Li [163], was used to solve the

following:

$$min||f(\mathbf{x})||_2^2 = min(f_1(\mathbf{x})^2 + f_2(\mathbf{x})^2 + ... + f_i(\mathbf{x}))^2) \tag{4.5}$$

The algorithm minimised the squared 2-norm of the residual error which was computed by the objective function, $f(\mathbf{x})$. To evaluate the validity of using a single objective optimisation (SOO) or a multi objective optimisation (MOO), two objective functions were utilised and formulated using the weighted sum approach:

$$f(\mathbf{x}) = \begin{bmatrix} f_1(\mathbf{x}) \\ f_2(\mathbf{x}) \end{bmatrix}^2 \tag{4.6}$$

$$\begin{aligned} f_1(\mathbf{x}) &= \frac{w}{T_{max}^{exp}} \sum_{k=1}^{K} [T_k^{exp} - T_k^{pre}] \\ f_2(\mathbf{x}) &= \frac{(1-w)}{W_{max}^{exp}} \sum_{m=1}^{M} [W_m^{exp} - W_m^{pre}] \end{aligned} \tag{4.7}$$

where w is the weight parameter, T_{max}^{exp} is the maximum experimental temperature, W_{max}^{exp} is the maximum experimental melt pool width, T_k^{exp} and T_k^{pre} was the experimental and predicted temperature for discrete data point k, W_m^{exp} and W_m^{pre} was the experimental and predicted melt pool width for discrete data point m. The optimisation vector contained the thermal model parameters which were refined as part of this process. This vector was bound by upper and lower limits defined using the physical constraints of the problem. A bound model was used to restrict the solution space to increase the rate of convergence and to minimise the non-uniqueness of the solution.

The optimisation was implemented using the inbuilt MATLAB function *lsqnonlin*. The heat transfer model was used to predict the melt pool geometry and temperature history profile for the current set of heat source parameters. The FE model was evaluated for the entire weld path as outlined in Figure 4.2.

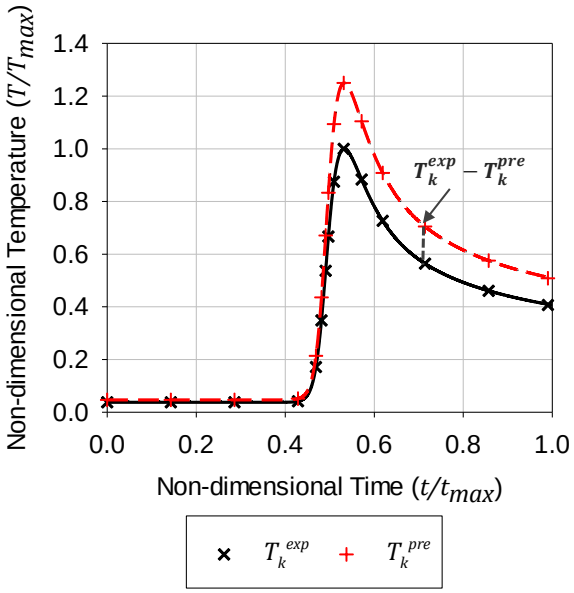

(a)

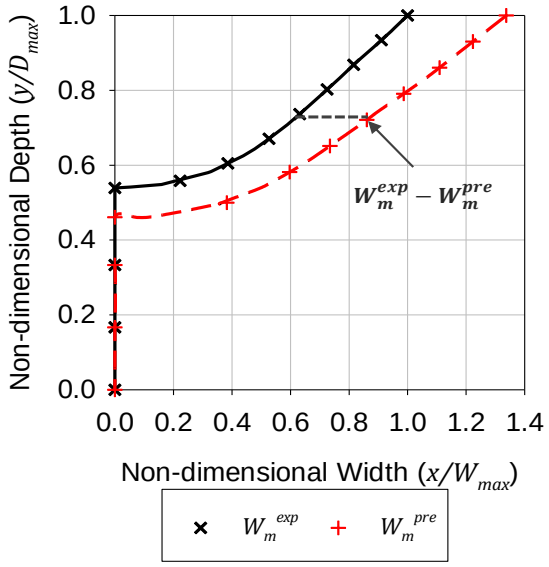

(b)

Figure 4.5: Schematic of the inverse approach for (a) Calculating the residual error for the thermal profile (b) Calculating the residual error for the melt pool geometry.

The thermal history profile being determined from the nodal coordinate (3, 50 ,0). The melt pool profile was determined from the $x - z$ planar isotherm at y =50 mm, at the step time where the melt pool area was at a maxima. The melt pool profile was determined from the $x - z$ planar isotherm at y =50 mm,

at the step time where the melt pool area was at a maxima. For each iteration of the optimisation algorithm the aim was to identify another point in space which reduced the magnitude of the global objective function ($f_{(\mathbf{x})}$) [163]. The optimisation parameters were varied inside a neighbourhood ($\mathbf{N}$), which was of spherical shape and sits in 3D space around the current point of interest, referred to as the trust-region. A trial step (s) was calculated at each iteration and was used to alter the optimisation parameters to drive the convergence in the steepest decent direction [164]. After the objective function was evaluated at $\mathbf{x} + s$, the dimension of the trust-region was altered to improve convergence. If the trial step minimised the objective function, the dimension of the trust region was reduced as the solution does not exist outside of that space. This continued until the absolute minimum change of the residual error was less than a threshold value. It should be noted that each objective function was non-dimensionalised with respect to the maximum corresponding experimental value. This ensured that the difference in magnitude between the two objective functions did not bias the error contribution to the global objective function.

During the optimisation procedure, multiple variants of the thermal parameters were evaluated at each iteration. Therefore, the melt pool geometry would have a varying cross section which could range from a partial to a fully penetrative profile. To ensure that the residual error was calculated at the sample point m, regardless of the melt pool geometry, M data points were equispaced throughout the thickness of the work piece. If no melting occurred during the evaluation of the current parameter set, the width was assigned a value of zero for the corresponding depth. To compute the residual error for both objective functions, the predicted data was linearly interpolated using the sampling points of the experimental data. This ensured that each objective function ($f_1(\mathbf{x})$ and $f_2(\mathbf{x})$) was evaluated at the specific points k and m respectively. It should be noted that the total number of data points in each objective function was gov-

erned by the experimental temperature data collection. An equal number of data points was selected for both objective functions to ensure that the contribution of error to each function was not weighted due to an uneven number of data points [111].

4.3 Implementation of the Thermal Calibration

To implement the calibration procedure test cases were fabricated using laser beam welding (LBW). As the energy density available was higher than conventional arc welding (10^{10} W/m^2 compared to 10^8 W/m^2 [165]), the laser beam can operate in both the conductive and keyhole regime [165]. Therefore, the melt pool geometry generated in each regime was different due to the complex distribution of heat flux within the workpiece. From this, the geometry of the melt pool can range from a shallow elliptical shape with a low penetration depth in the conductive regime [166] to a narrow, parallel sided geoemtry, with a deep penetration depth in the keyhole regime [167–169]. The latter is often referred to as the nail head geometry. The process parameters used for this study covered the entire process parameter window for the current experimental set up.

4.3.1 Experimental Methods

Nine samples were fabricated using the laser rig set up (Section 3.4.1), with the process parameters presented in Table 4.1. A schematic of the experimental setup for this application is presented in Figure 4.6. All the samples were cooled in air to room temperature after the weld was completed. For each sample, a total of three in-situ temperature measurements were recorded, at the substrate mid-length (y =50 mm), using the method outlined in Section 3.4.2. After the laser centre passed this position, data was still collected to obtain the cooling portion of the thermal history. To determine the cross-sectional melt pool profile, met-

allographic examination was performed on specimens (20 x 10 x 6 mm), which were prepared as documented in 3.4.3. To implement the optimisation procedure, the coordinates (x, z) of the melt pool geometries were extracted from the micrographs using an edge detection algorithm as outlined in Section 3.4.4

Table 4.1: Process parameters used for the experimental validation of the calibration procedure.

Parameter Set	Power (W)	Traverse Velocity (mm/min)
1	1800	400
2	1350	400
3	900	400
4	1800	250
5	1350	250
6	900	250
7	1800	100
8	1350	100
9	900	100

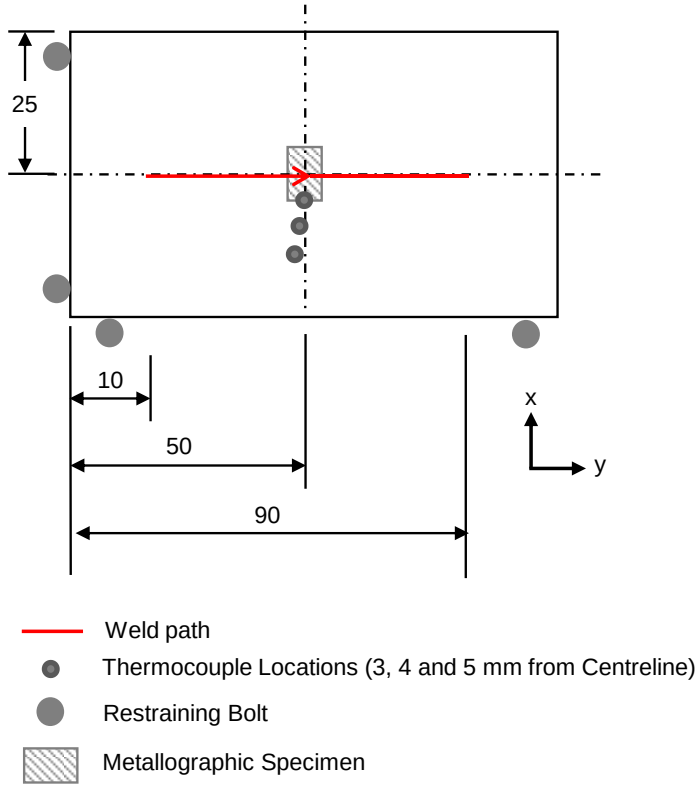

Figure 4.6: Schematic of the experimental setup showing the weld path, thermocouple locations and the extracted sample location of metallographic examination.

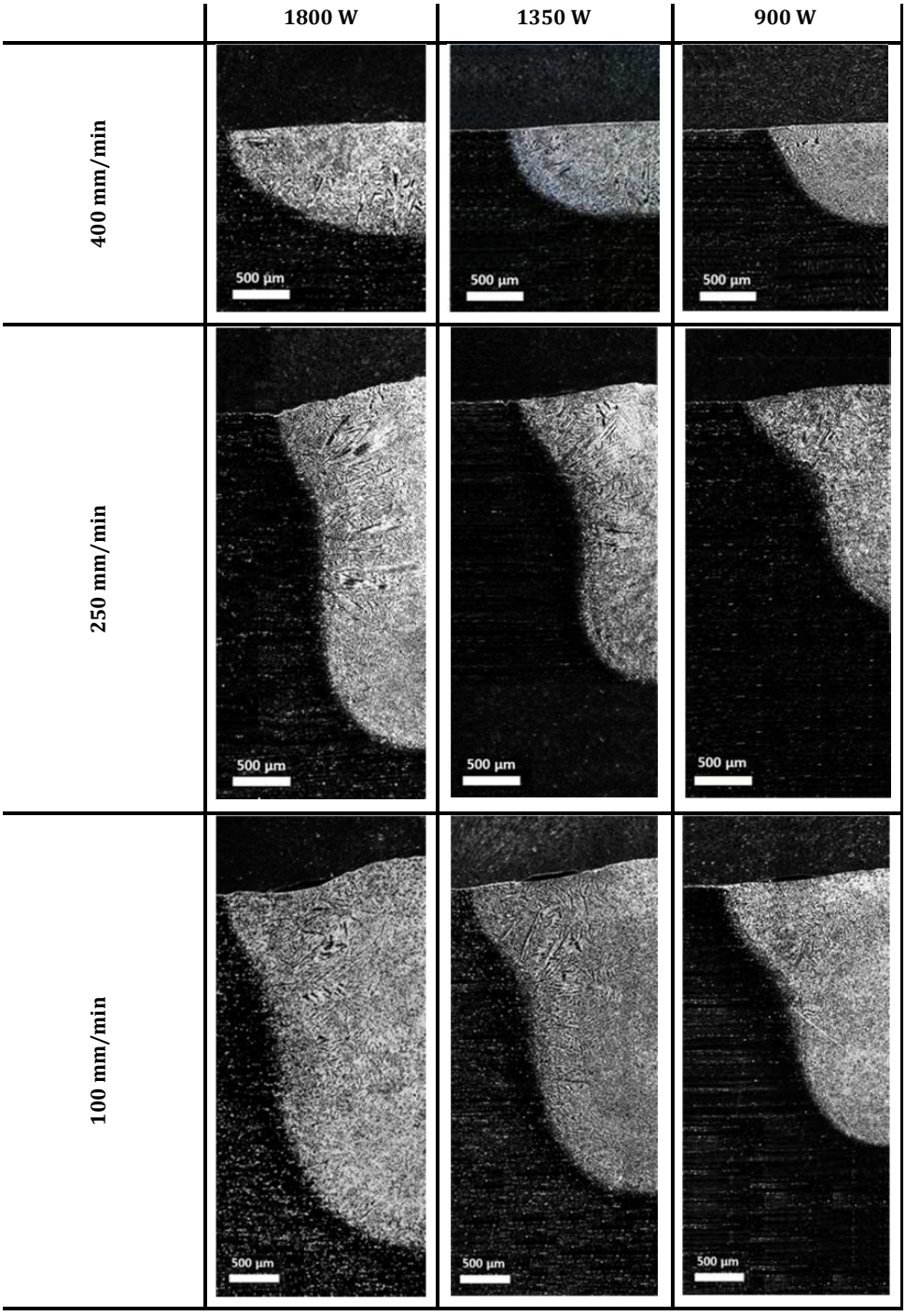

Figure 4.7: Cross sectional micrographs obtained from the fabricated test specimens.

4.3.2 Heat Source and Material Model

From metallographic examination of the test specimens, it is apparent from Figure 4.7, that the laser was operating in both the conductive and keyhole regime, as the geometry of the melt pools reflect the characteristics outlined in [166, 167]. To allow for both regimes to be represented within the thermal FE model, the superposition of a Gaussian disc and cylindrical heat source model was used [94]. The heat source model had the following form:

$$\begin{gathered} Q_{total} = fQ_{disc} + (1-f)Q_{cylindrical} \\ Q_{disc} = \frac{\eta P}{\pi r_s^2} exp\left(-\frac{r^2}{r_s^2}\right) \\ Q_{cylindrical} = \frac{3\eta P}{\pi 4 r_c^2 (z_u - z_l)} exp\left(-\frac{3r^2}{r(z)^2}\right) \quad -h_c \leq z \leq 0 \\ r(z) = r_c + \frac{z}{h_c} \end{gathered} \tag{4.8}$$

where f is the heat flux partition factor, η is the process efficiency, P is the laser power, r_s is the Gaussian heat source radius, r_c is the cylindrical heat source radius, $r = x^2 + y^2$, z_u and z_l is the upper and lower limit of the cylindrical heat source respectively and h_c is the height of the cylindrical distribution. Convective and radiative losses were applied to all of the free surfaces as outlined in Section 3.3.1. The thermal properties were temperature dependant and were assigned the values in Section 3.3.2. The thermal effects due to solidification of the melt pool were also included through the latent heat of melting as presented in Table 3.3.

4.3.3 Initiation of the Thermal Calibration

For the presented test case, the initial guess vector, $\mathbf{x}_0$ had the following form:

$$\mathbf{x}_0 = [r_s, r_c, h_c, f, \eta, h_{bed}] \tag{4.9}$$

Belitzki *et al.* [111] determined that the initial guess, supplied to a gradient based optimisation algorithm, severely effects the final optimised results. This was because several local optima existed for the same melt pool geometry and thermal profile. As an alternative to using arbitrary starting values as presented by Belitzki *et al.* [111], the initial guess was determined from physical measurements of the experimental melt pool geometry and from physical constraints of the current problem. The following assumptions were made to derive the initial guess vector for both operating regimes, with Figure 4.8 providing a visual representation of the initial values used for the geometrical parameters of the heat source model:

a) Process Efficiency (η)

   For both regimes, this was assumed to equal the absorptivity coefficient of Inconel 718 (IN718) and was therefore set to 0.3 [170].

b) Heat flux partition factor (f)

   For the conductive regime, it was assumed that the cylindrical portion of the heat source model was not required. This was due to the shallow penetration depth; therefore, f was set to 1. For the keyhole regime, due to the complex heat flux distribution, the value was set to 0.25. This was based on the work by Ducharme *et al.* [171] and Xia *et al.* [94].

c) Gaussian radius (r_s)

   An average value of the melt pool width was used in the conductive regime and for the keyhole geometry which had no narrow section. If the geometry had the characteristics of a nail head, the parameter equated the average width bound by the inflection point and the penetration depth.

d) Cylindrical radius (r_c)

   This parameter was equal to the Gaussian radius for both the conductive and keyhole regime with no narrow section in the weld profile. For a nail head geometry, this parameter was equal to the width of the melt pool at

the start of the narrow region.

e) Height of the cylindrical distribution (h_c)

For both regimes this was equal to the penetration depth of the melt pool geometry.

f) Thermal contact coefficient (h_{bed})

For both regimes, this was set to the free surface value of 25 W/m^2K as a better approximation of this value could not be achieved.

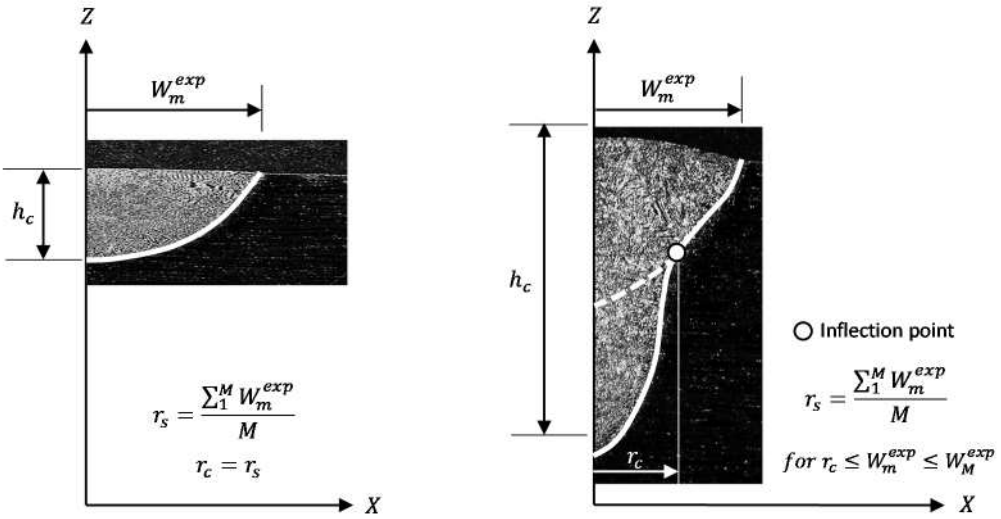

(a) (b)

Figure 4.8: Schematic of the geometry used to define the initial guess for the heat source parameters for (a) The conductive and keyhole regime where no narrow section of the weld was present (b) The keyhole regime where a narrow weld section was present.

The setup of all the FE models used for the calibration of the thermal model was automated; therefore, the dimensions of the test specimens and the process parameters were specified as scalar variables at the start of the analysis. As a bound solution was required, the upper and lower limits on the thermal parameters were defined as follows:

a) Process efficiency (η)

The upper and lower bound of the process efficiency were selected as 0.25 and 0.75 respectively. These values were based on the maximum and minimum energy transfer efficiency for laser beam welding, in the conductive and keyhole regime, as documented by [165].

b) Heat source partition factor (f)

The upper and lower bound was set to 0 and 1 respectively to include/not include the cylindrical heat source.

c) Gaussian radius (r_s)

The minimum value was assumed to equal the minimum focused spot radius of the laser, which for this current experimental set up was 0.5 mm [172]. The upper bound was equal to the maximum experimentally measured melt pool width (2 mm).

d) Cylindrical radius (r_c)

For this parameter, the lower bound was set to zero and for consistency, the upper bound was equal to the maximum Gaussian radius.

e) Height of the cylindrical distribution (h_c)

The upper and lower bounds were set to 0 mm and 6 mm to reflect the maximum and minimum penetration depth of the weld geometry.

f) Thermal contact coefficient (h_{bed})

The lower bound for this parameter was chosen as the free surface value of 25 W/m^2K for IN718 [145]. Due to the higher rate of heat exchange between the work piece and the welding apparatus [113], a higher magnitude value of 2000 W/m^2K was used for the upper bound.

4.3.4 Determining Convergence Criteria

To determine a baseline value for the minimum allowable change in the melt pool area and an acceptable value for the coefficient of determination (R^2) determined from the temperature profile, a parametric study was conducted. For the current process parameter window (Table 4.2) [173], a prediction of the melt pool geometry and thermal profile was conducted for element sizes ranging between 2 mm and 0.125 mm.

Table 4.2: Welding and heat source parameters for the parametric study to determine the convergence criteria (Parameter set was designed from the original set 1-9).

	Parameter Set					
Assumed Model Parameter	**A1 (Conductive)**	**A3 (Conductive)**	**A7 (Partial Penetration)**	**A9 (Partial Penetration)**	**A7 (Full Penetration)**	**A8 (Full Penetration)**
η	0.3	0.3	0.3	0.3	0.35	0.55
f	1	1	0.25	0.25	0.25	0.25
r_s (mm)	1	1	1	1	1	1
r_c (mm)	0	0	1	1	1	1
h_c (mm)	0	0	4	4	6	6
h_{bed} (W/m^2K)	25	25	25	25	25	25
Melt Pool Geometry Schematic	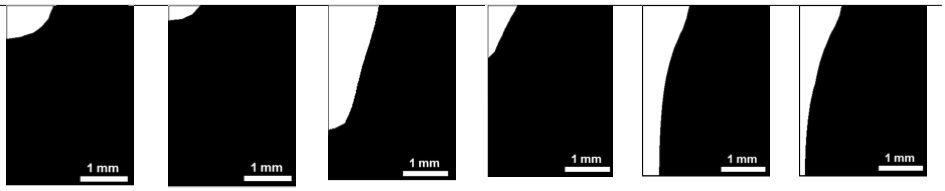					

For each reduction in mesh size, the coefficient of determination (Equation 4.3), the change in melt pool area (Equation 4.4) and the computational time required to complete the analysis were calculated. The final convergence value was selected based on a trade-off between the increase in the solution accuracy from reducing the element size and the time required for the analysis to complete. To estimate the heat flux entering the domain for the parametric study, the radii of both heat sources were assumed to equal 1 mm. The remaining heat

source parameters were determined based on the assumptions outlined in section Section 4.3.3. It should be noted that a higher process efficiency was required to achieve a full penetration weld profile, when the power was equal to 900 W. To determine the convergence criteria for the mesh sensitivity study, a series of test cases were evaluated. The coefficient of determinations (R^2) for the thermal history, the change in melt pool area (ΔA) and the computational time were calculated for mesh sizes ranging from 2 mm to 0.125 mm, with the results being presented in Figure 4.9. For all of the trial cases, the computational time increased exponentially due to the reduction in element size. The computational time ranged from approximately 1 minute up to 3 hours for the 2 mm and 0.125 mm element size respectively. When analysing the results across all the trial cases, it is apparent that mesh independence was achieved for the temperature profile before the melt pool geometry meaning that more nodal points were required to represent the geometry of the melt pool. The melt pool area should therefore be used in conjunction with a thermal profile to ensure that complete mesh independence was achieved.

For the conductive regime (Figure 4.9(a) and Figure 4.9(b)), mesh independence was attained for a 0.5 mm element size, as no reduction in error was achieved through a further reduction in element size. Therefore, for both cases, an optimum element volume of 0.5 x 0.5 x 0.5 mm^3 in the HAZ was required. The increase in the error associated with the melt pool area, observed for the case A1, was as a result of the heat flux distribution being better represented by the FE domain in subsequent iterations due to the increase in discretisation points present within the domain. Therefore, this altered the predicted thermal field and as a result, the melt pool geometry.

For the keyhole regime, mesh independence was not as definitive as the error between the predicted melt pool areas was still changing when reducing the element size from 0.25 to 0.125 mm. For both of the partial penetration cases, a

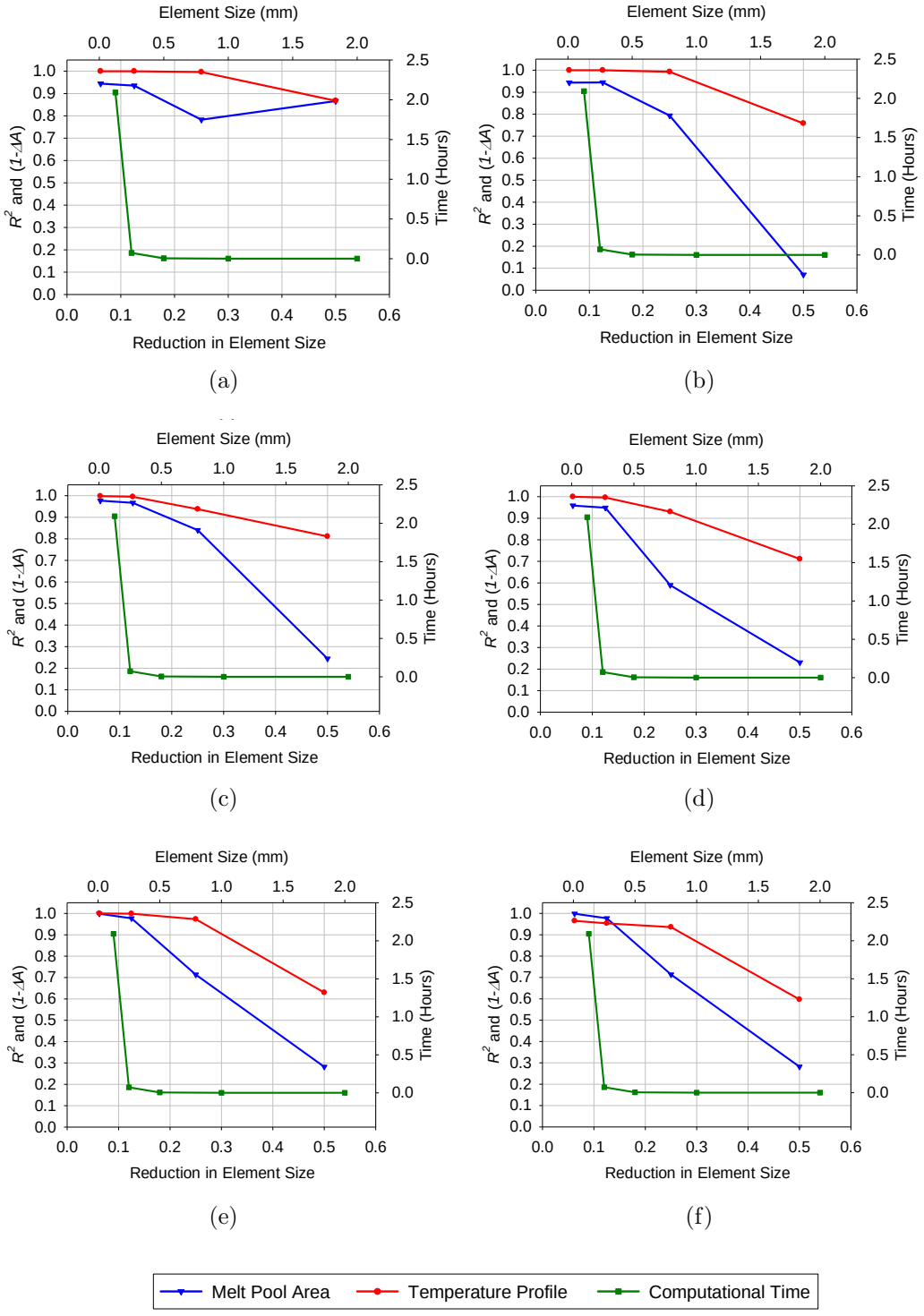

Figure 4.9: Results from the parametric study showing the change in melt pool area $(1 - \Delta A)$ and the coefficient of determination (R^2) for each element size. (a) Set A1-Conductive (b) Set A3-Conductive (c) Set A7-Partial Penetration (d) Set A9-Partial Penetration (e) Set A7-Full Penetration (f) Case A9-Full Penetration.

maximum reduction in error of 1% was achieved between the melt pool geometries for a two hour increase in computational time. As no considerable reduction in error was attained for such a large computational deficit, the optimum element size was determined as 0.5 mm for both cases. As, the same phenomena was present for both of the full penetration cases, the same element size was selected. For all of the test cases, the element size to achieve mesh independence was determined as 0.5 mm. The minimum change in melt pool area, to achieve the optimum element size (0.5 mm), for the presented cases was 6.5% (Figure 4.9(a)); therefore this value was used for the convergence criteria. For consistency, the same value was used for the coefficient of determination, for the temperature profile, i.e. $R^2 \leq 0.935$.

4.3.5 The effect of w on the Solution

To determine if a MOO was required, the value of the weight applied to the composite objective function was varied and the effect on the solution was monitored. The weights applied to the objective function have to sum to unity when implementing a weighted sum method [105], therefore the weight (w) was varied from 0 to 1. This was completed for the test cases outlined in Table 4.3.

These parameters defined a known solution for the optimisation, which will be referred to as the target solution. It should be noted that the assumed model parameters here are different from Table 4.2, to ensure that three common melt pool geometries (elliptical, nail head and full penetration) were evaluated. The initial guesses were determined from the numerically derived melt pool geometries (Figure 4.12), using the same assumptions previously outlined in Section 4.3.3. It should be noted that a w value of 0 and 1 provided a SOO based on the melt pool geometry and the temperature history respectively. The results of the parametric study are presented in Figure 4.10.

Table 4.3: Parameters for the test cases used to generate the target solutions to evaluate the use of a SOO or MOO for the optimisation algorithm. (Parameter set was designed from the original set 1-9).

	Parameter Set		
Assumed Model Parameter	**B1 (Conductive)**	**B8 (Partial Penetration)**	**B7 (Full Penetration)**
η	0.3	0.35	0.3
f	1	0.25	0.3
r_s (mm)	1	1	1.2
r_c (mm)	0	0.6	1
h_c (mm)	0	4	6
h_{bed} (W/m^2K)	500	500	500
Melt Pool Geometry Schematic	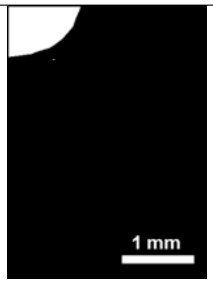	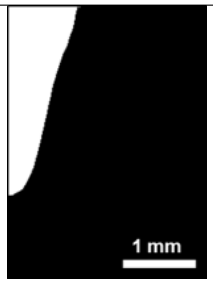	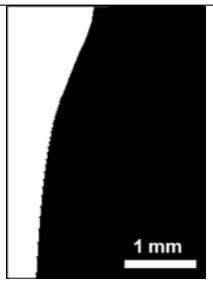

From the review of previous literature, some authors [110, 111, 174] calibrated the heat source model using a SOO, considering only the temperature history or the melt pool geometry. However, from Figure 4.10 it was apparent that a SOO is not sufficient to calibrate the parameters of a thermal FE model. For all three cases using the hybrid heat source model, a MOO was required. When only using a SOO the maximum value of the cumulative percentage error was greater than when a combination of the two objective functions were considered. When the weight parameter was zero, i.e. a SOO for the melt pool geometry data, the parameters of the heat source were determined with accuracy; however, a high error was presented for the thermal contact coefficient. This was because the optimisation algorithm had no temperature data for the cooling phase of the process. Therefore, this parameter was governed only by the thermal history data and not by the geometry of the melt pool.

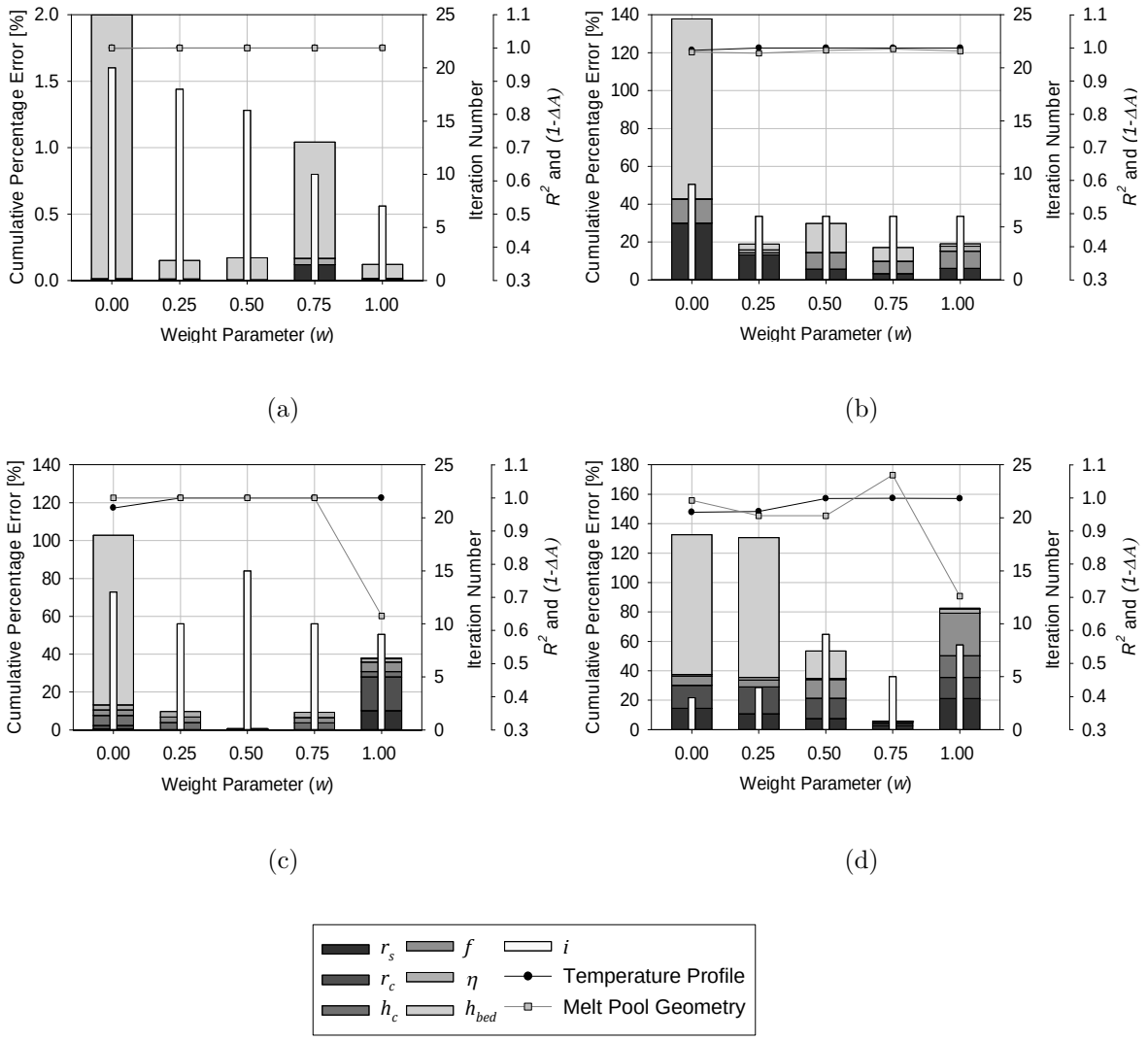

Figure 4.10: Cumulative percentage error between the target solution and the optimised parameters for different weight values. (a) Set B1 using Gaussian heat source only (b) Set B1 using combined heat source (c) Parameter Set B8 (d) Parameter Set B9.

When the weight parameter equalled one, the residual error for the convective coefficient was reduced due to the inclusion of the cooling phase of the process. From Figure 4.10, it is apparent that a SOO could be used for the conductive regime when only the Gaussian disc heat source was used, as this gave the lowest cumulative error between the target and optimised solution. This was because, for the Gaussian disc model, only three optimisation parameters were required, with the efficiency and Gaussian radius governing the temperature history and

melt pool profile. Therefore, when the optimisation algorithm varied these two parameters, the associated solution for the thermal history and melt pool geometry were coupled. This means, for this case only, the same thermal history will always generate the same melt pool geometry because of the limited variation in heat flux distribution achievable from this heat source model. Therefore, it is recommended that when a multi-parameter heat source model is required a MOO should be implemented. To ensure that all regimes and melt pool geometries could be calibrated using the outlined process, the hybrid heat source model was implemented. This would also increase the flexibility of the approach as no previous identification of the laser operating regime was required before the calibration process could be implemented.

It should be noted that although the cumulative percentage error was higher when this heat source was implemented, the conductive regime was still represented with accuracy. This can be validated from analysing Figure 4.11(a), Figure 4.11(b), Figure 4.12(a) and Figure 4.12(b), as no change in the melt pool geometry or thermal history was generated through the use of the hybrid heat source model. From analysing Figure 4.11 and 4.12 in conjunction with the coefficient of determination (R^2) for the temperature profile and the change in the melt pool area ($1 - \Delta A$), it was apparent that multiple variants of heat source parameters could provide the same solution for the thermal profile and the melt pool geometry. This therefore supports the work presented by Beltizki *et al.* [111]. However, for the fully penetrative keyhole case Figure (4.10(d)), only one optimum solution existed and this was when the cumulative percentage error was at a minimum value.

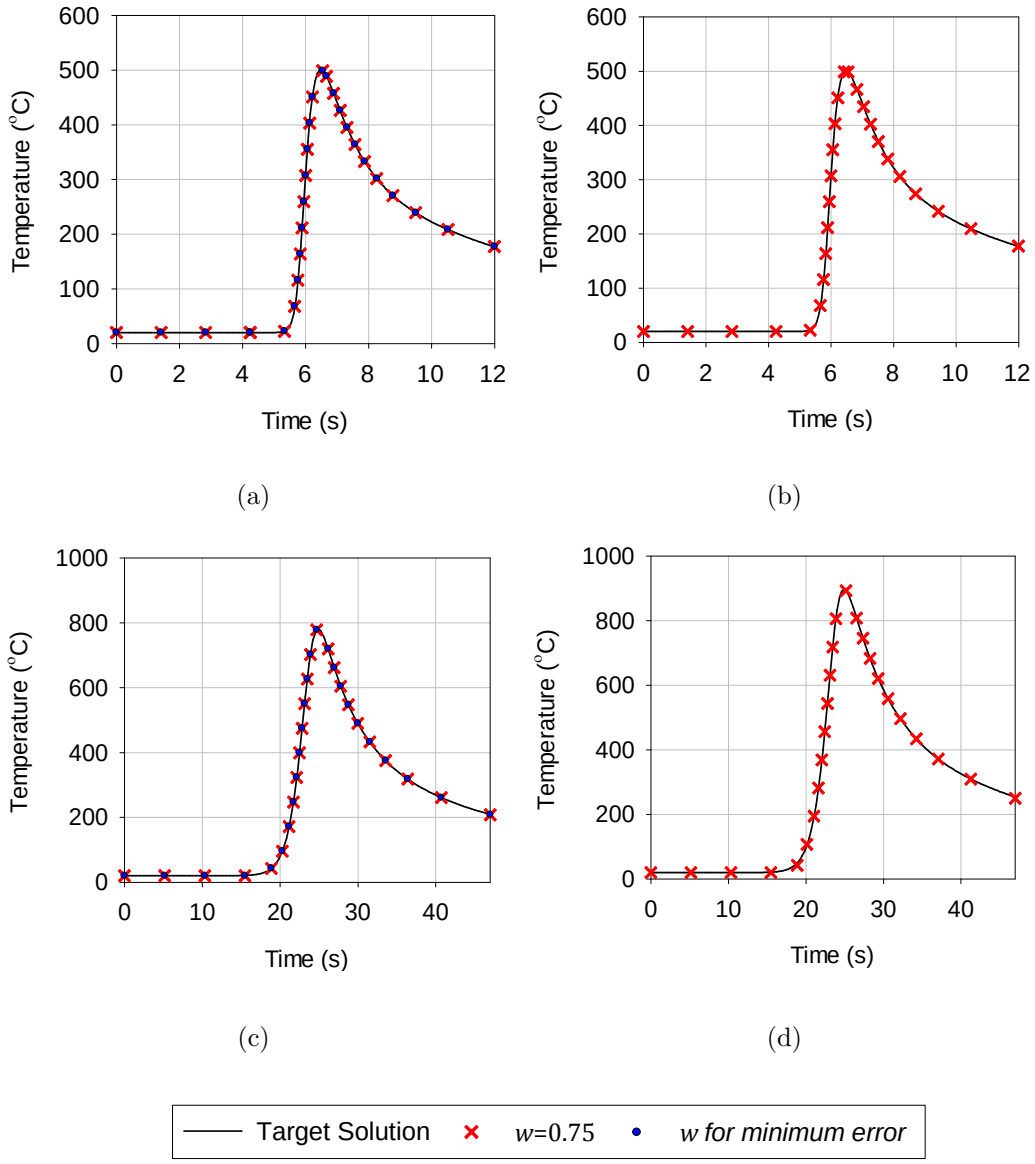

Figure 4.11: A plot comparing the target thermal solutions with the solution for w=0.75 and for w giving the minimum error (a) Set B1 no cylindrical heat source (b) Set B1 with the hybrid heat source (c) Set B7 (d) Set B8.

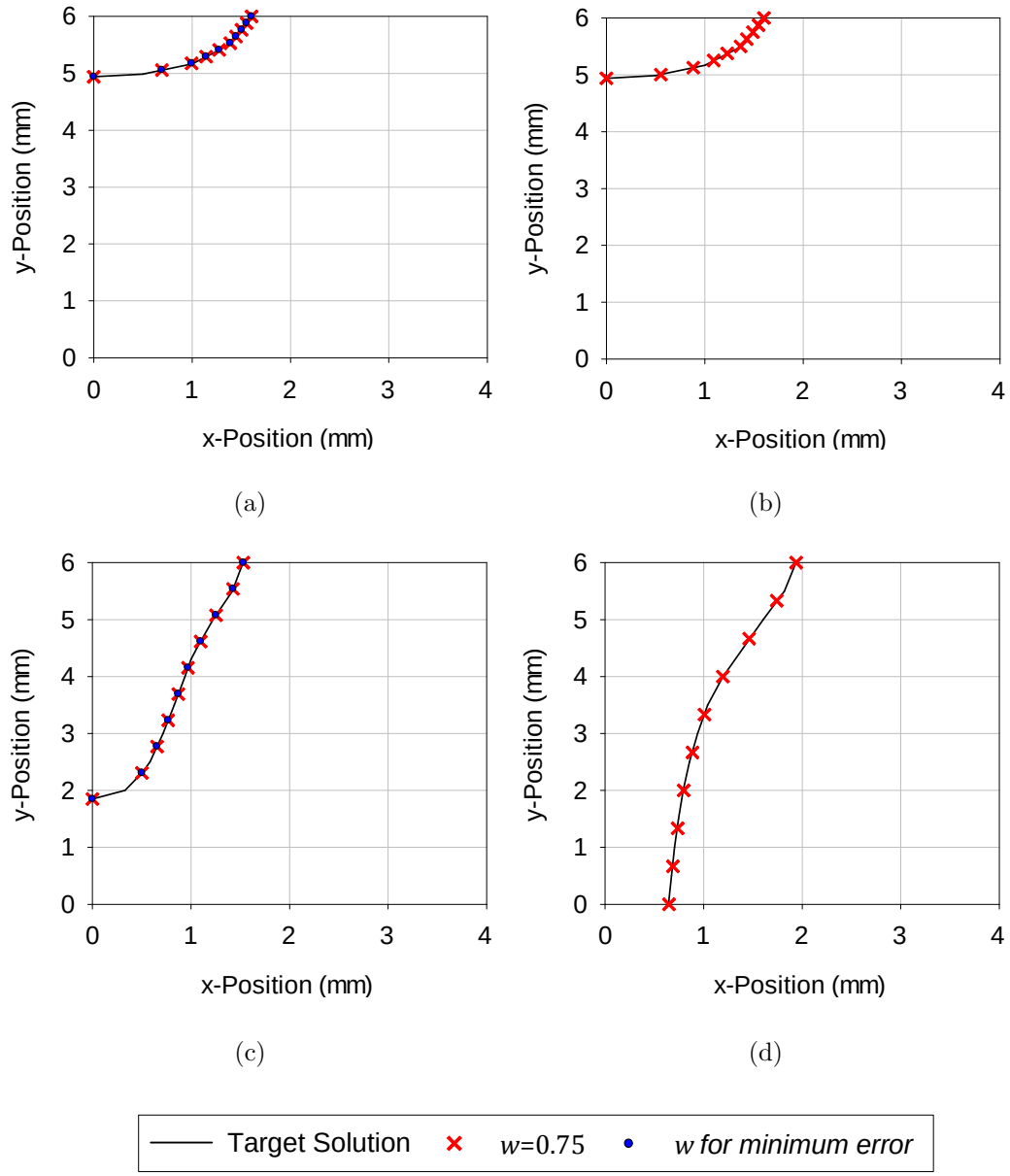

Figure 4.12: A plot comparing the target melt pool geometries with the solution for w=0.75 and for w giving the minimum error (a) Set B1 no cylindrical heat source (b) Set B1 with the hybrid heat source (c) Set B7 (d) Set B8. It should be noted for (a) and (b) the optimum was for w=0.75.

The optimum weight was selected based on the value which provided the lowest cumulative percentage error with respect to the target solution. For the conductive regime and the fully penetrative keyhole case, the optimum weight value was 0.75; however, for the partially penetrative keyhole case, the optimum value was 0.5. When the value was 0.75, the temperature profile influenced the optimisation

procedure by a ratio of approximately 3:1. However, when the weight was 0.5 the ratio was 1:1. Therefore, for the partial penetration case, artificial reduction of each objective function was not required to provide an equal contribution of error to the global objective function. However, for the other three cases, an artificial reduction was required. To ensure that the calibration procedure can be used for any melt pool geometry and to ensure that the operating regime does not have to be pre-determined, the value of w was taken as 0.75 for the optimisation. Using this value was valid for the partial penetration case, as the cumulative percentage error was less than the maximum value obtained for the other two operating conditions, for the same weight.

4.4 Results and Discussion

The proposed heat source model was calibrated for nine experimental samples across the entire process window for the current experimental set up. This provided melt pool geometries ranging from shallow elliptical fusion zones to deep penetration welds with narrow parallel sides, therefore testing the full capability of the proposed methodology.

4.4.1 Mesh Independence Study

The first stage of the calibration procedure achieved mesh independence based on an initial guess of the thermal model parameters. Figure 4.13 and Figure 4.14 present example results for the mesh sensitivity analysis. The initial element sizes used for the optimisation study are presented in Table 4.4. From analysing Figure 4.13 and Figure 4.14, it was apparent that the selected convergence criteria was appropriate, as visually, there was minimal deviation in the shape of the melt pool geometry from the optimum element size (Table 4.4) to the next element size evaluated by the study. It was also apparent that the change in melt pool

geometry was more severe during the early stage of the mesh sensitivity study, with the melt pool profile for the 2 mm and 1mm element size being very dissimilar to the converged solution. Therefore, this highlights the importance of completing a mesh independence study to ensure that subsequent solutions from the optimisation were accurate. It also ensures that a solution representative of the true melt pool geometry was achievable from the optimisation.

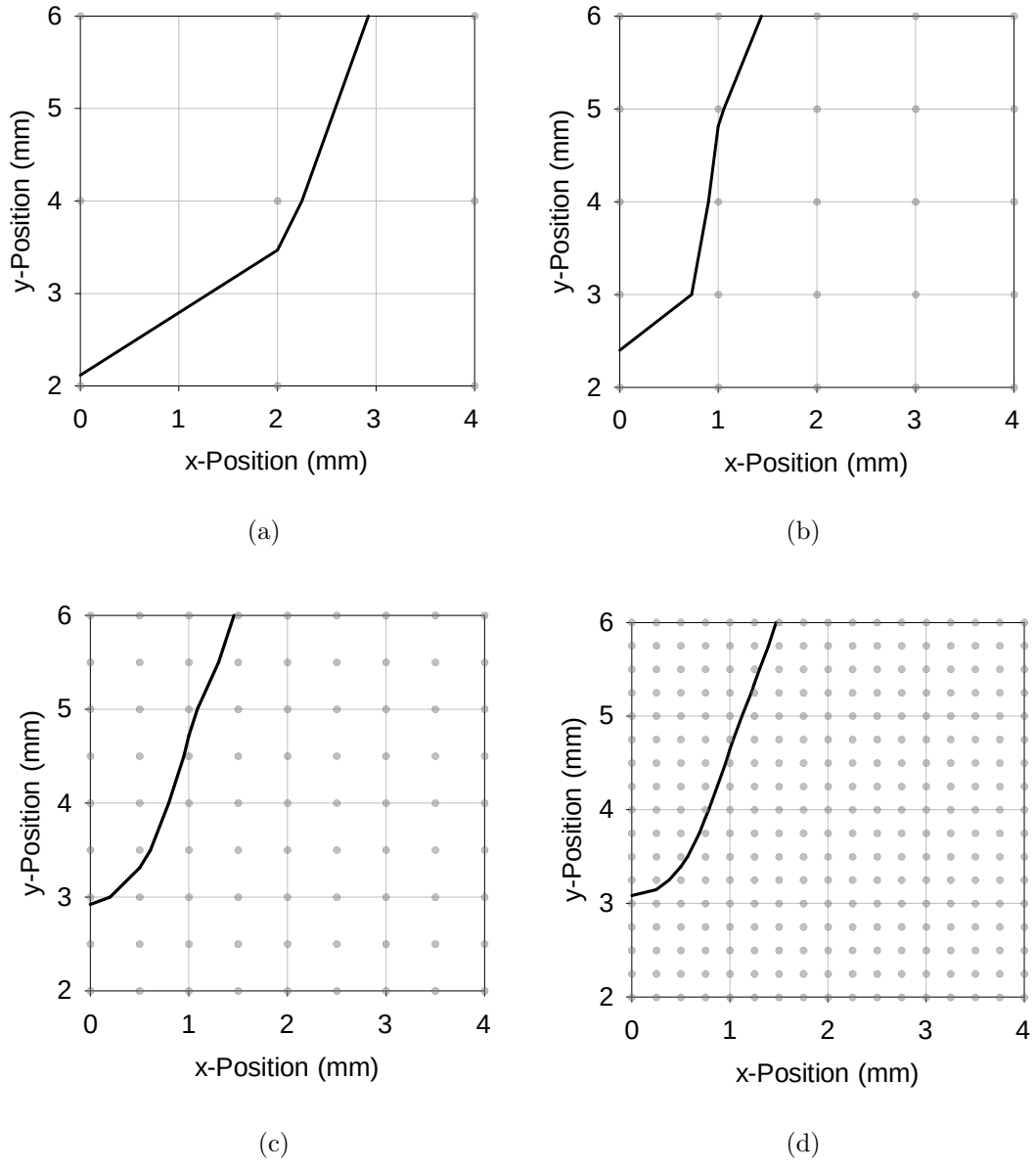

Figure 4.13: Mesh sensitivity results for parameter set 4 for element size (a) 2 mm (b) 1 mm (c) 0.5 mm (d) 0.25 mm.

Commonly, previous authors [107, 108, 174] have neglected this stage from the calibration procedure. Therefore, the validity of the previous approaches may lead to an inaccurate representation of the thermal field due to mesh independence not being achieved. However, it should be noted that variation in the shape of the melt pool geometry was more severe within the keyhole regime for larger element sizes. This could be due to an inaccurate representation of the heat flux distribution, as the initial guess values for the heat source parameters were often smaller than the 2 mm and 1 mm element size. Also, as the heat flux distribution was volumetric, an adequate number of elements were required through the thickness of the work piece. For the conductive regime, the elliptical melt pool geometry was present for all of the evaluated element sizes; therefore, this heat flux distribution could be represented with a larger element size when the combined heat source model was not used.

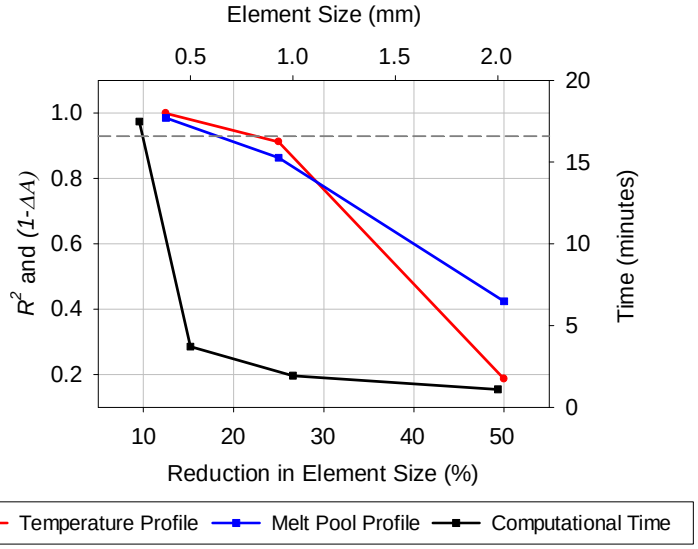

Figure 4.14: Example convergence data for the mesh sensitivity study for parameter Set 4.

Table 4.4: Initial element size for the optimisation study.

Parameter Set	Initial Element Size (mm)
1	0.5
2	0.5
3	0.25
4	0.5
5	0.25
6	0.25
7	0.5
8	0.5
9	0.25

Across the entire process window, only two element sizes were required to achieve mesh independence (0.5 mm and 0.25 mm). As only two element sizes were required, it can be concluded that a reduction in the step size between element evaluations could be implemented. Although a greater number of evaluations of the model would be required, an element size which was between 0.25 mm and 0.5 mm may have provided an accurate solution independent of the mesh. Therefore, this would lead to reduced computational times for the optimisation and for subsequent thermo-mechanical analyses. However, the benefit of reducing the element size by half ensured that negligible error was introduced during the linear interpolation of the data, as only one data point was interpolated between two true data points. From Table 4.4, an increased element size can be used when a larger linear energy density (P/V) was present. With an increase in energy density, a greater magnitude of the heat flux distribution would be present. For these cases, the initial guess for the heat source radii were in the range of 2 mm and 0.9 mm. Therefore, a greater proportion of the domain was covered by the heat source distribution. This allowed the number of discretisation points, which represented the Gaussian profile of the heat sources to be reduced. As a result, larger element sizes can be used. Another reason may be due to

the size of the melt pool geometry which was predicted by the FE model. With an increase in linear energy density, a greater molten region would be present; therefore, the melt pool geometry would inherently cover an increased portion of the through thickness domain. This reduced the number of nodes and in turn elements required to capture the fidelity of the profile which represented the melt pool geometry. Although, there appears to be an apparent trend with linear energy density and element size, an anomaly was present for case 6. For this case, a smaller element size was required to achieve mesh independence than for case 8, even though a reduced linear energy density was present. In comparison to case 6, a more complex melt pool geometry existed for case 8; therefore, the element size was not only dictated by the linear energy density, but it was also governed by the profile of the melt pool geometry. As no definitive relationship between process parameters and the optimum element size to achieve mesh independence could be determined, it is advised that this portion of the calibration procedure is always implemented.

Upon checking if mesh independence was still achieved for the optimised parameter set, it was determined that no further refinement was needed for any of the cases. Therefore, the optimisation was not repeated for any of the presented cases.

4.4.2 Calibrated Thermal Model Parameters

A comparison between the experimental and calibrated results are presented in Figure 4.15 to Figure 4.17. It should be noted that the white profile was determined through the use of the image analysis and was used as the experimental data for the optimisation. A good agreement was achieved between the determined profile and the experimental macrograph showing validity in the applied methodology. The optimised parameters for all of the presented cases are provided in Table 4.5.

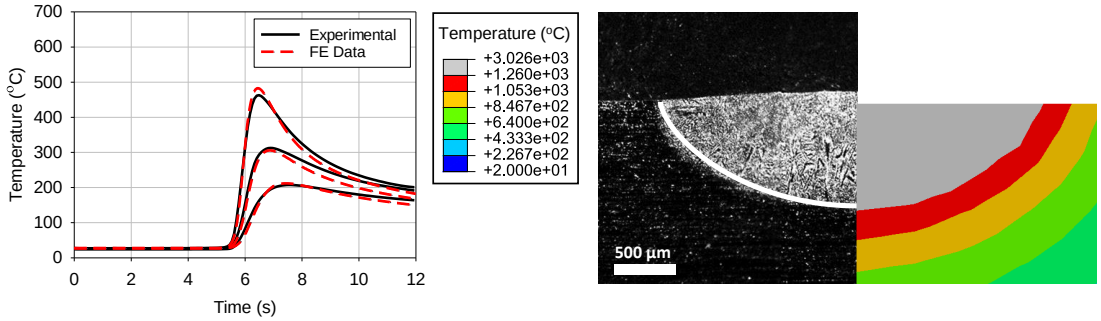

(a)

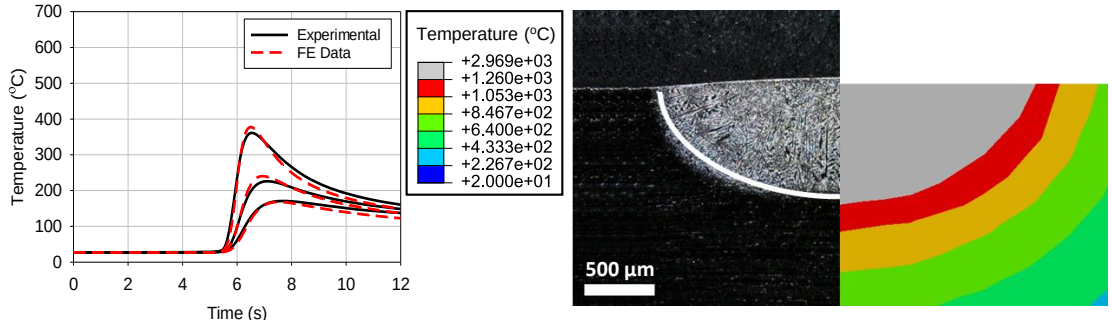

(b)

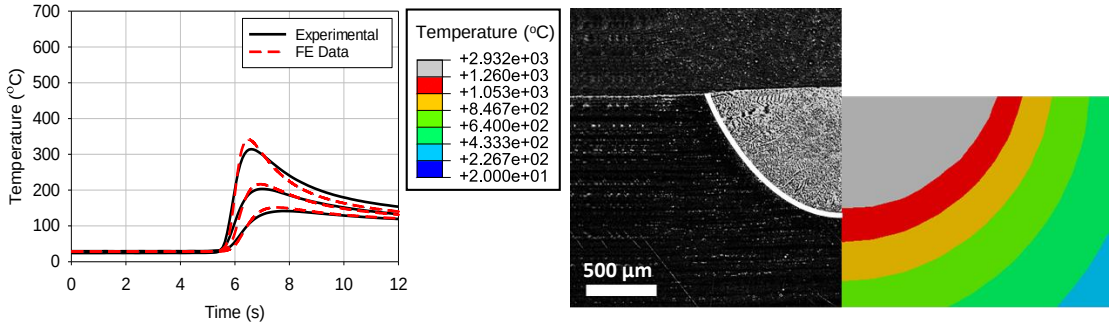

(c)

Figure 4.15: A comparison between the experimental and predicted thermal histories/melt pool geometries in the conductive regime for (a) Parameter set 1 (b) Parameter set 2 (c) Parameter set 3.

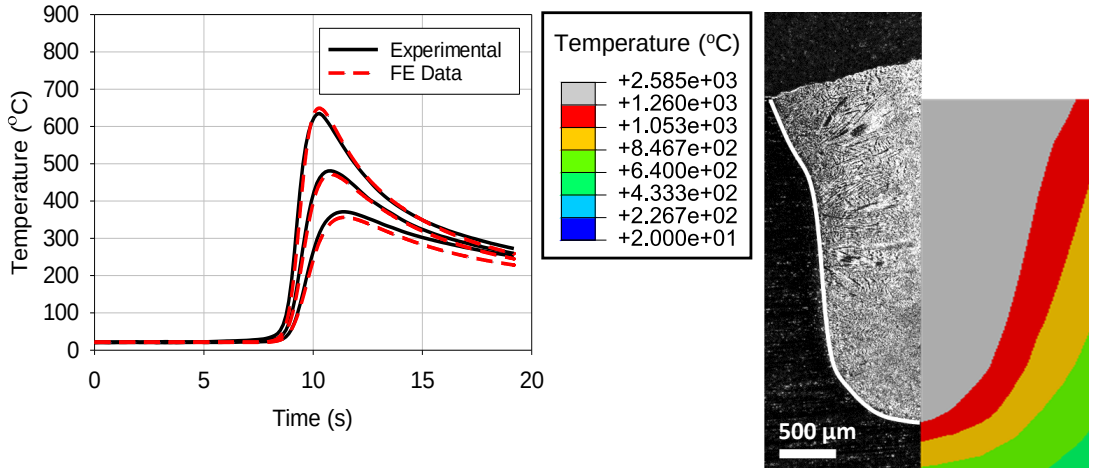

(a)

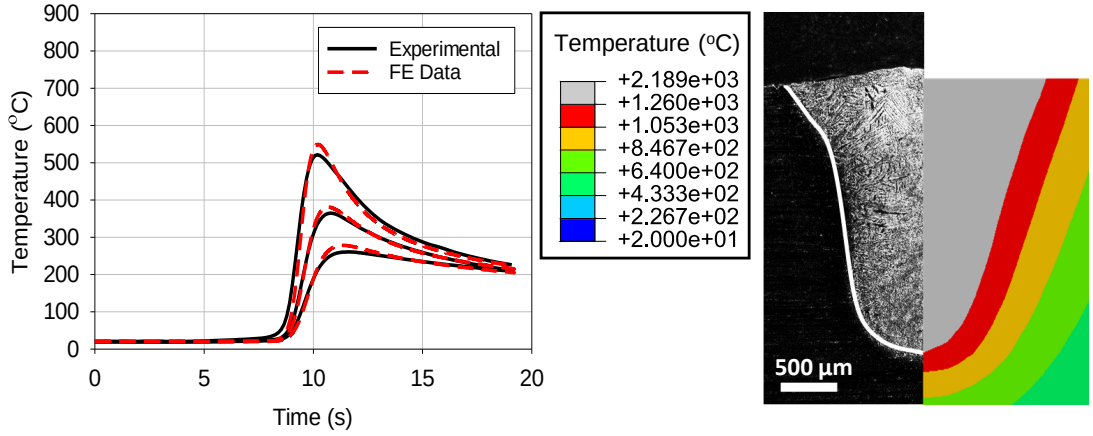

(b)

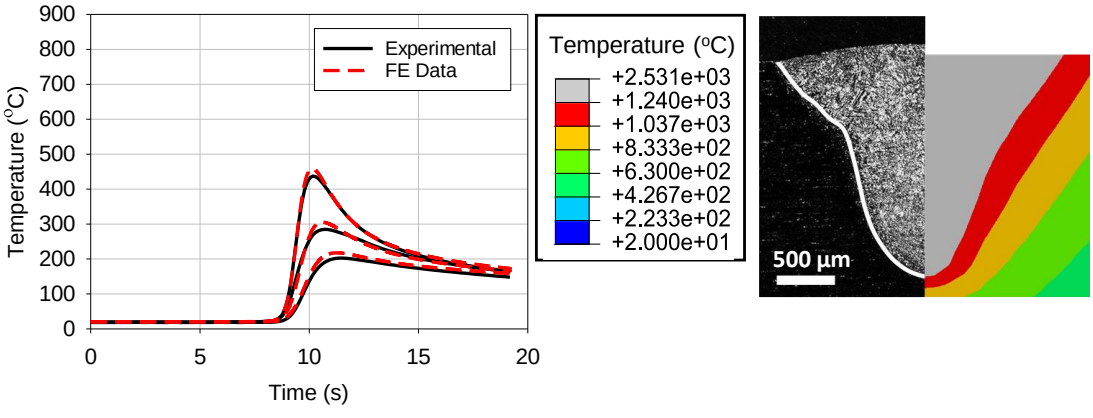

(c)

Figure 4.16: A comparison between the experimental and predicted thermal histories/melt pool geometries in the conductive regime for (a) Parameter set 2 (b) Parameter set 3 (c) Parameter set 4.

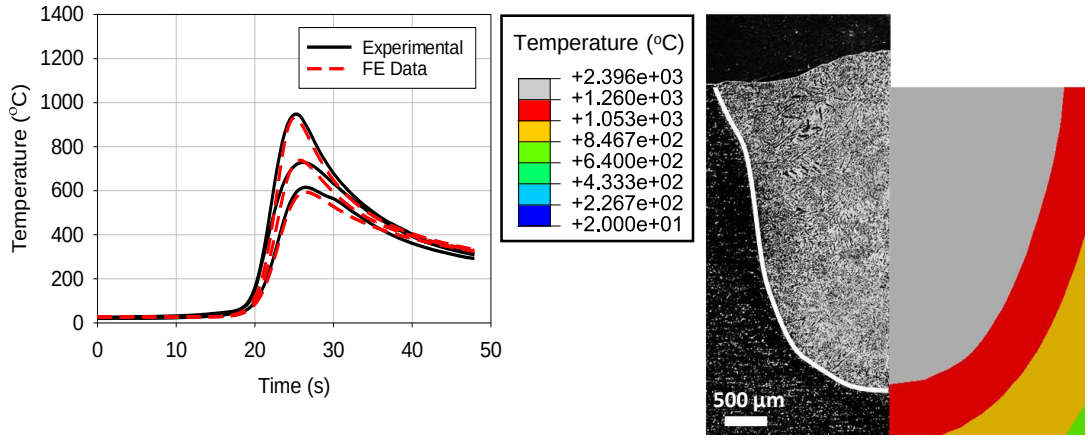

(a)

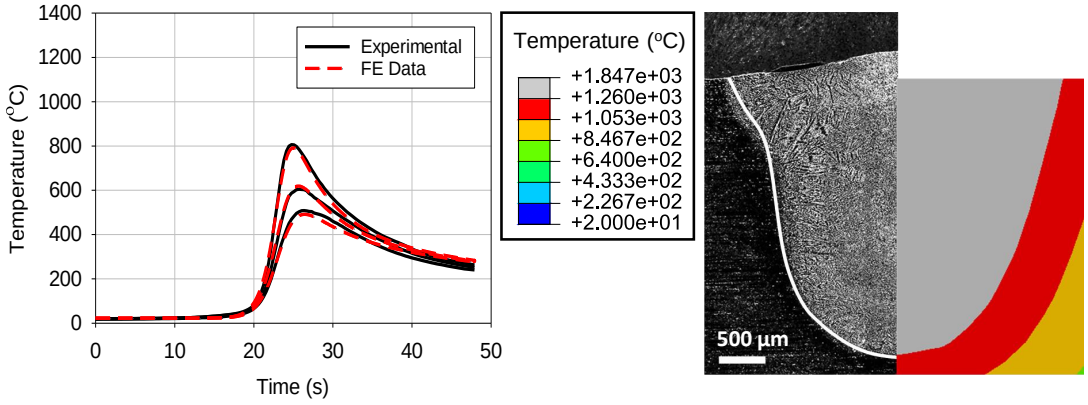

(b)

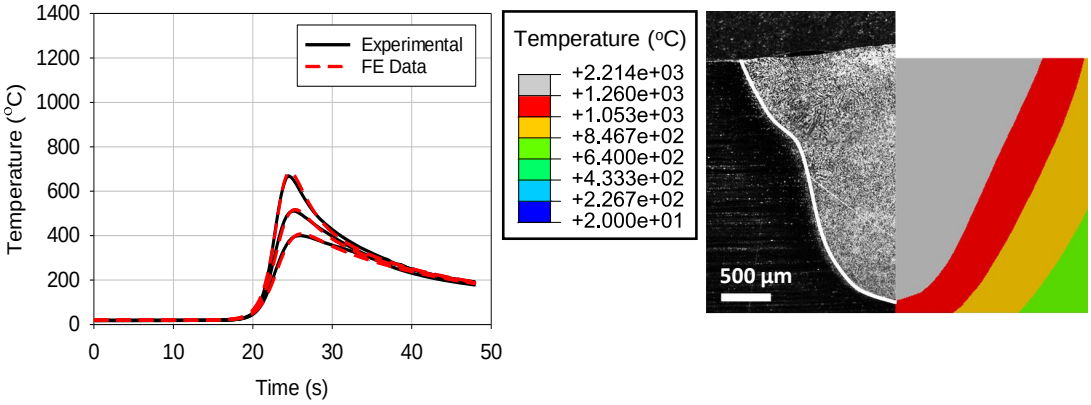

(c)

Figure 4.17: A comparison between the experimental and predicted thermal histories/melt pool geometries in the conductive regime for (a) Parameter set 2 (b) Parameter set 3 (c) Parameter set 4.

Table 4.5: Optimised heat source parameters for the combined heat source model derived using the experimental cases.

Parameter Set	η	f	r_s (mm)	r_c (mm)	h_c (mm)	h_{bed} (W/m^2K)
1	0.27	0.98	1.15	0.54	1.74	25.33
2	0.29	1.00	0.89	0.87	0.73	25.00
3	0.36	0.99	0.70	0.65	0.81	25.08
4	0.39	0.17	1.81	0.54	2.86	25.16
5	0.36	0.27	1.36	0.84	2.72	25.44
6	0.38	0.50	1.28	0.38	1.86	51.17
7	0.36	0.28	1.87	1.87	3.60	181.50
8	0.35	0.19	2.00	2.00	3.02	187.48
9	0.39	0.38	1.33	0.73	2.53	344.31

For the conductive regime, the optimisation determined that a majority of the flux distribution was required from the Gaussian disc heat source as the heat flux partition factor was greater than 0.97 for all three cases. For cases 2 and 3, the heat flux was predominately represented by the Gaussian disc heat source, with a 0% and 1% contribution from the cylindrical heat source respectively. A higher contribution was required for case 3; however, as this was less than 5% it was determined that the Gaussian disc heat source model was appropriate for modelling the heat flux distribution for the conducive regime. As the total flux contribution from the cylindrical heat source was less than 5% for case 1-3, this confirmed that these process parameters were within the conductive operating regime. For case 1, the contribution of the cylindrical heat source was 2%, which was greater than for the other two cases in the conductive regime. Firstly, it should be noted that with the current optimisation algorithm, each parameter of the model was altered in an attempt to reduce the global error of the objective function. Therefore, for early iterations of case 1, the optimisation deemed it advantageous to include the heat flux distribution from the cylindrical heat source

to reduce the global error. However, as the iterations proceeded, the algorithm compensated for this inclusion by dissipating the cylindrical contribution over a greater volume. This was completed by increasing the height (h_c) of the heat source model to be greater than the penetration depth of the melt pool. Therefore, it is believed that this parameter set was within the conductive regime and was not transitioning into the keyhole regime. For all three of these cases, the reduction in linear energy density was compensated by a reduction in the Gaussian radius (r_s), with the optimised values being less than the experimental melt pool width. Therefore, the melt pool was predominately governed by the conduction of heat flux in the area of the HAZ. It should be noted that the parameters of the cylindrical heat source were included for this operating regime; however, the values were greater than the experimental melt pool geometry showing that the flux distribution was dissipated over a larger volume, further validating that these cases were within the conductive regime. With regards to the process efficiency (η), the value determined for all three cases fell within the range of published values for the absorptivity of IN718 [170, 175]; therefore, it was concluded that the absorption of the laser power in the conductive regime was highly dependent upon the surface finish of the workpiece.

For the keyhole regime, a greater percentage of the heat flux distribution was required from the cylindrical portion of the heat source model. The contribution ranged from 50% to 83%; therefore, a more complex distribution of heat flux was required. The radii of the Gaussian disc and cylindrical heat source determined the final geometry of the predicted melt pool. For the cases where a nail head weld profile was present (Figure 4.16 and Figure 4.17(c)), the Gaussian radius was always greater than the cylindrical radius. Therefore, the radius of the disc heat source model dictated the width of the melt pool at the surface, with the narrow section being governed by the cylindrical radius. Across cases 4 to 9, the surface width of the melt pool reduced with linear energy density, which was

compensated through a reduction in the Gaussian radius and an increase in the contribution from the disc heat source model. However, this compensation was not present for case 7, as the radius of the cylindrical heat source was smaller than the experimentally measured surface width. For the height of the cylindrical distribution, this was approximately equal to the total penetration depth of the melt pool for cases 4 to 9. A maximum and minimum percentage error between the height of the heat source model and the experimental penetration depth was 9.3% and 0.25% respectively; therefore, showing that the assumption for the initial guess of this parameter was reasonable. For most of the cases in the keyhole regime, the process efficiency determined from the optimisation was greater than for the conductive regime; therefore, identifying that keyhole welding is more efficient than operating the laser in the conductive regime, agreeing with the work presented by Messler [165]. However, the published values for the efficiency of a keyhole welding process range from 0.5-0.75 [165], which are greater than the values determined by the optimisation. A possible reason for this may be due to the surface finish of the work piece, as the absorption of the laser heat energy is highly dependent upon the roughness of the material [176]. Another physical phenomena causing this discrepancy maybe because the laser heat source, was not operating solely in the keyhole regime, i.e. transitioning between the conductive and keyhole regime. When calculating the peak heat flux from the optimised parameters, the maximum and minimum value were $1.18 \times 10^{11}\ W/m^2K$ and $7.68 \times 10^{9}\ W/m^2K$ respectively. As the lower limit on the range of values was less than the published value for keyhole welding ($10^{10}\ W/m^2K$ [165]), it is believed for some of the presented cases (Case 7 and 8), the weld was in a transitioning state, therefore a lower process efficiency was determined. This can also be validated by analysing Figure 4.17(a) and Figure 4.17(b) where the weld geometry was predominately elliptical in shape. Therefore, the distinct geometrical features of a keyhole weld, as outlined by Wiklund *et al.* [167], were not present. A numerical

reason for the discrepancies between the determined and published values for the process efficiency, may have arisen from the method in which the optimisation was reducing the error of the objective function. The iteration history for the heat source radii and the process efficiency are presented in Figure 4.18.

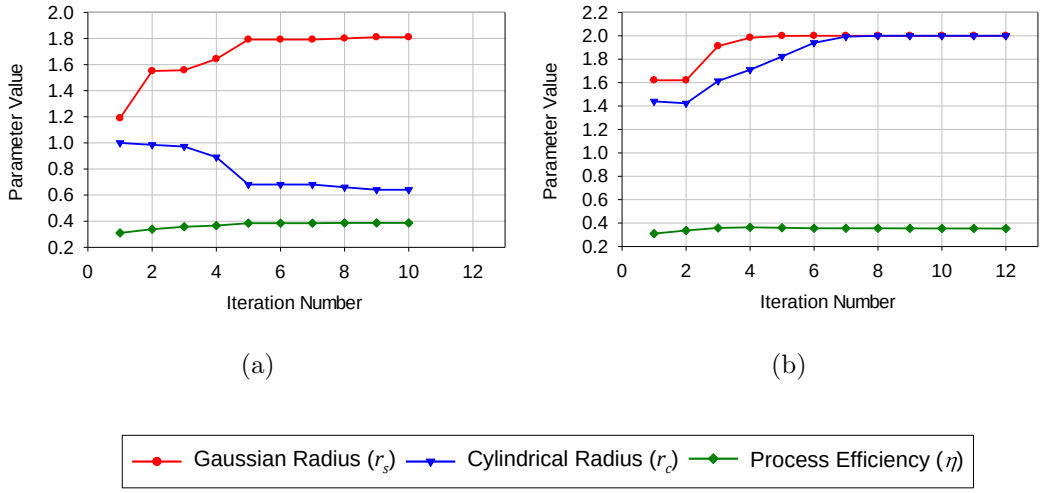

Figure 4.18: An example of the iteration history for the heat source radii and the process efficiency for (a) Parameter set 4 (b) Parameter set 5.

From analysing Figure 4.18, it was apparent that to minimise the objective function in early iterations of the optimisation, the solution was more sensitive to variation in the radii of the heat source. This is shown through the greater step size between the radii in comparison to the process efficiency, with a maximum percentage change of 30% and 9.3% respectively. Therefore, the process efficiency acts as a sliding scale, which was used to refine the final solution in an attempt to further reduce the error of the objective function. For cases 7 to 9, a large contribution of the cylindrical heat flux distribution was required to generate the deep penetration geometry. Again, the height of the cylindrical heat source model reflected the penetration depth of the experimental weld. It should be noted, that a large percentage error was present for the width of the melt pool at the throat of the narrow section, for case 7 and 8. From analysing Figure 4.17(a) and Figure 4.17(b), the nail head section was not predicted, with the geometry

being represented as a single elliptical profile. The nail head portion did not exist as the radii of the heat source were equal, therefore a complete cylindrical distribution of the heat flux was present for these cases.

4.4.3 Accuracy of the Refined Model Parameters

To assess the accuracy of the calibration, the percentage error between the predicted and experimental peak temperature and the percentage error for key geometrical characteristics of the melt pool are presented in Table 4.6 and Table 4.7 respectively. Overall, a good agreement was obtained between the experimental and predicted data sets, for both the thermal history and melt pool geometries. The predicted peak temperatures agreed well for each location, with a maximum error of 8.6% for case 3. For the cooling phase, a good agreement was achieved; however, an overestimate in the cooling rate was present. From Table 4.5, the convective transfer coefficient was approximately 25 W/m^2K for all of the cases in the conductive regime. This was equal to the lower bound set on the optimisation vector, $\boldsymbol{x}$. Therefore, the reason for this error could be the assumption that the lower bound for this parameter equating the free surface value was incorrect or the value determined by Dye *et al.* [145] was not suitable for the current experimental set up. Also for these cases, it should be noted that the losses may have been predominately governed by conduction within the work pieces and convection to the environment rather than directly to the CNC bed.

Table 4.6: Percentage error between the experimental and predicted peak temperature at 3 mm, 4 mm and 5 mm from the weld centreline.

Parameter Set	**Percentage Error for 3 mm Peak Temperature (%)**	**Percentage Error for 4 mm Peak Temperature (%)**	**Percentage Error for 5 mm Peak Temperature (%)**
1	4.3	2.2	2.2
2	4.5	6.3	1.7
3	8.6	6.5	7.1
4	2.2	2.0	4.0
5	5.3	4.4	6.7
6	4.9	7.2	7.4
7	1.8	1.3	8.3
8	1.9	2.3	3.3
9	2.6	1.2	1.8

The prominent use of the Gaussian disc heat source model captured the elliptical profile of the melt pool geometry with accuracy, with a minimum error of 4.1% and 3.2% for the melt pool width and depth respectively. The maximum error was for case 3, where the predicted melt pool geometry was overestimated. Unlike for case 1 and 2, a shallow elliptical geometry was not present for the experimental melt pool; therefore, it is apparent that the heat source model could not replicate this shape with accuracy. Due to this and the use of a MOO, a compromise between attaining an accurate thermal history and melt pool geometry was achieved. This phenomena was reflected in the low iteration count for this case, as a minimum solution was obtained after only two iterations, showing that a significant reduction in error was unachievable from the initial guess of the parameters.

Table 4.7: Percentage error between the experimental and predicted melt pool surface width (W_s), the throat width at the inflection point (W_t), the total penetration depth (D) and the melt pool area (A_{melt}).

Parameter Set	**Percentage Error in W_s** (%)	**Percentage Error in W_t** (%)	**Percentage Error in D** (%)	**Percentage Error in A_{melt}** (%)
1	4.1	N/A	3.2	3.4
2	4.7	N/A	4.0	1.0
3	8.4	N/A	3.5	11.0
4	2.2	5.8	0.8	1.8
5	8.2	13	2.3	4.1
6	4.6	4.6	1.4	8.1
7	1.5	14.2	3.0	9.2
8	2.2	12.8	1.6	0.3
9	6.5	2.6	0.3	6.0

For the keyhole regime a good agreement between the predicted and experimental thermal field was achieved due to the lower percentage error in Table 4.5. From Figure 4.16, the high thermal gradient at the start of the heating phase was captured for all cases, except for case 5. Instead, a greater heating rate was predicted than experimentally measured. A maximum and minimum error of 7.4% and 2% for the predicted peak temperature was reported, showing an accurate representation of the thermal histories utilising the hybrid heat source model. For the cooling phase, a better representation of the cooling rate was achieved than for the conductive regime. It should be noted for case 4, the discrepancy in the cooling phase, for the 5 mm thermal history, was due to error in the experimental data. This was because a sharp transition was present in the cooling phase, which does not match the other two curves. From Table 4.5, the thermal contact coefficient was not dissimilar from the free surface value, therefore showing that the conduction to the welding apparatus for these cases was negligible. However, in

comparison to the conductive regime (Figure 4.15), the cooling rate was greater, showing that some thermal energy was lost to the bed. This increase was due to the greater penetration depth of the weld, therefore allowing heat to dissipate from the bottom surface of the workpiece. From the comparison of the melt pool geometries in Figure 4.16, the combined heat source model provided an accurate representation of the characteristic features of the keyhole melt pool geometry. For each case, the inflection point was captured generating the common nail head cross section for each case. However, the depth of the broad section, for case 5 and 6, was underestimated, with the gradient between the predicted surface width and inflection point being shallower in comparison to the experimental melt pool. For case 6, the depth of the nail head was predicted with accuracy; however, the inflection point was not as defined for the predicted melt pool when compared to the experimental macrograph. The narrow vertical section of the melt pool was replicated for all three conditions; however, the predicted geometry was shallower in this region, with the vertical portion in Figure 4.16(a) and Figure 4.16(b) not being predicted. Again, this highlighted the difficulty in representing the complex heat flux distribution within keyhole welding, using FE heat source models. However, the selected heat source model provided a good estimate as the maximum error for the melt pool surface width, the throat width and the penetration depth was 8.2%, 5.8% and 2.3% respectively.

From analysing Table 4.6, the predicted peak temperatures, at all three thermocouple locations agreed well with each other, with a maximum and minimum error of 8.3% and 1.2% respectively. The maximum error arised due to an underestimate in the predicted peak temperature for case 7, at the location of y=5 mm. When analysing the peak temperatures at the location of y=3 mm and 4 mm, a better agreement between the data sets was achieved, with a maximum error of 1.8% and 1.3% respectively. Therefore, the large percentage error may occur due to error in the positioning of the thermocouple. As these were po-

sitioned manually, a consistent comparison between the two data sets may not have been achieved. It should also be noted that from the FE model, a 0.25 mm change in position gave rise to an 8.9% difference in the temperature value at each location. The overall error may have occured due to the uncertainty in the measurements obtained using the thermocouples. Error in the thermal measurements may have arisen from positioning and/or systematic errors, with the error analysis presented in Table 4.8 which was completed using BS 60584 [177]. The error due to the thermocouple extension cables and NI DAQ data collection equating ±2.5°C and ±0.83°C respectively [178]. The combined systematic error was calculated using the Root Sum of Squares (RSS) method. For the positioning error, the uncertainty in the positioning of the thermocouples was ±0.5 mm with the corresponding temperature difference being determined from the FE model.

Table 4.8: Systematic error analysis for peak temperature measurements using BS 60584 [177].

Parameter Set	**Error in TC Junction** (±°C)	**Total Systematic Error (RSS)** (±°C)	**Positioning Error** (±°C)	$\lvert\mathbf{T}^{exp} - \mathbf{T}^{pre}\rvert$ (±°C)
1	3.5	4.3	64.5	19.9
2	2.6	3.7	51.4	16.3
3	2.5	3.6	43.5	27.1
4	4.9	5.6	65.1	14.3
5	3.9	4.7	54.5	27.8
6	3.3	4.2	50.6	21.5
7	7.0	7.5	65.1	17.5
8	6.0	6.5	72.8	15.6
9	5.1	5.7	52.7	17.2

When analysing the difference between the peak experimental and predicted temperatures the systematic error would not account for the discrepancies between the two data sets. It was apparent that the greatest error arose from positioning of the thermocouples; however, the maximum difference between the two data

sets fell within the error limits showing confidence in the final solution. It should also be noted that the difference between the experimental and predicted peak temperatures, for all data sets, was less than the positioning error; therefore, the error in the position must be less than ±0.5 mm. The response time for the thermocouple wire used (0.3 mm diameter), was 0.28 seconds. If the temperature change between room temperature and the peak temperature was assumed to be instantaneous, the minimum time taken to achieve this was 1.28 seconds; therefore, the response time would have negligible effect on the experimental data.

For the cooling phase, the cooling rate was predicted with accuracy, with a higher thermal contact coefficient being required for all three cases (Table 4.5). The determined values for the bed coefficient were 6.2%, 6.5% and 12.8% higher than the free surface value, with this parameter increasing with an increase in the applied linear energy density. To evaluate the effect of the thermal contact coefficient, the cooling rate (dT/dt) was determined across the temperature range for which γ' enters solution (1150°C) and recrystallizes (1020°C) [73]. The thermal history data was taken from the nodal coordinate (1.5, 50, 0), which was located at the melt pool width for when P=900 W and V=100 mm/min. The cooling rate was evaluated for coefficient values between the upper and lower values prescribed to the optimisation. The results are presented in Figure 4.19. A max-

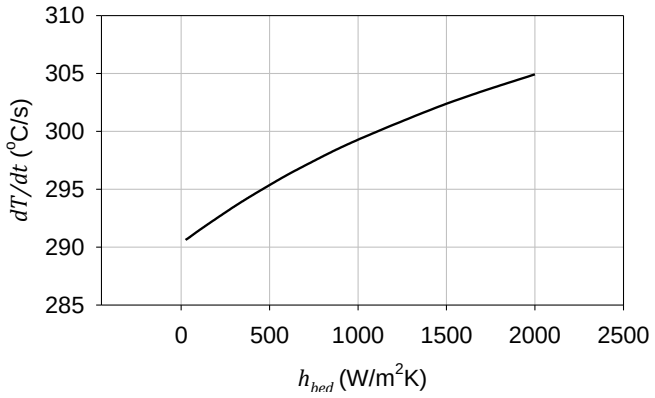

Figure 4.19: A graph showing the effect of the cooling rates through variation of the thermal contact coefficient. The cooling rate was determined for the temperature range governing recrystallization of γ'for IN718 for P=900 W and V=100 mm/min.

imum percentage increase of 4.9% was observed in the cooling rate, across all of the investigated thermal contact coefficient values. Although varying magnitudes of the convective coefficient were present, a significant difference in the convective coefficient had minimal effect on the cooling rate. When comparing case 7 to 9, the maximum difference in the convective coefficient was 47.4%; however, the difference in cooling rate was 0.5%. The same issue can also be highlighted when comparing case 4 to 6 where a 51% increase in the convective coefficient was determined which would only alter the cooling rate by 0.1%. A potential reason for why a significant difference was observed, for similar process parameters, may be due to the method in which the thermal model parameters were altered during the optimisation. To calculate the step size for the next iteration of the optimisation, a quadratic sub-problem, which approximated the behaviour of the objective function, was solved [179]. For each step size, the lowest possible value of the quadratic sub-problem must be achieved, through the steepest possible decent direction, to ensure an efficient convergence was obtained [164]. Therefore, it is believed, that for case 6 and 9, the significant increase in the convective coefficient was due to the optimisation solver, generating a large step size for this parameter, as this provided a more efficient convergence rate through the steepest decent method. However, as previously mentioned, this had a negligible effect on the actual physics of the process model.

4.4.4 Reasons for Error in the Calibration Procedure

General reasons for the errors associated with the calibration procedure may occur due to the method in which the heat flux was applied to the FE domain, the type of heat source model and/or the formulation of the optimisation algorithm. For the majority of the presented cases, the predicted peak temperatures were overestimated for the thermal history closest to the weld centreline. An overestimate from the FE model was to be expected, as unlike other FE codes, the

method in which ABAQUS applies the heat flux to the domain was not adaptive. Therefore, the sum of the thermal energy entering the domain was not monitored or maintained, as this was not a part of the user subroutine DFLUX [149]. However, as the maximum difference between the peak temperatures was 30°C, this effect was negligible for this work.

For the entire study, a combined heat source model consisting of a Gaussian disc and cylindrical model was utilised. For some of the presented cases, the predicted melt pool geometry differed slightly from the experimentally determined profile. This occurred when either the nail head geometry occurred over a small depth (Figure 4.17(a) and Figure 4.17(b)), or when vertical sided, narrow sections were present. As previosuly noted, the heat flux distribution for the keyhole regime was complex, as the entrained energy was distributed over the penetration depth, leading to multiple reflections and Fresnel absorption of the laser energy inside the keyhole. A compromise of the physical phenomena occurring in the melt pool was required when implementing FE heat source models, as the true physics were replaced with a simplified geometrical representation of the heat flux distribution. Therefore, the final solution for the thermal field and melt pool geometry was also governed by how well the heat source model represented the heat flux distribution. Therefore, this could always lead to a discrepancy between the predicted and experimental data sets. In recent years, other heat source models have been developed in attempt to capture a more realistic representation of the flux distribution within the keyhole. This includes the Double-Conical [169], Double Ellipsoid-Cylindrical [119] and the rotary volumetric heat source [180]. However, the issue with implementing these heat source models is the number of parameters which require calibration. For each of the heat sources, a total of 7, 11 and 8 parameters would need to be determined respectively. It should be noted that the number of evaluations of the objective function, for one iteration of the optimisation, equated the length of the optimisation vector ($\mathbf{x}$).

Therefore, the computational deficit may not outweigh the reduction in error, which could be achievable through implementing a more complex heat source model.

Other reasons for the errors associated with the calibration technique, could be due to the method in which the non-linear optimisation algorithm (*lsqnonlin*) determined an optimised set of heat source parameters. To include the melt pool profile within the optimisation, equispaced points were distributed throughout the thickness of the work piece. For the keyhole regime, the number of data points used to represent the nail head feature, ranged from 19 to 22 points. As this feature was only represented by a minimal number of data points, the error contribution to the global error function would be less in comparison to the remainder of the points representing the melt pool profile. Therefore, the optimisation algorithm would be biased to generating parameters which reduced the error in the remainder of the profile, as a greater reduction in the global error would have been achieved. Therefore, the attainable resolution for the small geometrical characteristics of the melt pool would be affected by this phenomena. Another potential issue was the use of zeros to represent where no molten region was present in the melt pool profile. When calculating the residual error, for each objective function, all of the data points were considered; however, as some of these points were zero, they would not contribute to the global error. Therefore, it is believed that artificially scaling the objective function with respect to the number of data points would negate this effect. This could potentially reduce the error between the experimental and predicted melt pool geometries; however, in order to determine the effect of further scaling the objective function, a lengthy parametric investigation would be required. It should also be noted that for the conductive regime, the number of non-zero values was less than zero values, with the results showing a high degree of confidence in the current procedure. Therefore, the reduction in error through further scaling may not be advantageous.

As determined from this study and the work presented by Belitzki et al. [111], the initial guess would dictate the accuracy of the final solution when using gradient based optimisation techniques such as non-linear optimisation and Sequential Quadratic Programming (SQP). In some, cases a poor initial guess may lead to divergence of the model. The reason for this is that SQP and the trust-region algorithm are locally convergent, meaning that a solution potentially exists, at a distant point in space, which would provide the absolute minimum response to the objective function. For the current problem, it is believed that the response from the objective function was highly non-linear, as multiple parameter sets provide an identical solution, as determined from Figure 4.10(a) to Figure 4.10(b). Therefore, there were multiple local minima which existed on the response surface of the objective function within the selected bound constraints. When using an arbitrary guess of the heat source parameters, as completed by Belitzki et al. [111], a poor solution was attained, therefore a better initial guess should be provided to ensure the optimisation falls into the correct local minima. With this study, using a MOO and physical measurements of the melt pool geometry for the initial guess, a better solution was determined; however, error was still present in the final solution. Therefore, a method is required to predict the location of the global minima, to ensure the absolute minimum of the objective function was achieved. Global optimisation algorithms, such as the Genetic algorithm (GA), can determine the global minimum of the solution. However, global optimisation algorithms are computationally expensive, analysis times are often lengthy and in some cases, global optimisation cannot be achieved [181].

4.5 Conclusions

- Overall, the proposed calibration procedure allowed automation of a key step in the thermal modelling of welding processes, therefore increasing the

efficiency of the sequentially coupled FE approach for industrial application.

- The optimised parameters provided an accurate representation of both the thermal history and melt pool geometry when comparing the numerical and experimental data. The maximum and minimum error for the peak temperatures were 8.6% and 1.2% respectively. The maximum and minimum error between the predicted and experimental melt pool area were 11% and 0.3%.

- A good initial guess for the optimisation was determined through physical measurements of the experimental melt pool geometry; however, a method is required which can estimate these parameters, to ensure global convergence is achieved.

- The weighted sum method with a MOO was required to ensure an accurate solution was obtained. Future work should include determining a method to select the desired weight value without the need to use a comprehensive parametric study.

- From previous work in the literature, a SOO was used which was appropriate for when the heat source model had one geometrical parameter which provided a coupled thermal history and melt pool geometry. For cases where the heat source model has more than one geometrical parameter a MOO should be considered.

Chapter 5

Numerical-Analytical Modelling for Single-Track Depositions

5.1 Introduction

To determine the thermo-mechanical effects induced through a single-track deposition, an experimental and numerical investigation was conducted. The aim of this chapter was to validate a semi analytical-numerical approach, which allowed the prediction of the track geometry in conjunction with the thermal and mechanical effects of the process. An analytical method is also presented which determines the powder catchment efficiency of the process. The modelling methods adopted in this chapter provide superior fidelity in modelling of the deposition process through inclusion of a realistic track geometry in a sequentially coupled thermo-mechanical Finite Element (FE) analysis. Experimental validation of each key stage of the modelling strategy was completed. Finally, a comparison was drawn between using simplified geometrical representations of the track geometry and the use of realistic track geometries for the sequentially coupled FE approach.

5.2 Computational Model

A semi analytical-numerical approach was devised, with the methodology presented in Figure 5.1. An iterative analytical model was implemented to predict the track profile as presented in Section 3.2.3. The powder distribution on the substrate surface was assumed to be Gaussian and was modelled as outlined in Section 3.2.1. The calculated track profile was then used in a sequentially coupled thermo-mechanical FE model to predict the thermal and mechanical induced effects of the process. The numerical models assumed that the formation of residual stress is driven predominately through thermal effects. Therefore, mass transfer, fluid flow and phase transformations were not included in the analyses [182].

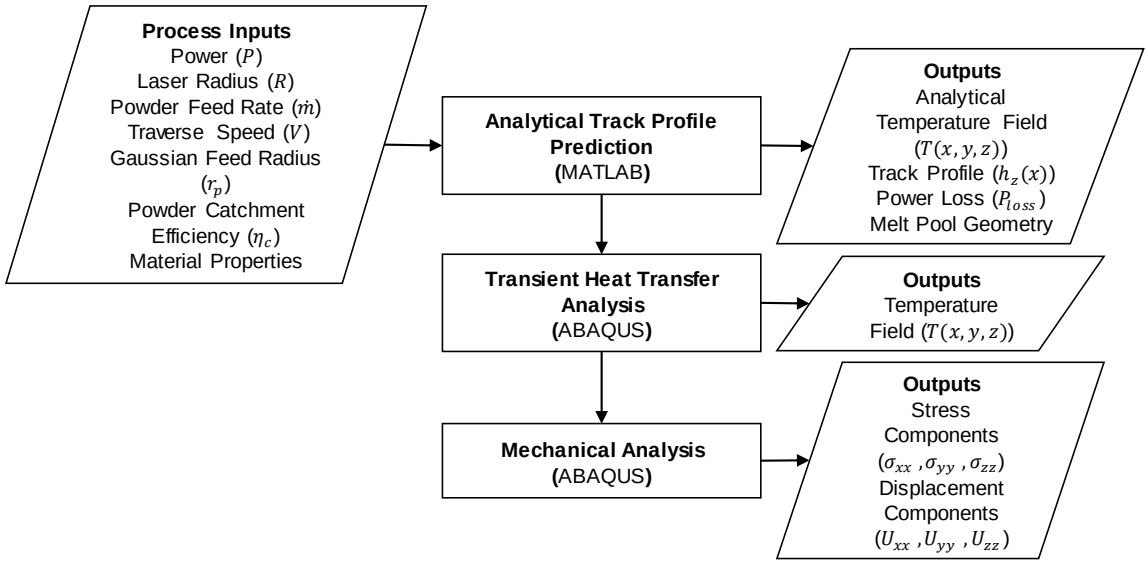

Figure 5.1: A flowchart showing the required inputs for the model and the associated outputs at each stage of the modelling process.

5.2.1 Analytical Powder Catchment Efficiency

The Direct Energy Deposition (DED) experimental setup for this study utilises a blown powder feed as outlined in Section 3.4.1. Therefore, to model the track profile with accuracy the catchment efficiency had to be accounted for within the model. The model presented in Section 3.2.3 assumed that all the powder

bound by the melt pool was assimilated. The current model uses an analytical representation of the powder flux distribution (q_{pf}) and integrates this surface between the melt pool limits to determine the track profile. A visual representation is presented in Figure 5.2, which shows the predicted melt pool superimposed onto the corresponding powder flux distribution. The process parameters and associated analytical catchment efficiencies are presented in Table 5.1 and Table 5.2 respectively. The parameters used here were based on the process parameter window determined by Abioye *et al.* [173].

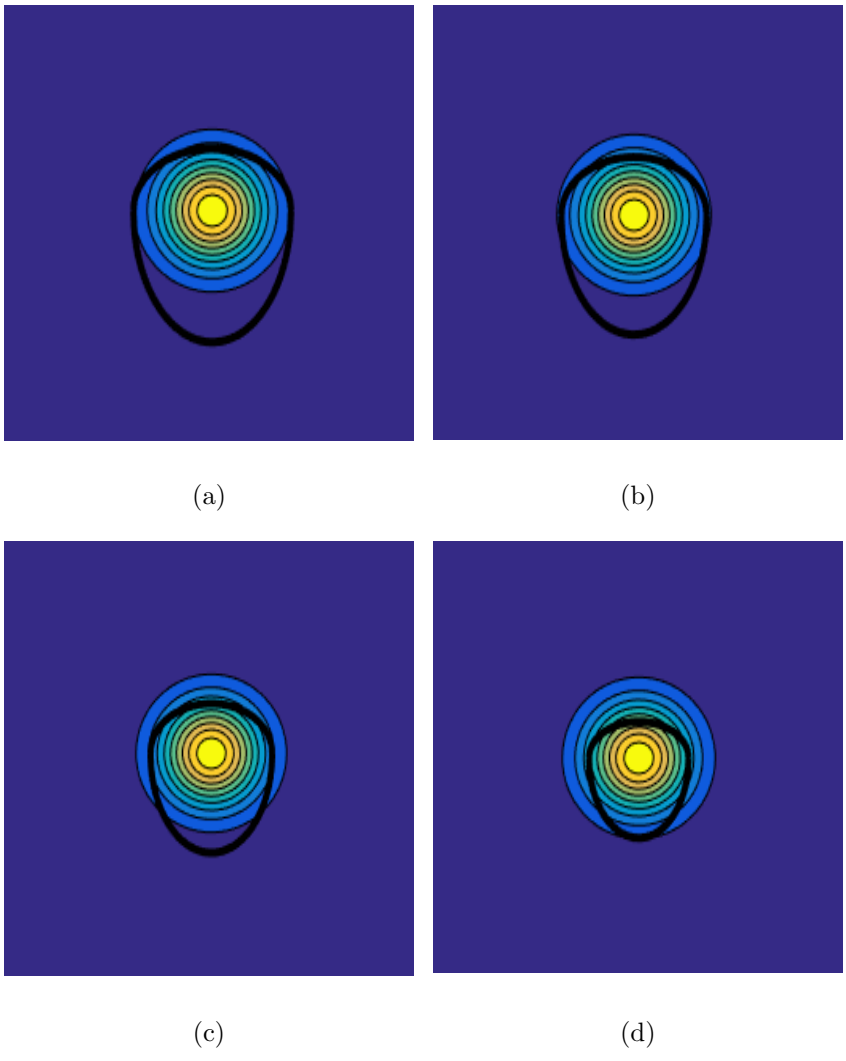

Figure 5.2: A schematic of the powder flux distribution (q_{pf}) superimposed with the predicted melt pool geometry for (a) Set 1 (b) Set 2 (c) Set 3 (d) Set 4.

Table 5.1: Process Parameters used to investigate the catchment efficiency.

Parameter Set	Power (W)	Velocity (mm/min)	Powder Feed Rate (g/s)
1	2000	400	20
2	1800	400	20
3	1500	400	20
4	1200	400	20

The current approximation of the catchment efficiency was an overestimate as not all of the powder entering the melt pool would be assimilated. Due to the high velocity carrier gas, some particles may not reach the melt pool as they are deflected from the surface of the substrate or they are remoeved from the stream due to particle interaction. Also due to the continuous deposition during the process, the geometry behind the centre of the heat source is evolving, therefore altering the catchment efficiency. A realistic representation of the catchment efficiency, including these phenomena was presented by Partes [138]. It should be noted that the following equations have been manipulated from [138] to represent the elliptical melt pool geometry as presented by Ahsan and Pinkerton [25] (Equation 3.7 and Equation 3.8). The total catchment efficiency equated the summation of two separate components:

$$\eta_{c_1} = \eta_1 + \eta_2 \tag{5.1}$$

The first component represented the powder caught directly within the molten region and the second component determined the powder which was lost to the surrounding areas of the melt pool. These components were calculated as follows:

$$\eta_1 = \int_{-W/2}^{W/2} \int_{y_r}^{y_f} S(x,y) dy dx \tag{5.2}$$

$$\eta_2 = \int_{-\infty}^{0}\int_{0}^{\sqrt{\left(\frac{W}{2}\right)^2-\frac{X_{min}^2}{4}}} S(x,y)dydx -$$

$$\left[\int_{y_r}^{0}\int_{0}^{\left(\frac{W}{2}\right)\sqrt{1-\frac{x^2}{y_r^2}}} S(x,y)dydx \int_{\frac{y_r X_{min}}{W}}^{0}\int_{\sqrt{\left(\frac{W}{2}\right)^2-\frac{X_{min}^2}{4}}}^{\left(\frac{W}{2}\right)\sqrt{1-\frac{x^2}{y_r^2}}} S(x,y)dydx\right] \tag{5.3}$$

where:

$$S(x,y) = \frac{1}{2\pi\sigma_x\sigma_y} exp\left[-\frac{1}{2}\left(\frac{x}{\sigma_x^2}+\frac{y}{\sigma_y^2}\right)\right] \tag{5.4}$$

$$\sigma_x = z_s\left[cot(\zeta-\phi) - cot(\zeta)\right] \tag{5.5}$$

$$\sigma_y = z_s tan(\phi) \tag{5.6}$$

$$X_{min} = \frac{\pi D_{particle}\rho_{powder}C_p\left(T_m - T_{amb}\right)\left(2D_{laser}\right)^2 v_{powder}}{6\alpha_{powder}P} \tag{5.7}$$

where W is the melt pool width, y_f and y_r are the front and rear limits of the melt pool, x, y are the Cartesian coordinates, z_s is the stand-off distance, P is the laser power, C_p is the specific heat capacity, T_m is the melting temperature of the material, T_{amb} is the ambient temperature, ζ is the inclination angle between the nozzle and powder stream (Table 3.1), ϕ is the divergence angle of the powder stream (Table 3.1), $D_{particle}$ is the diameter of the powder, ρ_{powder} is the density of the powder, D_{laser} is the spot diameter of the laser, α_{powder} is the absorptivity of the powder and v_{powder} is the velocity of the powder given by [183]:

$$v_{powder} = \frac{4\dot{V}}{\pi\left(d_o^2 - d_i^2\right)} \tag{5.8}$$

where $\dot{V}$ is the volumetric flow rate of the carrier gas, d_o and d_i are the outer and inner diameter of the nozzle respectively. It should be noted that the material properties used to represent the powder were the same as those used for the substrate. The reduction in the catchment efficiency from the comparison of

both approaches was calculated using a modified approach as follows:

$$\eta_c = \frac{\eta_{c2}}{\eta_{c1}} \tag{5.9}$$

Utilising the previous approaches, the catchment efficiencies for the same process parameters in Table 5.1 were calculated and are presented in Table 5.2.

Table 5.2: Calculated catchment efficiencies using the realistic (η_{c_2}) and the modified approach (η_c).

Parameter Set	η_{c_1}	η_{c_2}	η_c
1	0.92	0.52	0.57
2	0.90	0.48	0.53
3	0.85	0.36	0.42
4	0.73	0.29	0.39

It can be observed that the catchment efficiency determined from the analytical model by Ahsan and Pinkerton [25] overestimates the parameter by approximately 50% in comparison to the model derived by Partes [138]. As there was a reduction in the calculated catchment efficiency between the two methods, an overestimate in the peak mass flux of powder entering the molten region was prescribed to the Ahsan and Pinkerton [25] model. This arose as this model, unlike the model derived by Partes [138], did not include the loss of powder particles in the stream during flight or the loss due to interaction with the substrate and previously deposited material. From this study, it can therefore be approximated that nearly half of the powder flux is lost to the surroundings. Through a reduction of the analytical catchment efficiency, using the modified approach, a more realistic value was determined when compared to the published values in the literature [138, 184, 185]. Therefore, when implementing the analytical model to predict the track profile, the modified catchment efficiency was used.

5.2.2 Numerical Modelling

A sequentially coupled thermo-mechanical FE model was used to model the thermal and mechanical effects of the single-track deposition. The material properties were temperature dependant as shown in Section 3.3.2. A three-dimensional (3D) FE model was utilised with only half of the geometry modelled due to symmetry along the centre of the deposition track. The nodal positions at the interface between the track and substrate were coincident. The nodes in this region were joined using a tie constraint. Hexahedral elements were used throughout the mesh to allow post processing of the data to reflect the method used to validate the mechanical mode. A mesh sensitivity study was conducted for the thermal model using the methodology outlined in Section 4.2.2, with the results presented in Figure 5.3.

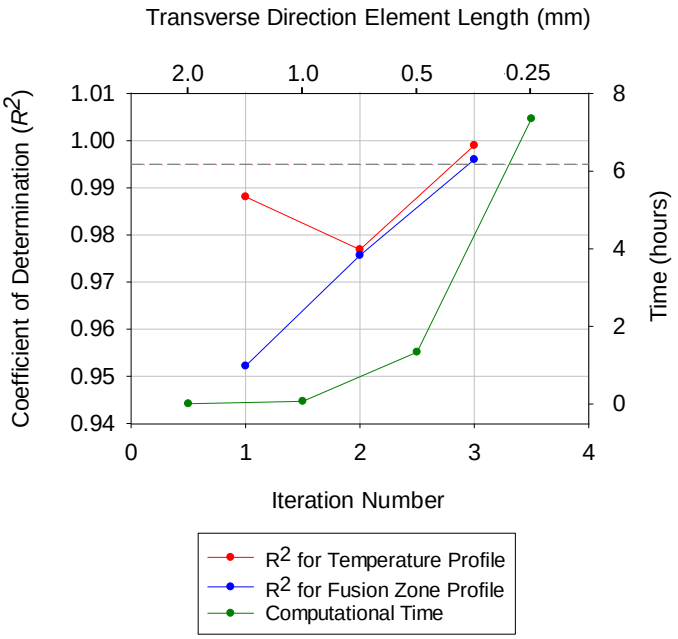

Figure 5.3: Mesh sensitivity study results showing the calculated convergence parameters for each mesh iteration.

From Figure 5.3, the third iteration satisfies the convergence limits of the mesh sensitivity study. A reduction in accuracy is observed for the second iteration, arising due to the finer element size being able to represent the heat flux

distribution of the FE heat source with greater accuracy. As expected the computational time increases exponentially through reduction of the element volume. The resultant mesh from the study is presented in Figure 5.4. The element volume directly below the track was 0.25 x 0.25 x 0.25 mm^3 increasing to 2 x 0.5 x 0.5 mm^3 at the extremity of the plate. The mesh design in Figure 5.4 was also implemented for the mechanical model. As the thermal solution was independent of the mesh, an accurate prediction of the transient temperature field could be achieved which was required to predict the residual stress fields with accuracy [186]. The increase in element size far field from the vicinity of the track was also valid because only the stiffness of the material needs to be represented beyond the melt pool zone. DC3D8 linear brick elements and C3D8R linear brick elements were used for the thermal and mechanical analysis respectively. Linear elements were used as there are no significant advantages in the results produced by higher order elements in welding simulations [187]. The total number of elements and nodes were 196,200 and 213,294 respectively. To evaluate the effect of how the track profile was represented geometrically within the model, three further mesh designs were implemented. The substrate mesh was identical as depicted in Figure 5.4; however, the track region was replaced by a square block. Three track modifications were made which included:

- A track profile with the same width and height as the realistic profile.
- A track profile with the same height as the realistic track profile with the width derived from the volume of the realistic track.
- A track profile with the same width as the realistic track profile with the height derived from the volume of the realistic track.

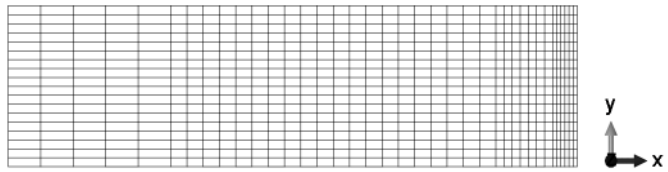

(a)

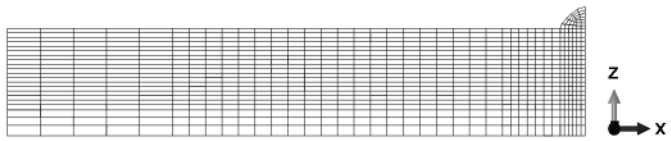

(b)

Figure 5.4: A Section of the FE mesh used for the thermo-mechanical models (a) Top surface view (b) Cross sectional view perpendicular to the track.

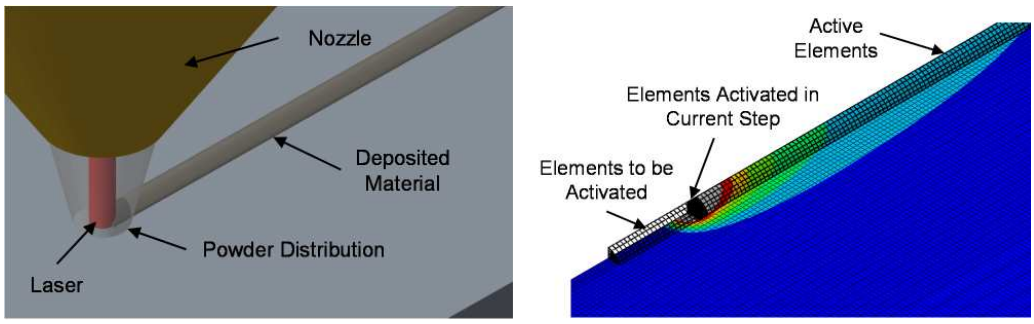

(a) (b)

Figure 5.5: (a) Schematic of the real life deposition process (b) Adopted FE modelling strategy for element activation to simulate the deposition process.

For all three mesh designs, the same size and number of elements was used within this region to allow an accurate comparison to be made between the modelling methods. For consistency between the analytical and numerical model, the circular disc heat source proposed by Pavelic *et al.* [92] was used and the Gaussian radius equated 1.5 mm. The heat source model was implemented using the user-subroutine *DFLUX* in ABAQUS. Material addition was modelled using the method outlined in Section 3.3.4. To ensure that the energy balance inside the melt pool was stable, the elements were reactivated offset from the centre of the melt pool. A total width of two elements were reactivated at each time step at

the melting temperature of the material. The deposition strategy implemented is outlined in Figure 5.5. The convection and radiation losses were defined only on the free surfaces using the method outlined in Section 3.3.1.

An isotropic hardening model (Eq 3.26) was used to represent the plastic behaviour within the mechanical model. The thermal strain was evaluated using the thermal history of the heating and cooling phase in conjunction with the thermal expansion coefficient. The mechanical boundary conditions for this model were defined as shown in Figure 3.4. Material addition was included in the mechanical analysis using the same deposition strategy as in the thermal analysis.

5.3 Experimental Validation

A single-track deposition was fabricated using the experimental set up outlined in Section 3.4.1. The process parameters were selected based on previous work using this apparatus [173]. The laser power (P) and powder feed rate ($\dot{m}$) were set to 1800 W and 4 rev/min respectively. This equated a powder mass flow rate of 26 g/min. The traverse velocity was set to 400 mm/min. Two identical samples, denoted Sample A and Sample B, were manufactured with a schematic of the experimental process shown in Figure 5.6. Sample A was used for in-situ temperature measurements, metallurgical examination and for the neutron diffraction (ND) measurements. Sample B allowed production of the strain-free reference (d_0) sample. Four bolts, acting as simple supports, were positioned along the width and length to restrict the plate's motion during the deposition process.

Three sequential steps were used in the experiment. For the first 5 mm of the traverse, powder was delivered to the substrate with no heating. After this point, the laser was switched on to begin formation of the track. After a distance of 115 mm both the laser and powder feed were switched off. The sample was then cooled

in air until it was at room temperature. In-situ temperature measurements were captured using the method outlined in Section 3.4.2. The thermocouples were positioned at three different locations from the centreline (Figure 5.6). To validate the melt pool geometry metallographic analysis was conducted on a specimen (20 x 10 x 6 mm) removed from centre of Sample A, as outlined in Figure 3.8. The sample was prepared for optical microscopy analysis using the method presented in Section 3.4.3, with the track being determined from the method in Section 3.4.4.

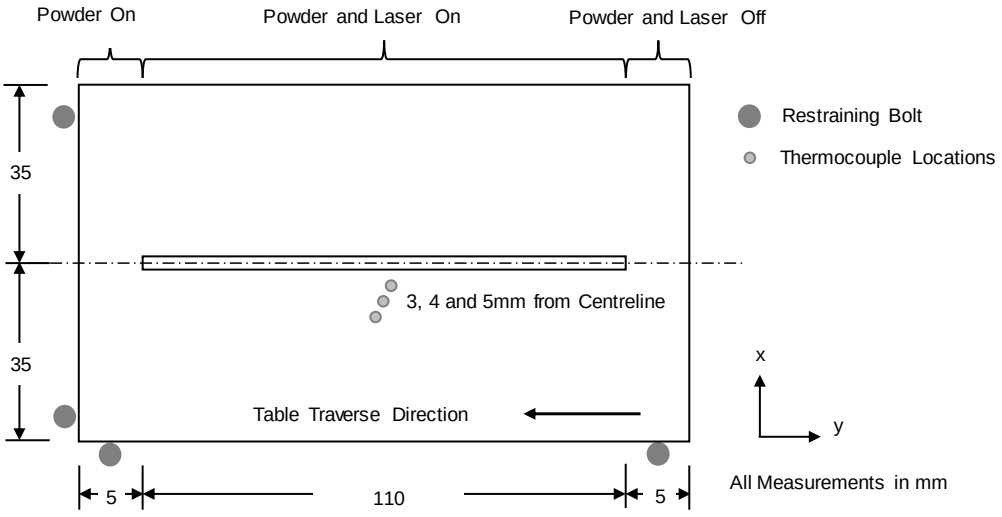

Figure 5.6: Schematic of the experimental set up showing the deposition procedure, restraining locations, thermocouple locations and the specimen used for metallographic analysis.

5.3.1 Neutron Diffraction Measurements

To obtain experimental stresses, ND was used for three line scans (Figure 5.7) across the fabricated specimen. The method to collect the required experimental data for the analysis is presented in Section 3.4.5. All measurements were conducted to the right of the sample centreline due to the geometrical symmetry, at 2 mm below the surface of the substrate. A gauge volume of 2 x 2 x 2 mm^3 was used for all measurements allowing for a good compromise between accuracy of the measurements and the spatial resolution at which they were conducted.

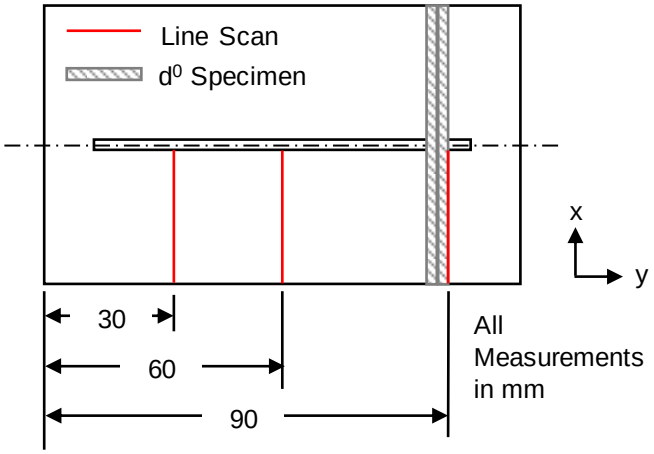

Figure 5.7: Schematic of Sample B showing the locations of the horizontal line scans (red lines) and the location where the d_0 specimens were extracted (hatched boxes).

To obtain the strain-free lattice spacing, two d_0 specimens were required because of the spatial resolution of the measurements. These specimens were removed from Sample B using electrical discharge machining (EDM) at the location highlighted in Figure 5.7. To relieve the internal strain, EDM was used to cut the d_0 specimens into a comb specimen as presented in Figure 5.8.

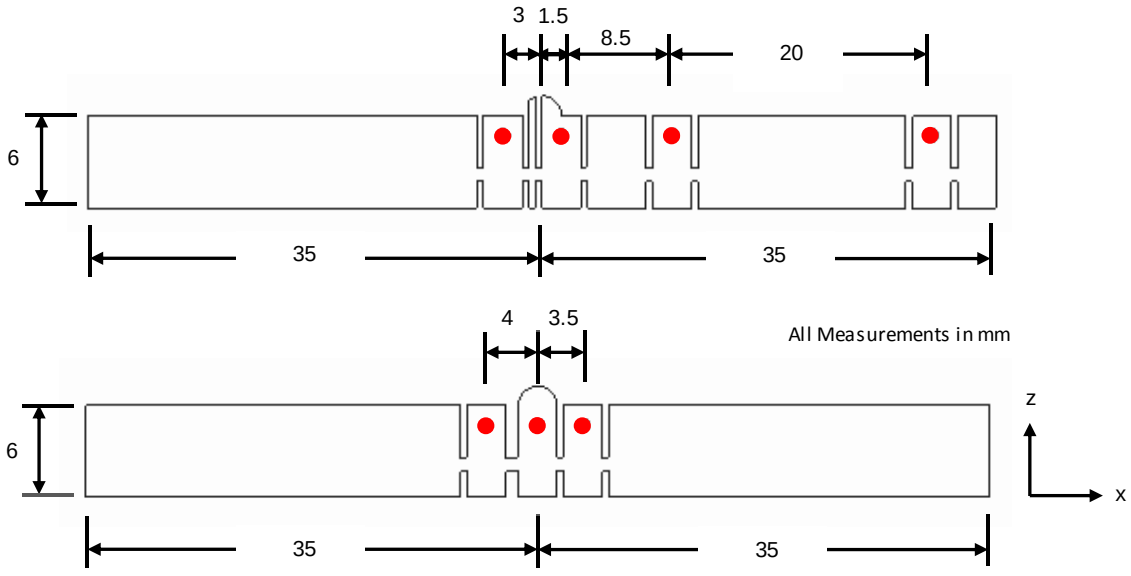

Figure 5.8: Details of the d_0 specimen cross section with the target location of the beam marked with a red circle.

An increased spatial resolution (smaller spacing between ND measurement po-

sitions) was used in the proximity of the deposited track to quantify the sharp gradient in residual stress. The spatial resolution was reduced in regions away from the deposited track as the stress gradients were expected to be lower. The same spatial resolution used to acquire the strain-free lattice spacings were used for the measurements in Sample A. The data was processed to determine the three stress components using the method presented in Section 3.4.5.

5.4 Results and Discussion

5.4.1 Catchment Efficiency and Track Profile Prediction

A 3D surface plot generated from experimental measurements of the track upon the substrate is presented in Figure 5.9. Comparisons of the analytical and experimental track profiles are presented in Figure 5.10. Three track profiles were calculated utilising the catchment efficiencies η_c, η_{c_1} and η_{c_2}. These values were derived as 0.51, 0.80 and 0.41 respectively.

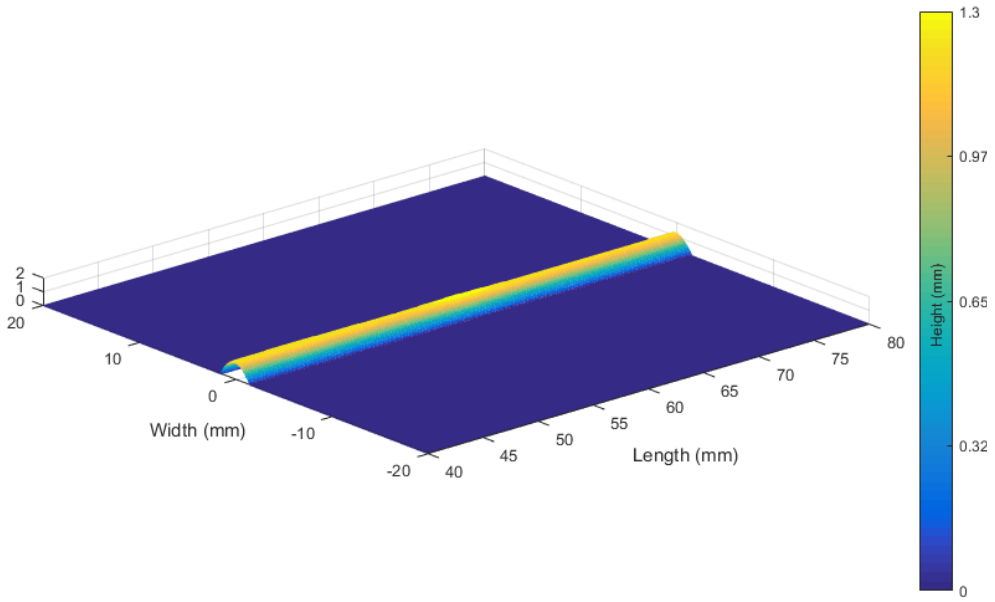

Figure 5.9: A 3D surface plot of the experimental track deposit upon the substrate generated from surface measurements of Sample A.

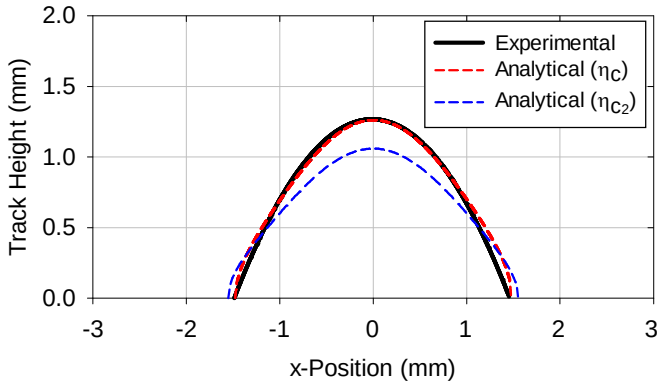

Figure 5.10: A comparison of the experimental and analytical track profile geometries utilising two catchment efficiency approaches, η_c=0.51 and η_{c_2}=0.41.

Utilising the analytical catchment efficiency presented by Partes [138] gives rise to an underestimate in the track height of 16%. However, the track width and shape was represented well by the analytical model. When taking into consideration the combined catchment efficiency (η_c) the track width and height are predicted with an error of 1.98% and 0.43% respectively. Overall, the profile shape was in good agreement with the experimental data. The coefficient of determination (R^2) was calculated as 0.982, with the greatest difference arising at the position of the maximum track width.

The derived value for the unmodified catchment efficiency was 0.80, which appears to be an overestimate when compared to the literature values which range from 0.20-0.65 [138, 188, 189]. When implementing the process parameters with no modification to the catchment efficiency (η_{c1}), a converged solution could not be obtained as no stable melt pool was achieved. This was because, during the analysis the power required to sustain mass addition reduced the effective power to 239 W. Therefore, the energy in the system could not reach an equilibrium state. Utilising the more realistic approach defined by Partes [138] lead to a catchment efficiency of 0.41 which falls within the literature values. Implementing this value into the analytical model lead to an underestimate in the height of the derived track profile, although the width was captured well. Therefore it is

apparent that the width and height of the track are predominantly governed by the melt pool geometry and the catchment efficiency respectively. Deriving the track profile utilising the modified catchment efficiency gives a better correlation with the experimental data; however, variations were still observed between the experimental and predicted data, more specifically for the derived width. This may arise from the assumption that the analytical powder flux distribution has a Gaussian profile [25], whereas in this experimental set up this may not be the case. The formulation of the analytical track height requires the height of the track to be zero at the integration limits. In reality, the nature of the process allows for a completely smooth transition between the substrate and the track material. Therefore, the track profile would not terminate as severely at the interface between the track and substrate as observed. As the analytical model represents the process as quasi-stationary, fluid flow interaction between the molten track and substrate was neglected. Therefore no change in the geometry during solidification was accounted for. Typically, spreading of the material occurs upon cooling due to the shearing of the liquid [190], which would result in a shallow contact angle between the track and substrate. This was observed in the experimental track geometry but not for the predicted profile.

5.4.2 Thermal Analysis

Validation of the heat source was conducted through comparing in-situ temperature measurements to the predicted thermal histories. Figure 5.11 shows the comparison of the two data sets. Both thermal histories show a good agreement with one another, however a maximum error of 3.1% was observed at the peak temperature. The temperature gradients as the laser approaches the thermocouples during heating were predicted with good accuracy, this was also the case during the cooling phase. The predicted weld pool profile and experimental micrographs are presented in Figure 5.12.

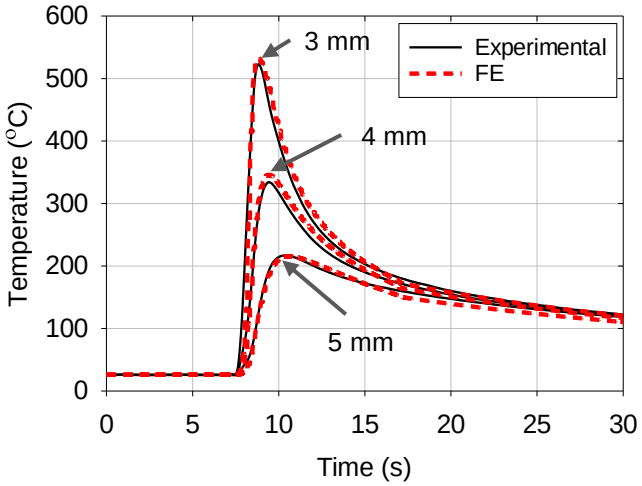

Figure 5.11: Comparison of experimental and numerically predicted thermal histories for three thermocouple locations positioned at the mid length of the substrate at; 3 mm, 4 mm and 5 mm from the track centreline.

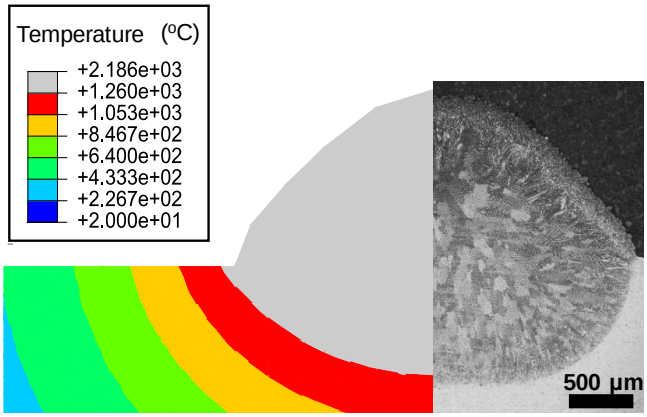

Figure 5.12: Comparison of the numerically predicted fusion zone and the metallographic specimen at the centre of the deposition i.e. y=65 mm.

The isotherm from the FE model was taken at 65 mm in the transverse direction, at a point in time in which the fusion zone (FZ) was at maximum width. The FZ is highlighted in grey, through restricting the contour to the solidus temperature (1260°C). A low penetration depth of approximately 1.0 mm was observed in the micrograph. This was captured well by the FE model through utilising a small element volume directly below the track and in the weld vicinity. The overall shape of the FZ was predicted accurately, showing accuracy in the calibrated FE heat source model.

Numerical predictions of the thermal histories and the shape of the fusion zone correlated well with the experimental data. The heating and cooling phases agreed well with the experimental data. The largest discrepancy arised for the peak temperature after the heat source passes the thermocouple. An overestimate from the FE code was to be expected, as the method in which the heat source was applied to the model was not adaptive. Therefore, the heat energy entering the mesh was not monitored or maintained [149]. The difference may also arise due to the artificial boundary condition used to model the heat sink effect between the CNC bed and the substrate. The true regime of heat loss at this location is through conduction. This may also give rise to the minimal difference observed in the cooling phase when analysing the thermocouple furthest from the deposition. However, to consider the CNC bed in the model would significantly increase the complexity and computational burden of the approach. It was observed that with a laser heat source, a low penetration depth was achieved in a thick substrate. This was due to a high concentration of the power flux density, therefore leading to a reduction in the size of the HAZ. It was apparent from the isotherms, that the volume of elements in the vicinity of the melt pool are valid because both the shape and geometrical parameters have been represented well. Overall, the fusion zone of the process and the associated temperature field have been predicted with a high fidelity (3.1% maximum error). Therefore, the expansion and contraction of the material due to the heating and cooling phases of the process would be correctly represented by the mechanical analysis.

5.4.3 Mechanical Analysis

The stress evolution for all three stress components are presented in Figure 5.13. The selected point was at the substrate mid length, on the track centre line, at the centre of the melt pool depth. Before the heat source is in the proximity of the selected node, zero stress is present throughout the substrate. The heating

and cooling occurring before 6 seconds has minimal effect on the stress evolution. Between the pre-heat region and the peak temperature (7.8 to 8.95 seconds) a balance in the direction of the stresses can be observed between all three components. As the heat source passes over the respective node, a compressive stress state existed, which arose due to the high temperatures in and around the melt pool causing an expansion of the material, which was constrained by cooler material further afield. Before and after the heat source, a tensile and compressive region developed respectively. This was due to the cooling and subsequent contraction of material behind the heat source and the expansion of material ahead. Upon cooling, all three stress components were tensile, with the largest magnitude in the longitudinal direction. The normal stress component in this region can be assumed to equal approximately zero.

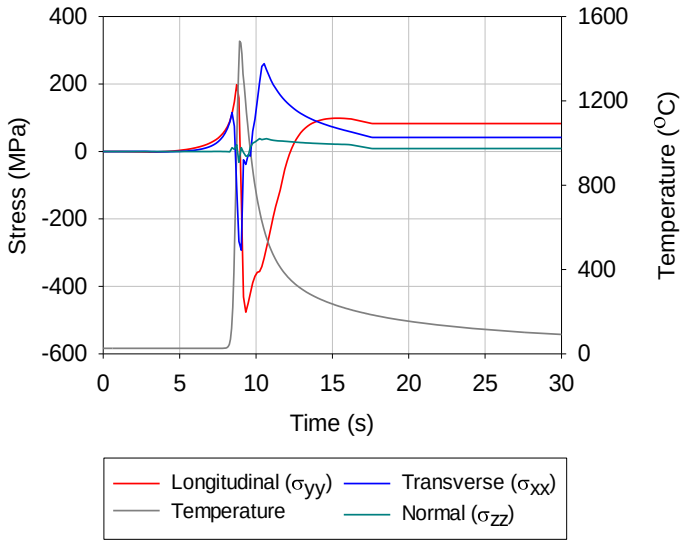

Figure 5.13: Numerical prediction of the transverse, longitudinal and normal stress components during the deposition process, in the steady-state track region. The nodal point selected was at the mid length of the substrate (y=60 mm) at the track centreline at the centre of the fusion zone (0.375 mm below the substrate surface).

To coincide with Figure 5.13, contour plots of the through thickness stress distribution, at different time periods throughout the process, for all three stress components, are presented in Figure 5.14-Figure 5.16. Four distinct regions of

the process were selected which include; the heating phase, the time at which the peak temperature was observed, the cooling phase and the final residual stress distribution at room temperature. From Figure 5.14, before the deposition has occurred, the stress field was predominately compressive due to the expansion of the material in front of the heat source. At the peak temperature (Figure 5.14(b)) the deposition was present which caused a tensile region to be present at the interface between the track and substrate, with the remainder of the stress field being unaltered at this stage of the process. The tensile region occurs due to the addition of track material which would cool rapidly in comparison to the melt pool. Upon cooling to room temperature the final residual stress state (Figure 5.14(d)) fluctuated between a compressive and tensile stress state. Figure 5.15(a) shows the longitudinal stress component during the heating phase of the process which had a similar distribution to Figure 5.14(a); however, the tensile region at the bottom surface of the substrate was not present. The stress distribution remained compressive until the cooling phase (Figure 5.15(c)) where the track and the region directly below become tensile, this was present until the specimen was cooled to room temperature. The final residual stress state for the longitudinal component in the vicinity of the HAZ was tensile, this was balanced by a compressive region far field as shown in Figure 5.15(d). For the normal stress component (Figure 5.16), the stress distribution did not vary discernibly during the deposition process. Below the track, during the heating phase, the stress field was compressive and for the remainder of the process the normal stress component was tensile. Outside the vicinity of the HAZ a small compressive region is present due to the addition of material at the substrate surface. Far field the stress distribution was tensile and upon cooling remained in this state. With regards to the stress distribution within the track, before cooling, all three components had a uniform distribution with a compressive direction being exhibited, becoming tensile during the cooling phase. Upon cooling to room temperature,

a tensile region was observed between the interface of the track and substrate. This arose due to the interaction between the deposited track and the substrate. If a high stress gradient occurs in this region, separation of the track from the substrate could occur, therefore the modelling methodology presented here can also help to mitigate this issue. Averaging the FE stress predictions over the track volume presents a tensile stress state, 317.7 MPa and 1.6 MPa (24.4% and 0.1% of UTS), for the longitudinal and normal stress component respectively. A compressive stress, 9.0 MPa (0.7% of UTS), in the track was observed for the transverse stress component. Therefore, the stress direction in the track reflects that of the substrate, directly below the track.

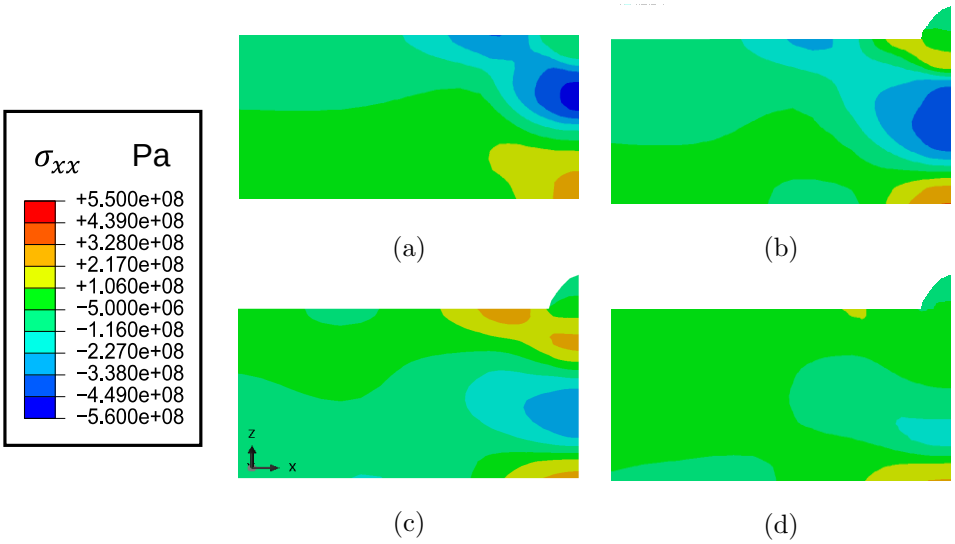

Figure 5.14: FE contour plots showing the through thickness stress distribution for the transverse stress component, σ_{xx}, at different time intervals through the heating and cooling phase of the process. Cross section taken at the mid length of the substrate i.e. y=60 mm. (a) During the heating phase at t=8.25 s (b) At the peak temperature where t=8.95 s (c) During the cooling phase at t=12.15 s (d) Final residual stress field upon being fully cooled.

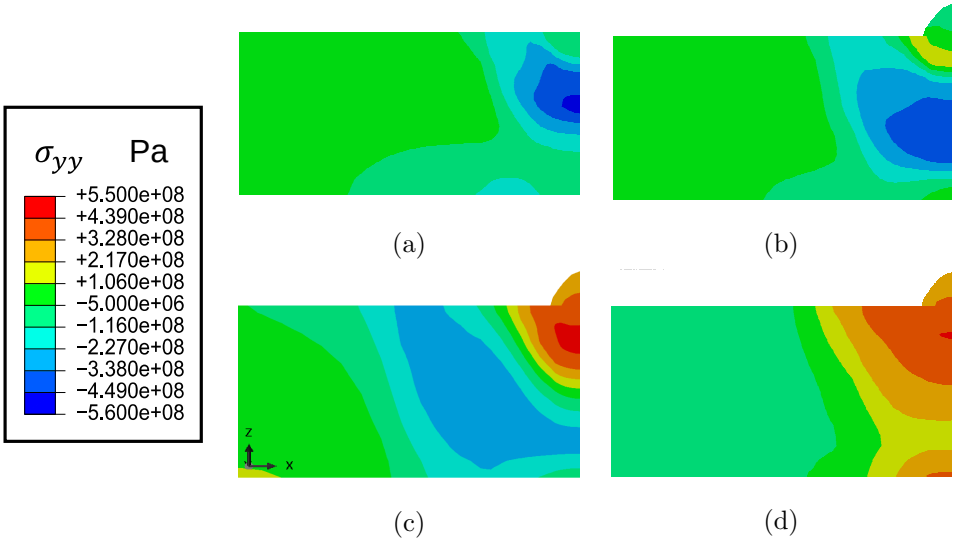

Figure 5.15: FE contour plots showing the through thickness stress distribution for the longitudinal stress component, σ_{yy}, at different time intervals through the heating and cooling phase of the process. Cross section taken at the mid length of the substrate i.e. y=60 mm. (a) During the heating phase at t=8.25 s (b) At the peak temperature where t=8.95 s (c) During the cooling phase at t=12.15 s (d) Final residual stress field upon being fully cooled.

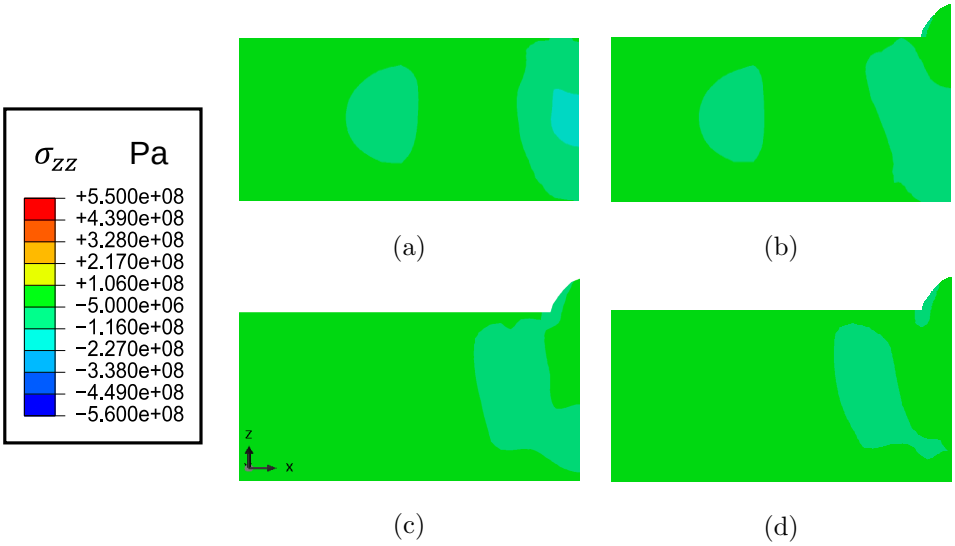

Figure 5.16: FE contour plots showing the through thickness stress distribution for the normal stress component, σ_{zz}, at different time intervals through the heating and cooling phase of the process. Cross section taken at the mid length of the substrate i.e. y=60 mm. (a) During the heating phase at t=8.25 s (b) At the peak temperature where t=8.95 s (c) During the cooling phase at t=12.15 s (d) Final residual stress field upon being fully cooled.

To validate the mechanical FE model, residual stress predictions were compared to the ND measurements. For consistency, the FE predictions were aver-

aged over a volume equal to the gauge volume used in the experimental procedure. Figure 5.17 shows the comparison between the predicted and measured residual stress in the longitudinal, transverse and normal stress directions. It can be observed that the agreement between the experimentally and numerically derived residual stress profiles was good for the longitudinal and normal stress profiles; however, both the magnitude and trend for the transverse stress component differed greatly. In the vicinity of the track, the FE predictions and ND data present a tensile and compressive stress state respectively. As expected, from analysis of the stress components for each data set, at each line scan location, there was little variation present. This was because the process parameters utilised were constant throughout the deposition process. The longitudinal stress component showed the typical trend of a single pass weld at each line scan, for both the predicted and experimental values. This consisted of a tensile region within the HAZ, with the peak value at the centre of the heat source. Both data sets also show a compressive region far field to balance the tensile region, with a good agreement with one another. For a thick substrate, the normal stress in a traditional weld has been shown to exhibit a plane stress condition [38]; however, in Figure 5.17 a peak stress was present at a location below the track width.

5.4.4 Sources of Error in Residual Stress Prediction

Validation of the mechanical FE model was conducted through the use of ND measurements. The residual stress profiles for the longitudinal and normal stress profiles correlated well. However, the trend and magnitude for the transverse component differed greatly. For all three stress components, the gradient of the stress profile far from the weld was different. This difference may have arisen due to the restraining bolts changing the stress evolution. The restraints in the FE model were neglected to reduce the complexity of the simulation. Other possible reasons for the overall differences between the experimental and FE data may have

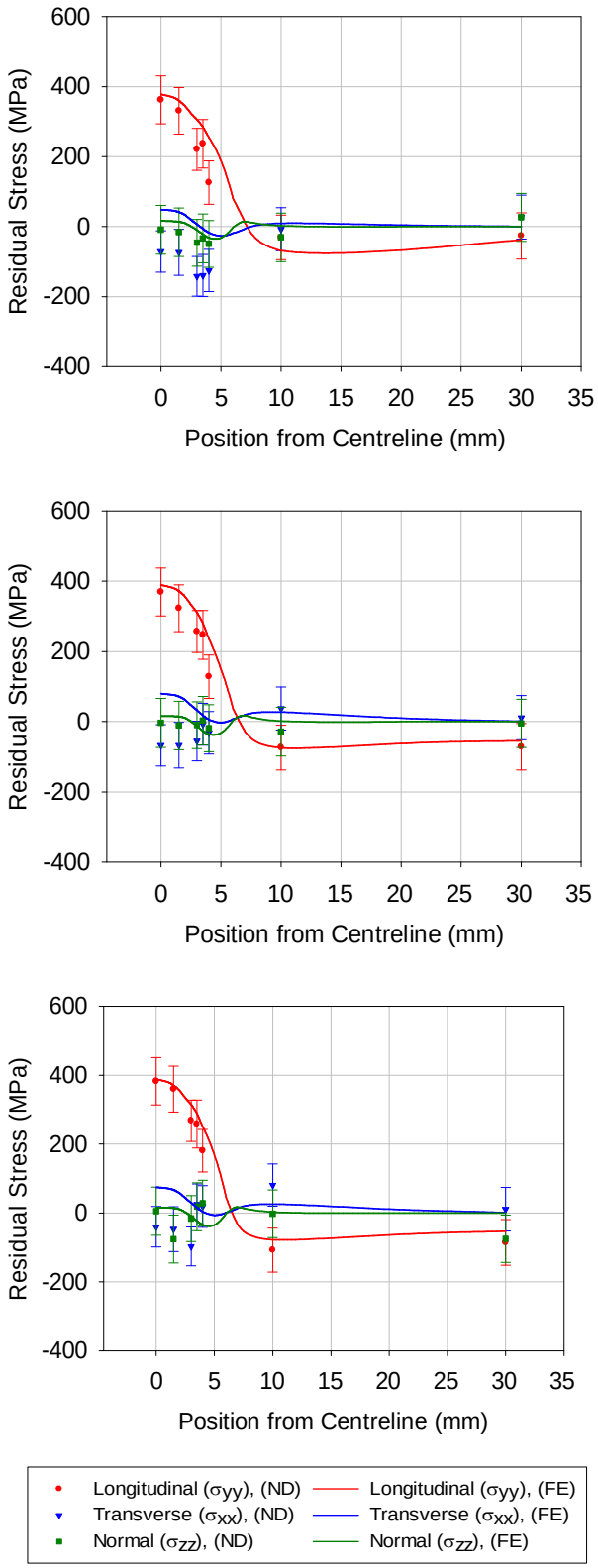

Figure 5.17: Comparison of experimentally measured and numerically predicted tri-axial residual stresses at 2 mm below the surface for each line scan position; (a) y=30 mm; (b) y=60 mm; (c) y=90 mm.

arisen from; changes in temperature, microstructure changes and/or positioning errors. As the allocated beam time required measurements to be taken during the day and overnight, the measurements were not taken concurrently under identical ambient temperatures. Inconsistency in the ambient temperature will therefore reduce the validity in the derived stress values as a 1 K temperature rise gives rise to a change in lattice spacing by 10^{-5} [26], thus altering the magnitude of the stress value by 0.5%. Therefore, a 10 K change in temperature between the strain free reference and the component being measured will give a significant effect on the lattice spacing [26]. The greatest difference between the predicted and experimental results occurred below the track. This may arise due to utilising the lattice spacing's from one strain free sample at each horizontal line scan, therefore microstructure changes and the associated intergranular stress were not accounted for [26]. Microstructure variation could occur due to different cooling rates and through varying amounts of dissolution of the powder into the melt pool at each location. Therefore the lattice parameter derived for the strain free sample may not be a true representation at the locations where the ND line scans were conducted. Positioning issues were believed to be the fundamental reason why the transverse stress profiles determined experimentally do not correlate with the FE model. It was apparent that the substrate had deformed, however when completing the experiment, this distortion was not taken into consideration. It should also be noted that the datum surfaces chosen to use as a zero reference location were the external faces on the x-y and y-z plane. As the surfaces were not truly square or flat, the original reference frame was not a true datum location. Therefore, error will be transferred to the subsequent measurement locations. This misalignment may have given rise to sporadic strain values being measured due to a shift in diffraction angles as the gauge volume may have been partially filled. From further analysis of the FE model, the through thickness transverse stress profile is presented in Figure 5.18 for all three horizontal line scan positions.

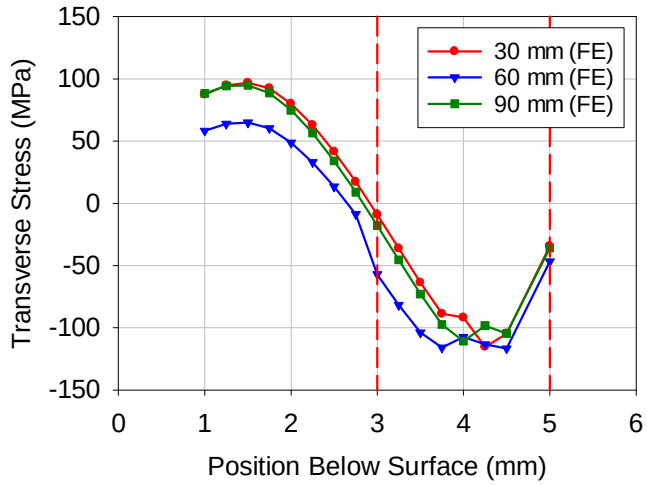

Figure 5.18: Residual stress prediction averaged over the ND gauge volume along the y-direction (transverse stress) directly below the track.

A transition in the stress state below the surface from a tensile state to compressive was observed. Therefore, a misalignment of the ND measurement location by 1 mm would cause a shift in the determined stress value from tensile to compressive. The trend observed in the transverse stress profile in the FE model presented in this work also agreed with the work presented by Pirch *et al.* [191]. It was apparent that from these findings that a small misalignment of the beamline to the initial reference datum could cause a significant alteration in the stress state that was measured. Therefore, it is believed that the location in which the ND measurements were taken were at 3 mm below the surface of the substrate. A comparison between the ND data and the FE residual stress prediction, at 3 mm below the surface, are presented in Figure 5.19. Although there are slight discrepancies between the two data sets due to the aforementioned reasons, a better correlation was observed. Furthermore, the overall underestimate between the two data sets could be due to the plasticity model utilised (isotropic hardening). Using this plasticity model would result in an overestimate in the elastic region during cyclic loading [192] due to the underestimate in the evolution of plastic strain. This arised as no translation of the yield surface could occur,

thus resulting in an underestimate of the residual stresses within the component [193]. Therefore a conservative approach should be utilised when implementing this model to predict residual stress.

Often, cyclic loads of varying magnitude are present in components during operation. From this study, tensile stresses are present throughout the substrate. The service life of the component could be severely reduced as this direction of stress promotes the initiation of material failure modes. Therefore, through heat treatment or tailoring the process parameters the high magnitude residual stresses should be reduced. As the resultant stresses induced are predominately governed by thermal strain arising from the localised heating effects, an optimum power and spot size should be determined in order to control the generation of high magnitude residual stress.

5.4.5 Comparison of the Geometrical Representation of the Track Profile

Comparisons between utilising a modified and a realistic track profile were evaluated by assessing the difference in the thermal histories and residual stress profiles at the substrate mid-length. The substrate mid-length was used as there was minimal deviation in the residual stress profiles in the the traverse direction, as observed in Figure 5.17. The thermal histories and residual stress profiles for each modified geometry are presented in Figure 5.20 and Figure 5.21 respectively.

From analysing Figure 5.20, utilising a modified track geometry caused an overestimate in the peak temperatures at all of the measurement locations. The maximum percentage difference between the peak temperatures for the realistic and the modified track profiles, for Figure 5.20(a)-Figure 5.20(c), were 7.3%, 5.9% and 7.7% respectively. Overall, a good agreement was attained between the thermal profiles for each geometry modification, with the track profile having the same height providing the best comparison to the realistic track profile.

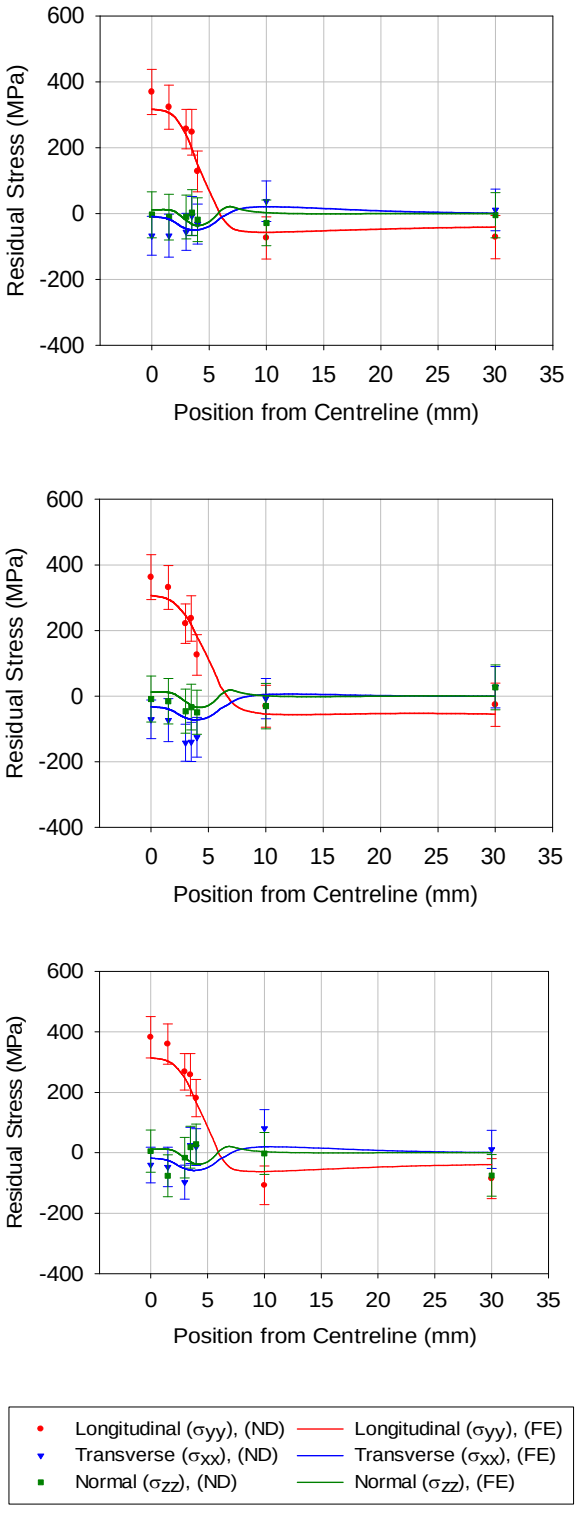

Figure 5.19: Comparison of experimentally measured and numerically predicted tri-axial residual stresses at 3 mm below the surface for each line scan position (a) y=30 mm (b) y=60 mm (c) y=90 mm.

From Figure 5.20(a), the difference in the peak temperatures may have occurred due to the inclusion of a greater thermal flux within the domain. As the square geometry had the same width and height as the realistic profile, the volume of the deposited material would not be identical; therefore, more deposition material would have been included. When analysing the cooling rate for this track modification (Figure 5.20(a)), a slower cooling rate was observed. A possible reason for this was due to a greater total of thermal flux in the domain; therefore, for the same convective and conductive coefficient values, a greater time period was required to dissipate the thermal energy away from the material. For Figure 5.20(c), a good agreement for the cooling region of the thermal history profile was achieved; however, utilising this geometry, the highest peak temperature percentage error was observed. When both the track width and melt pool geometry were coincident with each other, a superposition of thermal flux occurs, which in turn increased the total width of the melt pool geometry. This phenomena was more prominent for the square geometry, therefore causing the increase in the peak temperature for this geometry modification. For the square geometry with the same height, this phenomena was not observed because the track and melt pool width were different. This caused a reduced error between the peak temperatures as the melt pool width was determined with a greater accuracy. Based on this, an overestimate in the peak temperatures would always be present when a true energy balance was achieved within the melt pool region i.e. when the track profile and melt pool width are equal. From Figure 5.20(b), it is apparent that from implementing the modification with the same height, the best correlation to the realistic thermal history was achieved. However, it should be noted that a true energy balance within the melt pool was not achieved as the deposition material no longer filled the entire melt pool width. If a simplified track profile was required to model the thermal field, the profile with the same width and height as the true profile should be used, as this will allow a more representa-

tive energy balance within the melt pool region to be attained. However, as the total volume of material added to the domain was overestimated, a conservative approach should be taken.

With regards to the mechanical model, a good agreement was attained for all three stress components, for all three track modifications. It can be observed that there was minimal deviation in the transverse and normal stress component, with a maximum percentage error of 17.6% and 10.2% respectively. This occurs for the track profile with the same geometry and width as the realistic track respectively, therefore coinciding with the maximum peak percentage error for the thermal history profiles. For the longitudinal stress component, the peak stress was captured for all three track profiles, with a maximum percentage error of 2.7%, 2.9% and 3.5% respectively for Figure 5.21(a)-Figure 5.21(c). The main difference between the modified and realistic track, for the longitudinal stress, was the location where the stress transitions from tensile to compressive. This may have occurred due to the error associated with the thermal histories, as a greater peak temperature will cause a greater volume of molten material. This would therefore alter the final residual stress distribution within the substrate. From Figure 5.21(a)-Figure 5.21(c), due to a good correlation between the data sets, all three track modifications are acceptable to model the residual stresses; however, to be consistent with the thermal field approach, the profile with the same geometry as the realistic track profile should be used.

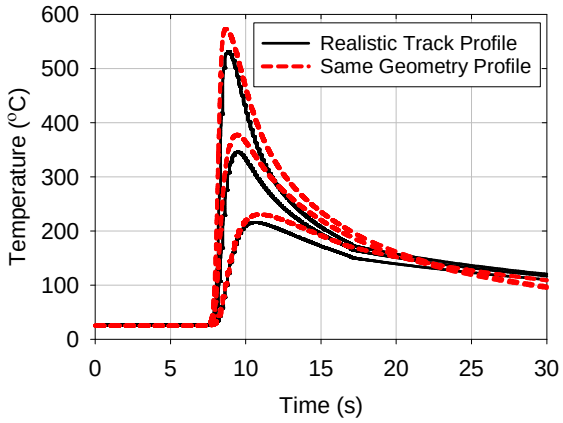

(a)

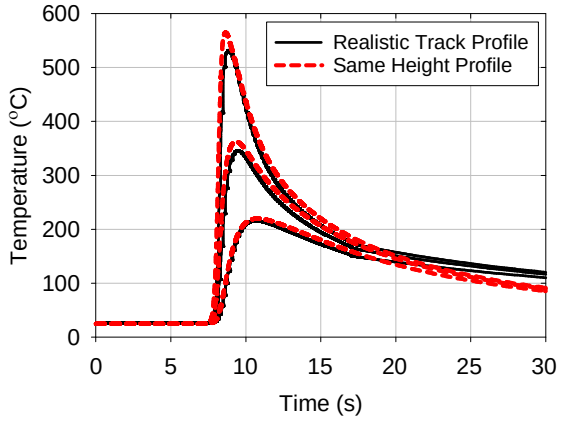

(b)

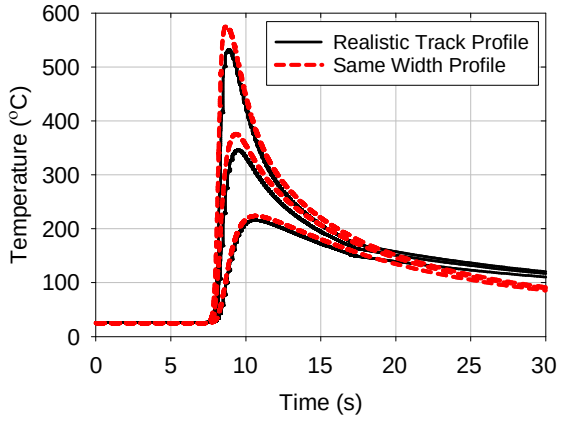

(c)

Figure 5.20: Comparison of thermal history profiles at the substrate mid length at x=3,4 and 5 mm for (a) Square track profile with the same geometry, (b) Square track profile with the same height and (c) Square track profile with the same width.

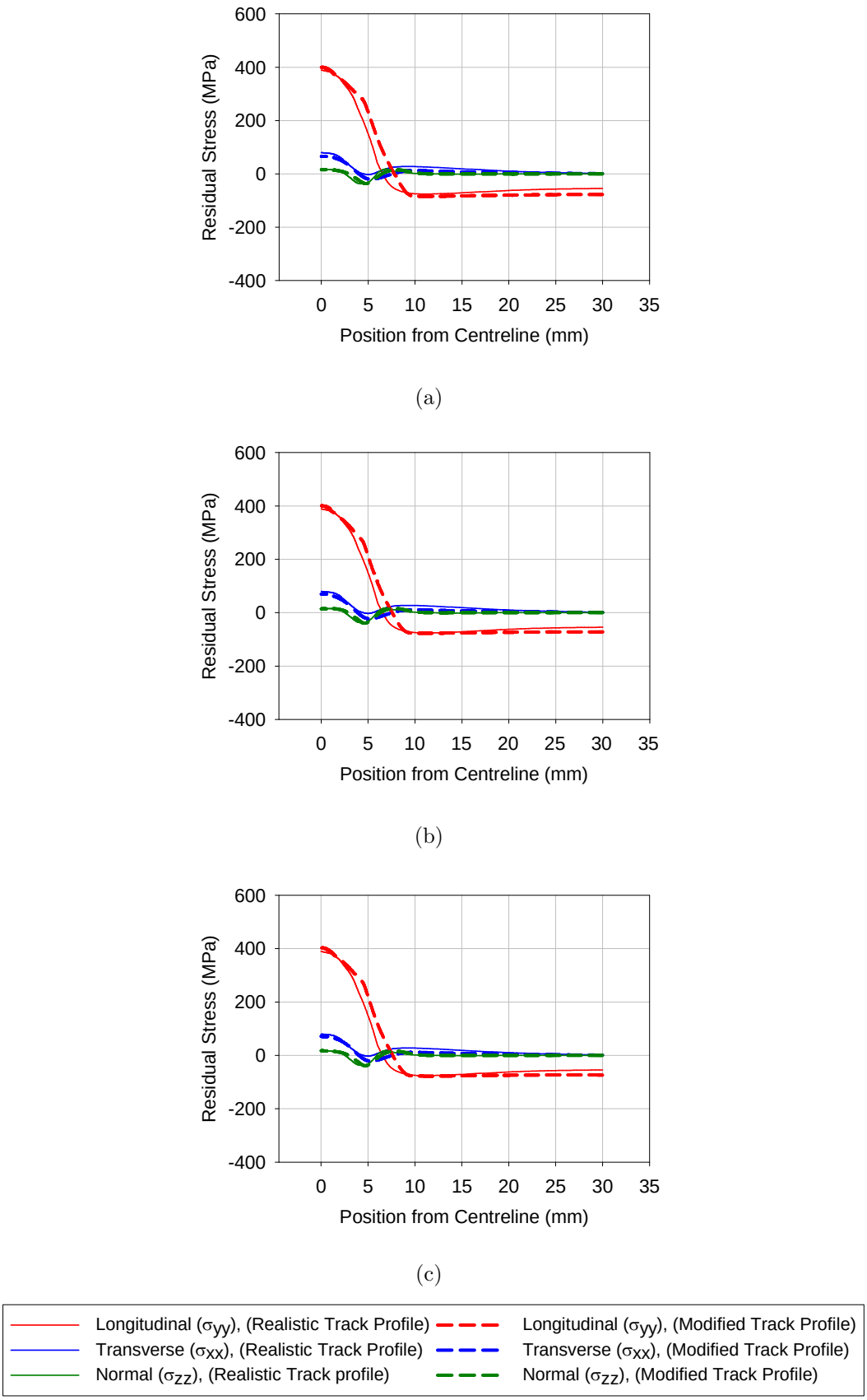

Figure 5.21: Comparison of the longitudinal, transverse and normal residual stresses at y=60 mm for (a) Square track profile with the same geometry, (b) Square track profile with the same height and (c) Square track profile with the same width.

5.5 Conclusions

- An improved modelling methodology has been developed to predict a realistic track geometry and evaluate the thermo-mechanical effects of the DED process for a single-track deposition based on key process parameters.

- A good agreement was attained between the experimental and predicted data sets showing confidence in the devised modelling methodology. The track profile was predicted with a maximum error of 1.98% and 0.43% for the width and height respectively. The maximum error for the peak temperature and residual stress was 3.1% and 18% respectively.

- Although there was an addition of material during the process the resulting longitudinal residual stress profile shows a similar trend to a traditional single pass weld. Therefore this component of stress was driven predominantly by the expansion/contraction of weld material in the substrate. The transverse and normal stress components show similar trends to one another and although a thick substrate was used a plane stress condition was not exhibited. A non-uniform residual stress distribution was predicted between the substrate and the track.

- Utilising the experimental procedure in this study, a powder catchment efficiency of 51% was calculated. This was required as an input for the model as this parameter effects the accuracy of the predicted track height.

- A simplified track profile could be used to model the thermo-mechanical effects of the DED process. If this was required, a square geometry which had both the same width and height as the realistic track profile should be used.

Chapter 6

Transient Numerical Modelling of Adaptive Process Control

6.1 Introduction

The nature of the direct energy deposition (DED) process allows for in-situ modifications to the process parameters, which would result in greater control of the track geometry, cooling rates and subsequently the mechanical properties of the component. As not all repairs are identical, this type of deposition strategy would inherently allow bespoke and flexible repairs to be implemented. The development of more flexible solutions would also allow the distortion and the evolution of stresses within the component to be controlled during repair, reducing the need for additional processing such as heat treatment or further machining. Variations in the process parameters will not only lead to a transient geometry being formed, but variations in the temperature fields, which drive the stress conditions during solidification and cooling will occur. Therefore, a tool which allowed the prediction of the track profile, thermal field and residual stress evolution, due to process parameter variation is presented in this chapter.

6.2 Numerical Modelling Strategy

The DED process allows for in-situ variation to process parameters during the deposition of a track. As the heat source, powder feed and traverse table are all coupled with a CNC system, effectively near infinite combinations of process parameters are achievable. When a constant set of parameters was utilised, a uniform track was produced which can be referred to as the steady-state region; however, in-situ modification of the parameters results in the process being in a transient state.

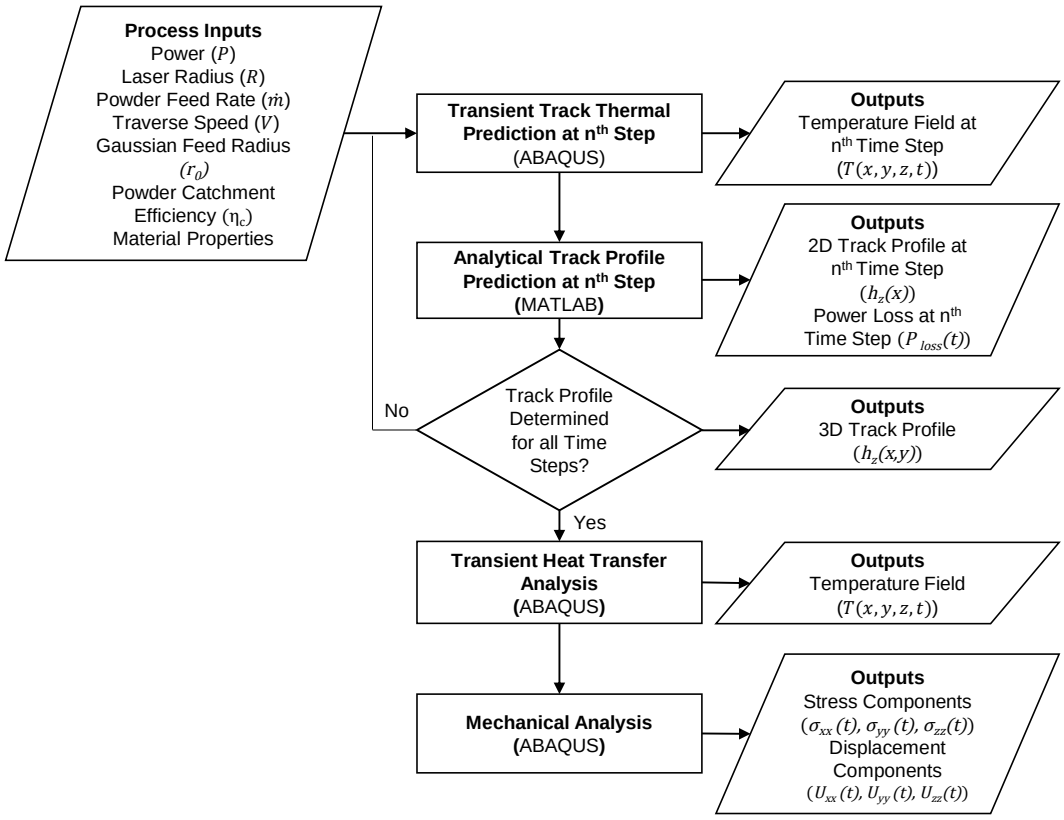

Figure 6.1: A flowchart of the modelling strategy used to predict the track profile, thermal histories and residual stress fields. The associated inputs and corresponding outputs are shown at each stage of the modelling process.

The modelling strategy incorporated the key process variables in order to model the DED process as a single entity. A flowchart of the modelling strategy used in this study is presented in Figure 6.1. Firstly, the transient track geometry was predicted using a FE heat transfer model to calculate the evolution of the melt

pool geometry. This enabled a two-dimensional (2D) track profile to be predicted at each time step (t_n) of the analysis. The predicted track geometry was then implemented into a sequentially-coupled thermo-mechanical FE analysis, allowing the thermal and mechanical effects induced by the process to be predicted.

6.2.1 Track Profile Model

As a result of using adaptive control of the process parameters, a transient thermal field will exist during the process, leading to a variation in the track geometry. To allow this phenomena to be represented, a transient Finite Element (FE) heat transfer analysis, coupled with an analytical model was utilised. The process parameters, material properties and the meshed FE domain were specified manually with each subsequent step of the analysis being automated. The flowchart of the modelling process is presented in Figure 6.2.

To determine the thermal field during the deposition, the transient heat conduction equation was solved as outlined in Section 3.3.1. The process parameters were input as a function of time ($P(t), V(t)$ and $\dot{m}(t)$)) and were used to determine the track profile at each time step of the model. The heat flux was implemented into the FE model through the user subroutine DFLUX, utilising the following heat source model:

$$Q(x,y,z,t) = \frac{\alpha P(t) - P_{loss}(t)}{\pi r_0^2} exp\left[-\frac{x^2 + (y - V(t)t)^2}{r_0^2}\right] \tag{6.1}$$

where $P_{loss}(t)$ is the power loss, t is the current time point, α is the material absorptivity, which was not considered to be temperature dependant, $P(t)$ and $V(t)$ are the laser power and traverse velocity expressed as a function of time, x, y and z are the Cartesian coordinates and r_0 is the Gaussian radius. To be consistent with the analytical approach, convective and radiative losses were neglected. A schematic of the analysis is presented in Figure 6.3.

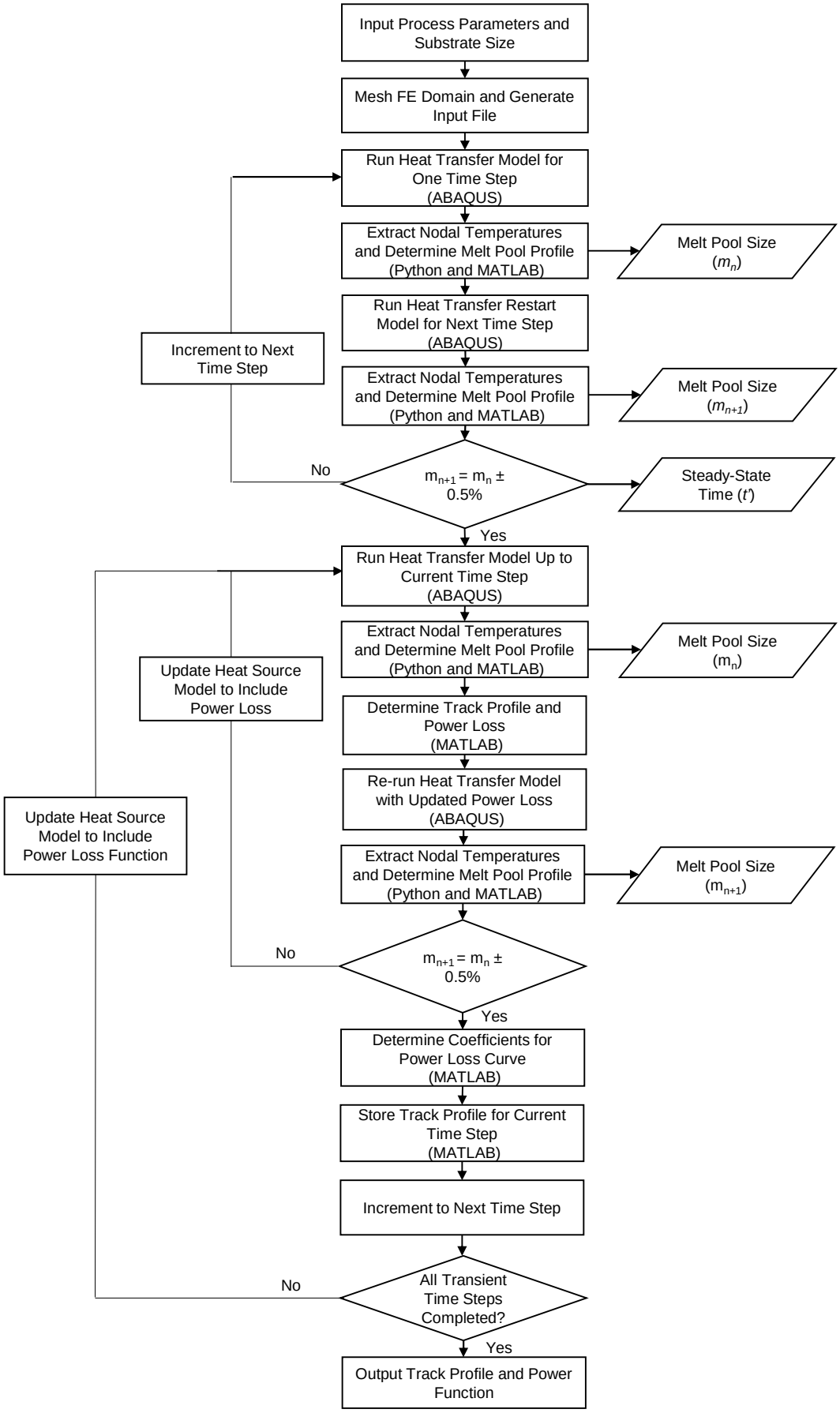

Figure 6.2: Flowchart of the modelling procedure used to determine the transient track geometry.

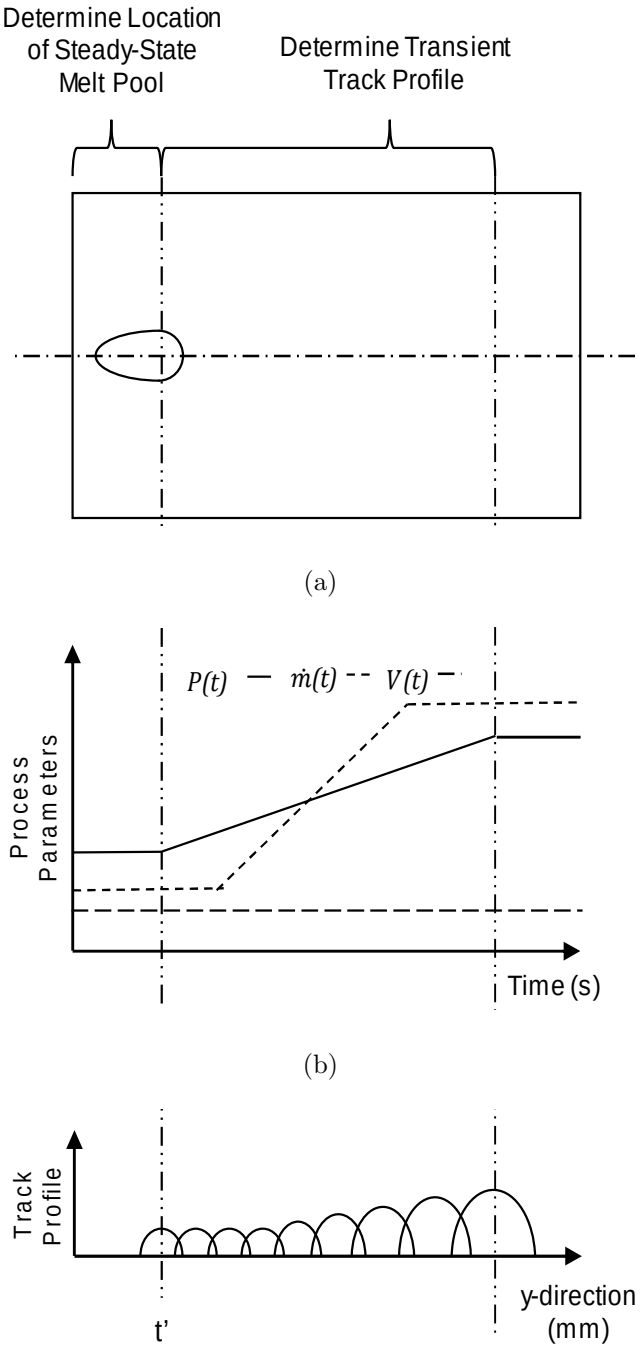

Figure 6.3: Schematic of the methodology used to determine a transient track profile. (a) Shows the substrate geometry identifying the two regions of the modelling process. (b) Presents the concept of varying process parameters during the deposition process (c) Schematic of the calculated track profile at each time increment.

Before the track profile could be predicted, an initial heat transfer model was used to determine the time required (t') for the melt pool to reach a steady-state

during the early time steps of the analysis. This time was then used to determine the starting location for which the first track profile was predicted. At each time step (t_n), a 2D track profile was predicted. The melt pool width and length were determined from the nodal FE temperatures. As only a 2D representation of the melt pool geometry was required, the through thickness nodes were neglected from the post-processing stage. The melt pool geometry for the current time step was represented using front (y_n^f) and rear elliptical (y_n^r) sections as outlined in Section 3.2.2. The track profile ($h_z(x)$) was predicted at each time step by integrating a Gaussian surface representing the powder flux distribution, between the melt pool limits:

$$h_z(x) = \frac{\eta_c(t_n)}{\rho V(t_n)} \int_{y_n^r}^{y_n^f} q_{pf} dy \tag{6.2}$$

$$q_{pf} = \frac{2\dot{m}(t_n)}{\pi r_p^2} exp\left[-2\frac{x^2+y^2}{r_p^2}\right] \tag{6.3}$$

where η_c is the powder catchment efficiency, ρ is the material density, $V(t_n)$ and $\dot{m}(t_n)$ are the traverse velocity and the powder mass flow rate at the current time step and r_p is the Gaussian feed radius determined using the method outlined in Section 3.2.1. Similar to Section 5.2.1, the catchment efficiency was determined through a modified approach and derived as a function of time to include the variability in melt pool dimensions and process parameters; therefore, the efficiency had the following form:

$$\eta_m = \int_{-W_n/2}^{W_n/2} \int_{y_n^r}^{y_n^f} S(x,y)dydx + \int_{-\infty}^{0} \int_{0}^{\sqrt{\left(\frac{W_n}{2}\right)^2 - \frac{X_{min}^2}{4}}} S(x,y)dydx - \left[\int_{y_n^r}^{0} \int_{0}^{\left(\frac{W_n}{2}\right)\sqrt{1-\frac{x^2}{(y_n^r))^2}}} S(x,y)dydx \int_{\frac{y_n^r X_{min}}{W_n}}^{0} \int_{\sqrt{\left(\frac{W_n}{2}\right)^2 - \frac{X_{min}^2}{4}}}^{\left(\frac{W_n}{2}\right)\sqrt{1-\frac{x^2}{(y_n^r)^2}}} S(x,y)dydx\right] \tag{6.4}$$

where W_n is the current melt pool width and $S(x,y)$ is defined in Section 5.2.1

and X_{min} equated:

$$X_{min} = \frac{\pi D_{particle} \rho_{powder} C_p \left(T_m - T_{amb}\right) \left(2D_{laser}\right)^2 v_{powder}}{6\alpha_{powder} P(t_n)} \tag{6.5}$$

where $D_{particle}$ is the diameter of the powder, ρ_{powder} was the density of the powder, C_p is the specific heat capacity, T_m is the melting temperature, T_{amb} is the ambient temperature, D_{laser} is the diameter of the laser, α_{powder} is the absoprtivity of the powder and v_{powder} is the velocity of the powder (Section 5.2.1). The catchment efficiency n_c was therefore equal to (Section 5.2.1):

$$\eta_c\left(t_n\right) = \frac{\int_{\infty}^{\infty} q_{pf} dy dx}{\int_{\frac{W_n}{2}}^{\frac{W_n}{2}} \int_{y_n^r}^{y_n^f} q_{pf} dy dx} \eta_m \tag{6.6}$$

As the computational deficit of the modelling approach was through determining the thermal field through a FE analysis, an efficient method to solve the analytical equations for each iteration was required; therefore, the thermal properties were assumed to be temperature independent when solving for the track profile. This increased the convergence rate for each iteration [25] and in turn, the global computational time was reduced. When implementing these equations, material properties were defined at a temperature halfway between the melting and ambient temperature (20°C) of the substrate (Section 3.3.2).

Two sources of power loss were accounted for during prediction of the track profile geometry; the energy required to melt the powder particles (P_m) [25] and the evaporation losses within the melt pool (P_{evap}) [194]. These losses were calculated at each time step of the analysis. The total power loss (P_{loss}) in the system was therefore equal to:

$$P_{loss} = P_m + P_{evap} \tag{6.7}$$

$$P_m = \rho V(t_n) \left[C_p(T_m - T_{amb}) + L_m\right] \int_{\frac{-W_n}{2}}^{\frac{W_n}{2}} h_z(x)dx \tag{6.8}$$

$$P_{evap} = \frac{\pi}{4} W(t_n) \left[L_n^f + L_n^r\right] \left[\frac{455.32exp\left[4.834 - \frac{18836}{T_{mean}}\right]}{\sqrt{T_{mean}}}\right] h_v \tag{6.9}$$

where L_m is the latent heat of melting, T_{mean} is the mean temperature in the domain, h_v is the latent heat of vaporisation, L_n^f and L_n^r is the length of the front and rear elliptical melt pool sections respectively. To allow the effective power to be defined at each time step in the transient region, the power loss was expressed as a function of time ($P_{loss}(t)$). The heat source model was then updated to include this function. A schematic of the power loss history and how it was represented in the model is shown in Figure 6.4.

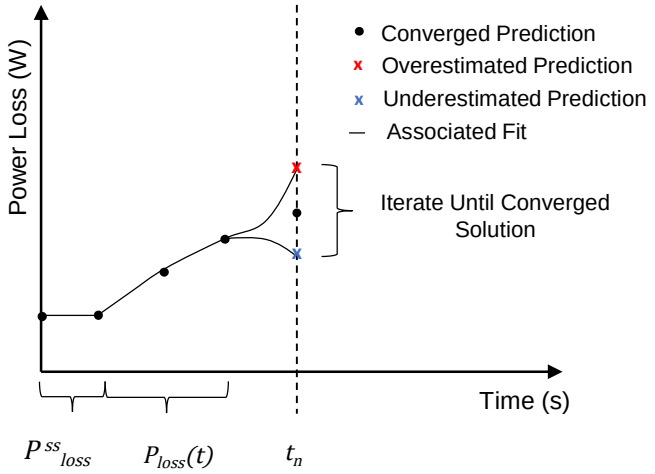

Figure 6.4: Schematic of the power loss function showing the three possible outputs of the model after an iteration during the current time step.

The power loss was calculated using an iterative solution procedure with the initial guess equating the power loss for the previous time step of the analysis. When the model was not in a transient state, the power loss was assumed to be constant (P_{loss}^{ss}) and was determined from Equation 6.7. For the first iteration, at the nth time step, the model overestimated the power loss and on the second iteration the losses were underestimated [25]. This process continued until a stable melt pool was achieved and the power loss converged. To enable the predicted

and converged values to be accurately input into the FE heat source model, the selected function had to be able to represent all three possible states of power loss that could be encountered, i.e. overestimate, underestimate and converged solution; therefore, a third order polynomial was selected of the following form:

$$P_{loss}(t) = at^3 + bt^2 + ct + d \tag{6.10}$$

where a, b, c and d are the coefficients of the equation. The overall solution procedure was iterative to ensure that a stable enthalpy balance and melt pool geometry were achieved at each time step. A stable melt pool occurred when the following criteria was valid:

$$W_n = \pm 0.05 W_{n-1} \tag{6.11}$$

$$L_n = \pm 0.05 L_{n-1} \tag{6.12}$$

where W_n is the melt pool width and $L_n = L_n^f + L_n^r$ for the nth time step of the analysis. Upon a stable melt pool being determined, the power loss and the track profile for each time step were stored. The model was terminated when all the predefined time steps were completed. Each 2D track profile was concatenated to determine the final three-dimensional (3D) track geometry for the transient region of the model.

6.2.2 Thermo-mechanical Modelling

To determine the thermal histories and residual stress fields induced from a transient deposition, a sequentially coupled thermo-mechanical analysis was implemented. The track geometry obtained from Section 6.2.1 was imported into the FE domain; a schematic of the process and the adopted modelling strategy is presented in Figure 6.5.

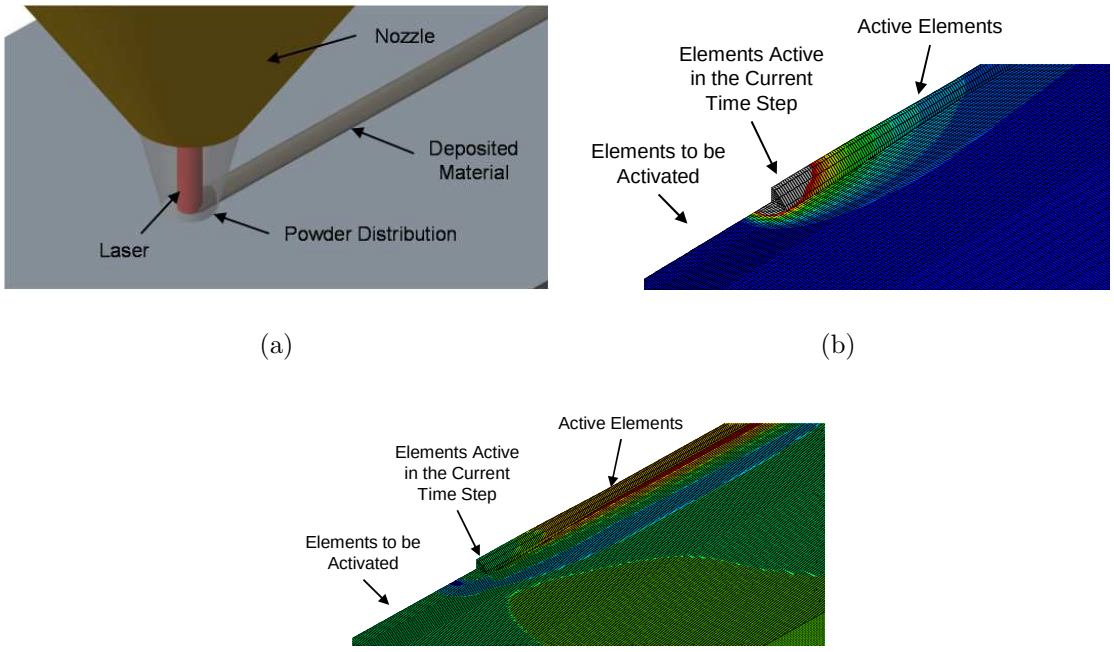

Figure 6.5: Schematic of the thermo-mechanical modelling process for DED. (a) Realistic representation of the DED manufacturing process. (b) Thermal model showing a thermal contour with the adopted element activation strategy. (c) Mechanical model showing a longitudinal stress distribution and the adopted element activation strategy.

A transient heat transfer analysis was used to solve the governing equation outlined in Section 3.3.1. To simulate the deposition of material, an active/inactive element approach was implemented for both the thermal and mechanical FE model (Section 3.3.4). Thermal effects, due to solidification of the melt pool, and both convective and radiative losses, accounted for using the Newton and Stefan-Boltzmann laws respectively (Section 3.3.1), were included in the model.

6.3 Validation of the Model

For the current study, a validation case is presented which implemented the proposed methodology to predict the transient deposition track, thermal history and residual stress field generated by an in-process modification to the laser power. A single track of Inconel 718 (IN718) was deposited along the centre of an IN718

substrate utilising the following laser power profile. The laser power was fixed at 900 W for the first 7.5 seconds of the deposition. This value was linearly increased to 1800 W over the duration of 3 seconds, with the power remaining at 1800 W for the remainder of the deposition. The total time required to complete the deposition was 18 seconds. The selected power profile was based on the upper and lower values of the previously determined process window for the alloy system and the experimental setup adopted for this work [173]. For the entire deposition, the traverse velocity (V) and the powder mass feed rate ($\dot{m}$) were kept constant at values of 400 mm/min and 26 g/min respectively.

6.3.1 Implementation of the Computational Model

As the thermal field for the track profile model was determined through the use of a transient FE model, a mesh independence study was conducted to determine the optimum element size which represented the heat flux within the domain. The FE domain used was the size of the substrate (120 x 70 x 6 mm) and was meshed with DC3D8 and C3D8R linear brick elements for the thermal and mechanical models respectively. The study was completed for the maximum and minimum laser powers, i.e. P=900 W and P=1800 W using the method outlined in Section 4.2.2. The results are presented in Figure 6.6. It should be noted that the reduction in accuracy observed at iteration 2, for P=1800 W (Figure 6.6), arose from increasing the number of nodal points used to represent the through thickness thermal field.

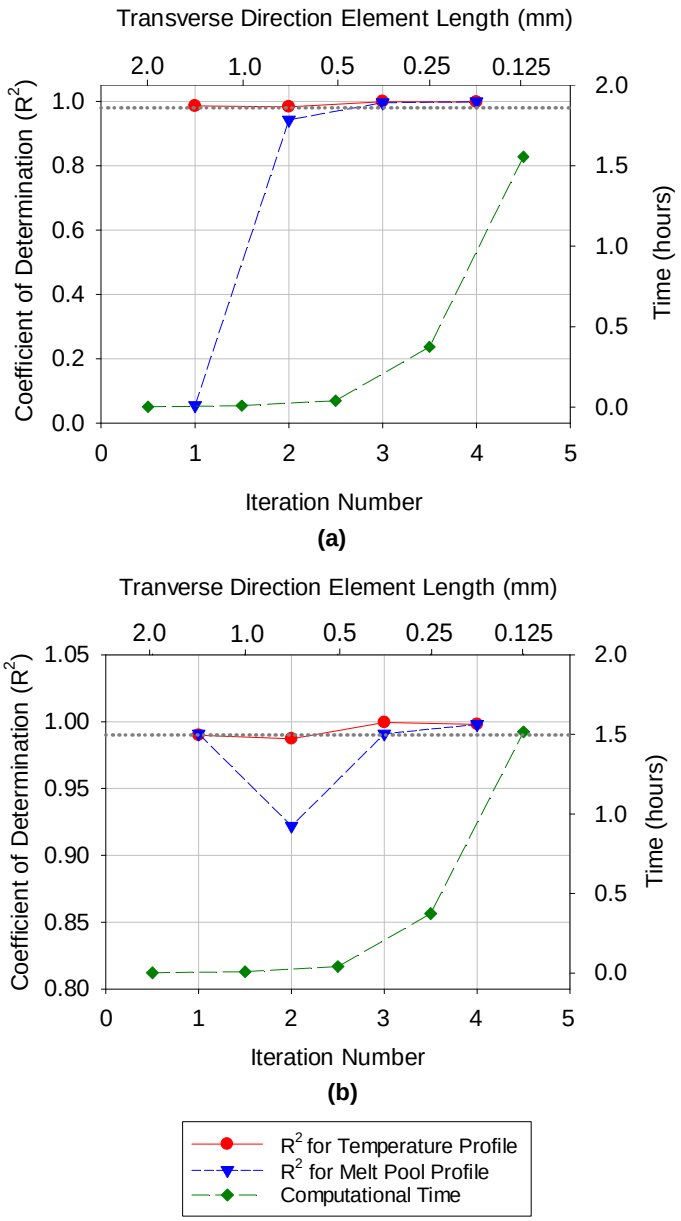

Figure 6.6: Mesh study results for (a) P=900 W and (b) P=1800 W. Each graph presents the convergence parameters and computational time for each mesh iteration. Convergence criteria is highlighted as a dotted grey line.

This caused the shape of the fusion zone to change from the previous iteration, resulting in a larger melt pool area. For both sets of process parameters, iteration 4 satisfied the convergence limits, therefore an element volume of 0.25 x 0.25 x 0.25 mm^3 was utilised in the vicinity of the heat source, i.e. $-5 \leq x \leq 5$ mm. Outside of the heat source region, i.e. $x \leq -5$ mm and $x \geq 5$ mm, an element volume of 1 x 0.25 x 0.25 mm^3 was utilised. The total number of elements and

nodes in the mesh were 622,800 and 656,850 respectively. An example section of the mesh used for the track profile model is presented in Figure 6.7.

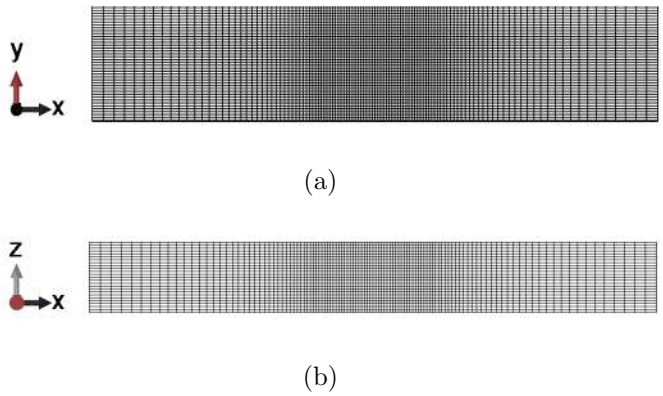

Figure 6.7: Final mesh design utilised for the numerical track prediction mode (a) A section of the mesh used in the traverse direction (b) Through thickness mesh design. For both images, the laser scanning direction is denoted by the red arrow (y-direction).

For the thermo-mechanical model a second mesh was required to include the predicted track geometry. As a variation in the track profile was present, a reduction in element size was required in the transient region. As a converged solution was obtained for a 0.25 x 0.25 x 0.25 mm^3 element volume, this was utilised for the high-power region, i.e. P=1800 W. The element volume was reduced to 0.125 x 0.125 x 0.125 mm^3 for the low power region, i.e. P=900 W. From Figure 6.6 it can be observed that the use of a 0.125 x 0.125 x 0.125 mm^3 element volume provided a negligible difference in the solution accuracy; therefore, mesh independence was still achieved. Hexahedral elements with a constant volume were used throughout the domain to allow the predicted stresses to be volumetrically averaged to compare against the experimental ND data. A total of 717,818 nodes and 672,000 elements were present in the domain. Sections of the mesh from each track region are presented in Figure 6.8.

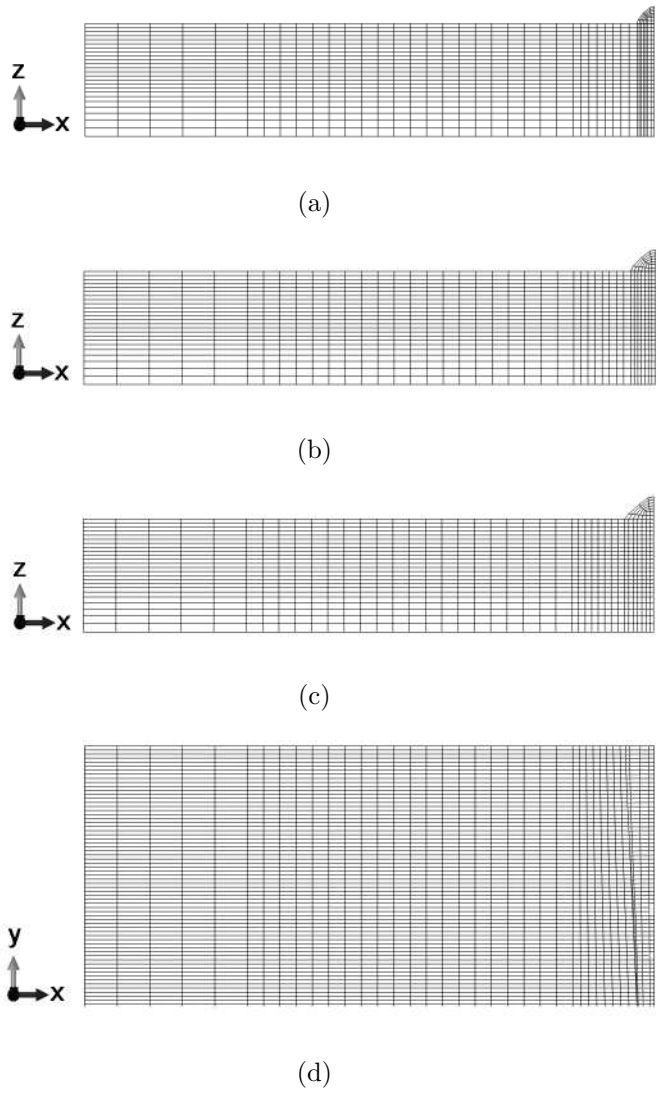

Figure 6.8: FE mesh utilised for the thermo-mechanical model showing the through thickness design at (a) y=30 mm (b) y=60 mm (c) y=90 mm. (d) Presents a top view of the mesh design in the transient region.

Due to the variation in the laser power, the circular disc heat source model had the following form:

$$Q(x,y,z,t) = \frac{\alpha P(t) - P_{loss}}{\pi r_0^2} exp\left[-\frac{x^2 + (y - V(t)t)^2}{r_0^2}\right] \tag{6.13}$$

$$for\ t \leq t_{ss(1)} \ \rightarrow \ P_{loss} = P^{ss}_{loss(1)}$$

$$for\ t \geq t_{ss(2)} \ \rightarrow \ P_{loss} = P^{ss}_{loss(2)}$$

$$for\ t_{ss(1)} \leq t \leq t_{ss(2)} \ \rightarrow \ P_{loss} = P_{loss}(t)$$

where $t_{ss(1)}$ and $t_{ss(2)}$ are the total times for which the deposition was in a steady-state condition. The Gaussian radius was assumed to equal 1.3 mm for this study. Through implementing Equation 6.7, the power loss for both the steady-state track regions ($P^{ss}_{loss(1)}$ and $P^{ss}_{loss(2)}$) was constant due to the melt pool having a fixed width and length in this region. Therefore, the power loss in these regions were represented within the FE heat source model as a single value for the corresponding time steps. In the transient region, due to the changes in the melt pool dimensions at each time increment, the power loss function ($P_{loss}(t)$) was defined within the user subroutine *DFLUX*. Other losses including the convective and radiative losses at the free surfaces was included with the coefficients defined in Section 3.3.1.

As different melt pool sizes were present throughout the analysis, the number of elements reactivated to simulate the deposition of material, per time step, was not uniform. This was required to ensure that a stable energy balance within the melt pool itself was achieved. For the region where P=900 W, two element lengths per time step were reactivated, in all other regions a total of four element lengths were reactivated.

For the thermo-mechanical FE model, temperature dependent material properties were utilised, as defined in Section 3.3.2. The latent heat of melting was included for the respective solidus and liquidus temperatures. The thermal properties used to implement the analytical expressions for the track profile model are presented in Section 3.2.3 with the density and specific heat capacity being temperature independent defined at 630°C. The mechanical analysis was defined using the methodology outlined in Section 3.3.1, with the boundary conditions applied for modelling half of the specimen geometry.

6.3.2 Experimental Validation

A track of IN718, with a varying cross-sectional geometry was deposited utilising a variation in the laser power profile. The experimental set up is documented in Section 3.4.1. Two identical samples denoted Sample A and Sample B were manufactured, with a schematic of the experimental set up shown in Figure 6.9. The coordinate system remained constant throughout, with the build direction being in the positive z axis and the x-y axis forming a plane perpendicular to the build direction. Sample A was used for in-situ temperature measurements, metallurgical examination and for the ND measurements. To obtain the elastic strain within Sample A using ND, a strain-free reference value (d_0) was obtained from a comb specimen manufactured from Sample B (Figure 6.10). The full track length equated 110 mm and upon its completion, the sample was cooled in air to room temperature.

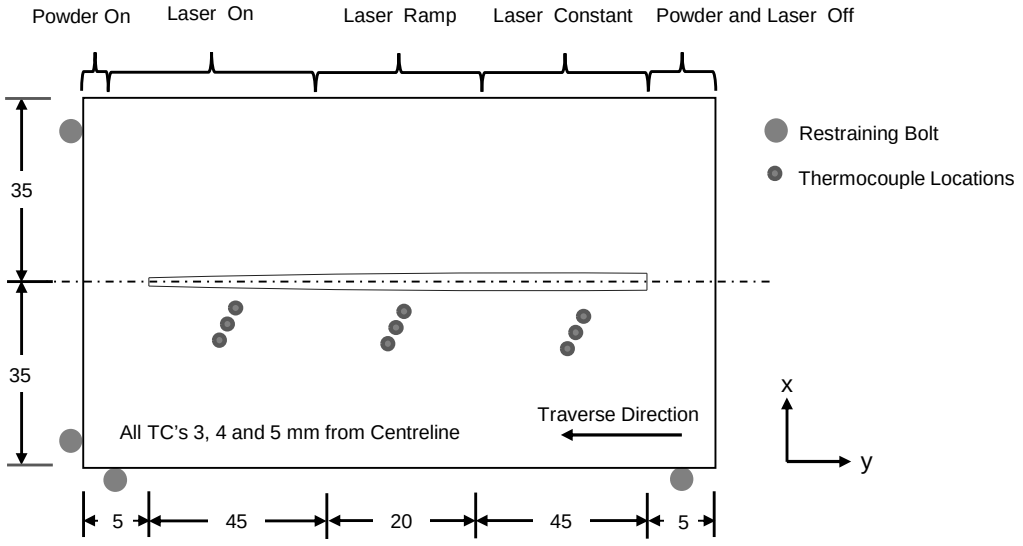

Figure 6.9: Schematic of the experimental set up showing the locations of the restraining bolts, thermocouples used to collect thermal histories and the order in which the laser and powder feed were activated/deactivated.

A total of nine in-situ temperature measurements were recorded in the region of the HAZ, using the method outlined in Section 3.4.2. To verify the predicted melt pool geometry, metallographic analysis was conducted on Sample A. Speci-

mens were removed from each of the three regions of the track by waterjet cutting, as shown in Figure 6.10. The track profile was obtained using the method outlined in Section 3.4.4.

The method required to collect the ND data to validate the mechanical model is presented in Section 3.4.5. All measurements were conducted to the right of the sample centreline due to the geometrical symmetry, at 2 mm below the surface of the substrate. A gauge volume of 2 x 2 x 2 mm^3 was used for all measurements allowing for a good compromise between accuracy of the measurements and the spatial resolution at which they were conducted. It should be noted that the beam time allocation did not allow for a strain-free reference sample to be measured at each line scan location.

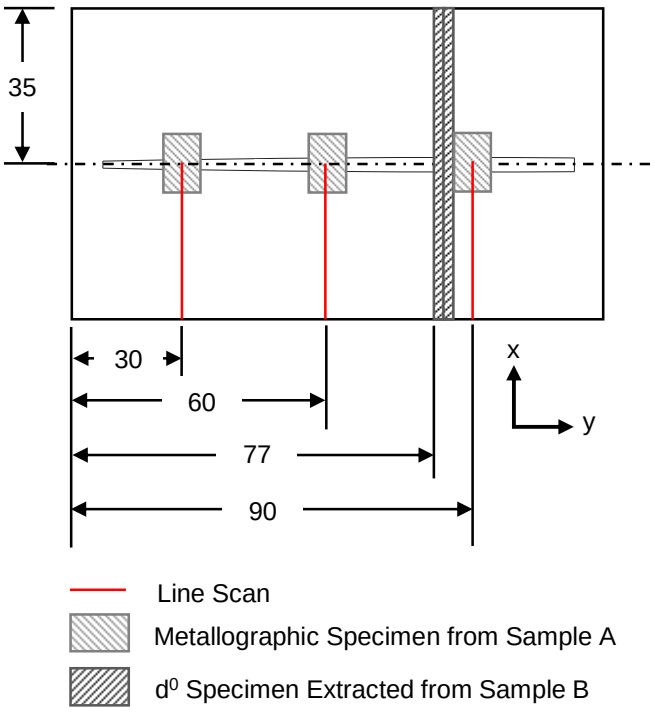

Figure 6.10: Locations of the specimens used for metallographic examination and the strain-free reference sample. Horizontal line scan locations used for the ND measurements shown in red.

6.4 Results

6.4.1 Numerical Track Prediction

A 3D surface plot generated from experimental measurements of the track is presented in Figure 6.11. A comparison between the experimental and predicted track profiles, for the steady-state and transient region are presented in Figure 6.12 and 6.13 respectively. The error and coefficient of determination (R^2) between both data sets is presented in Table 6.1.

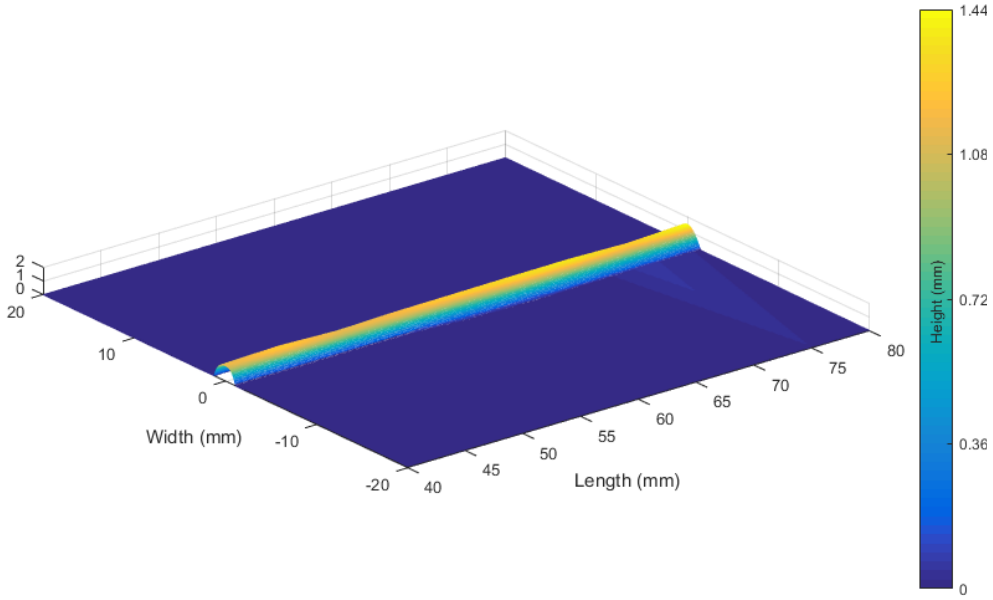

Figure 6.11: A 3D surface plot of the experimental track deposit upon the substrate generated from surface measurements of Sample A.

From analysing both sets of data, the track width and height increased during the transient phase, reaching a steady-state profile at the end of the transient region. However, the experimental track width appears to reach a constant value before the end of the transient region. The predicted shape of the track profile in all three regions agreed well with the experimental data, as the majority of the R^2 values are greater than 90%, showing confidence in the predicted values.

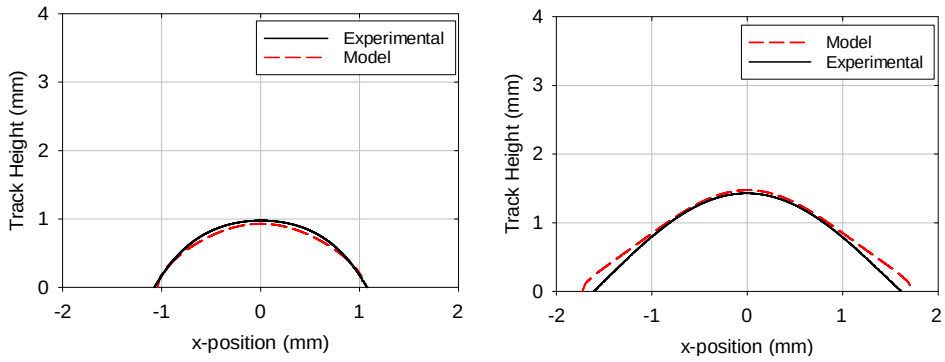

(a) (b)

Figure 6.12: A comparison of the experimental and predicted track geometry for two laser powers (a) P=900 W and (b) P=1800 W.

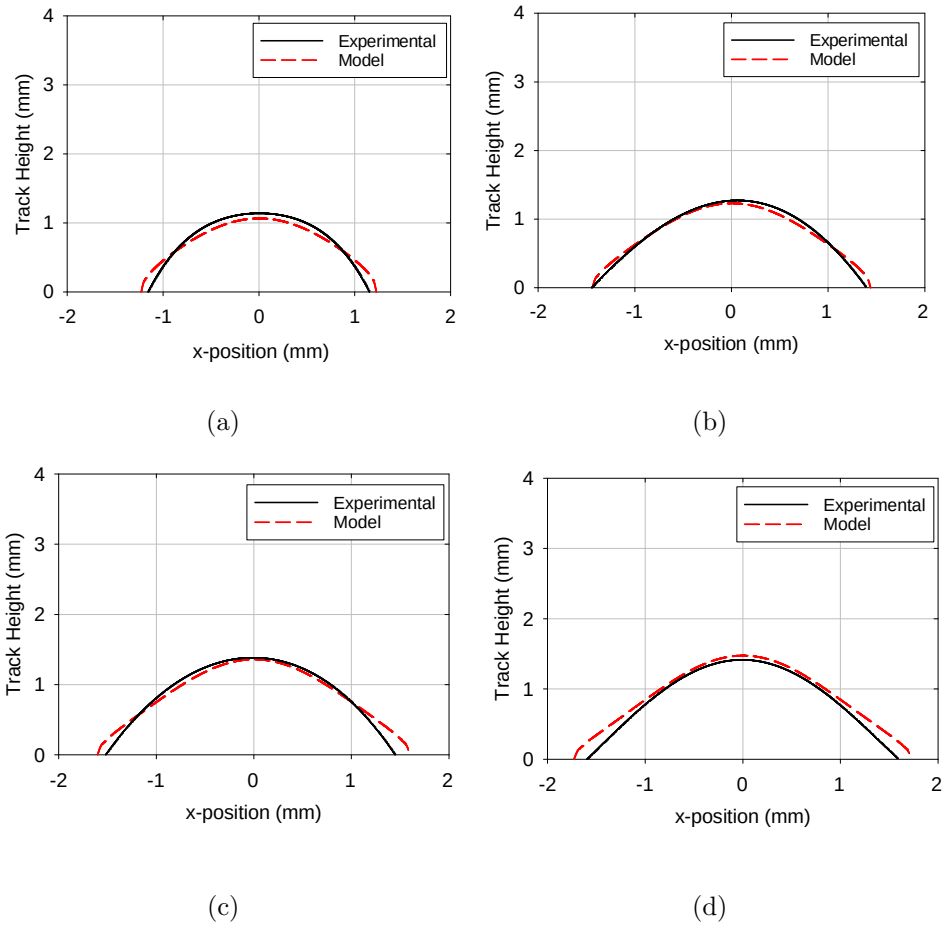

(a) (b)

(c) (d)

Figure 6.13: A comparison of the experimental and predicted track geometry at four locations within the transient region. (a) y=55 mm (b) y=60 mm (c) y=65 mm (d) y=70 mm.

Table 6.1: Error and R^2 Values for Experimental and Predicted Track Profiles.

Distance (mm)	Error W_{max} (%)	Error h_{max} (%)	Coefficient of Determination R^2
$5 \leq$ y ≤ 50	3.79	4.81	0.962
55	5.38	6.50	0.934
60	7.08	4.38	0.921
65	3.47	1.77	0.937
70	7.62	4.25	0.992
$75 \leq$ y ≤ 114	6.73	3.25	0.994

It should be noted that for y=60 mm and y= 65 mm, the experimental bead geometry was asymmetric, therefore the error between the track height and width maybe due to the model not accounting for this phenomena. The numerical model predicts the track profile with a greater accuracy at the low laser power. During the transient phase of the process, the height was captured well by the model; however, the predicted track width was overestimated when compared to the experimental data. The maximum error between the predicted and experimental data arose for the final transient profile and for the profile used in the second steady-state region. In these regions, the peak height of the profile was predicted with accuracy, therefore the error must have arisen from the derivation of the melt pool width.

The power loss (P_{loss}) and the effective power (P_{eff}) utilised in the transient portion of the numerical FE model is presented in Figure 6.14. For the steady-state regions, i.e P=900 W and P=1800 W, the power loss (P_{loss}^{ss}) was calculated as 71.1 W and 165.7 W respectively. The power loss over the duration of the deposition followed a linear trend, with a greater reduction in the effective power observed for an increase in the laser power. This was due to the melt pool geometry enlarging at each time step; therefore leading to an increase in the mass of powder which was being assimilated by the melt pool, resulting in a

higher energy requirement to sustain mass addition. This therefore reduced the power available at the substrate, which was represented by the effective power in the model. The catchment efficiency used for the transient portion of the model is presented in Figure 6.15. For the steady-state regions, the calculated value for the catchment efficiency equated 0.38 and 0.48 for where P=900 W and 1800 W respectively. The overall trend for the transient catchment efficiency was approximately linear. At higher laser powers the melt pool geometry will increase in size due to the increase in heat energy available at the substrate. Therefore, the total amount of powder which could be assimilated would rise as the melt pool now covered a greater portion of the powder flux distribution.

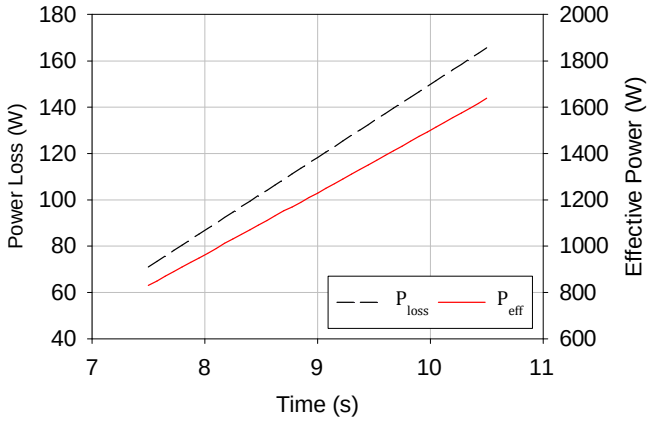

Figure 6.14: Predicted power loss and effective power utilised during the transient portion of the model.

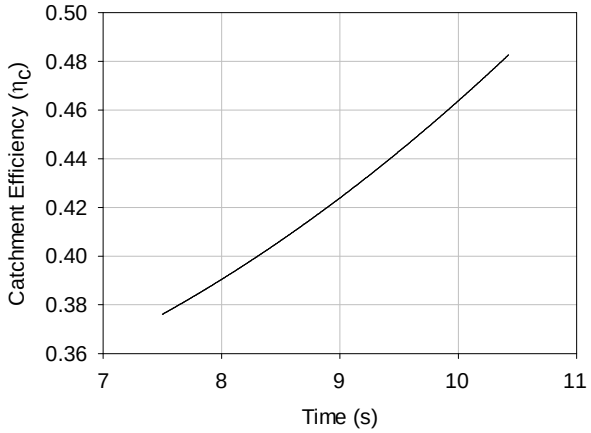

Figure 6.15: Predicted catchment efficiency used during the transient portion of the deposition.

6.4.2 Thermal Analysis

In-situ temperature measurements were compared with the thermal histories from the FE model as shown in Figure 6.16. For all three locations, the overall trend was replicated well. The peak temperatures for all thermocouple locations was overestimated by the FE model, with a maximum error of 6.2% in the transient region. The predicted thermal gradient prior to the heat source pass, for all three regions, had a sharper gradient than expected when compared to the experimental data. For the thermocouple measurements at y=60 mm, there were fluctuations in the data collected by the far most thermocouple. This could be due to noise or as a result of the junction not being in contact at x=5 mm, potentially leading to the difference observed in the peak temperature value at this thermocouple location. In the cooling phase of the model the thermal losses provided a good estimate of the cooling rate after the heat source passed the measurement location.

A comparison of the predicted weld pool and the experimental micrograph are compared for each of the three track regions in Figure 6.17. The isotherms presented were taken at the widest point at each location investigated. The grey region represents the fusion zone with contour restricted to the solidus temperature (1260°C). Overall a good agreement between the predicted and experimental weld pool is apparent at all three locations. However, the greatest deviation between the two data sets was for the weld pool depth at y=35 mm and y=65 mm. Overall, the shape of the fusion zone was captured with accuracy, with the variation in penetration depth and melt pool width being captured at all three locations. For the predicted data set in both the transient and high laser power region, the melt pool geometry no longer encompasses the track material. However, it can be observed in Figure 6.17(b) and Figure 6.17(c) that this happens in reality due to a layer of powder adhering to the track surface. The layer of powder varies from a thin layer at the low laser power and increases in thickness throughout the deposition.

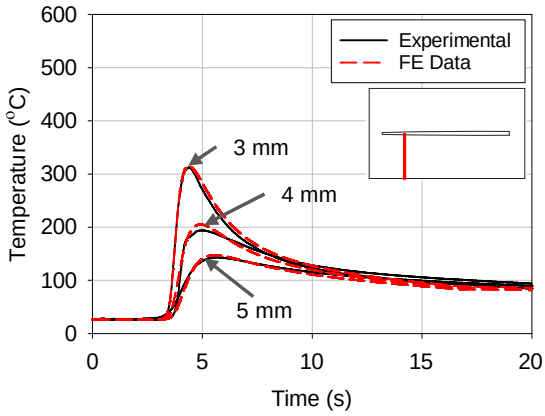

(a)

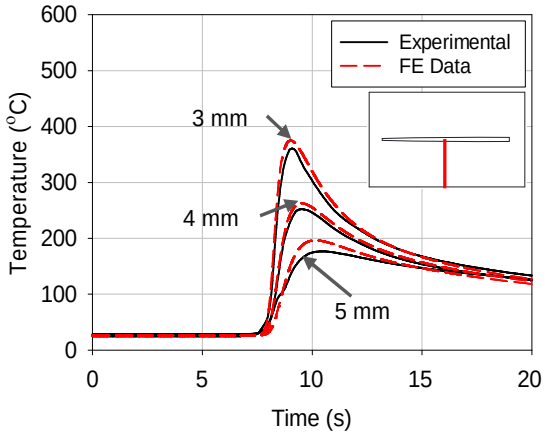

(b)

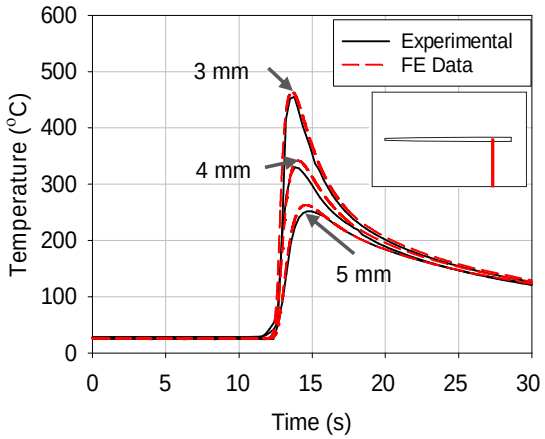

(c)

Figure 6.16: A comparison of experimental and numerically predicted thermal histories at three locations along the substrate at (a) y=30 mm, (b) y=60 mm and (c) y=90 mm for three thermocouple's positioned at; 3 mm, 4 mm and 5 mm from the track centreline.

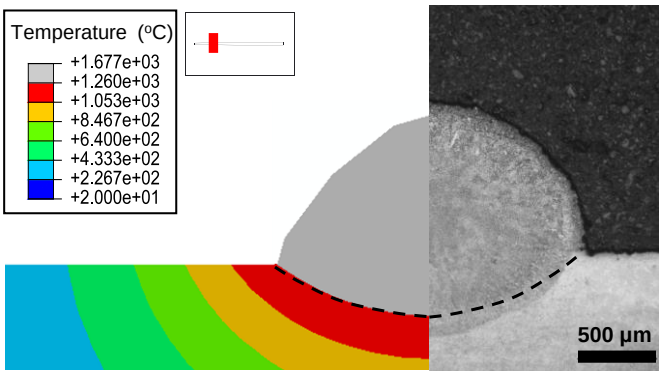

(a)

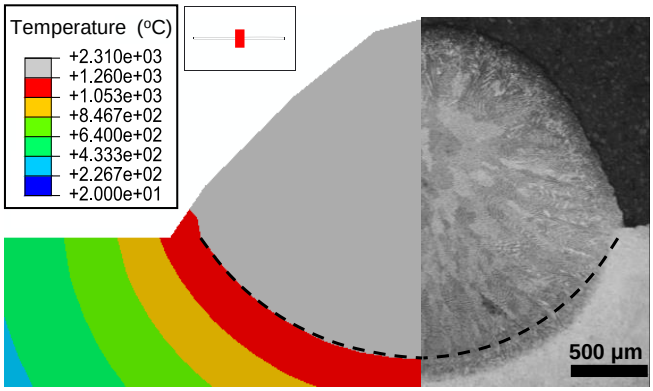

(b)

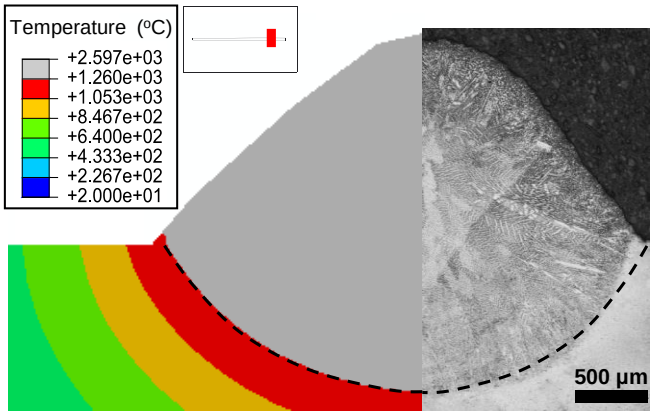

(c)

Figure 6.17: A comparison of the numerically predicted fusion zone and the metallographic specimen at three locations (a) y=35 mm (b) y=65 mm and (c) y=95 mm.

6.4.3 Mechanical Analysis

The evolution of stress at a position in the melt pool for each track region is presented in Figure 6.18, with corresponding contour plots presented in Figure 6.19-6.27. The normal stress component was zero during the deposition until the peak temperature was reached. As the temperature approaches the melting temperature (1260°C) of the material, all three stress components, at all three locations, were compressive. The magnitude of the compressive stress upon reaching the peak temperature was constant at all three locations, therefore, the stress evolution directly below the track was independent of the size of the melt pool. Shortly after the peak temperature was achieved, all three components of stress enter a tensile state, at the same rate, for all three locations. Upon cooling the component to room temperature, the time required to reach the final residual stress state reduced with an increase in laser power. In the region where P=1800 W, the transverse stress reached a peak value and did not decay to a lower value upon cooling. This arose due to the increased cooling rate ($-dT/dt$) observed in the high laser power region (2150°C/s) compared to the low laser power region (1560°C/s); therefore maintaining the current stress state within the component. At room temperature, the longitudinal and transverse stresses were tensile, with varying magnitudes at each location. The variation in stress magnitude occurred due to the evolution of the melt pool geometry at each location, this dictated the amount of expansion and contraction of material occurring in front and behind the heat source. The normal component returns to approximately zero for the low laser power; however, an increase in magnitude was observed with an increase in laser power.

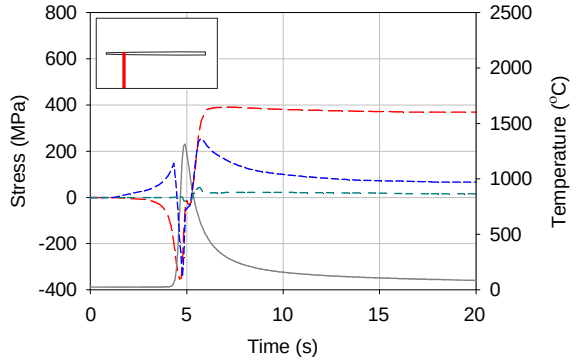

(a)

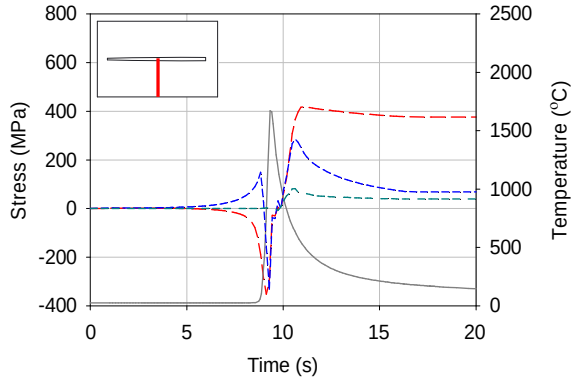

(b)

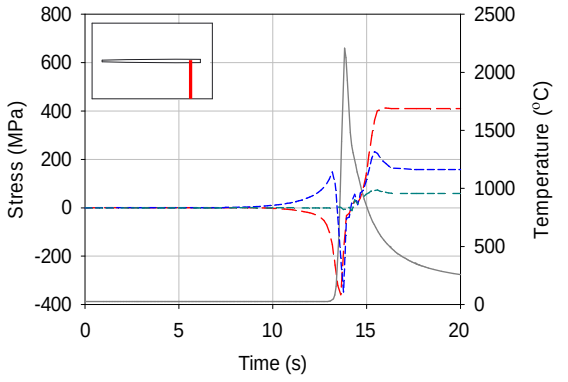

(c)

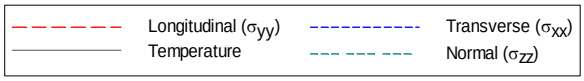

Figure 6.18: Numerical prediction of the transverse, longitudinal and normal stress components during the deposition process, in three region of the track (a) y=30 mm (b) y=60 mm (c) y=90 mm. The nodal point was at the track centreline 0.25 mm below the substrate surface.

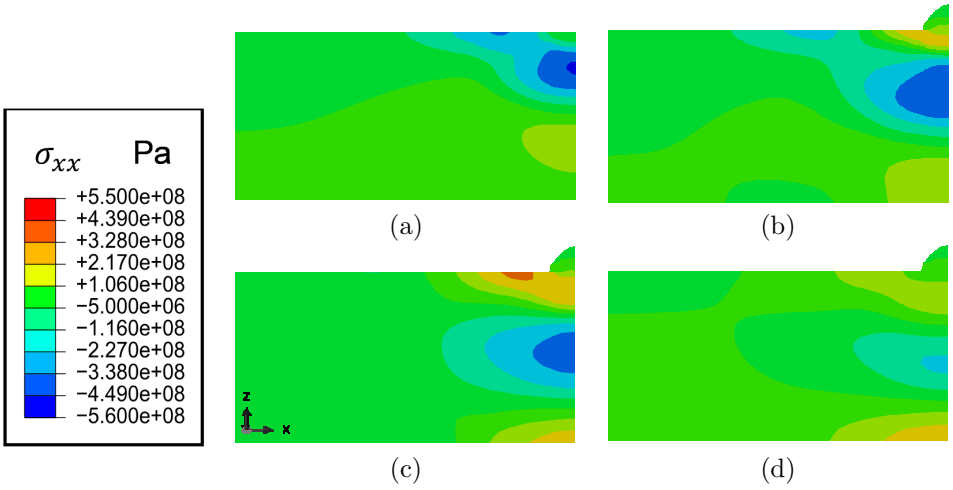

Figure 6.19: FE contour plots at y=30 mm showing the through thickness stress distribution for the transverse stress component, σ_{xx}. (a) During the heating phase at t=8.25 s (b) At the peak temperature where t=8.95 s (c) During the cooling phase at t=12.15 s (d) Final residual stress field upon being fully cooled.

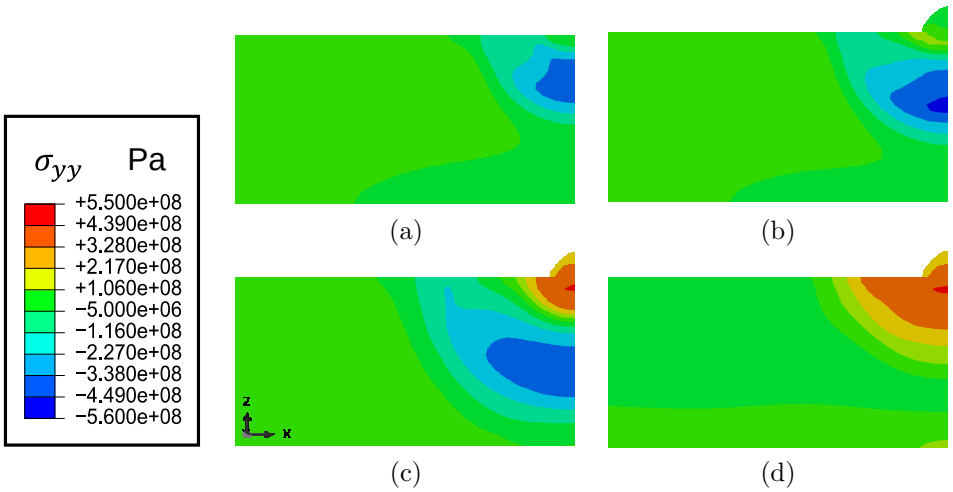

Figure 6.20: FE contour plots at y=30 mm showing the through thickness stress distribution for the longitudinal stress component, σ_{yy}. (a) During the heating phase at t=8.25 s (b) At the peak temperature where t=8.95 s (c) During the cooling phase at t=12.15 s (d) Final residual stress field upon being fully cooled.

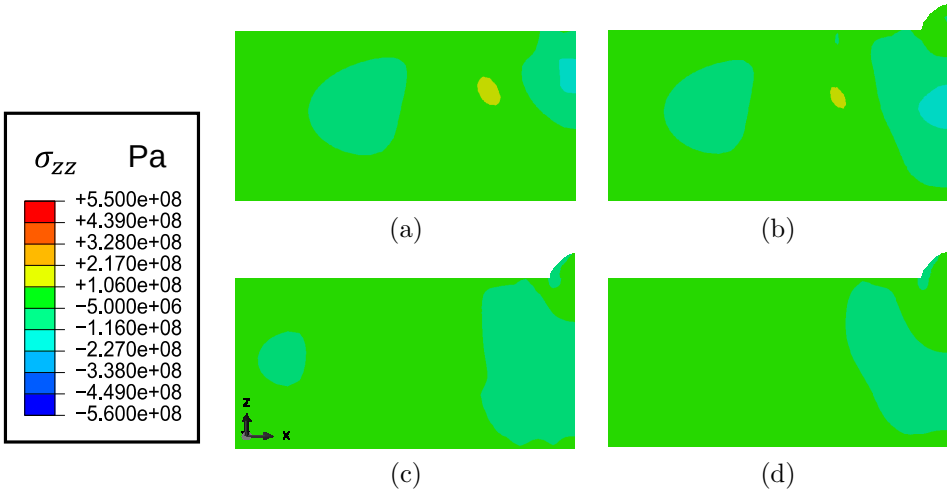

Figure 6.21: FE contour plots at y=30 mm showing the through thickness stress distribution for the normal stress component, σ_{zz}. (a) During the heating phase at t=8.25 s (b) At the peak temperature where t=8.95 s (c) During the cooling phase at t=12.15 s (d) Final residual stress field upon being fully cooled.

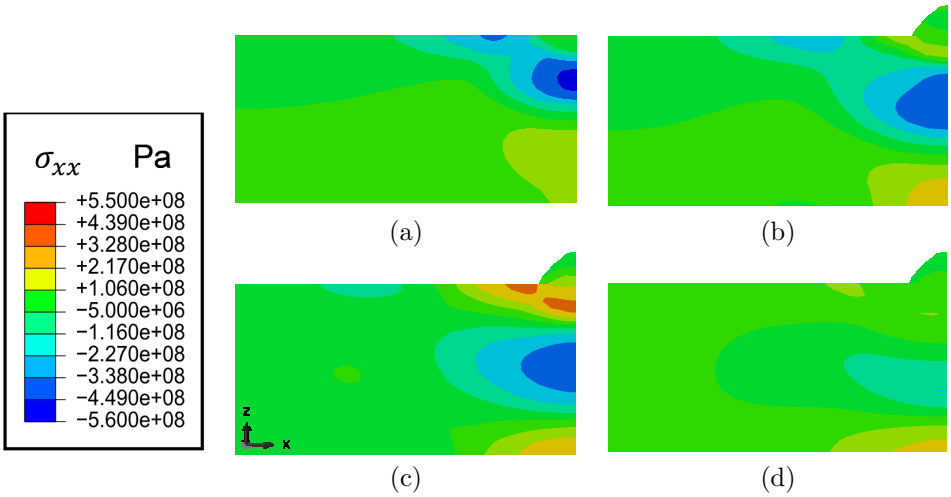

Figure 6.22: FE contour plots at y=60 mm showing the through thickness stress distribution for the transverse stress component, σ_{xx}. (a) During the heating phase at t=8.25 s (b) At the peak temperature where t=8.95 s (c) During the cooling phase at t=12.15 s (d) Final residual stress field upon being fully cooled.

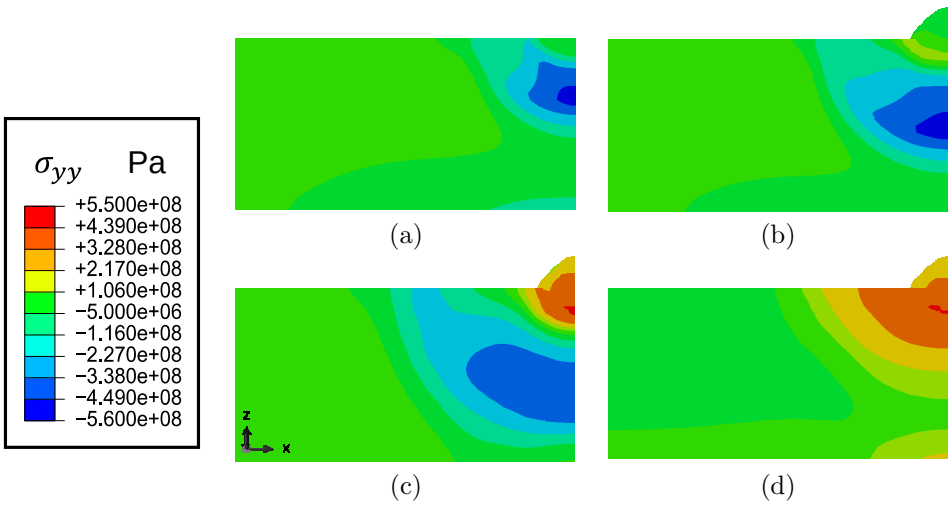

Figure 6.23: FE contour plots at y=60 mm showing the through thickness stress distribution for the longitudinal stress component, σ_{yy}. (a) During the heating phase at t=8.25 s (b) At the peak temperature where t=8.95 s (c) During the cooling phase at t=12.15 s (d) Final residual stress field upon being fully cooled.

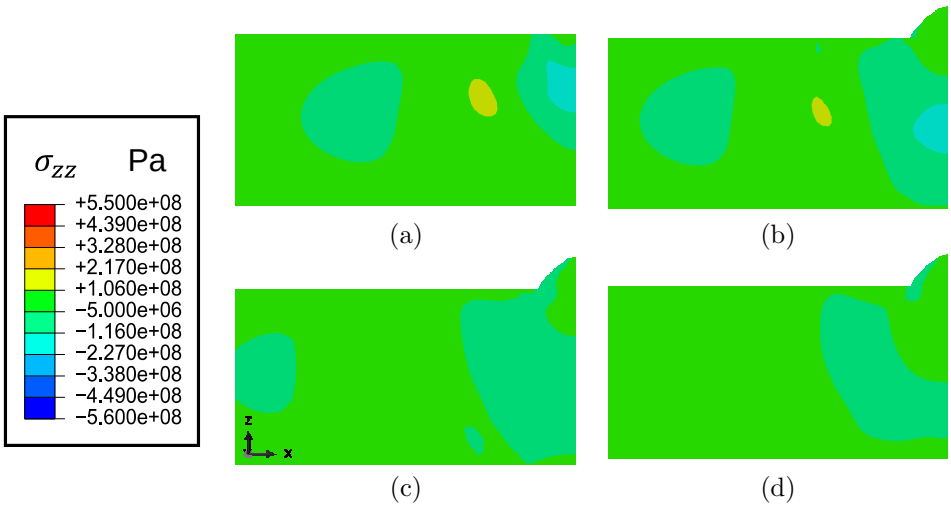

Figure 6.24: FE contour plots at y=60 mm showing the through thickness stress distribution for the normal stress component, σ_{zz}. (a) During the heating phase at t=8.25 s (b) At the peak temperature where t=8.95 s (c) During the cooling phase at t=12.15 s (d) Final residual stress field upon being fully cooled.

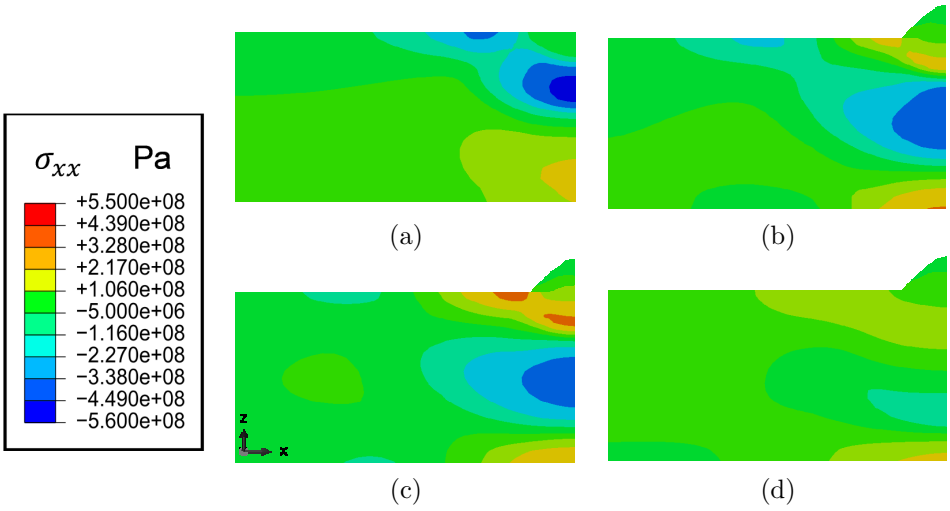

Figure 6.25: FE contour plots at y=90 mm showing the through thickness stress distribution for the transverse stress component, σ_{xx}. (a) During the heating phase at t=8.25 s (b) At the peak temperature where t=8.95 s (c) During the cooling phase at t=12.15 s (d) Final residual stress field upon being fully cooled.

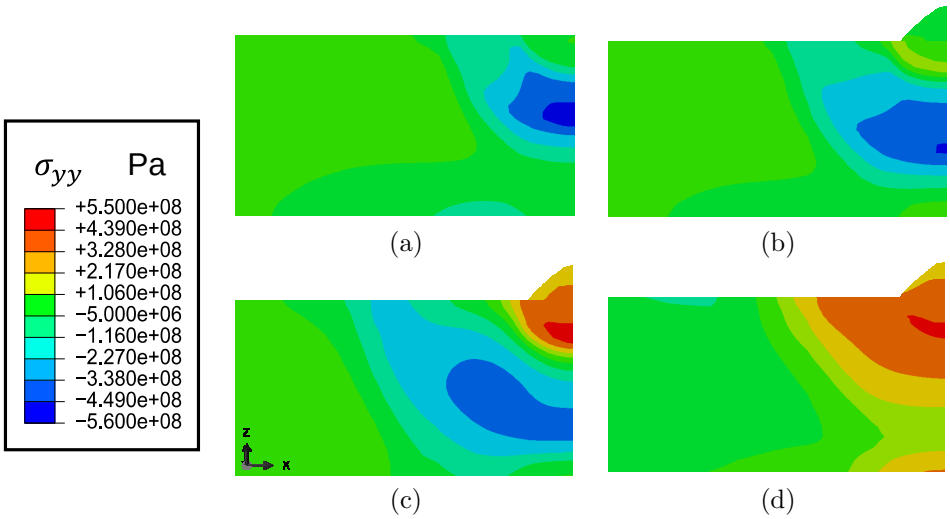

Figure 6.26: FE contour plots at y=90 mm showing the through thickness stress distribution for the longitudinal stress component, σ_{yy}. (a) During the heating phase at t=8.25 s (b) At the peak temperature where t=8.95 s (c) During the cooling phase at t=12.15 s (d) Final residual stress field upon being fully cooled.

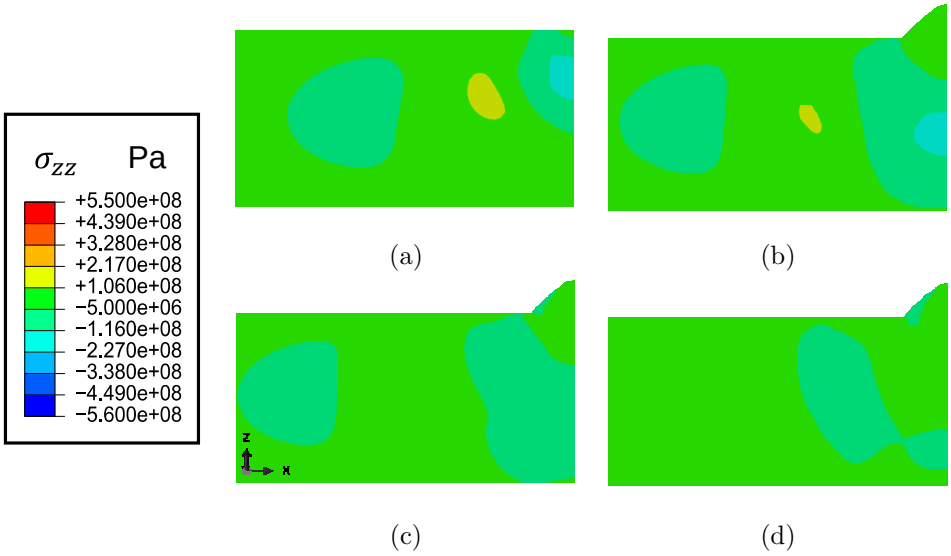

Figure 6.27: FE contour plots at y=90 mm showing the through thickness stress distribution for the normal stress component, σ_{zz}. (a) During the heating phase at t=8.25 s (b) At the peak temperature where t=8.95 s (c) During the cooling phase at t=12.15 s (d) Final residual stress field upon being fully cooled.

To validate the mechanical analysis, a comparison between residual stress predictions and ND measurements was completed for all three horizontal line scans. Figure 6.28 shows the two data sets for the longitudinal, transverse and normal stress directions. A good agreement between the experimental and predicted data sets was achieved for all three stress components. The majority of predicted stress values fall within the experimental error showing a high degree of confidence in the results. Due to the variation in the laser power, a higher magnitude longitudinal stress was present in the high laser power region compared to the low power region; therefore following the expected trend. The transverse stress component in the track vicinity was of equal magnitude at all three locations, exhibiting a tensile stress state. At the location of y=30 mm and 60 mm, a sharp stress gradient was present in the vicinity of the track for the transverse stress component. In this location, a compressive stress was observed; however, this was not present for y=90 mm as the transverse stress profile remained tensile for the entire width.

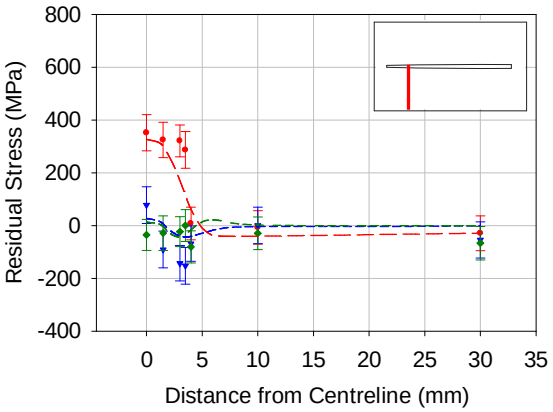

(a)

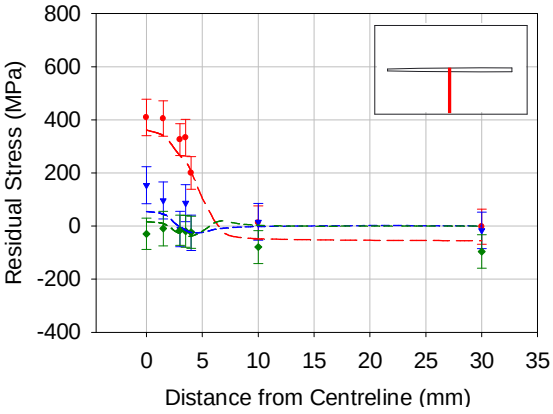

(b)

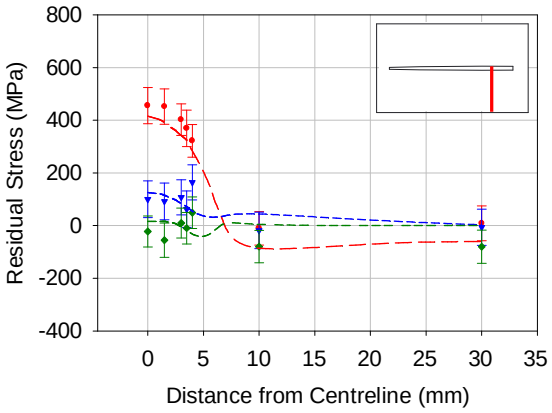

(c)

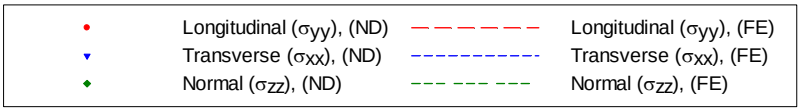

Figure 6.28: Comparison of experimentally measured and numerically predicted tri-axial residual stresses at 2 mm below the surface for each line scan position (a) y=30 mm (b) y=60 mm (c) y=90 mm.

The normal stress followed the same trend as the transverse component at each horizontal location. The largest error occurred below the track at y=30 mm, for the transverse stress, as a greater magnitude was measured than predicted at x= 3 mm and 3.5 mm.

6.5 Discussion

The work conducted in this chapter presents a novel modelling strategy, allowing in-situ process parameter control within DED to be modelled, by encompassing the key physics and parameters of the process. The modelling strategy can be utilised to conduct parametric investigations to determine the effects of the process parameters on the resultant temperature and residual stress fields. Through the use of the modelling strategy presented here, tailored repair strategies can be devised and implemented for the repair of components utilising DED.

6.5.1 Track Profile Prediction

The evolution of the track profile was predicted using a numerical method and compared to experimental measurements. A good agreement was attained between the predicted and experimental shape of the track profile at all of the locations. As the shape of the profile was governed by the powder distribution, an accurate representation of this variable was achieved. The maximum error for the track profile shape was 7.9% this was due to the formation of an asymmetric bead profile. This was not captured by the model as the fluid flow upon solidification was not included. Through increasing the laser power by a scale factor of 2, the track height increased by 58.7%; therefore, a directly proportional relationship was not observed. A maximum error of 6.5% was determined between the predicted an experimental track height. As the track height was predominantly governed by the powder catchment efficiency, the low error validates the method

by which this parameters was derived. Therefore, the error in the predicted height maybe because some powder particles did not reach the melt pool, as they could be melted in flight and/or be deflected from the substrate due to the high velocity carrier gas. Overall a higher percentage error was determined between the predicted and experimental track width. As this was governed by the maximum melt pool width, the assumption that the absorptivity was temperature independent may have caused this error as this would determine the peak heat flux entering the domain. For the track profile model, temperature independent material properties were used to implement the analytical expressions. The reason for this was to enable a more efficient solution to the analytical equations [25]; however, this simplification may cause the discrepancies observed between the predicted and experimental track profile. To assess the validity of this assumption, track profiles were derived for the steady-state regions, defining the material properties for temperatures greater than 630°C. Across this range of material properties, the maximum error associated with the track height equated 1.4%. Therefore, using temperature independent properties has a negligible effect on the derived bead geometry, validating the assumption. It should be noted that the convective and radiative losses were neglected from this section of the model. Therefore, the predicted thermal energy within the domain was overestimated and in turn will result in an overestimate of the melt pool geometry. Therefore, this could lead to the discrepancies observed between the predicted and experimental track profiles. The difference in the shape of the profile maybe due to the limitations of the analytical model as outlined in Section 3.2.3. As the Gaussian distribution has a sharp gradient from the rounded top, more circular track geometries similar to the one presented in Figure 6.17(a) are unachievable using this method. It should also be noted that, from the substrate deforming, the laser spot size will change; therefore, it cannot be assumed that the Gaussian radius was constant throughout. As the melt pool width was also dependent upon the power loss

history, derived from the mass-enthalpy balance, the analytical approximation of the power loss may have been underestimated. This may result in the overestimate between the predicted and experimental melt pool size observed in Figure 6.17.

6.5.2 Thermal History and Melt Pool Profile

The experimental and numerical predictions of the thermal histories correlated well with one another. The heating and cooling phases were captured by the FE model with accuracy, with slight discrepancies in the thermal gradient before the heat source pass. An overestimate in the peak temperature values for all thermocouples was observed, this was due to the method in which ABAQUS applies the heat source model to the FE domain [149]. It appears that the cooling rate at each horizontal location changes, which may arise due to the in-situ deformation of the substrate, reducing the contact area between the substrate and the CNC bed. It should be noted that the thermocouple was mounted to the substrate manually and from the FE model, a 0.2 mm position change gave rise to a 9% difference in the temperature.

To further validate the FE heat source, a comparison of the predicted fusion zone and the one derived from the experimental micrograph was conducted. The overall predicted shape of the fusion zone agreed well with the experimental micrograph, with an increase in penetration depth observed with an increase in laser power. The width of the fusion zone was predicted accurately; however, the predicted penetration depth was underestimated for the low power and transient regions. A possible reason for why this inaccuracy was present within the model maybe due to the melt pool and track width not being coherent. This could be due to an overestimate in the predicted track geometry for the aforementioned reasons. Another cause maybe due to the assumption that the absorptivity was constant and assumed to be temperature independent throughout the analysis.

6.5.3 Residual Stress Predictions

Through the use of ND measurements, the mechanical aspects of the FE model were validated. Overall, the residual stress profiles for the experimental and predicted data sets correlated well for all three stress components at each horizontal line scan. At each line scan location, the trends of the tri-axial residual stresses were captured well by the FE model. Almost all of the predicted residual stress values fell within the confidence limits of the experimental measurements; however, the greatest error occurred within the vicinity of the track. This maybe due to the limitations of the modelling approach, which could include neglecting the phase transformation and subsequent material property variation in the analysis. Limited variation was present during the evolution of stress within the melt pool region and in the final residual stress state of the component. The transverse stress component differed at each horizontal location, with the stress direction at y=90 mm being entirely tensile, as the increased cooling rate in this region did not allow a redistribution of stress to occur. At y= 30 mm and 60 mm a sharp stress gradient was present in the vicinity of the track, as the reduced cooling rate allowed the track material to contract and exhibit a compressive stress at the substrate surface. At each horizontal line scan location, an increase in magnitude of the longitudinal stress component was observed, with this being captured well by the FE model; however, a greater increase was determined from the experimental measurements. This may have arisen due to the underestimate in the penetration depth from the thermal FE model, resulting in a smaller volume of material contracting upon cooling. Another potential reason for this error may be due to neglecting the restraining bolts from the FE model, as this would alter the evolution of stress within the substrate. Including this effect within the FE model would inherently increase its complexity and simulation time. Other reasons for the discrepancies observed between residual stresses obtained from the ND measurements and FE model could include; experimental positioning errors,

microstructure evolution within the substrate and the variation in measurement temperature. To ensure that a reliable stress measurement was derived from the ND measurements, the location at which the ND measurement was taken in the region of interest and within the strain free reference sample had to be identical. As these measurements were not taken utilising the same datum reference, a positioning error could be introduced, leading to an incoherent comparison between the two data sets. At the location of y=30 mm and y=90 mm, a positioning error at x=3 and 3.5 mm was believed to be the reason for the large difference observed between the predicted and experimental residual stress. As the substrate will deform during the deposition process, the camber and butterfly distortion should be considered and accounted for whilst creating the datum for the ND measurements. This was not completed for this experiment and could have led to the error observed between the two data sets.

Due to the evolution of the track geometry and the variation in laser power, microstructure variation could be present at each horizontal line scan. The strain free reference sample was extracted from the location where P=1800 W. In this region, the highest peak melt pool temperature was present (2598°C), allowing sufficient time for the diffusion of the strengthening precipitates, γ" (Ni_3Nb) and γ" (Ni_3Al) [195], to take place. This occured due to the peak temperature in the melt pool exceeding the optimum temperature (1150°) [73] for the precipitates to enter solution, therefore resulting in crystallographic mismatch. This, in turn, gives rise to varying magnitudes of intergranular strain in the vicinity of the HAZ, at the position of each horizontal line scan. From analysing the location where the thermal field equated the recrystallisation temperature (1020°C) of IN718 [195], the approximate width and depth of the HAZ was 1.6 x 0.75 mm^2 and 2 x 1.25 mm^2 for P=900 W and P=1800 W respectively (Figure 6.29). In the high-power region, the gauge volume included a greater volume of the HAZ compared to the low-power region, leading to an incoherent comparison between the strain-free

lattice spacing and the region of interest. This was true for the horizontal line scan at y=30 mm and y=60 mm, as the variation of intergranular strain was not accounted for utilising one d_0 specimen.

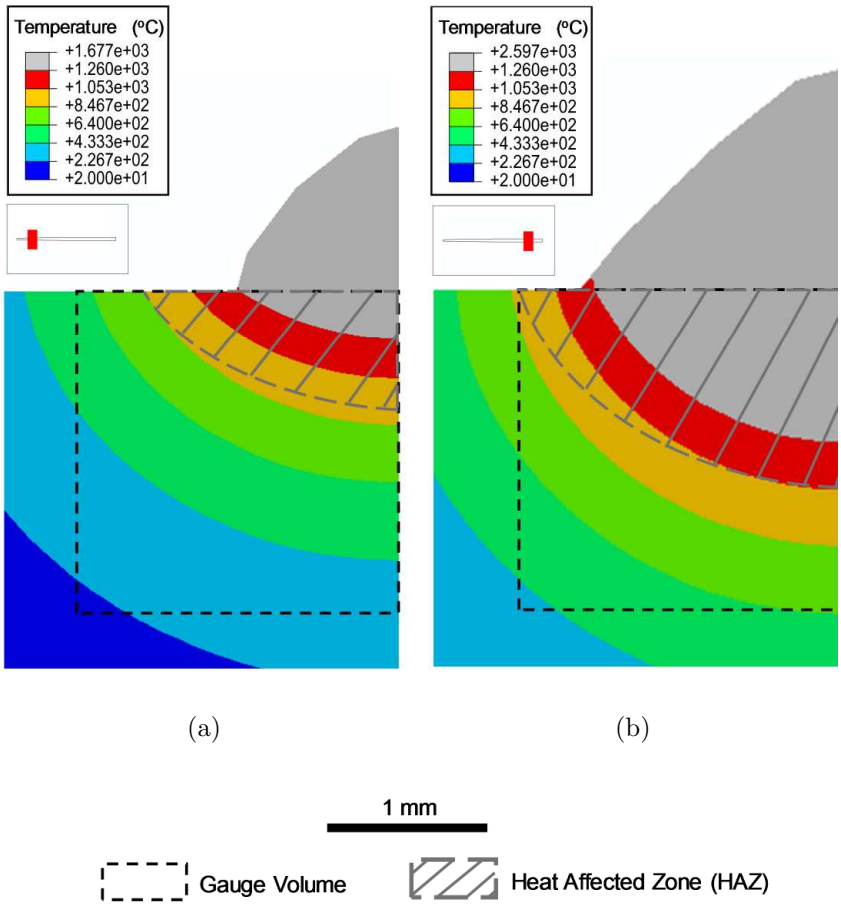

Figure 6.29: Schematic of the estimated HAZ and the ND gauge volume for (a) y=30 mm and (b) y=90 mm.

As the macrostress was of interest, a shift in this variable will be present, as the difference between the lattice spacing before cutting of the d_0 specimen, and the reference spacing measured for the same region was no longer proportional to the macrostress [26]. Therefore, to reduce the error obtained in the experimental residual stress profiles, a strain free reference specimen should be utilised at each horizontal line scan location. Finally, the ND measurements were not completed at constant ambient conditions and would cause thermally induced intergranular

strains, due to anisotropic thermal expansion [26]. As the measurements were completed over a 24 hour period, a significant change in lattice spacing would therefore occur.

From this work, it is confirmed that high magnitude residual stresses are present within DED manufactured components; therefore, methods to control the evolution of these stresses in DED parts will need more attention in order to extend the service life of components repaired using this technology. From this study, a variation in the laser power does not considerably alter the evolution of residual stresses as there was minimal variation in the trend and magnitude at each line scan location. As the cooling rates for the process were high, it is believed that controlling this phenomenon before or after the deposition would help to reduce high magnitude residual stress formation.

6.6 Conclusions

- The modelling strategy presented here could aid in devising an optimum set of process parameters to ensure a geometrically accurate build was attained and to assess the combination of process parameters which could control the cooling rate and the evolution of stress within the repaired component.

- The presented model allowed deposition tracks with varying cross sections to be predicted; therefore, an optimum tool path could be determined to ensure a more efficient use of the deposition material by only refilling the damaged area of the component. As a more tailored repair solution could be determined using the proposed tool, a reduction in the secondary processing of the repaired component may be apparent, which is advantageous for reducing repair costs.

- The developed method could allow for bespoke repair strategies to be designed, without the need for lengthy and costly experimental trials. Com-

plex parametric studies could be conducted using the presented methodology; therefore, an assessment of the proposed repair strategy on the distortion and residual stress formation within the repaired component could be completed.

- The validated case presented in this study agreed well with the experimental data showing confidence in the modelling strategy. The maximum track height and width were predicted with a maximum error of 6.5% and 7.62% respectively. The peak temperatures and residual stresses were underestimated with an error of 6.2% and 11.4% respectively.

- Minimal variation was observed in the trend for the stress evolution and the final residual stress state at each horizontal location. The longitudinal stress increased with laser power, with negligible deviation in the other two stress components. A plane stress condition was not observed due to the interaction of the track geometry and the substrate at the interface between them.

- High magnitude residual stresses were present in the deposit with a minimal reduction being observed through controlling the laser power. As these types of stresses will reduce the life of the component, further study should be conducted to determine methods that adaptively control the evolution of high magnitude stresses

Chapter 7

Numerical-Analytical Modelling of Multi-Track Deposition

7.1 Introduction

To repair the components structure using Direct Energy Deposition (DED), a number of tracks are deposited at a prescribed overlap ratio (OR), this process is repeated until the section of geometry that needs repairing has been refilled. A number of different approaches exist within the literature to predict the geometry of the overlap region; however, they are predominantly based on an empirical fit to an experimentally measured track geometry. A number of common tool paths exist for depositing multiple tracks, with the spiral and zig-zag pattern being the most common. A prediction of the deposition geometry in the overlap region is important to ensure that subsequent layers contain minimal porosity as this will act as an initial void for crack initiation. The combination of process parameters, tool path and overlap ratio that can be used will inherently affect the geometry of the build, the thermal history cycles and the residual stress fields; therefore, a general modelling approach was required which includes these phenomena.

7.2 Multi-Track Geometry Prediction

A numerical-analytical approach was used to determine the geometry of a multi-track deposition using two common deposition strategies, which included the spiral and zig-zag strategy. A schematic of the two strategies is presented in Figure 7.1.

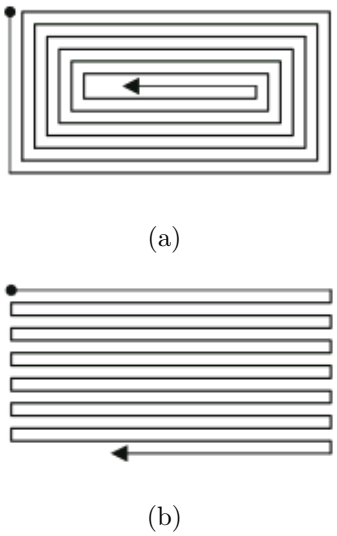

Figure 7.1: A schematic of two common DED tool paths. (a) Spiral strategy (b) Zig-zag strategy.

The process parameters, deposition strategy and the part geometry are all provided as a manual input to the model, with the remaining steps being automated. A two-dimensional (2D) thermal Finite Element (FE) model was used to determine the transient thermal field of the multi-track deposition process. The FE mesh was periodically updated to include subsequent depositions to allow a more accurate distribution of the heat flux to be included. The melt pool boundary was determined from the numerical thermal field, with the subsequent power losses being determined to ensure a stable mass/enthalpy balance was achieved. Upon prediction of the first track profile, the overlap geometry, based on a modified fillet model presented by Suryakumar *et al.* [128], was used. Depending on the deposition strategy, a modification to the track height was required to account for the flow of molten material when filling between two previously deposited tracks.

When the total number of prescribed track profiles were completed, the process was terminated and the profiles were concatenated to be used for subsequent analyses.

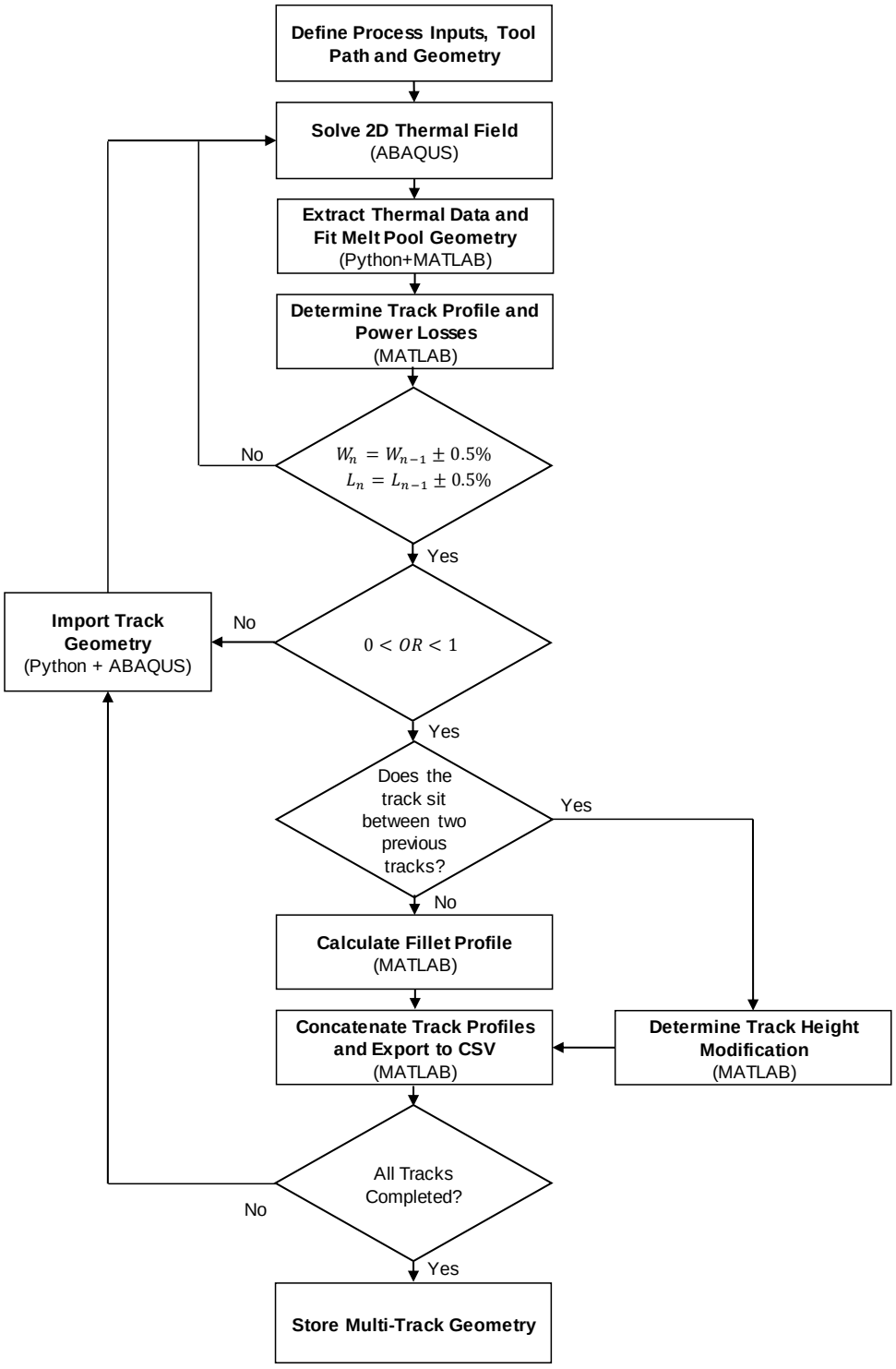

Figure 7.2: A flowchart of the process used to determine the geometry of a multi-track deposition.

7.2.1 2D Thermal Model

Due to the inclusion of a previously deposited track, the thermal field could no longer be predicted using the Cline and Anthony distribution [37] as outlined in Section 3.2.2. The main reason for this was because the distribution of the heat flux was now asymmetric on an inclined planar section, i.e the previous track surface. Previously, the Cline and Anthony [37] distribution gave efficient predictions for the single track thermal field, a similar method was required for this application; therefore, a 2D thermal FE model was used to reduce the computational deficit of the approach. The governing heat transfer equation (Equation 3.17) was solved, with the external heat flux applied using the Gaussian disc heat source model. The heat source model in Equation 3.21 was modified to include the track OR and to be used in a 2D analysis. The heat source model had the following form:

$$Q = \frac{\eta P}{\pi r_0^2} exp\left[-\frac{(x - x_{off})^2 + (y - y_0)^2}{r_0^2}\right] \tag{7.1}$$

where y_0 is the initial centre position of the heat flux distribution and x_{off} is the centre distance between the previous and subsequent track which had the following form:

$$x_{off} = W\left(1 - \frac{OR}{100}\right) \tag{7.2}$$

where the OR was expressed as a percentage. For this model, the Gaussian radius equated the measured spot radius of the laser (1.5 mm) and the process efficiency equated 0.3. To be consistent with the analytical track prediction model, presented by Ahsan *et al.* [25], no conductive or radiative losses were included in the FE model. For each deposition, two analysis steps were defined within ABAQUS. The total time for each step was equal to the time required to complete half of the deposition. After a track profile was predicted, it was included in the FE mesh by reactivating the track profile as outlined in Section 3.3.4. For each deposition, this was completed after the first analysis step, with the subsequent step com-

pleting the heat source pass for the current deposit. This methodology ensured that a more accurate representation of the thermal field was achieved, through the inclusion of the entire tool path within the FE model.

A schematic of a typical FE mesh used for the 2D thermal model is presented in Figure.7.3. The mesh consisted of a combination of hexahedral and tetrahedral elements for the substrate and the deposits respectively. The reason for using both element types was due to the positioning of the nodes at the interface between the tracks and substrate. If the nodal coordinates were not identical, then convergence of the model did not occur as the flow of heat flux across the interface could not be modelled correctly. Through development of the automated process, it was determined that no mesh partitioning strategy could be used across all of the potential overlap ratios to ensure the nodal coordinates were identical. Therefore, the use of tetrahedral elements in this region, in conjunction with mesh seeding rules, allowed flexibility in the mesh design when automating this step. The mesh seeding constraints for the entire FE domain are shown in Section 5.2.2 and were identical for each deposition strategy. The through thickness and track interface element size was equal to the size determined in Figure 5.3 due to utilising the same operating conditions. The seed constraints at the track interface were fixed to ensure that the nodal positions were identical at this location. Along the external surface of the track, a free seeding constraint was used. This ensured that the mesh was not over constrained, allowing an automated mesh to be generated. To reduce the computational time for the model, mesh biasing rules were used to double the element size far field from the deposit. To allow the heat flux to flow between the substrate and the deposited tracks, a tie constraint was required at this location. As each subsequent track was included within the model, tie constraints were added between each track interface when required.

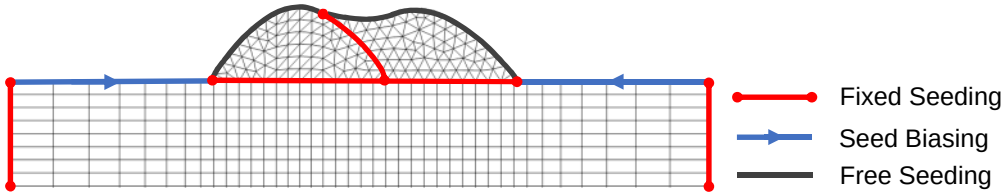

Figure 7.3: An example of the 2D FE mesh used for the multi-track model with the seeding constraints highlighted for each geometrical section.

Due to the evolution of the FE domain through inclusion of each deposited track, the definition of the heat flux distribution had to be updated periodically. An example of the heat flux surface definition for a three track deposition is presented in Figure 7.4.

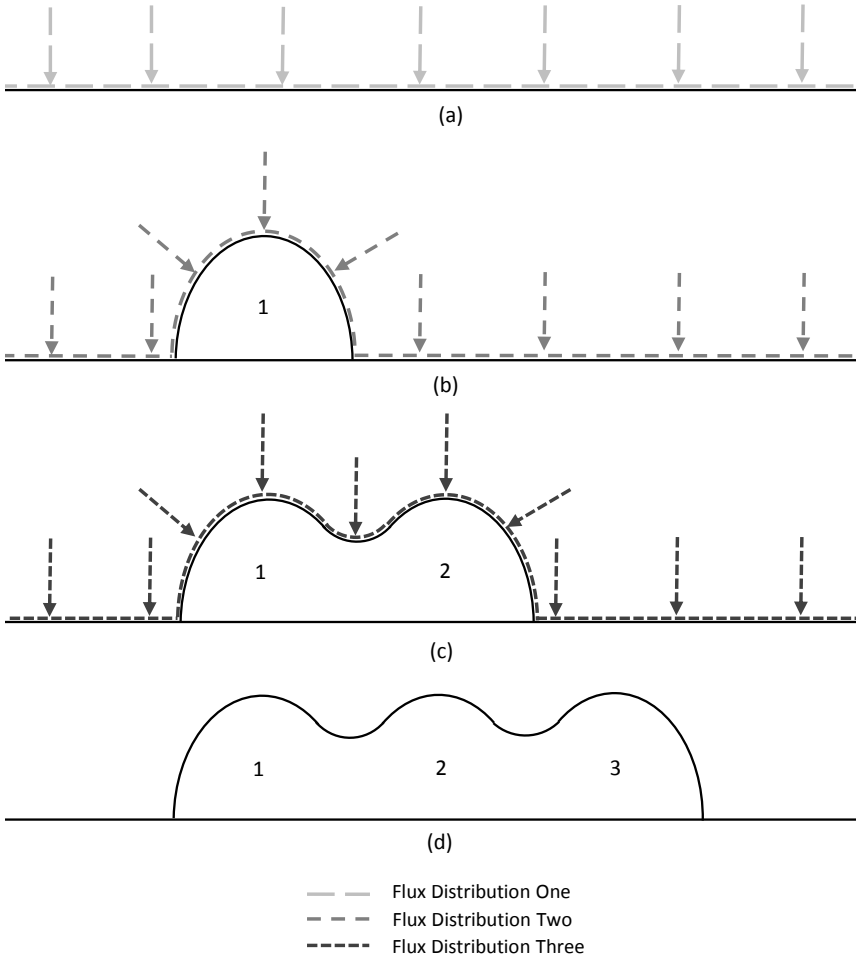

Figure 7.4: A schematic of the heat flux distribution for a three track deposition using the zig-zag strategy. (a) Initial heat source pass. (b) Heat flux definition after a single track deposition. (c) Heat flux definition after a double track deposition. (d) Final geometry for a three track deposition.

For the initial heat source pass, the heat flux distribution was defined across the entire width of the substrate surface. For subsequent analysis steps, when a track has been reactivated, the heat flux was defined across all of the upper free surfaces of the domain. This process was identical for each deposition strategy and can be repeated until the total number of tracks were predicted. It should be noted that after the first analysis step has been completed for the current deposition, the previous heat flux definition was deactivated to ensure that a superposition of heat flux did not occur within the model.

7.2.2 Melt Pool Geometry Prediction

The melt pool geometry was derived from the nodal temperatures from the surface of the substrate and the previously deposited track profile. Previously, the melt pool geometry could be approximated as a symmetric ellipse (Section 3.2.2); however, as the thermal distribution was no longer symmetric, this assumption was not valid. Ahsan *et al.* [124] presented a method to predict the melt pool geometry for overlapping tracks based on the thermal field determined from the Cline and Anthony distribution [37]. It was assumed that the melt pool was unaltered on the substrate surface and could be modelled as a half ellipse. For the inclined region, the melt pool was modelled as a triangular section, which was predicted based on the OR only; therefore not encompassing any geometrical features of the track or the physics of the process.

The nodal coordinates at the location where $T = T_m$ were extracted from the 2D FE thermal model at each corresponding integration time step. A schematic of the multi-track melt pool geometry is provided in Figure 7.5.

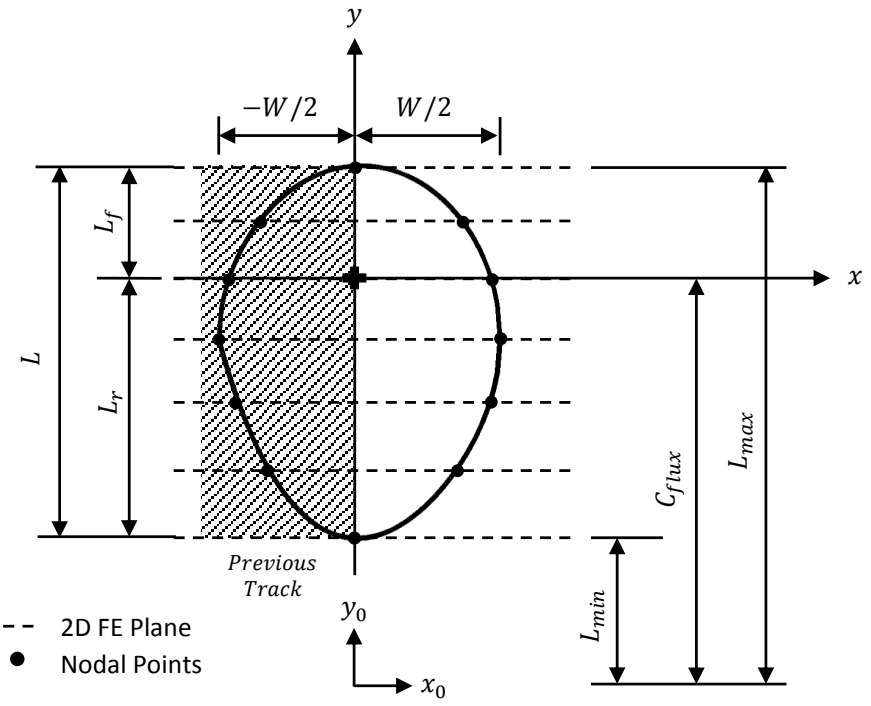

Figure 7.5: A schematic of the multi-track melt pool geometry and the associated coordinate systems and geometrical parameters.

The coordinates of the melt pool geometry can be described as follows:

$$T\left(\pm\frac{W}{2}, 0, 0\right) = T_m$$
$$L = V\sum_{i=1}^{N} t_i \tag{7.3}$$

where N is the number of 2D planes for which $T \geq T_m$, t_i is the integration time step, L is the melt pool length and L_e is the element length moved in one time step. The front and rear length of the melt pool were determined as:

$$L_f = L_{max} - (C_{flux} - L_{min})$$
$$L_r = C_{flux} - L_{min} \tag{7.4}$$

where L_{max} and L_{min} are the maximum and minimum length of the melt pool and C_{flux} is the centre of the heat flux distribution. A function based on an unsymmetrical ellipse was used to define the front and rear boundaries of the

melt pool geometry. To complete the geometrical fit, the coordinates of the melt pool were transformed so that the position of $(-W/2, C_{flux})$ was now located at the position $(0, 0)$. The front (y_f^n) and rear (y_r^n) boundaries of the melt pool were defined as follows:

$$\begin{aligned} y_f^n &= \frac{\sqrt{(W-b) - 2x + \sqrt{4bx + (W-b)^2}}}{\sqrt{2}} \sqrt{x}\,(d - \Upsilon x) \\ y_r^n &= -\frac{\sqrt{(W-b) - 2x + \sqrt{4bx + (W-b)^2}}}{\sqrt{2}} \sqrt{x}\,(d - \Upsilon x) \end{aligned} \tag{7.5}$$

where W is the width of the melt pool, x is the Cartesian coordinate, b and d are geometrical fitting parameters and Υ is a skewness factor. Each of these variables were determined using a non-linear regression fit, completed using the inbuilt MATLAB function *nlinfit*, utilising the default function settings. The initial guess for the geometrical parameters and the skewness factor was equal to the length of the melt pool (L) and zero respectively. To allow the track profile to be predicted, the coordinates were transformed so that $C_{flux} = 0$.

To determine the track profile based on the melt pool geometry, a Gaussian powder distribution was integrated across the melt pool limits. For the nth track, the equation had the following form:

$$h_0^n(x) = \frac{\eta_c}{\rho V} \int_{y_r^n}^{y_f^n} \frac{2\dot{m}}{\pi r_p^2} exp\left[-2\frac{\left(x \pm x_{off}^n\right)^2 + y^2}{r_p^2}\right] dy \tag{7.6}$$

where η_c is the powder catchment efficiency, ρ is the material density, V is the traverse velocity, $\dot{m}$ is the powder mass flow rate, r_p is the Gaussian feed radius and x, y are the Cartesian coordinates. Upon determining the unaltered track geometry for two subsequent deposits, the geometry of the overlap region could be determined.

7.2.3 Overlap Geometry Prediction

To ensure that the geometry of the multi-track depositions could be presented with accuracy, the geometry within the overlap region was modelled based on an analytical model presented by Suryakumar *et al.* [128]. Unlike Ahsan *et al.* [25] and Ding *et al.* [127], this model was chosen as it correctly represents the geoemtry in the region of the overlap, as observed in the experimentally collected track profiles (Figure 7.6). A schematic of the overlap region and the corresponding variables used to define this region is presented in Figure 7.7. For the model presented by Suryakumar *et al.* [128] it was assumed that all of the deposited tracks have identical geometry and can be defined as a second-order parabola. The variables of the equation were defined from experimental measurements of the initial track width and depth. To neglect the experimental measurement of the track profiles, which would reduce the effectiveness of the approach, the physics of the DED process were included by combining the analytical model presented by Ahsan *et al.* [25] and Suryakumar *et al.* [128]. It should be noted that as the previous model assumed a constant track height for each deposition, with the inclusion of the thermal field, melt pool geometry and the prediction of the multi-track deposit, a constant track height may not be present; therefore, a modification of the fillet overlap model was required.



(a)



(b)

Figure 7.6: An example of the experimentally determined track profile for (a) Spiral deposition strategy and (b) Zig-zag deposition strategy.

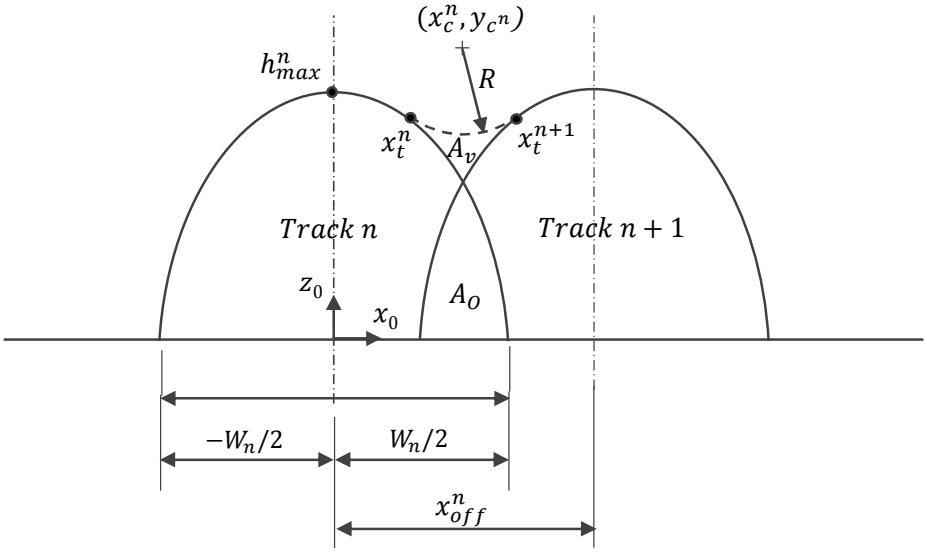

Figure 7.7: A schematic of two overlapped tracks and the geometrical parameters used to define the geometry.

The first step of the analytical model was to determine the radius of the fillet (R^n) and the tangential point to the track (x_t^n), for each deposit denoted n. A system of linear equations was determined to define the tangential point and the radius of the fillet, this was completed through equating the gradient of the fillet and the track profile at the tangential point, giving the following equation [128]:

$$\left(x_t^n - \frac{x_{off}}{2}\right) + \left(h_{max}^n - \frac{4h_{max}^n (x_t^n)^2}{W_n^2} - y_c^n\right)\left(-\frac{8h_{max}^n x_t^n}{W_n^2}\right) = 0 \tag{7.7}$$

Through equating the area of the valley (A_v) and the area of the overlap region (A_O), a second equation with the following form was defined [128]:

$$\frac{2x_t^n - x_{off}^n}{8}\sqrt{4(R^n)^2 - \left(2x_t^n - x_{off}^n\right)^2} + \frac{(R^n)^2}{2} sin^{-1}\left(\frac{2x_t^n - x_{off}^n}{2R^n}\right) - \frac{4h_{max}^n (x_t^n)^3}{3W_n^2} + \frac{y_c^n x_{off}^n}{2} - \frac{h_{max}^n W_n}{3} - y_c^n x_t^n + h_{max}^n x_t^n = 0 \tag{7.8}$$

To solve the system of equations (Equation 7.7 and 7.8), the non-linear regression algorithm *lsqnonlin* was implemented in MATLAB, which increased the computational efficiency of the model. When implementing the non-linear regression

solver, the initial guess, upper bound and lower bound for the algorithm, was selected from the criteria detailed by Suryakumar *et al.* [128]:

$$\begin{aligned} x_{initial} &= [0, 0] \\ x_{upper} &= \left[\frac{x_{off}}{2}, 100\right] \\ x_{lower} &= [0, 0] \end{aligned} \tag{7.9}$$

It should be noted that from solving the linear equations, the tangential points were determined for the original coordinate system (x_0, z_0), therefore the coordinates were transposed as follows:

$$x_t^n = x_{off}^n \pm x_t \tag{7.10}$$

where x_{off}^n is the current track offset from the original coordinate system and the $\pm$ operator was used depending if the start/end of the fillet section was to the left/right of the maximum track height (h_{max}).

A modification was made to the construction of the fillet to ensure that it was at a tangent between the current and previous deposition profile, when varying track heights were present. A schematic of the fillet overlap model is presented in Figure 7.8. The coordinates for the centre of the circle (x_c^n, y_c^n), which defined the fillet, was determined by finding the intersection point of the perpendicular bi-sectors (L_1 and L_2) of the chords *EF* and *FG*. The equations of the perpendicular bi-sectors had the following form:

$$\begin{aligned} L_1 : y_c^n - y_{EF}^{Mid} &= -\frac{1}{\left(\frac{dy}{dx}\right)_{EF}}\left(x_c^n - x_{EF}^{Mid}\right) \\ L_2 : y_c^n - y_{FG}^{Mid} &= -\frac{1}{\left(\frac{dy}{dx}\right)_{FG}}\left(x_c^n - x_{FG}^{Mid}\right) \end{aligned} \tag{7.11}$$

where the mid point of the lines *EF* and *FG* are calculated as:

$$\begin{aligned}(x_{EF}^{mid},\, y_{EF}^{mid}) &: \left(\frac{x_t^n + \frac{x_{off}^n}{2}}{2}, \frac{h_0^n\left(x_t^n\right) + R^n}{2}\right) \\ (x_{FG}^{mid},\, y_{FG}^{mid}) &: \left(\frac{\frac{x_{off}^n}{2} + x_t^{n+1}}{2}, \frac{R^n + h_0^{n+1}\left(x_t^{n+1}\right)}{2}\right)\end{aligned} \tag{7.12}$$

where the gradients of the lines *EF* and *FG* are equal to:

$$\begin{aligned}\left(\frac{dy}{dx}\right)_{EF} &= \frac{\frac{x_{off}^n}{2} - x_t^n}{R^n - h_0^n\left(x_t^n\right)} \\ \left(\frac{dy}{dx}\right)_{FG} &= \frac{x_t^{n+1} - \frac{x_{off}^n}{2}}{h_0^{n+1}\left(x_t^{n+1}\right) - R^n}\end{aligned} \tag{7.13}$$

The coordinates of the fillet radius were given by:

$$y_{fillet}\left(x\right) = \sqrt{R^n - \left(x - x_c^n\right)^2} + y_c^n \tag{7.14}$$

For two sequential tracks, n and $n+1$, which overlap, the track geometry was defined as follows:

$$\begin{aligned}h_0^n\left(x\right) \quad & for\, W_{min}^n \leq x \leq x_t^n \\ y_{fillet}\left(x\right) \quad & for\, x_t^n \leq x \leq x_t^{n+1} \\ h_0^{n+1}\left(x\right) \quad & for\, x_t^{n+1} \leq x \leq W_{max}^{n+1}\end{aligned} \tag{7.15}$$

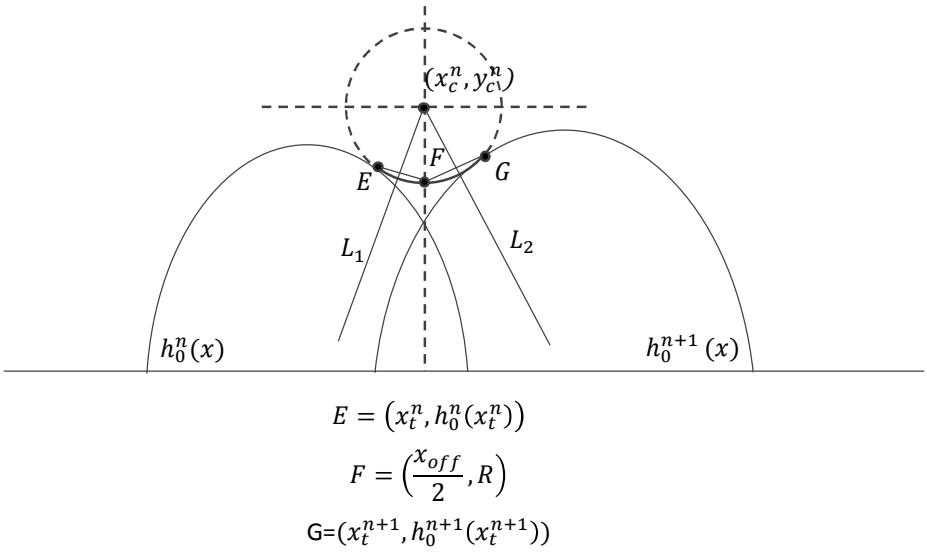

Figure 7.8: A schematic of the fillet overlap model denoted with the associated variables and geometrical features. The schematic is presented for two track profiles with the second track having a greater maximum height.

When predicting a track profile which was situated between two previous tracks, a modification to the model was required. Figure 7.9 depicts three studies used to determine how the final track height was modified for the spiral strategy, with the process parameters presented in Table 7.1.

Table 7.1: Process parameters used to investigate a modification to the final track height for the spiral deposition strategy.

Parameter	**Value**
Efficiency (η)	0.3
Power (W)	1800
Traverse Velocity (mm/min)	400
Catchment Efficiency (η_c)	0.5
Powder Feed Rate (g/s)	26
Overlap Ratio (%)	10
Spot Diameter (mm)	1.5

From Figure.7.9(a), the unaltered melt pool geometry is presented, which was used to determine the initial deposition geometry. The position of the melt pool geometry and the associated coordinate system was equivalent to the analytical

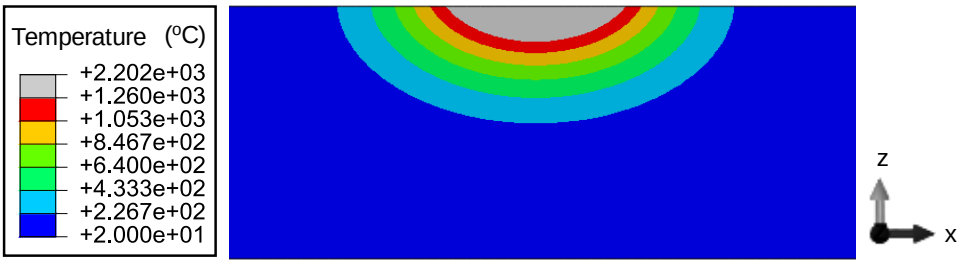

(a)

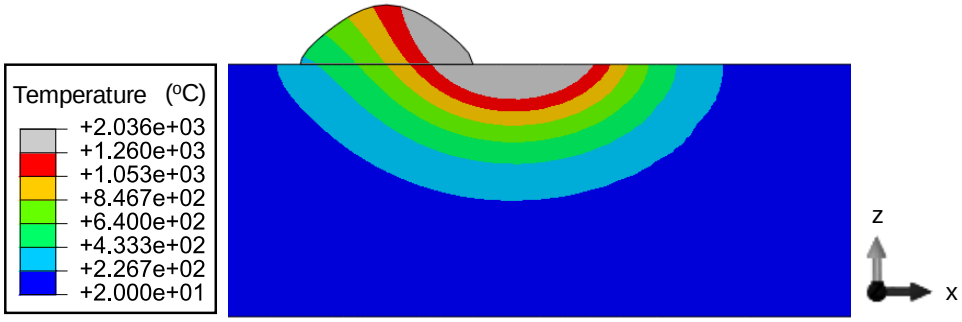

(b)

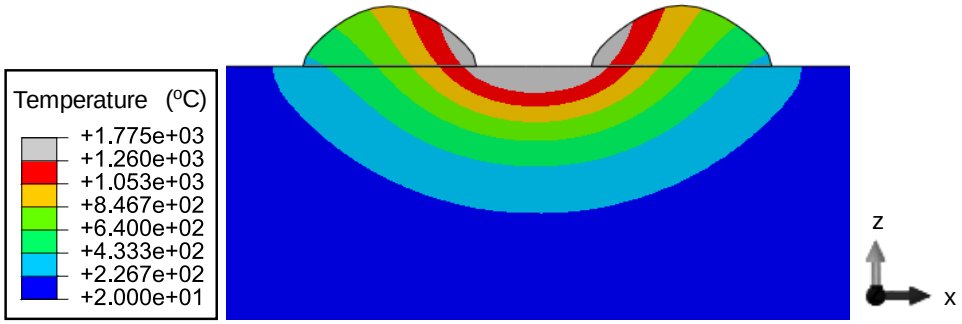

(c)

Figure 7.9: Results of a study depicting the through thickness melt pool geometry for (a) No previous deposition (b) Subsequent track using the zig-zag strategy (c) Final track using the spiral strategy.

track model presented by Ahsan *et al.* [124], therefore, the approach used in this study to analyse the interaction between the powder stream and melt pool geometry was also equivalent. A reference plane was therefore used to determine the region where the powder mass flux distribution could be integrated between the melt pool limits. For Figure 7.9(a), this plane was positioned on the top surface of the substrate, perpendicular to the traverse direction. It should be noted that the penetration depth of the melt pool was defined as the absolute distance between the reference plane and the maximum melt pool depth in the z-direction. For Figure 7.9(b), the zig-zag strategy was used to determine the melt pool geometry for a subsequent deposit. A re-melted region was now present within the model and due to the inclusion of a previous track, the peak temperatures were reduced; however, the penetration depth from Figure 7.9(a) and Figure 7.9(b) were identical. From this, it was assumed that the reference plane was still situated at the substrate surface and the re-melted region contributed to the formation of the concave region in the area of overlap. As the reference plane was still at the same location as the first case, the process of determining the unaltered track geometry remained the same as before. From Figure 7.9(c), the re-melted region has reduced in size, for the same OR, when using the spiral strategy in comparison to the zig-zag strategy. Although the process parameters were identical for all three cases, the penetration depth and peak temperature was reduced for the spiral case. As the DED process was operated at a fixed offset distance for the entire deposition, it was assumed that the positioning of the two tracks on the substrate surface presented in Figure 7.9(c) affect the position of the reference plane relative to the substrate surface. It was assumed that the reference plane for the final track had been transposed upwards by the difference between the penetration depth of the initial melt pool geometry (Figure 7.9(a)) and the final melt pool geometry (Figure 7.9(c)). The fillet geometry, determined between each track for the spiral strategy, was governed by the surface tension between the

new deposited material in the overlap region and the sharp inclination between the previous track and the modified central track. A schematic of the associated geometry and variables used to define this type of track is presented in Figure 7.10.

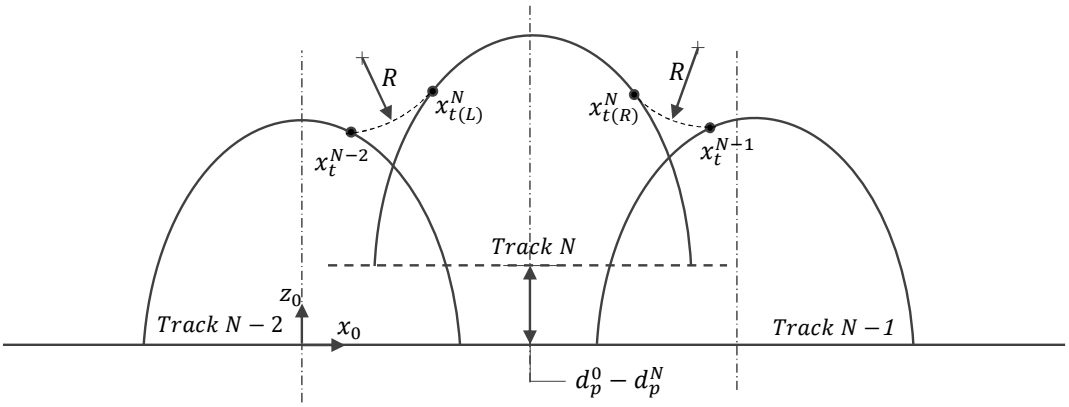

Figure 7.10: A schematic of a track positioned between two previous deposits and the associated parameters used to define the geometry.

The height of the central track was defined as follows:

$$h_0^n(x) = \left(d_p^0 - d_p^N\right) + \frac{\eta_c}{\rho V}\int_{y_r^n}^{y_f^n} q_{pf} dy \tag{7.16}$$

where d_p^0 is the initial unaltered penetration depth and d_p^N is the final penetration depth for the final track prediction. The fillet geometry was determined through solving Equation 7.3 and Equation 7.7-7.13 for the ante-penultimate $(N-2)$, penultimate $(N-1)$ and the final track (N). This gave three tangential points $(x_t^{n-2}, x_t^{n-1}\ and\ x_{t(L)}^N)$ with a fourth $(x_{t(R)}^N)$ being determined based on a reflection of the final tracks tangential point about its centreline as depicted in Figure 7.10. The final geometry for a track situated between two previous deposits was defined as follows:

$$\begin{aligned} &h_0^{N-2}(x) \quad for\ W_{min}^{N-2} \leq x \leq x_t^{N-2} \\ &y_{fillet}(x) \quad for\ x_t^{N-2} \leq x \leq x_{t(L)}^N \end{aligned} \tag{7.17}$$

$$h_0^N(x) \quad for\ x_{t(L)}^N \leq x \leq x_{t(R)}^N$$

$$y_{fillet}(x) \quad for\ x_{t(R)}^N \leq x \leq x_t^{N-1}$$

$$h_0^{N-1}(x) \quad for\ x_t^{N-1} \leq x \leq W_{max}^{N-1}$$

7.2.4 Validation of the Multi-Track Predictions

To validate the predictions of the multi-track depositions, a series of experimental trials were completed, utilising the laser deposition rig, as outlined in Section 3.4.1. A schematic of the experimental set up is presented in Figure 7.11.

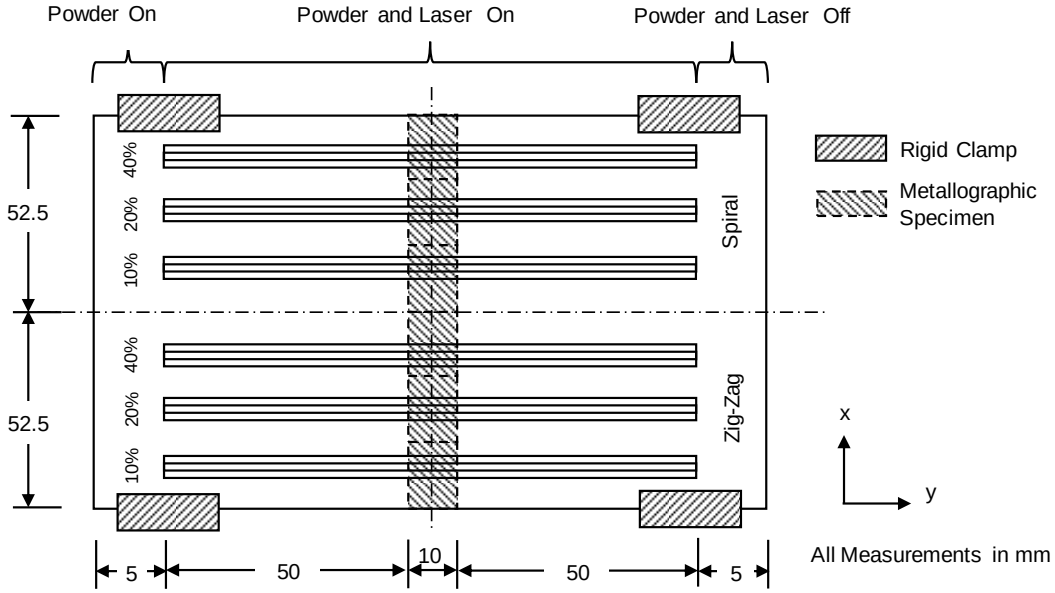

Figure 7.11: A schematic of the experimental set up which was used to obtain the metallographic specimens used to analyse the multi-track profile.

To validate the proposed model, two deposition strategies were implemented, for three different overlap ratios, using a constant set of process parameters, which are presented in Table 7.2.

Table 7.2: Process parameters used to fabricate the experimental specimens to validate the multi-track model.

Parameter	**Value**
Power (W)	1800
Traverse Speed (mm/min)	400
Powder Feed Rate (g/s)	26
Deposition Strategy	Zig-Zag and Spiral
Overlap Ratio (%)	10,20 and 40

A total of 24 tracks were deposited at a length of 110 mm. For each OR, a total of three tracks were used, these were then cooled in air to room temperature before subsequent deposits were completed. For both the zig-zag and spiral strategy, no dwell period was used between the deposition of each track. An offset distance of 5 mm between each three track cluster was utilised to ensure that no secondary heating effects altered the geometry of the previous depositions. The substrate (120 x 105 x 6 mm) was clamped to the CNC table to ensure that the in-situ deformations did not alter the geometry of the deposited tracks. It should be noted that to ensure a track was instantaneously formed at $y = 5$ mm, the power was switched on prior to the laser as shown in Figure 7.11. Upon completing all of the required depositions, and when the sample was at room temperature, the rigid clamps were all removed at the same time, this was completed to ensure that a constant stress relaxation rate was exhibited throughout the entire specimen. To determine the multi-track geometry profile, six metallographic specimens (10 x 15 mm) were removed from the specimen as shown in Figure 7.11. The metallographic specimens were prepared for examination using the method outlined in Section 3.4.3, with the track profile being determined from the specimens using the method outlined in Section 3.4.4.

7.3 Thermo-mechanical Modelling of Multiple Deposits

A multi-track deposition model was developed using the sequentially coupled thermo-mechanical approach, as outlined in Section 3.3.1. A baseline model was produced and validated to allow an investigation into how the OR and deposition strategy affect the thermal and mechanical fields of the process. Two common deposition strategies were implemented for each model which included the spiral and zig-zag strategy. Three adjacent tracks were modelled with a track offset equating 3 mm, this was completed to reduce potential error in the validation of the mechanical field, as outlined in Section 7.3.1. As no overlap between the tracks were present, the track profile was predicted using the method outlined in Section 3.2.3. For both deposition strategies, the total track length was 110 mm, with the laser power (P) and traverse velocity (V) equating 1800 W and 400 mm/min respectively.

Due to the thermal field being potentially asymmetric, a full 3D analysis was required with the entire domain. The geometry of the track profile, at the location where the heat source was changing direction, was not modelled; however, the heat source did follow the full tool path defined by the deposition strategy. Two element widths were reactivated per time step to fill the melt pool volume as outlined in Section 3.3.4. A tie constraint was used between the substrate surface and the track profile. The external heat flux was applied to the domain using the ABAQUS user subroutine *DFLUX*. A surface heat flux was defined for each track as a thermal load, this was required so that after each track was reactivated, the associated thermal load was deactivated to stop the superposition of the heat flux within the model. The disc heat source model was used with the Gaussian radius and process efficiency being defined as 1.5 mm and 0.3 respectively. Convective and radiative losses were applied as outlined in Section 3.3.1. Temperature de-

pendant material properties for Inconel 718 (IN718) were used for both analyses as shown in Section 3.3.2.

The mesh design used for both deposition strategies is presented in Figure 7.12. The optimum element size was determined based on the mesh sensitivity study conducted in Section 5.2.2. This was valid as both the process and modelling parameters were identical, therefore the same melt pool geometry and thermal history profile would have been predicted. The element volume directly below each track was therefore equal to 0.25 x 0.25 x 0.25 mm^3. With the use of mesh biasing, the element size in the Heat Affected Zone (HAZ) equated 0.5 x 0.5 x 0.5 mm^3 which was increased to 2 x 0.5 x 0.5 mm^3 at the extremity of the substrate. The mesh for the substrate was symmetrical about the central track centreline, and cuboidal elements were used throughout to allow a consistent comparison between the residual stress predictions and the experimental data. For each track profile, the same element length in the traverse direction was used with the cross sectional profile being meshed with an element size less than or equal to 0.25 x 0.25 x 0.25 mm^3. For the thermal and mechanical model, DC3D8 linear brick elements and C3D8R linear brick elements were used respectively. Linear elements were used as no significant advantage in using higher order elements has been observed for residual stress predictions in welding. The total number of elements and nodes were equal to 655,776 and 698,389 respectively.

The same mesh as shown in Figure 7.12 was used for both the thermal and mechanical models. Material addition was included in the mechanical model, using the same method as the thermal model. The mechanical boundary conditions applied to the FE domain are outlined in Section 3.3.1.

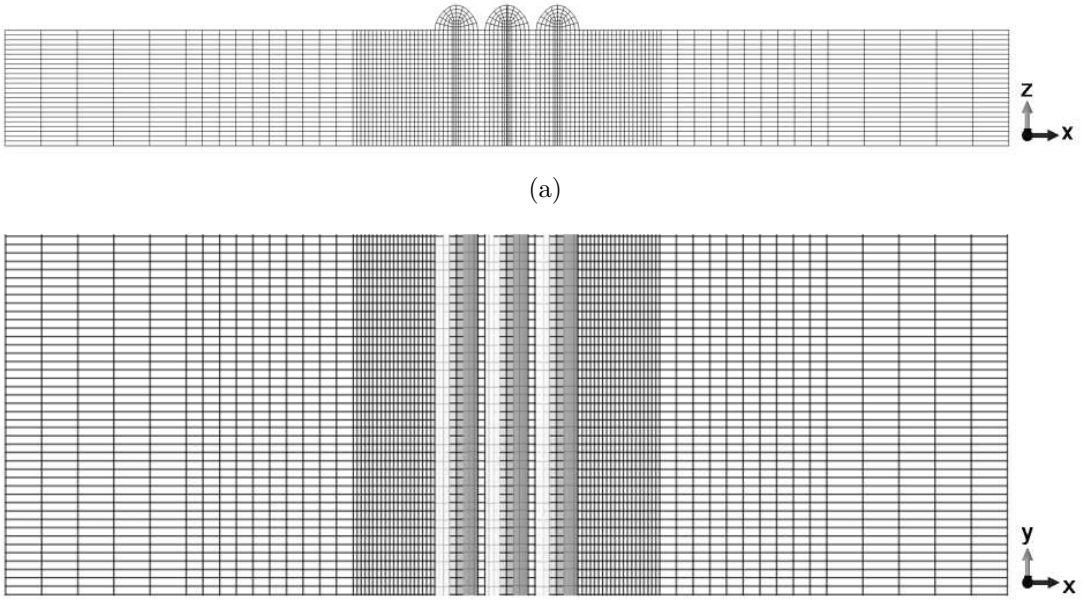

Figure 7.12: Mesh design used for the multi-track thermo-mechanical models for both the spiral and zig-zag deposition strategy. (a) x-z cross sectional planar view and (b) y-x cross sectional planar view.

7.3.1 Validation of the Multi-Track Thermo-Mechanical model

To validate the multi-track thermo-mechanical model, a combination of themocouple and Neutron Diffraction (ND) measurements were used. Two IN718 substrates were used with a total of three adjacent tracks being deposited on each, utilising both the spiral and zig-zag deposition strategy. These are denoted as Sample S and Z respectively. A further sample was fabricated using the zig-zag deposition strategy and was used to obtain the strain-free (d_0) reference sample. All deposits were completed using the laser deposition rig as outlined in Section 3.4.1.

A total of three thermocouple measurements were taken for each deposition strategy at a location of 6, 7 and 8 mm from the substrate centreline, as shown in Figure 7.13. This data was collected and post-processed using the method outlined in Section 3.4.2. The location of the ND line scans and where the d_0

specimen was fabricated from is presented in Figure 7.14.

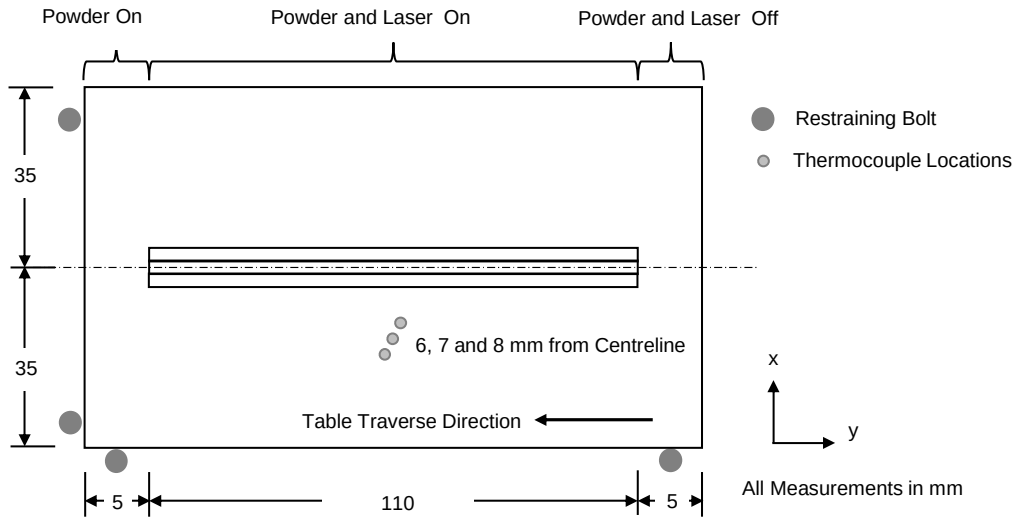

Figure 7.13: A schematic of the experimental set up used to validate the multi-track deposition model.

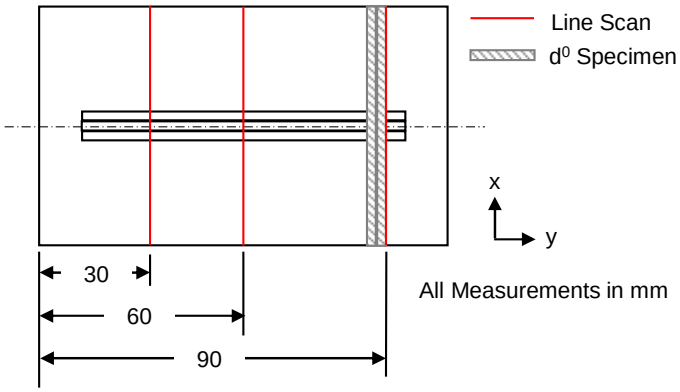

Figure 7.14: Locations of the ND horizontal line scans and the d_0 specimen.

The methodology used to validate the mechanical field is presented in Section 3.4.5. Data was collected for three horizontal line scans within the substrate in both Sample S and Z, utilising a 2 x 2 x 2 mm^3 gauge volume. All measurements within the substrate were completed at 2 mm below the substrate surface. These measurements were completed across the entire width of the plate to account for the unsymmetrical residual stress field. Further measurements were completed in each of the tracks using a 1 x 1 x 1 mm^3 gauge volume. Three track measurements were collected for each sample at the substrate mid length i.e. y=60 mm.

A strain free reference sample was obtained from the remaining sample using Electro Discharge Machining (EDM). Two specimens were required due to the gauge volume and the corresponding spatial resolution of the measurements. These were removed at the location shown in Figure 7.13. To relieve the internal strain, each d_0 specimen was cut into a combed specimen using EDM (Figure 7.15). A greater number of measurements were taken in the region of the deposit than far field, as the stress gradients were assumed to be greater. The same spatial resolution of the measurements used for the d_0 specimens were used for the measurements in Samples S and Z.

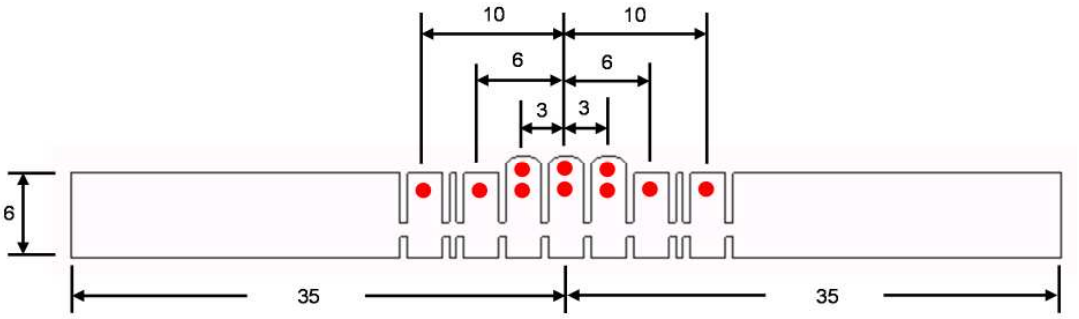

(a)

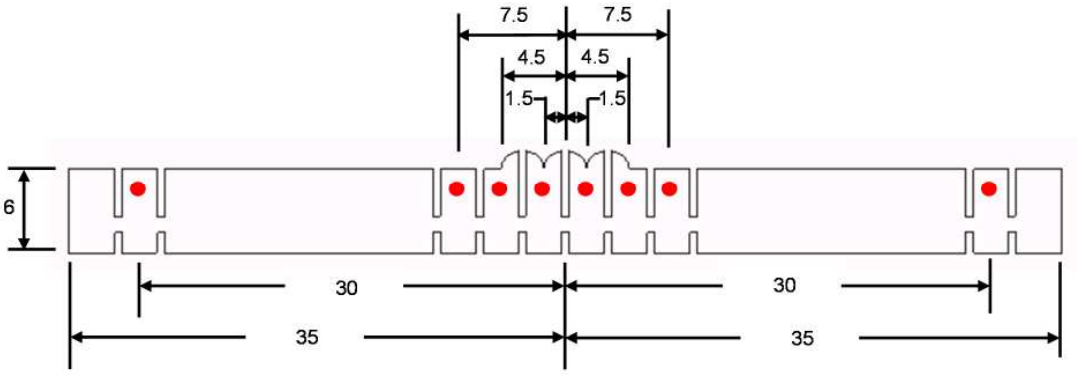

(b)

Figure 7.15: Details of the d_0 specimen cross section used for the multi-track ND measurements. The beam target is marked with a red circle.

As outlined previously, a gap between each track was generated during the experimental deposition. The primary reason for this was to reduce the texture

effects in the lattice spacing measurements. This had to be mitigated from the measurements as only one d_0 sample was used. If an overlap between the tracks was present, dissolution and reheat of both the HAZ in the substrate and track would have occurred. This would lead to different grain size formations adding texture in these regions. Therefore, with no overlap, there was no interaction in these regions, providing a more consistent comparison between the strain free specimen and the sample measurements.

From Section 5.4.4, it was apparent that due the sharp stress gradients below the surface of the tracks, the accuracy in the positioning of the ND incident beam had a great effect on the experimental residual stress data. Therefore, for this experimental set-up, a further stage was added in an attempt to mitigate this issue. A virtual experimental environment was produced using the SScanSS software, developed by ENGIN-X [196]. All of the measurement points were added to the virtual environment; however, instead of adding continuous horizontal line scans, the distortion of the sample was taken into consideration. Each measurement point was corrected to include the camber distortion of the specimen; therefore, using SScanSS, each measurement was offset 2 mm from the measured surface. In doing this, a more accurate comparison between the deformed FE model and the experimental data would be achieved. A comparison between the line scan used in Section 5.3.1 and the one used for the multi-track data collection is presented in Figure 7.16. Through implementing the corrected line scan, the gauge volume was fully filled by the substrate and track, therefore, no pseudo strains were introduced into the ND measurements. With the use of SScanSS, the entire experiment was automated, therefore reducing both the set up times and potential positioning errors for the experimental measurements.

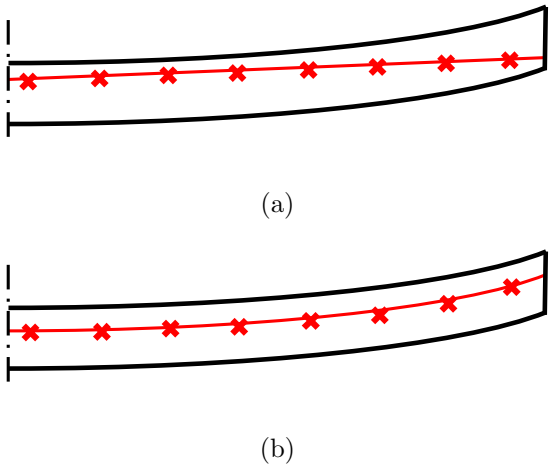

(a)

(b)

Figure 7.16: A comparison between the ND line scan used for (a) Single track deposition (b) Multi-track deposition. Line scan for each specimen marked with a red cross line.

7.4 Parametric Investigation into OR and Deposition Strategy

Upon validation of the multi-track thermo-mechanical model, a parametric investigation was completed to investigate the effect of both the OR and deposition strategy on the thermo-mechanical effects of the process. For this study, the same modelling methodology, as outlined in Section 7.3, was used. A total of 6 models were created for the parametric investigation using three OR's equating 10%, 20% and 40%. Both the spiral and zig-zag deposition strategy were implemented with the laser power, traverse velocity and powder feed rate being constant for all of the models. These parameters were defined as 1800 W, 400 mm/min and 26 g/min respectively. The track profiles were predicted using the method outlined in Section 7.2.3, with each geometry being used in a subsequent thermo-mechanical analysis.

The FE mesh design for the substrate was identical to the one used in Section 7.3; however, due to the overlap geometry, a reduced element size was required in this region to capture the elliptical geometry at this location. Therefore, the

minimum element size in this region was 0.1 x 0.5 x 0.5 mm^3. The mesh design for the spiral and zig-zag deposition strategy is presented in Figure 7.17 and Figure 7.18 respectively. The total number of elements and nodes for each model was presented in Table 7.3.

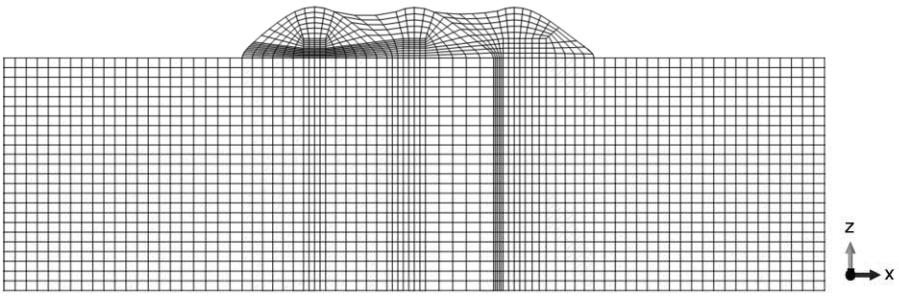

(a)

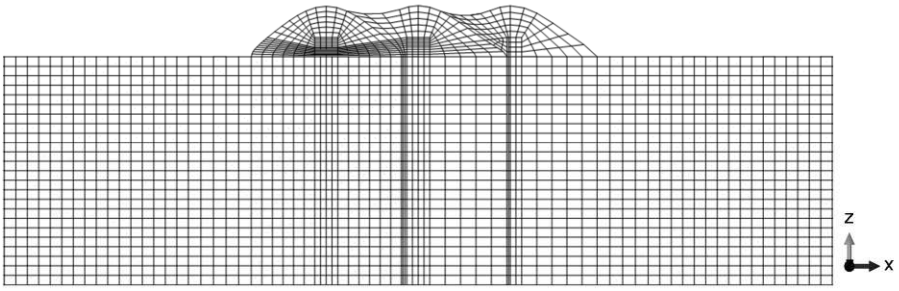

(b)

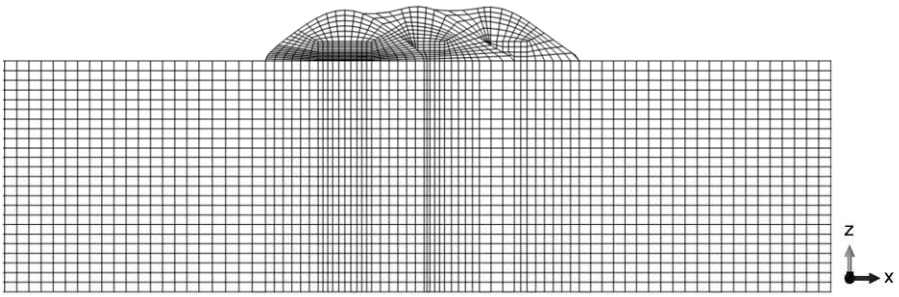

(c)

Figure 7.18: Mesh design used for the zig-zag deposition strategy for (a) 10% OR (b) 20% OR and (c) 40% OR.

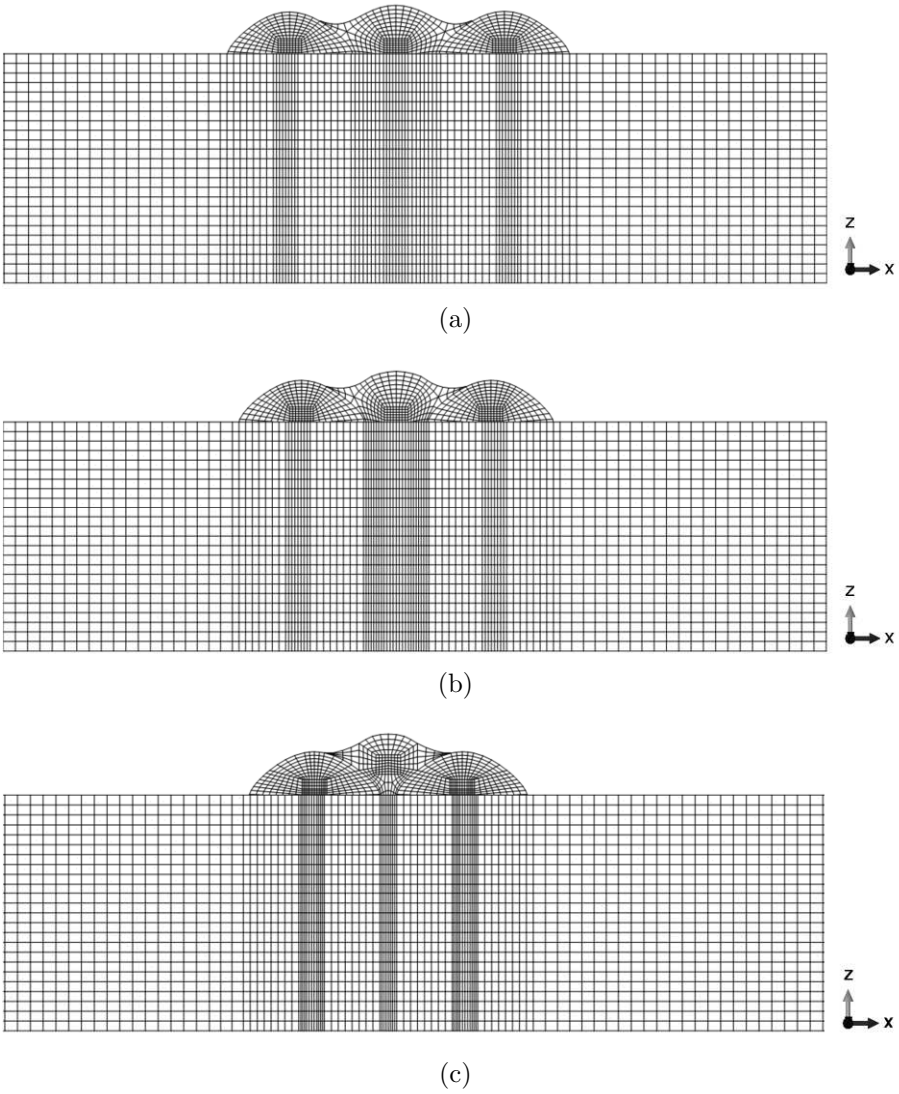

Figure 7.17: Mesh design used for the spiral deposition strategy for (a) 10% OR (b) 20% OR and (c) 40% OR.

Table 7.3: The total number of elements and nodes used for each mesh in the parametric investigation.

	Overlap Ratio (OR)					
	10 %		**20** %		**40** %	
	Nodes	**Elements**	**Nodes**	**Elements**	**Nodes**	**Elements**
Spiral	1,080,273	1,016,064	1,074,121	1,010,560	1,034,980	973,344
Zig Zag	838,546	786,024	776,864	728,304	891,591	838,400

With regards to post-processing of the models, three data sets were used to compare the effects of the thermo-mechanical fields when varying OR and deposition strategy. The thermal history was taken from the substrate surface at 6, 7 and 8 mm from the substrate centreline. With regards to the mechanical models, the residual stress field was determined at the substrate mid length, at 2 mm below the surface for each stress component. Also, the residual stress was analysed at the centre of each track, at the substrate mid-length.

7.5 Results and Discussion

7.5.1 Multi-Track Profile Predictions

A 3D surface plot showing the extent of the profile change, from a multi-track deposition is presented in in Figure 7.19. A comparison between the multi-track profile predictions and the experimental deposits is presented in Figure 7.20 and Figure 7.21 for the zig-zag and spiral deposition strategy respectively. For Figure 7.20 and Figure 7.21, the first track to be deposited was situated to the left of the substrate centre, which is located at x=0 and y=0. Overall, a good agreement between the experimental and numerical track profiles was attained for both deposition strategies, as the track shape, height and width were captured with accuracy by the numerical prediction. The associated error between each track height and the overall width, between the experimental and predicted data set

for the zig-zag and spiral deposition strategy, is presented in Table 7.4 and 7.5 respectively.

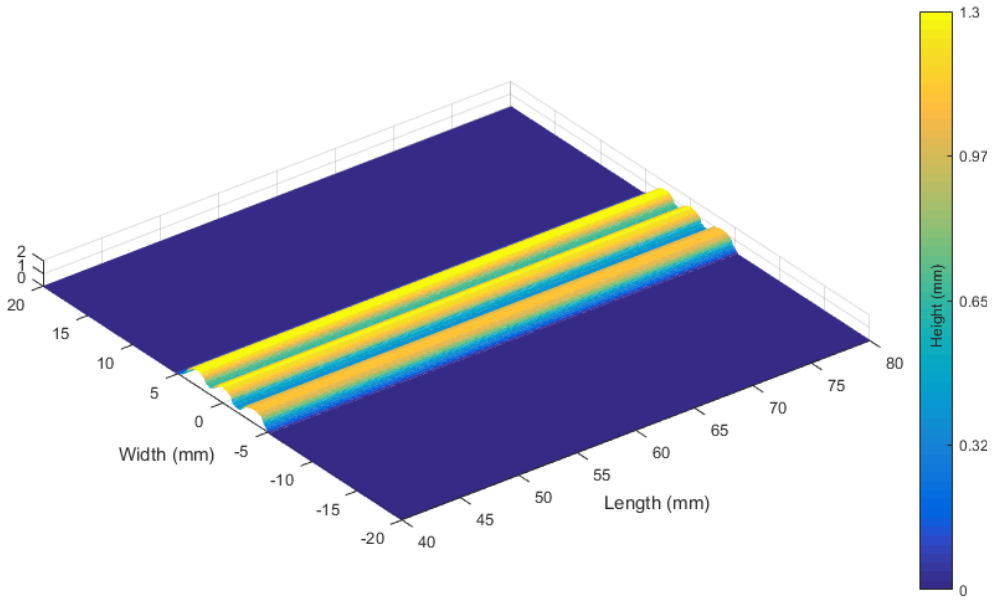

Figure 7.19: A 3D surface plot of the experimental multi-track deposit generated from the ENGIN-X laser scan data from Sample S.

Firstly from comparing the predicted and experimental track profiles in Figure 7.20 and 7.21, the use of the fillet model provided an accurate method to predict the geometry of the track in the overlap region. When comparing the results in the literature (Section 2.7.2) for the tangent overlap and the height addition model presented by Ahsan *et al.* [124] and Ding *et al.* [127] respectively, the predicted geometry in the overlap region would have not be a true representation of the experimental profiles presented here due to the overestimate of the material present within the overlap region. Therefore, for coaxial laser deposition, it is recommended that the fillet model is used for track profile predictions. From analysing Figure 7.20, there was minimal deviation in the experimental track height between each track for all of the investigated OR's. This was also captured by the numerical model for the same processing conditions.

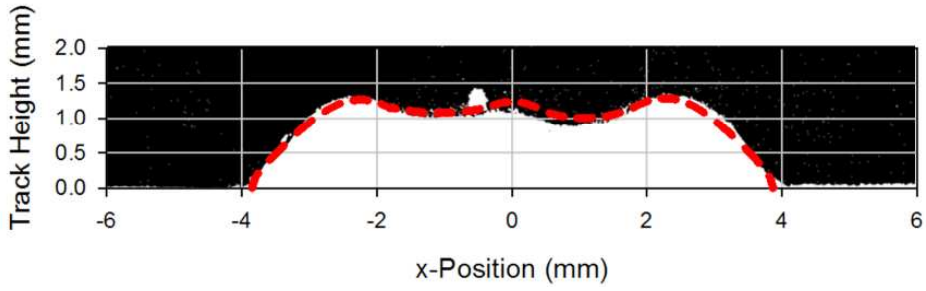

(a)

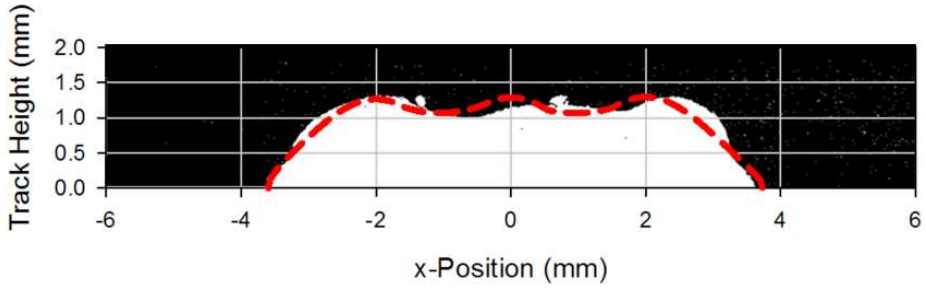

(b)

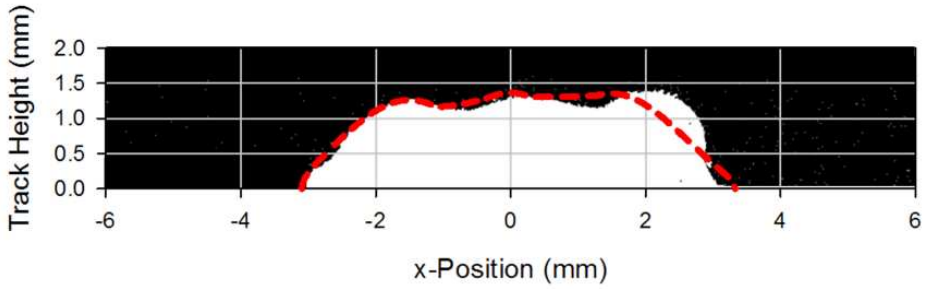

(c)

Figure 7.20: Comparison between the predicted multi-track profile (red line) and the experimental profile (black and white image) for the zig-zag deposition strategy. (a) 10% overlap ratio (b) 20% overlap ratio and (c) 40% overlap ratio.

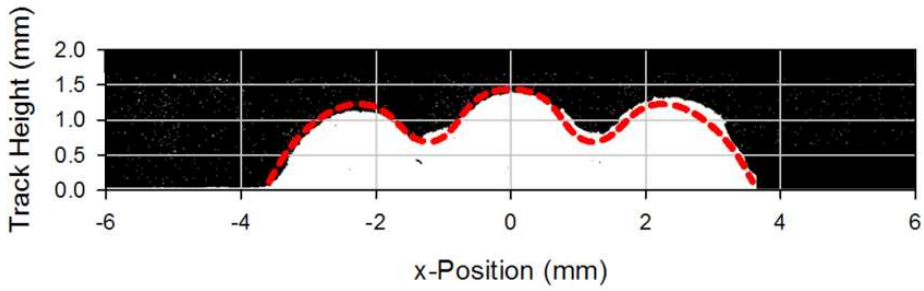

(a)

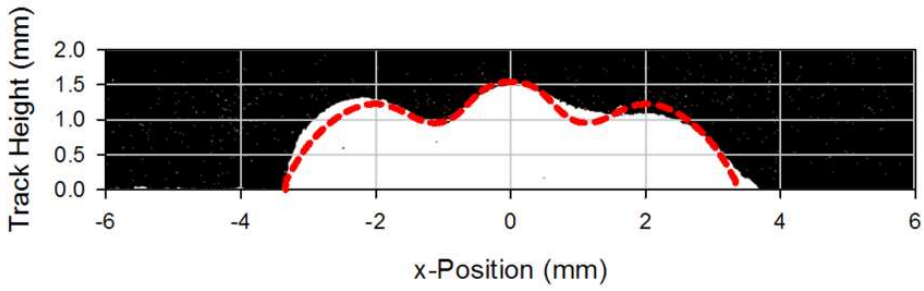

(b)

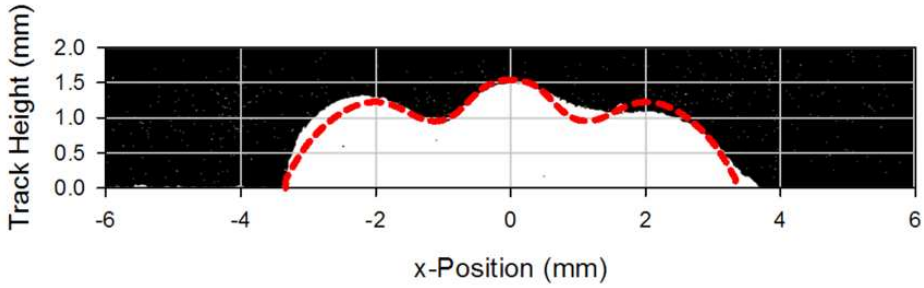

(c)

Figure 7.21: Comparison between the predicted multi-track profile (red line) and the experimental profile (black and white image) for the spiral deposition strategy. (a) 10% overlap ratio (b) 20% overlap ratio and (c) 40% overlap ratio.

Table 7.4: Error between the predicted and experimental multi-track profiles for each track height (h_1, h_2 and h_3) and the overall width (W_{total}) for the zig-zag deposition strategy.

	Error h_1 (%)	**Error** h_2 (%)	**Error** h_3 (%)	**Error** W_{total} (%)
10 %	7.50	9.36	1.13	1.66
20%	3.98	7.93	1.40	1.23
40%	0.78	2.18	1.42	1.55

Table 7.5: Error between the predicted and experimental multi-track profiles for each track height (h_1, h_2 and h_3) and the overall width (W_{total}) for the spiral deposition strategy.

	Error h_1 (%)	**Error** h_2 (%)	**Error** h_3 (%)	**Error** W_{total} (%)
10 %	1.55	4.50	9.66	1.66
20%	4.58	0.65	9.36	4.69
40%	0.78	3.33	6.78	5.5

As there was minimal deviation in the track height for each OR, the melt pool profile for each track was identical; therefore, this phenomena has been replicated with accuracy in the numerical model for the zig-zag strategy. The maximum and minimum error between the predicted and numerical track height was 9.36% and 0.78% respectively. The greatest error was observed for the 10% OR for the second deposit. This error arose due to the experimental track having a reduced height in comparison to the predicted profile. From analysing the experimental track profile in Figure 7.20(a), it was observed that the height for the second track was less than the other tracks; however, as the OR was only 10%, each track should have a similar height. A possible reason for this error maybe due to a choked powder flow during the experimental trials. This could lead to the powder particles not having a true Gaussian distribution, therefore leading to the accumulation of powder particles shown on the experimental track surface. This phenomena can also be observed in Figure 7.20(b) where a number of adhesions are present around the second track and the track height was compromised when compared to the other deposits. For the spiral geometry (Figure 7.21), the predicted track height was in a good agreement with the experimental data, with a maximum and minimum error of 0.78% and 9.66% respectively. For the final track in the spiral deposition, the maximum error between the two data sets was 4.5%, therefore this shows that the modification to the track height was required, otherwise the height would have been underestimated. The total overall width for each OR and

deposition strategy was predicted with accuracy as the maximum percentage error was 1.66%. This further highlights that the melt pool geometry, was predicted accurately using the numerical-analytical approach.

From Figure 7.20 and Table 7.4, a greater percentage error between the experimental and predicted track profile was present when the OR was increased for the zig-zag strategy. This was particularly prevalent for the final track, when using a 20% and 40% OR, as a discrepancy was observed between both the track profile and height. A possible reason for these errors may have been due to neglecting the powder present on the substrate surface for each subsequent deposition after the first track was completed. The current proposed model assumes that for each deposit, the domain was in a virgin state; therefore, no time history of the powder entering the domain, or its distribution on the substrate surface was monitored. During the deposition process, an accumulation of surface powder will be present, therefore, each subsequent deposition after the first track will have a greater overall volume. This additional powder may have caused the discrepancy between the third track profile for the 20% and 40% OR as the interaction between the Gaussian powder distribution, from the nozzle and the distribution of powder particles at the substrate surface, was not included. This phenomena was not present for the 10% OR (Figure 7.20(a)) as the distribution of previous powder particles would be over a greater area, therefore, this had a negligible effect on the total powder flux and its associated distribution for the 10% OR. It should also be noted that for the 20% and 40% OR using the zig-zag strategy, there was a discrepancy between the position of the maximum height when comparing the experimental and predicted data sets as shown in Figure 7.20(b) and 7.20(c) respectively. As the greatest distance between the predicted and experimental location of the maximum track height was 0.7 mm and due to a good agreement for the spiral strategy, this error was not due to an experimental setup or a CNC positioning error. It was therefore believed that this error arose

due to neglecting the fluid flow during the multi-track deposition process. With an increase in the OR, a greater proportion of the previously deposited track will become re-melted, therefore causing a certain volume of the previous track to flow into each subsequent track. This was more noticeable in higher OR's due to a greater volume of re-melted material being created. It should be noted that this phenomena was not present in the spiral deposition strategy. This could be due to the final track being bound by the first and second deposition.

Overall, an accurate methodology for predicting the multi-track deposition profiles, using a numerical-analytical approach, has been presented. Through utilising a 2D numerical thermal model, different process inputs and OR's can be investigated due to the solution not being restricted to quasi-stationary representation of the process. However, through neglecting certain physics of the process, a greater error between the predicted and experimental track profiles for the zig-zag strategy was present. Therefore, a conservative approach should be used when predicting track profiles using this approach for the zig-zag strategy. For both strategies, to predict one track profile using the method outlined in this section, a total time of approximately 10 minutes was required using 32 GB of RAM, with parallel processing on 4 CPUS. The presented method can be used to optimise the build geometry for repairing components to their original operating conditions; however, if a high number of tracks were required to complete the repair, there will be a high computational deficit due to the time required to solve the thermal FE model. However, the use of experimental trials would not only be time consuming, but also costly if a high number of design studies were required; therefore, the benefits of the modelling method presented here are prevalent over using an experimental methodology.

7.5.2 Thermo-mechanical Multi-track Validation Case

A comparison between the experimental and predicted thermal histories, for both the spiral and zig-zag deposition strategy are presented in Figure 7.22 and Figure 7.23 respectively. For both deposition strategies, the heating rate during the heat source pass was captured with accuracy, therefore, the geometry of the predicted melt pool was accurately determined to predict the associated heating effects in front of the heat source. With regards to the cooling portion of the thermal history, the cooling rate was predicted with accuracy for both strategies, as minimal deviation was observed between the experimental and predicted thermal profile.

From Figure 7.23, a better comparison between the cooling portion of the curve was achieved for the zig-zag strategy when compared to the spiral strategy. A potential reason for the greater deviation may arise from not including the convective heat loss in the FE model, on each track surface, during the deposition process. Therefore, this potentially highlights that the dissipation of the heat flux for the spiral deposition, was more complex than the zig-zag case; therefore, a smaller percentage of thermal flux was conducted through the substrate in comparison to the track surface for the spiral strategy. From analysing Figure 7.22 and Figure 7.23, a good agreement between the predicted and experimental data sets was achieved for each thermocouple location; however, the the maximum error occurred for the 6 mm thermocouple location for both deposition strategies. The maximum error equated 7.2% and 9.3% between the predicted and experimental peak temperature, for the first heat source pass, for the spiral and zig-zag strategy respectively. It should be noted that this error did not arise due to incorrect positioning of the thermocouples. If a positioning error caused the discrepancy between the peak temperature for the first heat source pass, the same trend (overestimate/underestimate) would have been observed for the remaining peak temperatures.

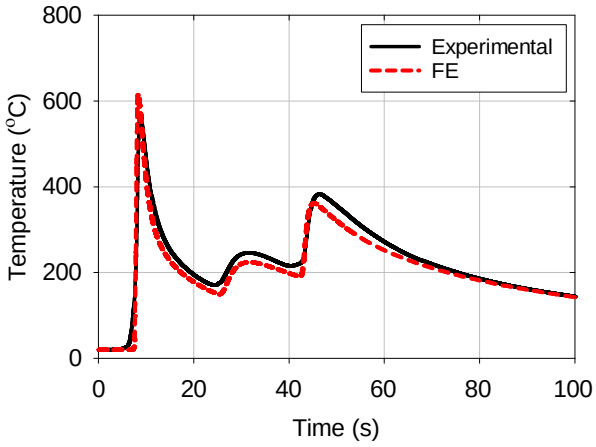

(a)

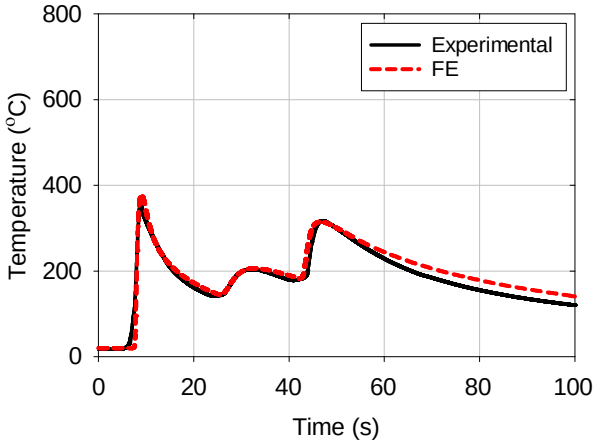

(b)

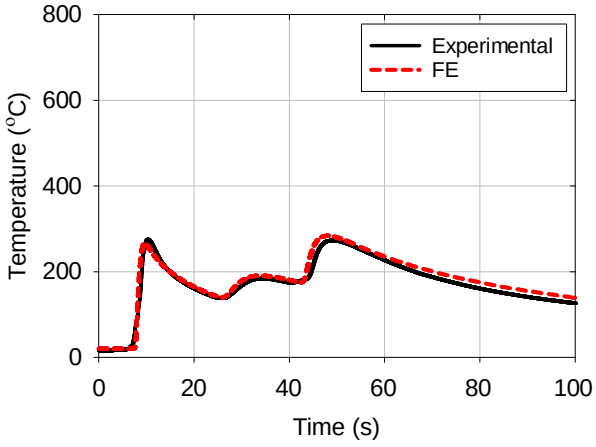

(c)

Figure 7.22: Comparison of the experimental and numerically predicted thermal histories for the spiral deposition strategy for thermocouple position (a) x=6 mm (b) x=7 mm and (c) x=8 mm. All thermocouples positioned at the substrate mid-length.

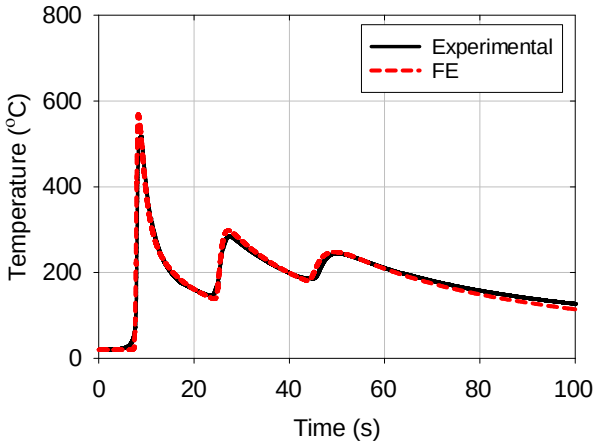

(a)

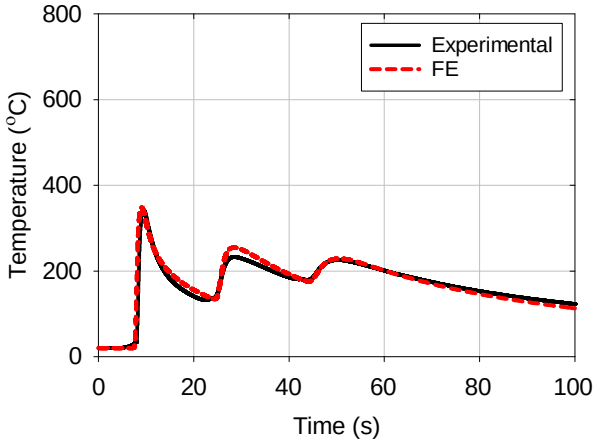

(b)

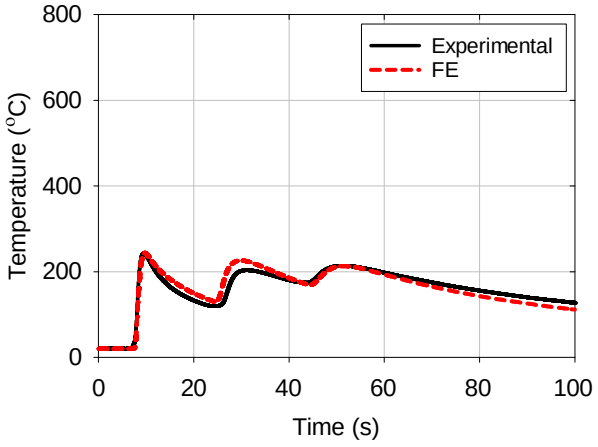

(c)

Figure 7.23: Comparison of the experimental and numerically predicted thermal histories for the zig-zag deposition strategy for thermocouple position (a) x=6 mm (b) x=7 mm and (c) x=8 mm. All thermocouples positioned at the substrate mid-length.

As the thermal FE model applies a constant heat flux magnitude, with a constant Gaussian distribution, the error must be associated with the experimental data, as the second and third heat source pass were in good agreement. Therefore, it was believed that this error was either due to variation in the supplied laser power during the deposition or due to an inconsistent surface finish altering the reflectivity of the material.

The evolution of the longitudinal, transverse and normal stress components for each deposition strategy, at 0.5 mm below each deposited track, is presented in Figure 7.24 and Figure 7.25. From analysing the longitudinal stress component for the first track (Figure 7.24(a)), after the first heat source pass, the longitudinal stress was tensile at a maximum value of 488 MPa. Upon cooling of this region and due to the thermal effects from the second heat source pass, a redistribution of the previous stress state caused a reduction in the tensile component by approximately 50%. Upon completion of the third track, local heating of the previously generated HAZ causes a compressive stress to be generated at this stage of the process. When the specimen was cooled to room temperature, the final residual stress state for the longitudinal component was tensile, with a value approximately 50% less compared to the initial single heat source pass. For the transverse stress component under the initial track and prior to the heat source pass, a compressive stress was exhibited until cooling occurred which caused the stress to become tensile. For each heat source pass, the same trend occurred for the transverse component until final cooling caused the direction of the stress component to invert. The direction of the transverse stress component for all locations was out of phase with longitudinal component ensuring an equilibrium state was achieved during the process. The normal stress component at the location of the first track was approximately zero for the duration of the deposition process; however, at the end of each cooling phase, the component would become tensile. The final stress state remains tensile for the normal component to balance

the tensile longitudinal and transverse components. For the position investigated beneath the second track (Figure 7.24(b)), the same trend was observed as for the first track due to identical processing conditions. The only difference was that the position of the peak residual stress was shifted to later in the cycle, when the heat source was positioned above the second track. Again, similar to the first track, a reduction of approximately 50% was observed in the longitudinal component between the peak value and the magnitude of the final residual stress state. For the final track (Figure 7.24(c)), due to the pre-heating of the central region of the substrate, a tensile longitudinal stress was present during the deposition of the first and second track. This arose due to the first and second heat source pass, inducing a compressive longitudinal stress, which changed direction upon cooling. The transverse stress component during the first and second deposit, follows the same trend as the longitudinal component, but with a reduced magnitude. For this location, the normal stress was approximately zero for the entire process. At the end of the heat source pass for this location, all three residual stress components become compressive and upon cooling, the normal stress was of a reduced magnitude. The longitudinal and transverse components were of high magnitudes as no reheat of this region occurred after subsequent depositions were completed.

For the zig-zag deposition, a different evolution of the stress, beneath each track was observed in comparison to the spiral deposition strategy. For the first track (Figure 7.25(a)), the longitudinal peak stress was tensile and occurred after the peak temperature of the initial heat source pass. Upon further heating of the HAZ, a compressive longitudinal stress was exhibited; however, upon cooling, this returned to a tensile stress state with a reduction in magnitude. After completion of the final track, the HAZ under the first track was again reheated, this lead to a further reduction of the tensile longitudinal stress. From each heat source pass, a reduction of 22% and 120% was observed respectively for the longitudinal stress component.

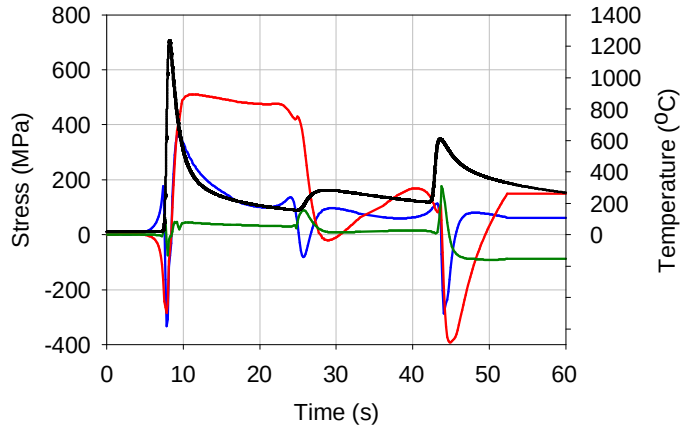

(a)

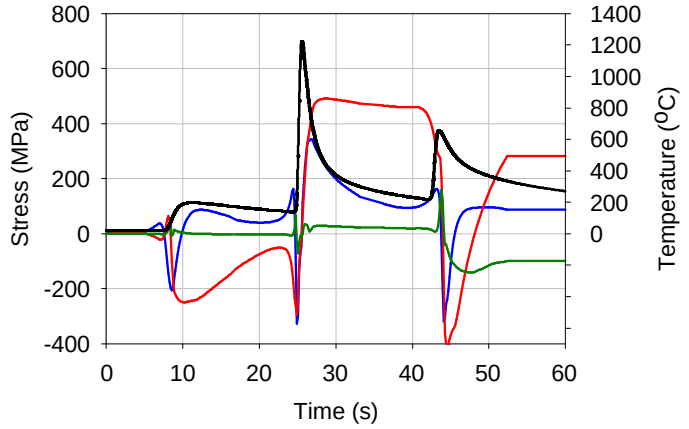

(b)

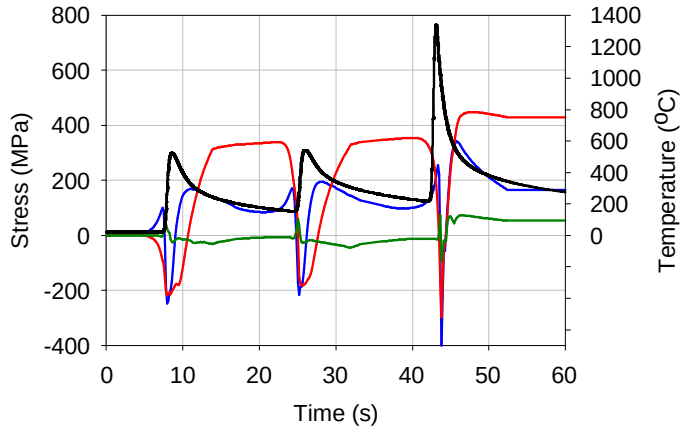

(c)

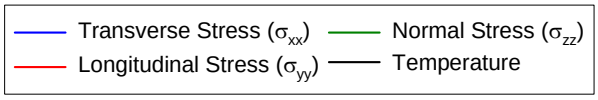

Figure 7.24: Numerical prediction of the longitudinal, transverse and normal stress components, during the multi-track deposition process, under each track, for the spiral deposition strategy. (a) Stress evolution at x=-3 mm (b) Stress evolution at x=3 mm and (c) Stress evolution at x=0 mm.

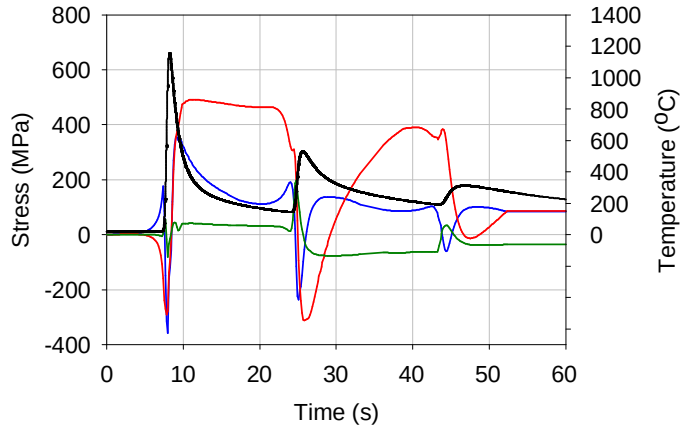

(a)

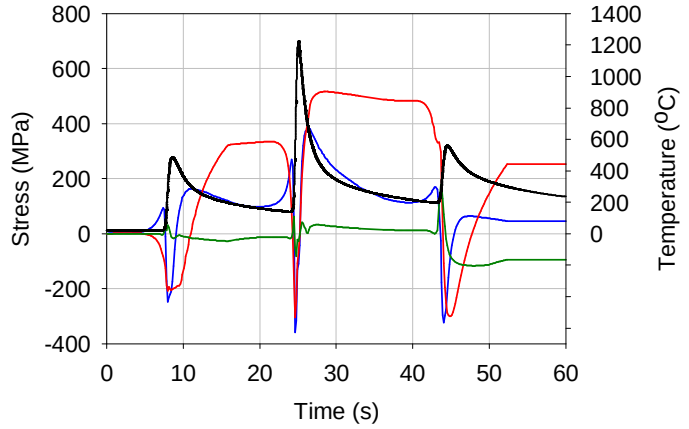

(b)

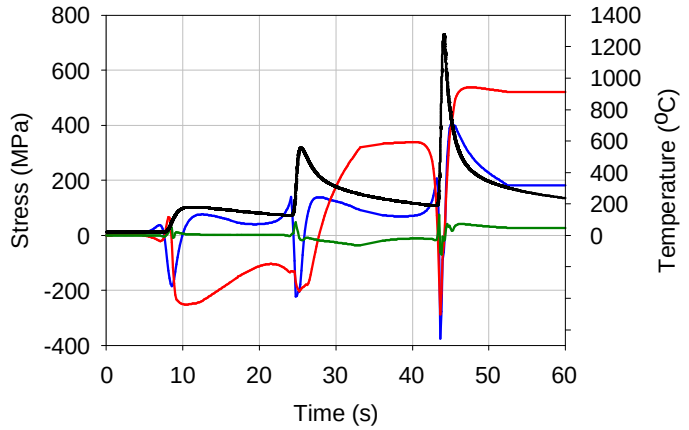

(c)

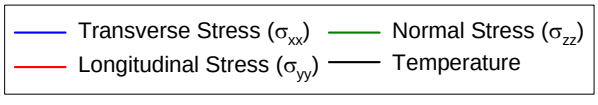

Figure 7.25: Numerical prediction of the longitudinal, transverse and normal stress components, during the multi-track deposition process, under each track, for the zig-zag deposition strategy (a) Stress evolution at x=-3 mm (b) Stress evolution at x=0 mm and (c) Stress evolution at x=3 mm.

The transverse stress, during the deposition process, followed a similar trend to the longitudinal component by fluctuating between a compressive and tensile stress state, after each heating and cooling cycle. The transverse component had a reduced stress magnitude in comparison to the longitudinal component; however, upon final cooling, the values of each component were of equal magnitude. For the initial track, the normal component was approximately zero for the first heat source pass. At the location beneath the second deposition (Figure 7.25(b)), the conduction of heat from the first heat source pass lead to a compressive longitudinal stress being formed. Through a reduced cooling rate, the stress direction was reversed, this generated a low magnitude tensile stress within the specimen. Upon the peak temperature being exhibited at the second heat source pass, a peak tensile residual stress, identical in magnitude to the first heat source pass was generated. However, the final heat source pass for the second track, when compared to the first deposit, did not cause as much of a reduction in the magnitude of the longitudinal stress component (77%). This was caused due to the area around the second track being subject to less cyclic thermal loading; therefore highlighting the potential benefits of heat treating/cyclic thermal loading of each deposit to reduce the high magnitude residual stresses. Similar to the first track, the transverse stress followed the same trend as the longitudinal component; however, the final magnitude was not identical to the longitudinal component. The normal stress was predominately zero for the first and second heat source pass, with the final state being compressive. Finally, for the third track in the deposition (Figure 7.25(c)), the longitudinal stress was initially compressive, changing to a tensile direction after the second and third heat source pass. After each heat source pass, the magnitude of the longitudinal residual stress increased by 40% and 50% respectively. Upon final cooling, the longitudinal component was at a peak value of 488 MPa; therefore, as there was no subsequent re-heat of this region, a reduction in magnitude was not observed. The transverse stress

component remained tensile for the entire deposition process, however, after each heat source pass the magnitude increased, similar to the longitudinal component. The normal stress component was approximately zero for each heat source pass.

Across both deposition strategies, a reduction in the magnitude of the longitudinal stress component for the final residual stress field was observed for both the first and second track. A greater reduction in the longitudinal stress component was observed after the first and second deposit for the zig-zag strategy when compared to the spiral strategy. As the modes of heat loss were identical for each strategy, the different cooling rates generated from the direction of each heat source pass altered the evolution of stress and the final residual stress state of the specimens; therefore, highlighting the effect of deposition strategy on residual stress. For the final deposition, the final residual stress field was unaltered from the initial state and occurred due to no re-heating of the previously inhibited HAZ. As the deposition strategy only altered the position in which the maximum residual stress occurred and did not reduce all stresses to an acceptable value, it can be concluded that for this case, the deposition strategy has minimal effect on reducing the magnitude of the residual stress at all locations of the deposit. However, as re-heating of previous tracks caused a reduction in stress magnitude, post heat treatment could be a beneficial method to reduce the high magnitude tensile stresses.

The comparison between the experimental and predicted longitudinal, transverse and normal stress component at each ND line scan location is presented in Figure 7.26-7.28 and Figure 7.29-7.31, for the spiral and zig-zag strategy respectively. Further to this, the comparison between the predicted and experimental residual stress in each track is presented in Figure 7.32.

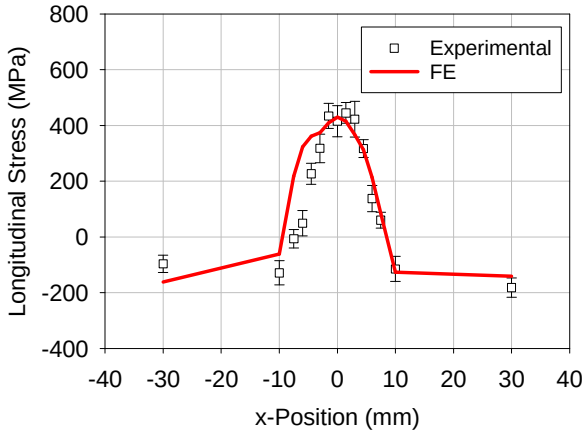

(a)

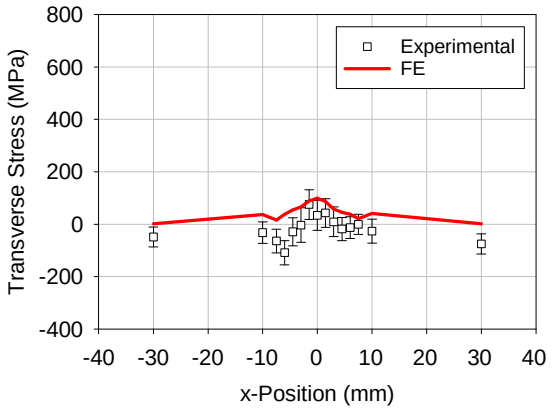

(b)

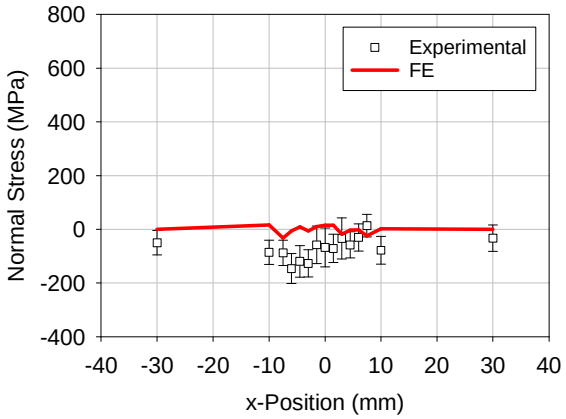

(c)

Figure 7.26: Comparison of the experimental and numerically predicted residual stress profiles for the spiral deposition strategy at y=30 mm for (a) Longitudinal Stress (σ_{yy}) (b) Transverse Stress (σ_{xx}) (c) Normal Stress (σ_{zz}).

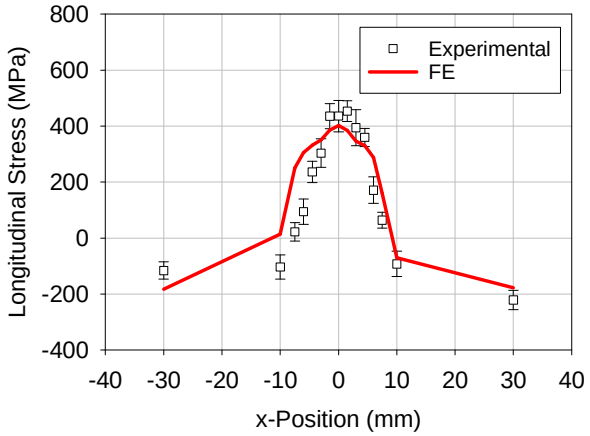

(a)

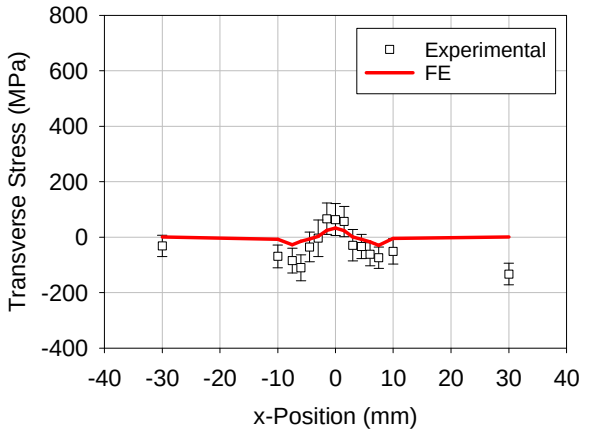

(b)

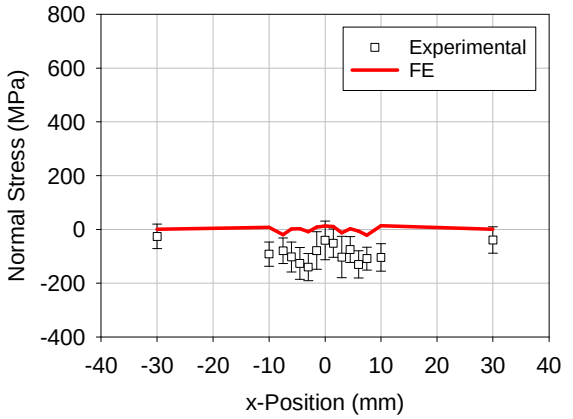

(c)

Figure 7.27: Comparison of the experimental and numerically predicted residual stress profiles for the spiral deposition strategy at y=60 mm for (a) Longitudinal Stress (σ_{yy}) (b) Transverse Stress (σ_{xx}) (c) Normal Stress (σ_{zz}).

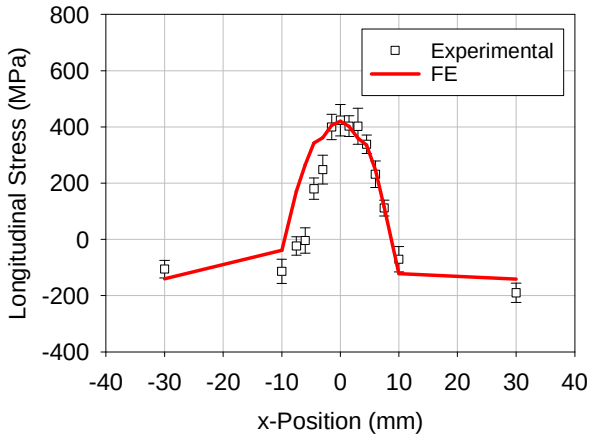

(a)

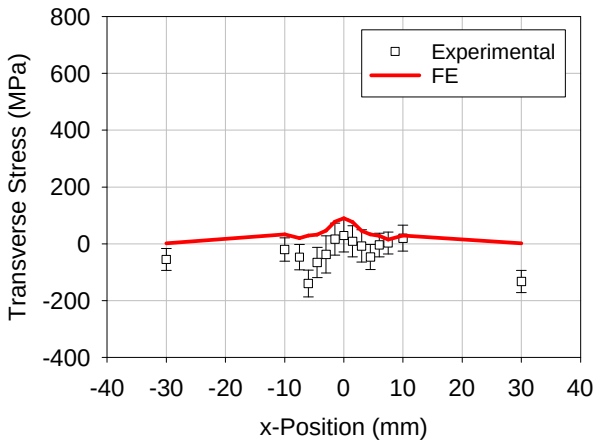

(b)

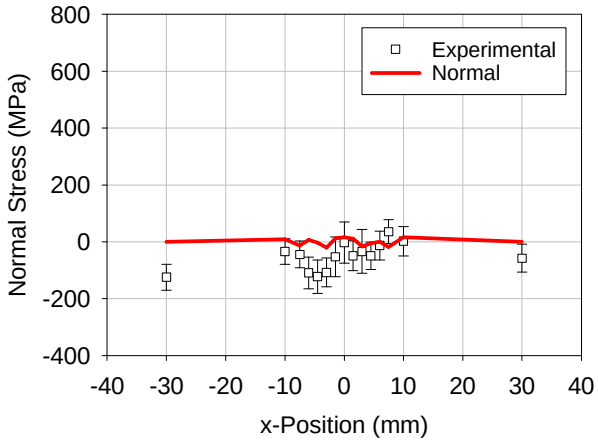

(c)

Figure 7.28: Comparison of the experimental and numerically predicted residual stress profiles for the spiral deposition strategy at y=90 mm for (a) Longitudinal Stress (σ_{yy}) (b) Transverse Stress (σ_{xx}) (c) Normal Stress (σ_{zz}).

For both deposition strategies at each line scan location, the peak residual stress for each stress component was captured by the FE model. The maximum percentage error for the peak residual stress was 7.2% and 6.4% for the spiral and zig-zag deposition strategy respectively. Overall, the trend for each component has been predicted with accuracy, as a high majority of the predicted stress values fall within the confidence limits of the experimental data set. The greatest correlation between the predicted and experimental data set, for all three stress components, was achieved at y=60 mm for the spiral strategy. For the zig-zag strategy, the predicted residual stress correlated well at all locations with the experimental data. As only the the motion of the heat source was included in the model at the end of each track, the material addition at these locations could have had a greater effect on the residual stress for the spiral strategy, as a better correlation between the residual stresses was observed for the zig-zag. This could have been a potential reason for the discrepancies observed at y=30 mm and 90 mm shown in Figure 7.26 and Figure 7.28. A reduction in correlation was observed for the normal stress component for both strategies at all scanning locations. As the other two predicted stress components agreed well with the experimental data sets, texture effects arising from the grain orientation in the normal direction could be a potential cause for this. Another possible reason for the discrepancies maybe due to the increased path length travelled by the neutrons. Due to the orientation of the plate and the detector bank, the diffracted neutrons have travelled through a greater section of the substrate material, which effectively caused experimental noise to be included in the data collection. However, despite these errors, the largest magnitude stress components (longitudinal and transverse) were captured with a high fidelity, therefore providing validity of the presented modelling strategy.

For both deposition strategies, at all of the investigated locations, there was minimal deviation in the residual stress profiles for each stress component. This

was to be expected as there was no transient variation in the process parameters used for this study. However, when comparing the trends for the final residual stress fields, between the zig-zag and spiral strategy, the overall distribution of the residual stresses were different. For all three stress components, using the spiral strategy, the trends were symmetrical about the substrate centreline, with the peak stress of each component being observed at x=0 mm. This symmetrical variation was captured by both the predicted and experimental data sets. The symmetrical residual stress profiles were present due to the first and second track having identical processing conditions and from the uniform reheating which arose from the deposition of the third track. The uniform reheating acts as an annealing effect for each track, causing the distribution of residual stresses to be evenly distributed about the substrate centreline. Unlike the spiral strategy, the residual stress profiles for the zig-zag strategy were asymmetric, with the peak stress, for each component arising at the location of the final track centreline i.e. x=3 mm. This phenomena was consistent with the findings of Foroozmehr *et al.* [133]. This shift in the peak residual stress was captured by the predicted data set. This shift in the peak magnitude will occur due to the asymmetric variation in the thermal flux heat source pass when compared to the spiral deposition strategy, due to the tool path and subsequent reheat of each track.

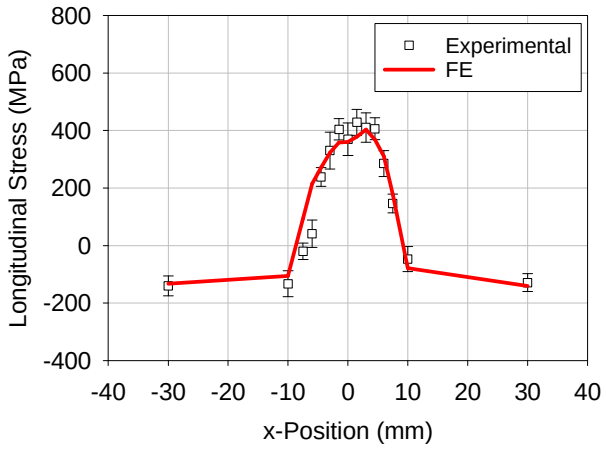

(a)

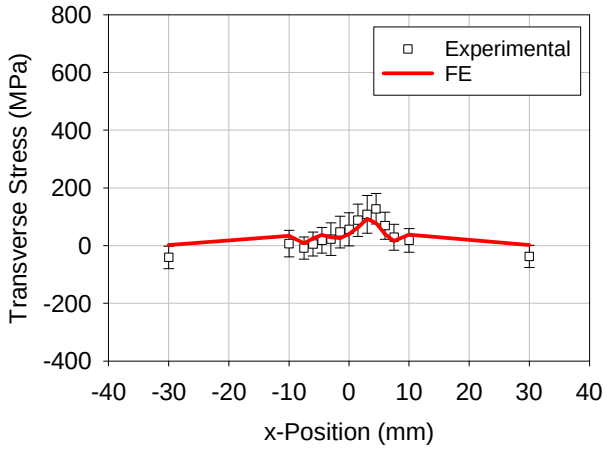

(b)

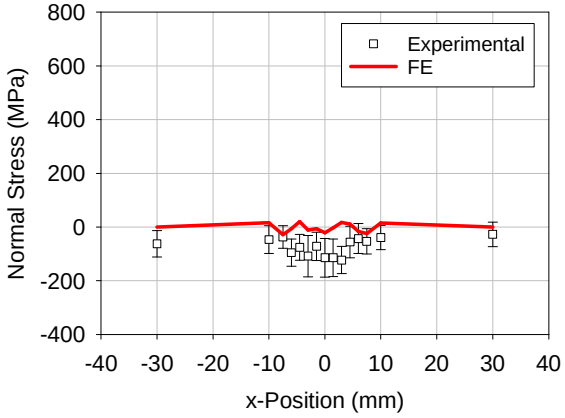

(c)

Figure 7.29: Comparison of the experimental and numerically predicted residual stress profiles for the zig-zag deposition strategy at y=30 mm for (a) Longitudinal Stress (σ_{yy}) (b) Transverse Stress (σ_{xx}) (c) Normal Stress (σ_{zz}).

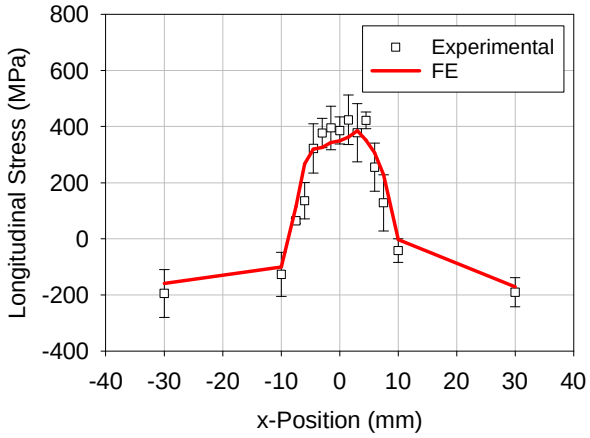

(a)

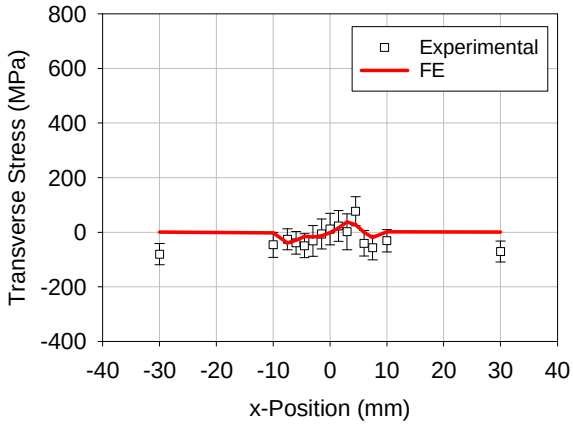

(b)

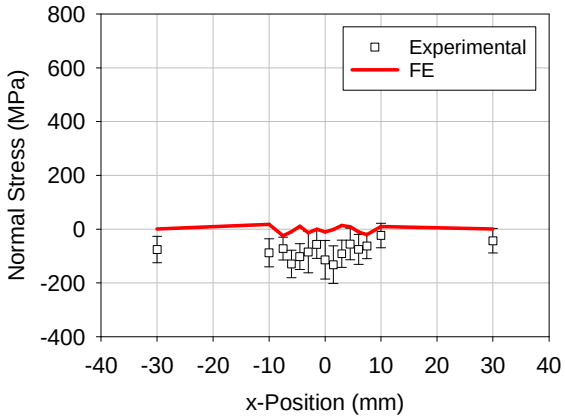

(c)

Figure 7.30: Comparison of the experimental and numerically predicted residual stress profiles for the zig-zag deposition strategy at y=60 mm for (a) Longitudinal Stress (σ_{yy}) (b) Transverse Stress (σ_{xx}) (c) Normal Stress (σ_{zz}).

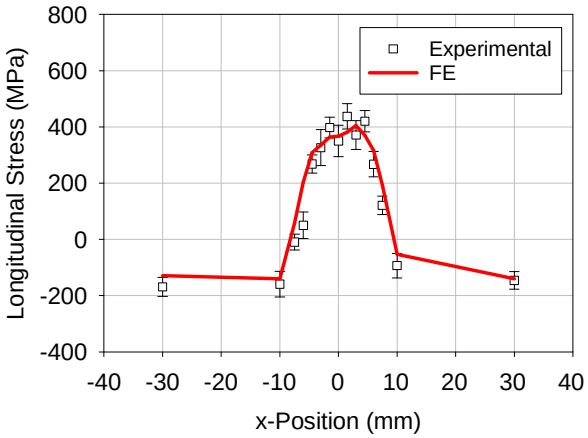

(a)

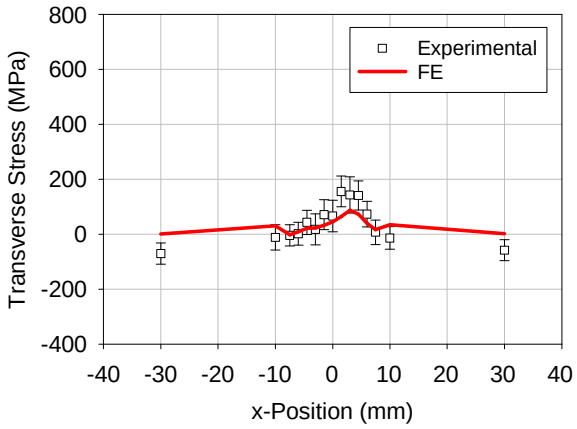

(b)

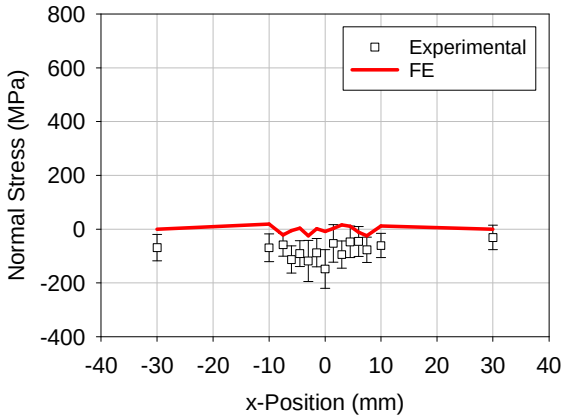

(c)

Figure 7.31: Comparison of the experimental and numerically predicted residual stress profiles for the zig-zag deposition strategy at y=60 mm for (a) Longitudinal Stress (σ_{yy}) (b) Transverse Stress (σ_{xx}) (c) Normal Stress (σ_{zz}).

It should be noted that there was a discrepancy between the width of the residual stress profile, when comparing the longitudinal component, for the spiral deposition strategy (Figure 7.26(a), 7.27(a) and 7.28(a)). A reduction in the width of the profile for stress values ranging from 0 MPa to the peak value (488 MPa) was present for the experimental data set in comparison to the numerical values. Also, a difference in the magnitude of the compressive stress at x=7.5 mm was present at all locations, for the transverse stress component (Figure 7.26(b), 7.27(b) and 7.28(b)). A potential reason for both of the differences may have arisen due to the overestimate of the predicted peak temperature, for the initial heat source pass, as observed in Figure 7.22. The HAZ in the FE prediction will be greater, therefore, causing a larger volume of molten material to be present. Upon cooling, a greater force in the localised region will be present due to the contraction of the material. This would therefore elongate the region where the high tensile longitudinal stress was being exhibited. For the discrepancy in the transverse component, due to the increased melt pool geometry in the predicted model, a greater magnitude of compressive and tensile forces will be acting in front and behind the melt pool region respectively. Upon cooling, these larger forces are predominately tensile in the longitudinal direction; therefore, to ensure equilibrium, a lower compressive stress was required.

A comparison between the experimental and numerical predictions, for the residual stress components within each track is presented in Figure 7.32. All of the predicted data points were within the error bars of the experimental data showing a high degree of confidence. The maximum percentage error for each deposition strategy was for the longitudinal stress component. This equated 18.1% and 22.2% for the spiral and zig-zag deposition strategy respectively.

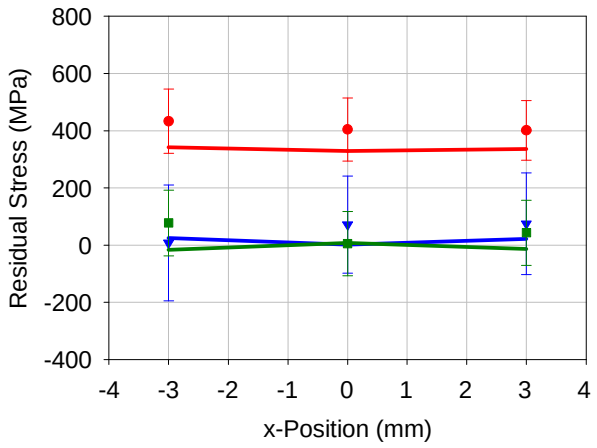

(a)

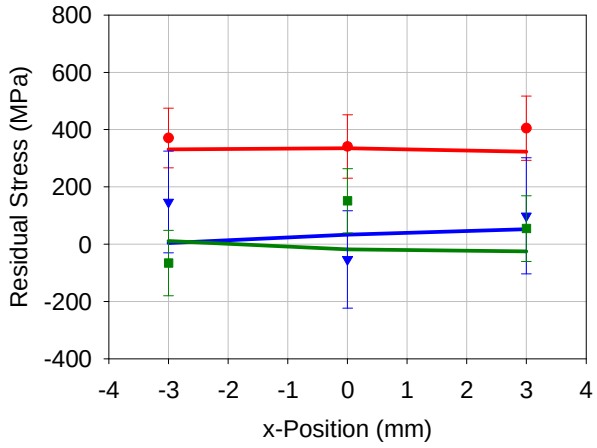

(b)

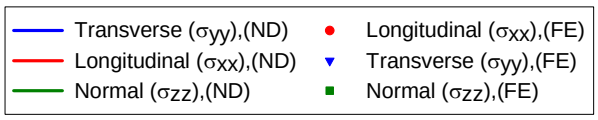

Figure 7.32: Comparison of the experimental and numerically predicted residual stress profiles for each bead for (a)Spiral deposition strategy and (b) Zig-zag deposition strategy. Both locations are at y=60 mm.

The magnitude of the longitudinal residual stresses were similar for each strategy, with a maximum percentage error of 16.6%; therefore, the magnitude of this residual stress within the track was governed by the peak melt pool temperature, as the processing conditions were identical. Again, similar to the above residual stress profiles, the distributions were symmetrical for the spiral strategy

and asymmetric for the zig-zag strategy. The shift in the peak magnitude for the residual stress occurred in the location of the last track, therefore, this was consistent with the residual stress profiles within the substrate as observed in Figure 7.29(a). For both strategies, the normal stress was approximately zero. It should be noted that from Figure 7.32, the magnitude and direction of the residual stresses were identical within the bead and the substrate, in the location directly below the track. Therefore, due to a significant amount of time being required to measure the lattice strain within the bead profile, the substrate measurements maybe sufficient to predict the residual stress magnitudes within the tracks.

Overall, a strong correlation was obtained between the experimental and predicted residual stress profiles for both deposition strategies. It should be noted that in comparison to the residual stress error presented in Section 5.4.4, this inconsistency in the direction of the stress component was not present here. Therefore, the use of SScanSS and the virtual experimental set up reduced the positioning error of each ND measurement, thus providing a greater correlation between the predicted and numerical results as previously observed. For any subsequent ND measurements of laser deposited specimens, it is therefore recommended that the experimental set up defined in this section is adopted. From Figure 7.26-7.31, some discrepancies are still present when comparing the experimental and predicted data sets. A potential source of error may have arisen due to inconsistent ambient conditions during the ND measurements. Due to the allocation of the beam time, measurements were taken over the cause of 120 hours. This variation in temperature would lead to a 0.5% variation in the stress magnitude [26]. Another reason for the error maybe due to the use of one d_0 specimen for both the spiral and zig-zag deposition strategies. As the lattice spacing measurements will be greatly affected by the size and orientation of the grains, an identical reference sample (d_0 specimen) should be used for each measurement location to mitigate

this issue. The maximum heating and cooling rate was calculated below each track, at the centre of the gauge volume for each deposition strategy, which is presented in Table 7.6. From this data, there was negligible difference between the heating and cooling rate at each location, for each deposition strategy. A maximum difference of 6.7% and 3.89% was observed respectively. Therefore, the grain size and microstructure formation should be similar in these regions. As there was no overlap between the tracks, no remelting and solidification of the track occurred. This, in combination with similar heating and cooling rates, should have generated similar material and microstructural properties within the d_0 specimen. Therefore, a fair comparison between the reference and measured lattice spacings was achieved. However, as the heat source pass in each strategy was in a different location and direction, the directional solidification of the track and melt pool would potentially have an affect on the lattice spacing. Often in welding, the longest dimension of the grain is in the traverse direction of the heat source. As the direction of the longest grain was different in each sample, the d_0 specimen used to derive the lattice strain for the spiral strategy was not consistent due to potential texture effects. As the d_0 specimen was fabricated from the zig-zag strategy, a better correlation between the experimental and predicted data was observed for this tool path (Figure 7.29-7.31).

Table 7.6: Maximum heating rate and cooling rate at the centre of each gauge volume, 1 mm below each track, for the spiral and zig-zag deposition strategy.

	Track 1		**Track 2**		**Track 3**	
Strategy	**Spiral**	**Zig-zag**	**Spiral**	**Zig-zag**	**Spiral**	**Zig-zag**
Maximum Heating Rate ($^{\circ}c/s$)	3611	3611	3313	3097	3173	3096
Maximum Cooling Rate ($^{\circ}c/s$)	1145	1145	1073	1021	988	1027

Finally, the material hardening law used in this study could have caused the discrepancies observed in the magnitudes of the residual stresses. Due to the

cyclic thermal loading, the use of the isotropic plastic hardening law would underestimate the accumulated plastic strain [192] and cause an overestimate in the residual stress prediction which was observed in this study and through the work presented by Mullins *et al.* [153]. To further enhance this modelling strategy for multi-track depositions, a mixed plastic theory (kinematic and isotropic) with a two-stage annealing approximation, would be required to attain better correlation [192]; however, this material law would be difficult to quantify due to the experimental calibration required.

7.5.3 Effect of OR on the Thermo-mechanical Fields

The effect of the OR on the thermo-mechanical fields was investigated for a 10%, 20% and 40% OR, for both the spiral and zig-zag deposition strategy. The results from the thermal histories are presented in Figure 7.33. The thermal history data was taken at the nodal coordinate (-6, 60 ,0) for all three OR's. The trends of the thermal history profiles for the spiral and zig-zag deposition in Figure 7.33 are identical to the trends in Figure 7.22 and 7.23 respectively. This was to be expected as the process parameters and path of the heat source were the same for each deposition strategy. For the first heat source pass, the thermal history was identical, at all of the investigated locations, as the heat source was traversing past the same nodal position at the same offset value. It should also be noted, that the thermal history for the first heat source pass was identical to the experimental data presented in Figure 7.22 and 7.23, therefore, showing validity in the modelling approach. For both deposition strategies, with increasing OR, the peak temperature for each subsequent heat source pass increases. This was to be expected as the heat source passes closer to the nodal reference point due to the reduction in the track offset distance. For each OR, the heat generation and cooling rate for each heat source pass was identical; therefore, this highlights that the OR has minimal impact on this phenomena.

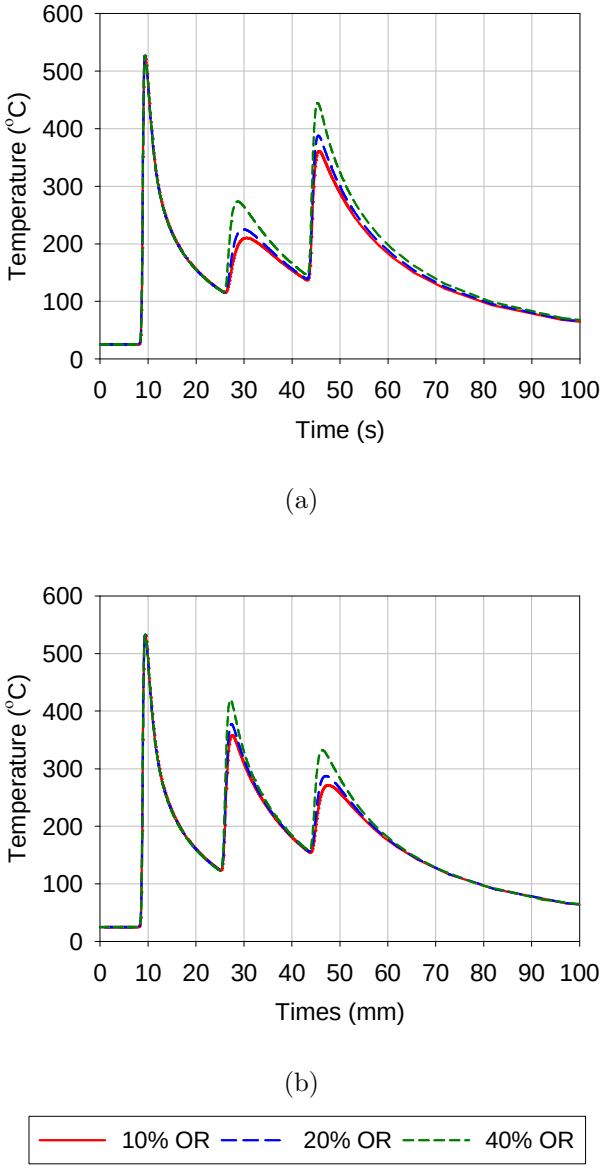

Figure 7.33: A comparison between the thermal history predictions, for an OR of 10%, 20% and 40% for (a) Spiral deposition strategy and (b) Zig-zag deposition strategy.

The residual stress profiles at y= 30, 60 and 90 mm, for the spiral and zig-zag deposition strategy, at 2 mm below the substrate surface, are presented in Figure 7.34 and 7.35. For consistency with the validation cases presented in Section 7.5.2, the data was averaged over a 2 x 2 x 2 mm^3 volume. For both the spiral and zig-zag deposition strategy, it can be observed that there was negligible deviation in the presented residual stress profiles when comparing each OR. It can therefore

be determined that the sub-surface residual stresses, were independent of the OR used for the deposition. It should also be noted that there was minimal variation observed in the peak residual stress for each component when comparing each OR. The maximum percentage difference for the spiral strategy was 2.6% 10.9% and 18.36% for the longitudinal, transverse and normal component respectively. The maximum percentage difference for the zig-zag strategy was 0.8% 14.8% and 14.1% respectively. It should be noted that with an increase in OR, for the spiral deposition, an increase in the peak longitudinal stress was observed which was balanced through a reduction in both the transverse and normal stress component. This phenomena was not observed for the zig-zag strategy. From this study it can be concluded that the OR had a negligible effect on the peak residual stress profiles. As each of the OR's investigated had a constant set of process parameters, the peak residual stress was primarily a function of the peak temperature within the melt pool and the associated cooling rate. This can also be supported by the validation cases presented in Section 7.5.2, as when no track overlap was present, similar peak stress values were obtained when compared to the 10%, 20% and 40% OR. When analysing the residual stress profiles for the spiral strategy (Figure 7.34), a symmetrical stress distribution was obtained, similar to the results of the validation case presented in Figure 7.26-7.28. For the zig-zag strategy, an asymmetric profile was observed, with the peak residual stress being located at the final track centreline, again this was similar to the validation case as presented in Figure 7.29-7.31. It should be noted that for the 10%, 20% and 40% OR, the peak stress was greater by 10.3% when compared to implementing an OR of zero.

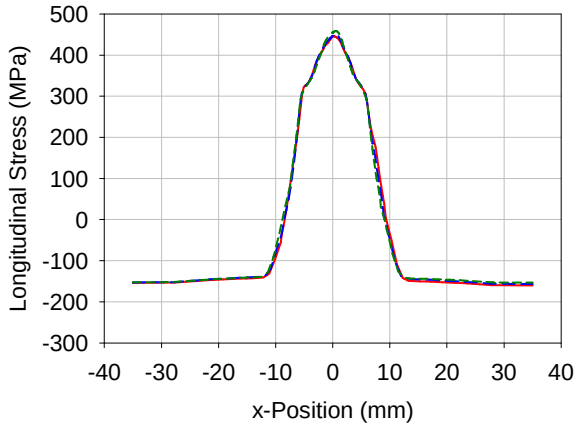

(a)

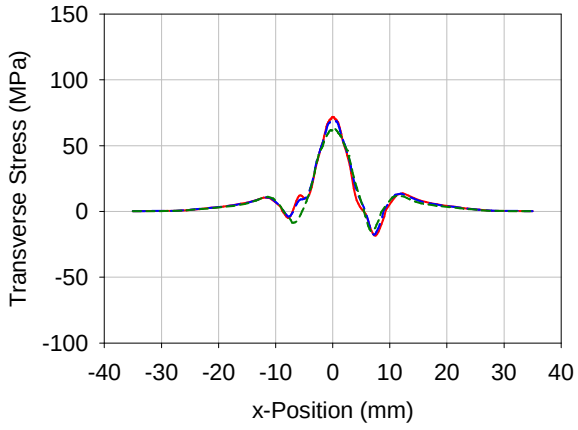

(b)

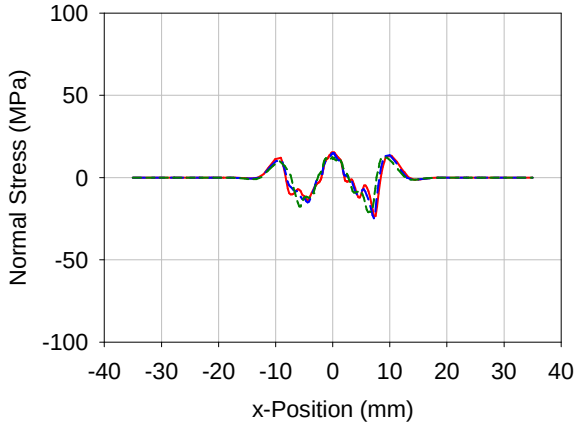

(c)

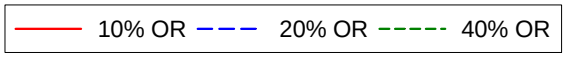

Figure 7.34: A comparison between the numerical predictions, for an OR of 10%, 20% and 40% for the spiral deposition strategy for (a) Longitudinal stress (σ_{yy}) (b) Transverse stress (σ_{xx}) and (c) Normal stress (σ_{zz}).

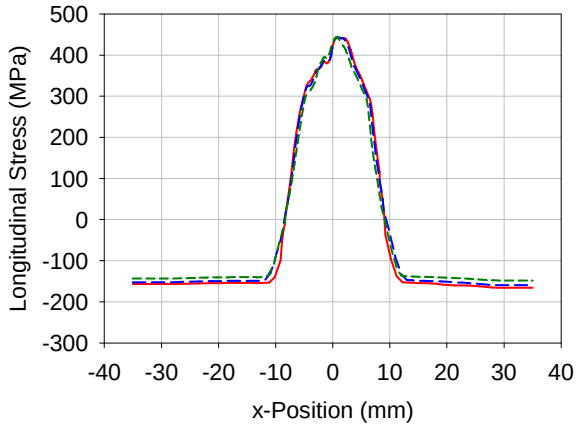

(a)

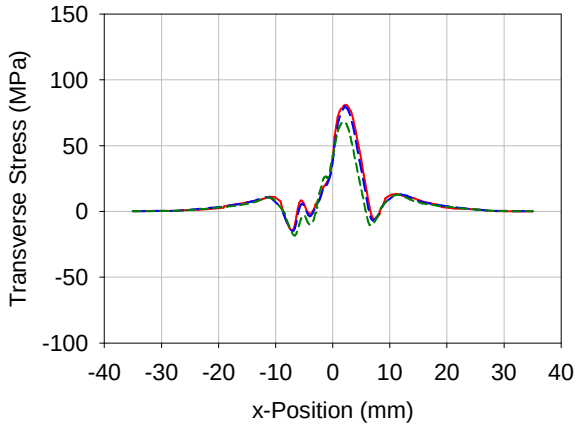

(b)

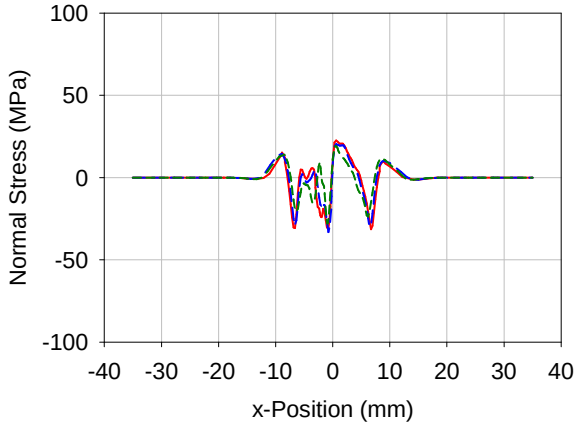

(c)

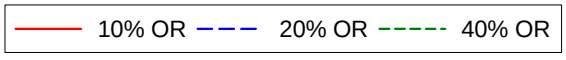

Figure 7.35: A comparison between the numerical predictions, for an OR of 10%, 20% and 40% for the zig-zag deposition strategy for (a) Longitudinal stress (σ_{yy}) (b) Transverse stress (σ_{xx}) and (c) Normal stress (σ_{zz}).

A comparison between the residual stresses, within the track, for the spiral and zig-zag deposition strategy, are presented in Figure 7.36 and 7.37 respectively. The data was taken at the centre of each bead and averaged over a 1 x 1 x 1 mm^3 volume to be consistent with the validation cases (Section 7.5.2). From analysing Figure 7.36 and 7.37, the OR had a greater effect on the profile and magnitude of the residual stress within the deposition than for the sub-surface stresses.

For the spiral deposition strategy (Figure 7.36), it was observed for a greater OR, the magnitude of the longitudinal stress reduced for the first and second track of the deposition. The greatest reduction was observed between the 10% and 40% OR which equated 11.8%. For the final track, the magnitude of the longitudinal stress was identical for all of the OR's. For the 10% and 20% OR, between the first and second track, there was a reduction of 0.55% and 0.44% in the longitudinal stress component. The first and second track for this deposition strategy should have very similar peak residual stresses due to the identical processing conditions. As the percentage difference was so small, this reduction in peak residual stress, between the first and second track, can be accounted for by numerical error in the FE analysis. The reduction observed in the longitudinal stress, for an increase in OR was due to the increase in re-melted volume of the first and second track. This would cause and annealing effect in these regions which would reduce the accumulated strain to zero. As the 40% OR has the greatest volume of re-melted track, a larger proportion of the deposition region would have had a reduction in the accumulated strain, when compared to the other two OR's. Due to this, a reduction in the amount of accumulated strain, in the the first and second track, during the final deposition would have occurred; therefore, this lead to the residual stress in each track being approximately equal. The transverse stress component, presented in Figure 7.36(b) was approximately constant within each track, for each of the investigated OR's. Again the variation in the magnitude was due to numerical error as aforementioned. Similar to the longitudinal component, a

reduction in magnitude of the transverse component was observed for an increase in the OR, this again could be due to the amount of re-melted track region and the redistribution of the accumulated strain. For the normal stress component (Figure 7.36(c)), both the magnitudes and profile of the residual stresses, within the bead, were approximately equal for each OR.

From Figure 7.37, it was apparent that a greater variation in the magnitude of the residual stresses and the subsequent profiles for each component were determined for the zig-zag strategy when compared to the spiral strategy. For the longitudinal component, the residual stress profile for the 10% and 20% OR were similar, with the greatest stress magnitude being at the location of the first and second track. A reduction in the stress magnitude was observed for the final track, with the value being equal to the final track in the spiral strategy. For the 40% OR, a reduction in the longitudinal stress was observed for each track, with the peak stress being present in the first deposition. Unlike the spiral strategy, a reduction in the magnitude of the residual stress for the first and second deposition was not observed through a greater volume of re-melted track. As the peak stress was at the location of the first track, it was believed that directional effects due to the motion of the heat source had an effect on the redistribution of strain after annealing has occurred. For the spiral strategy, the first and second track were reheated in the same direction across the entire length of the track. For the zig-zag deposition, the heat source was traversing in alternating directions. Therefore, each previous track was reheated form a different direction, introducing directional solidification effects into the sample.

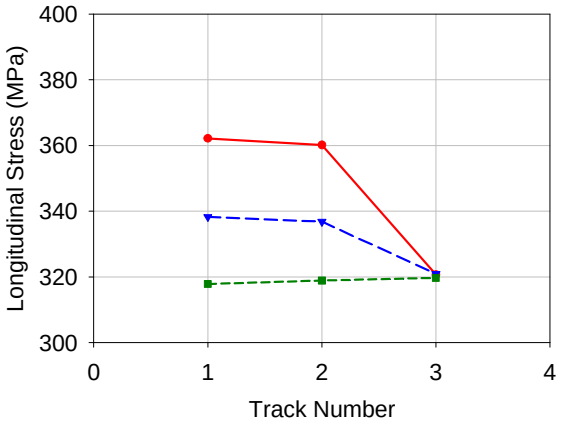

(a)

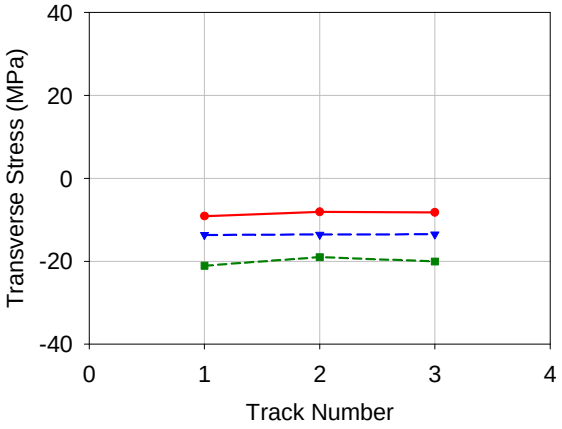

(b)

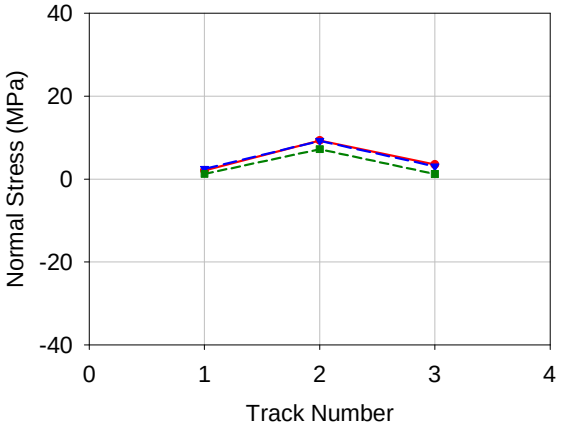

(c)

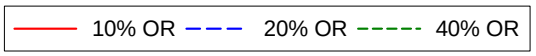

Figure 7.36: A comparison between the numerical predictions, for an OR of 10%, 20% and 40% for the spiral deposition strategy, at the track centre, at y=60 mm for (a) Longitudinal stress (σ_{yy}) (b) Transverse stress (σ_{xx}) and (c) Normal stress (σ_{zz}).

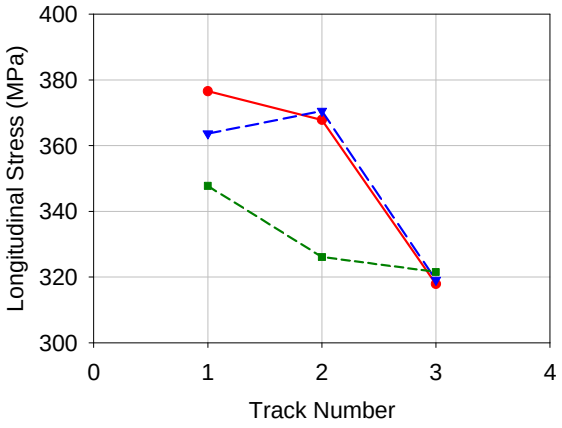

(a)

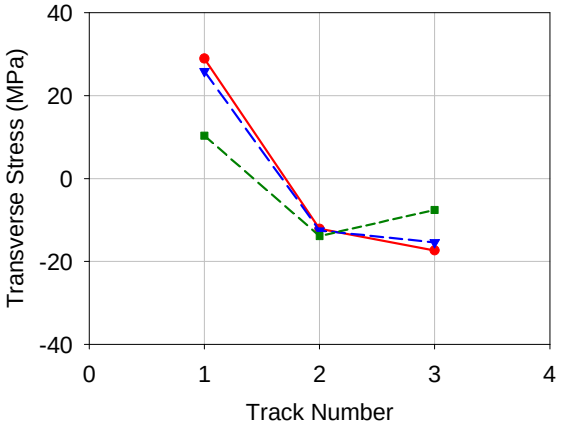

(b)

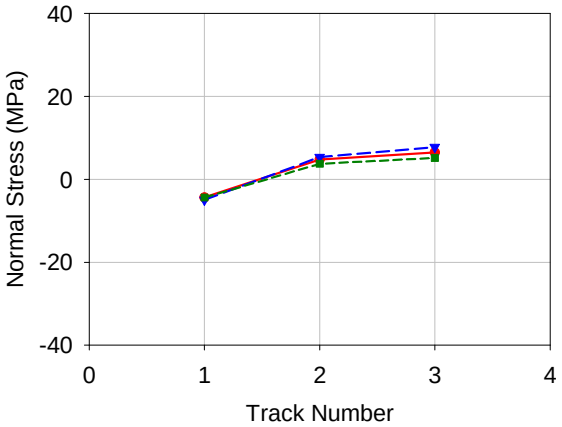

(c)

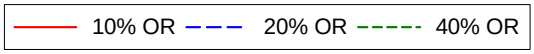

Figure 7.37: A comparison between the numerical predictions, for an OR of 10%, 20% and 40% for the zig-zag deposition strategy, at the track centre, at y=60 mm for (a) Longitudinal stress (σ_{yy}) (b) Transverse stress (σ_{xx}) and (c) Normal stress (σ_{zz}).

This phenomena could be a potential cause of the higher peak stresses exhibited in the first and second track. In comparison to the spiral strategy, uniform reheat directions could be the reason for the reduction observed in the peak stresses (Figure 7.36), thus highlighting that the directional effects of the heat source are less important for the spiral deposition strategy. For the transverse stress component (Figure 7.37(b)), both the magnitudes and profile for the 10% and 20% OR were similar, showing a reduction in magnitude for each track. Again, similar to the longitudinal component, the 40% OR exhibited different stress magnitudes, having a different profile when compared to the other two OR's. Again, similar to the spiral strategy, both the magnitude and profile for the normal residual stress component were approximately equal for each OR (Figure 7.37(c)).

7.6 Conclusions

- For the multi-track profile, a maximum and minimum error between the experimental and predicted track height for the spiral strategy was 7.93% and 0.78% respectively. For the zig-zag strategy, the percentage error was 9.66% and 0.78% respectively. The maximum and minimum error for the total deposition width for the spiral strategy was 1.66% and 1.23% respectively. This equated 4.69% and 1.66% for the zig-zag strategy respectively.

- The overlap region between two adjacent tracks, fabricated using coaxial deposition, can be modelled using a circular fillet. A modification to the height of the final deposition for the spiral strategy was required due to the interaction of the heat source between the gap of the two previously deposited tracks.

- The melt pool geometry of a multi-track deposition can be captured using a combination of a semi-elliptical region and a skewed half ellipse. This was

described using a geometrical relationship which allowed the track profile to be determined based on Gaussian powder distribution.

- A good correlation was obtained between the experimental and numerical peak residual stresses with a maximum error of 7.2% and 6.4%, for the spiral and zig-zag deposition strategy respectively. It should be noted that the use of laser scanning and a virtual experimental environment should be implemented to mitigate positioning errors for ND measurements; therefore reducing the overall error in the residual stress profiles.

- The sub-surface residual stresses within the substrate were not effected by the deposition OR. A greater variation was observed for the residual stress within each track when comparing the effects of the OR and deposition strategy.

- For the spiral strategy, a reduction in the peak residual stress was observed within the bead for an increase in OR. A constant magnitude of stress was present in each track for the 40% OR and was due to the greater volume of re-melting causing a greater relaxation in the accumulated strain.

- For the zig-zag strategy, a greater peak residual stress was observed for the first and second track, with no reduction in the peak stresses for subsequent deposits; therefore, this highlights the possible directional effects of the heat source on the redistribution of residual stresses.

Chapter 8

Conclusions and Future Work

8.1 Conclusions

The key findings and conclusions from the presented research work are as follows:

- When implementing the thermal model calibration, it allowed a key stage of the sequentially coupled thermo-mechanical approach for welding/deposition to be automated. The developed method allowed prediction of the optimum element size, thermal model parameters and heat source parameters to be determined from experimental specimens based on an inverse approach. The developed approach allows a more accurate and efficient prediction of the thermal fields of DED for industrial application.

- To completely calibrate the thermal DED model, a weighted sum multi objective optimisation was required. From previous work in the literature, a single objective optimisation was used which was appropriate for when the heat source model has one geometrical parameter; however, for all other cases, a multi objective function should be considered. However, the current issue with the proposed method was that a good initial guess was required due to a local optimisation algorithm being used. A good initial guess for the optimisation was determined through physical measurements of the

experimental melt pool geometry, but global minimisation of the problem may still not be achieved.

- An improved modelling methodology was developed for single-track deposition. This allowed a realistic track geometry to be predicted and used to evaluate the thermo-mechanical effects of the DED process based on key process parameters. Although there was an addition of material during the process, the resulting longitudinal residual stress profile shows a similar trend to a traditional single pass weld. Therefore this component of stress was driven predominantly by the expansion/contraction of the substrate material. The transverse and normal stress components show similar trends to one another, and although a thick substrate was used, a plane stress condition was not exhibited. A non-uniform residual stress distribution was predicted between the substrate and the track. Reducing this high stress gradient is required to ensure the track does not separate from the substrate.

- Simplified track geometries can be used to replace the true track geometry to predict the thermal and mechanical effects of the DED process. From analysing multiple combinations of simplified geometry, a square profile which has the same width and height as the true profile, should be used. This provided a negligible difference between the thermal histories and residual stress profiles when implementing a true track profile. With the use of the simplified geometry, a better representation of the build geometry would be achieved for multiple tracks; however, a conservative approach should be adopted when using the simplified geometry, as a greater volume of material will be present in the analysis. It should also be noted that no attempt can be made to determine the geometry of overlapped tracks when using a square profile. Therefore, this methodology should only be used for

single track analysis or where the geometry of the repair was not of interest.

- The modelling strategy presented here can aid in devising an optimum set of process parameters to ensure a geometrically accurate build is attained and to assess the combination of process parameters which can control the cooling rate and the evolution of stress within the component.

- A generalised methodology to model the effects of adaptive process control was developed, allowing the variation in track profile, thermal history and residual stress fields to be predicted. The presented model allows deposition tracks with varying cross sections to be predicted; therefore, an optimum tool path can be determined to ensure a more efficient use of the deposition material by only refilling the damaged area of the component. The developed method will allow for bespoke repair strategies to be designed, without the need for lengthy and costly experimental trials. Complex parametric studies can be conducted using the presented methodology; therefore, an assessment of the proposed repair strategy on the distortion and residual stress formation within the repaired component, can be completed.

- It was determined that through adapting the in-situ laser power, minimal variation was observed in the trend for the stress evolution and the final residual stress state at three distinct locations within the track. The longitudinal stress increased with laser power, with negligible deviation in the other two stress components. A plane stress condition was not observed due to the interaction of the track geometry and the substrate at the interface between them. High magnitude residual stresses are present with a minimal reduction being observed through controlling the laser power.

- A generalised approach to predict the track profile, thermal and residual stress fields for multi-track deposition was devised. It was determined that the overlap region between two adjacent tracks, fabricated using coaxial

deposition, can be modelled using a circular fillet. A modification to the height of the final deposition for a spiral tool path was required due to the interaction of the heat source between the gap of the two previously deposited tracks. The melt pool geometry of a multi-track deposition can be captured using a combination of a semi-elliptical region and a skewed half ellipse.

- When analysing the effects of the overlap ratio (OR) and deposition strategy on the residual stress fields, the sub-surface residual stresses within the substrate were not affected by the overlap ratio. For the spiral strategy, a reduction in the peak residual stress was observed within the track for an increase in overlap ratio. A constant magnitude of stress was present in each track for the 40% overlap ratio and was due to the greater volume of re-melting causing a greater relaxation in the accumulated strain. For the zig-zag strategy, a greater peak residual stress was observed for the first and second tracks, with no reduction in the peak stresses for subsequent deposits; therefore, this highlights the possible directional effects of the heat source on the redistribution of residual stresses.

- With regards to experimental validation of the modelling methodologies, the use of metallographic specimens was satisfactory to evaluate both the track geometry and melt pool shape and compare these to the corresponding predictions. For the mechanical portion of the model, a number of neutron diffraction measurements were used which provided a good correlation with the predicted stress profiles. It should be noted that to ensure a high degree of accuracy was attained in the neutron diffraction measurements, the use of laser scanning and a virtual experimental environment should be implemented. This mitigates positioning errors for the measurements; therefore reducing the overall error in the residual stress profiles.

8.2 Future Work

As part of this research work, four key areas, which are used to identify if DED is acceptable for repair based on simulation data, were presented. From the process flow in Figure 8.1, this included calibration of the FE model (Chapter 4), single-track (Chapter 5), multi-track (Chapter 7) and adaptive process control (Chapter 6) predictions.

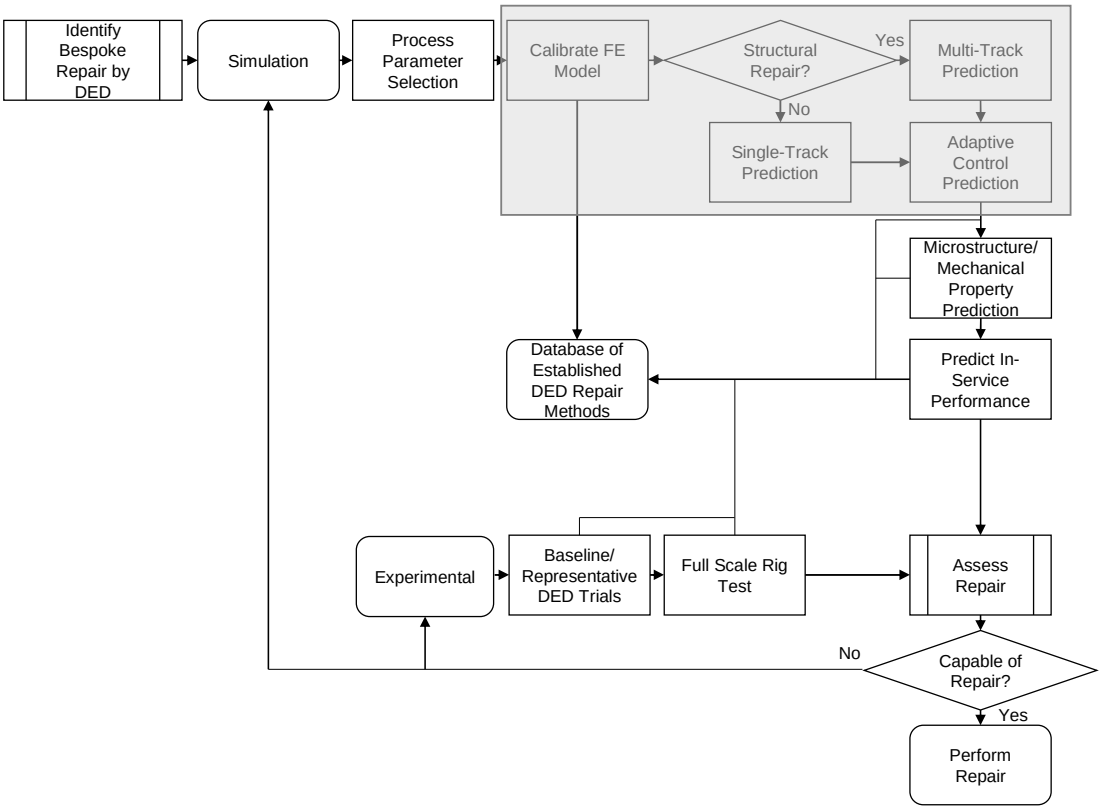

Figure 8.1: Process flow to identify the process capability of DED using experimental and modelling methods. The work as presented in Chapter 4-7 is highlighted in grey.

Although some simulation tools have been developed as part of this research work, to fully allow a bespoke repair solution to be identified and assessed, further work in in this field is required. Therefore, the recommendations for potential future work, which would improve and also extend the tool set presented in this study, are as follows:

- The initial guess for the optimisation was determined through physical mea-

surements of the experimental melt pool geometry. A method which determines these parameters, based on a global optimisation algorithm, would be beneficial to ensure the true local minima of the solution was determined. Secondly, a method to determine the optimum weight which allows the correct contribution from each objective to be achieved should be designed, instead of relying on an extensive parametric study.

- In all of the thermo-mechanical analyses, the material properties of both the deposit and substrate were not altered throughout the analysis to include the effects of microstructure and phase changes during the heating and cooling phase of the process. Therefore, numerical methods, such as Monte-Carlo and Cellular Automata (CA), could be coupled with the devised FE methods to predict the microstructure evolution during the repair.

- From the presented studies, high magnitude residual stresses were present in all of the specimens. As these types of stresses will reduce the life of the component, further study should be conducted to determine methods that control the evolution of high magnitude stresses. This could be achieved through adaptive process control or devising novel tool paths for multi-track deposition.

- A major drawback of the presented methodologies was the computational deficit of using the FE method. For the thermal model, a more computationally efficient approach, such as the Finite Difference (FD) method, could be used to increase the efficiency of predicting transient thermal fields. As it would be difficult to devise an analytical method for predicting residual stresses, the deficit arises due to rebuilding of the stiffness matrix during the reactivation of the elements. Therefore, a novel method of element reactivation could be devised to alleviate the computational time associated with this process. Also, it should be noted that if the proposed models are

used to assess the repair for large geometries, a significant computational time will be required, therefore, the use of a sub-modelling methodology could be used to assess parts of the repair with a higher fidelity in the key regions of interest.

- A database of results to devise process maps could be determined through implementing the methodologies outlined in this work. This would enable the process parameters of the repair to be quickly determined, increasing the efficiency of the repair process. However, as this would be computationally expensive, a neural network could be implemented which has been trained using the numerical methods in this work. This would allow the process parameters to be determined by defining the final requirements of repair which could include; the build height, cooling rates and peak residual stresses at key locations.

- The current methods presented in this work are an accurate representation of the DED process; however, in order to implement the models, a balance between the accuracy and efficiency of the solution needs to be attained. Utilising simplified geometries has been analysed as part of this study, however, this should be extended to analyse its affect on multi-track deposits. Another improvement could be made through implementing full layer-by-layer reactivation instead of the element-by-element method currently used. This could be further extended to determine if element activation is needed for only the thermal/mechanical model or if this modelling technique is not required. Different modelling techniques could also be used to improve the efficiency of the current approaches. This could include; steady-state models for the thermal prediction, local-global modelling depending on the required size of the analysis and using the inherent-strain method for mechanical predictions.

Bibliography

[1] S L Sing et al. *3D printing of metals in rapid prototyping of biomaterials: Techniques in additive manufacturing*. Second Edition. Elsevier Ltd., 2020, pp. 17–40. ISBN: 9780081026632. DOI: 10.1016/B978-0-08-102663-2.00002-2.

[2] Bintao Wu et al. "A review of the wire arc additive manufacturing of metals : properties , defects and quality improvement A review of the wire arc additive manufacturing of metals : properties , defects and quality improvement". In: *Journal of Manufacturing Processes* 35.July (2020), pp. 127–139. ISSN: 1526-6125. DOI: 10.1016/j.jmapro.2018.08.001.

[3] K S Derekar. "A review of wire arc additive manufacturing and advances in wire arc additive manufacturing of aluminium." In: *Materials Science and Technology* 34.8 (2018), pp. 895–916. DOI: 10.1080/02670836.2018.1455012.

[4] Joel C. Najmon, Sajjad Raeisi, and Andres Tovar. "2 - Review of additive manufacturing technologies and applications in the aerospace industry". In: *Additive Manufacturing for the Aerospace Industry*. Ed. by Francis Froes and Rodney Boyer. Elsevier, 2019, pp. 7 –31. ISBN: 978-0-12-814062-8. DOI: https://doi.org/10.1016/B978-0-12-814062-8.00002-9.

[5] Gary P. Halada and Clive R. Clayton. "Chapter 19 - The Intersection of Design, Manufacturing, and Surface Engineering". In: *Handbook of Environmental Degradation of Materials (Third Edition)*. Ed. by Myer Kutz.

Third Edition. William Andrew Publishing, 2018, pp. 397 –422. ISBN: 978-0-323-52472-8. DOI: https://doi.org/10.1016/B978-0-323-52472-8.00019-8.

[6] Paola M Cordero and Jorge Mireles. "Evaluation of monitoring methods for electron beam melting powder bed fusion additive manufacturing technology". In: *Progress in Additive Manufacturing* 2.1 (2017), pp. 1–10. ISSN: 2363-9520. DOI: 10.1007/s40964-016-0015-6.

[7] Richard Bibb. "5 - Physical reproduction – rapid prototyping technologies". In: *Medical Modelling*. Ed. by Richard Bibb. Woodhead Publishing Series in Biomaterials. Woodhead Publishing, 2006, pp. 59 –96. ISBN: 978-1-84569-138-7. DOI: https://doi.org/10.1533/9781845692001.59.

[8] Nima Shamsaei et al. "An overview of Direct Laser Deposition for additive manufacturing; Part II: Mechanical behavior, process parameter optimization and control". In: *Additive Manufacturing* 8 (2015), pp. 12–35. ISSN: 22148604. DOI: 10.1016/j.addma.2015.07.002. arXiv: arXiv:1011.1669v3.

[9] Jennifer Bennett et al. "Repairing Automotive Dies With Directed Energy Deposition: Industrial Application and Life Cycle Analysis". In: *Journal of Manufacturing Science and Engineering* 141.2 (Dec. 2018). 021019. ISSN: 1087-1357. DOI: 10.1115/1.4042078. eprint: https://asmedigitalcollection.asme.org/manufacturingscience/article-pdf/141/2/021019/6279819/manu_141_02_021019.pdf.

[10] Jinglei Wang et al. *Laser Aided Part Repair- A Review*.

[11] Orazio Svelto. *Principles of Lasers*. fifth. Springer US, 2010, pp. 1–31. DOI: 10.1007/978-1-4419-1302-9.

[12] Subhash Chandra Singh et al. *Nanomaterials: Processing and Characterization with Lasers*. First. Wiley-VCH Verlag GmbH & Co., 2012, pp. 1–34.

[13] Rudiger Paschotta. *Encyclopedia of Laser Physics and Technology*. 2008. DOI: https://www.rp-photonics.com/lasers.html.

[14] Andrew J. Pinkerton. "Advances in the modeling of laser direct metal deposition". In: *Journal of Laser Applications* 27.S1 (2015), S15001. ISSN: 1042-346X. DOI: 10.2351/1.4815992.

[15] Bei He et al. "Effect of weld repair on microstructure and mechanical properties of laser additive manufactured Ti-55511 alloy". In: *Materials and Design* 119 (2017), pp. 437–445. ISSN: 18734197. DOI: 10.1016/j.matdes.2017.01.054.

[16] P Peyre et al. "Analytical and numerical modelling of the direct metal deposition laser process". In: *Journal of Physics D: Applied Physics* 41.2 (2008), p. 025403. ISSN: 0022-3727. DOI: 10.1088/0022-3727/41/2/025403.

[17] Antonio Candel-ruiz, Sebastian Kaufmann, and Oliver Müllerschön. "Strategies for high deposition rate additive manufacturing by Laser Metal Deposition". In: 49.0 (2015), pp. 2–7.

[18] Torsten Petrat et al. "Laser metal deposition as repair technology for a gas turbine burner made of inconel 718". In: *Physics Procedia* 83 (2016), pp. 761–768. ISSN: 18753892. DOI: 10.1016/j.phpro.2016.08.078.

[19] Scott M. Thompson et al. "An overview of Direct Laser Deposition for additive manufacturing; Part I: Transport phenomena, modeling and diagnostics". In: *Additive Manufacturing* 8 (2015), pp. 36–62. ISSN: 22148604. DOI: 10.1016/j.addma.2015.07.001.

[20] Eun Mi Lee et al. "Study of the effects of process parameters on deposited single track of M4 powder based direct energy deposition." In: *Journal of Mechanical Science and Technology* 31 (2017), pp. 3411–3418.

[21] Bei He et al. "Effect of weld repair on microstructure and mechanical properties of laser additive manufactured Ti-55511 alloy". In: *Materials and Design* 119 (2017), pp. 437–445. ISSN: 18734197. DOI: 10.1016/j.matdes.2017.01.054.

[22] M Labudovic and Radovan Kovacevic. "A three dimensional model for direct laser metal". In: *Journal of Materials Science* 8 (2003), pp. 35–49.

[23] A.J. Pinkerton et al. "A Verified Model of Laser Direct Metal Deposition Using an Analytical Enthalpy Balance Method". In: *Proceedings of the 26th International Congress on Applications of Lasers and Electro-optics (ICALEO)* (2007).

[24] Chongliang Zhong et al. "Experimental study of effects of main process parameters on porosity, track geometry, deposition rate, and powder efficiency for high deposition rate laser metal deposition". In: *Journal of Laser Applications* 27.4 (2015), p. 042003. ISSN: 1042-346X. DOI: 10.2351/1.4923335.

[25] M. Naveed Ahsan and Andrew J. Pinkerton. "An analytical-numerical model of laser direct metal deposition track and microstructure formation". In: *Modelling and Simulation in Materials Science and Engineering* 19.5 (2011), pp. 1–22. ISSN: 09650393. DOI: 10.1088/0965-0393/19/5/055003.

[26] P. J. Withers et al. "Methods for obtaining the strain-free lattice parameter when using diffraction to determine residual stress". In: *Journal of Applied Crystallography* 40.5 (2007), pp. 891–904. ISSN: 00218898. DOI: 10.1107/S0021889807030269.

[27] Sebastian Nervi and Barna A Szabo. "On the estimation of residual stresses by the crack compliance method ´". In: 196 (2007), pp. 3577–3584. DOI: 10.1016/j.cma.2006.10.037.

[28] Michael B. Prime and Adrian T. DeWald. "The Contour Method". In: *Practical Residual Stress Measurement Methods*. John Wiley and Sons, Ltd, 2013. Chap. 5, pp. 109–138. ISBN: 9781118402832. DOI: 10.1002/9781118402832.ch5.

[29] P.J. Withers and H.K.D.H. Bhadeshia. "Residual stress. Part 1 – Measurement techniques". In: *Materials Science and Technology* 17.4 (2001), pp. 355–365. DOI: 10.1179/026708301101509980.

[30] Subodh Kumar et al. "Determination of layer thickness in direct metal deposition using dimensional analysis". In: *The International Journal of Advanced Manufacturing Technology* 67.9-12 (2013), pp. 2681–2687. ISSN: 0268-3768. DOI: 10.1007/s00170-012-4683-1.

[31] Yuwen Sun and Mingzhong Hao. "Statistical analysis and optimization of process parameters in Ti6Al4V laser cladding using Nd : YAG laser". In: *Optics and Lasers in Engineering* 50.7 (2012), pp. 985–995. ISSN: 0143-8166. DOI: 10.1016/j.optlaseng.2012.01.018.

[32] Ronald Guille et al. "Analysis and prediction of single laser tracks geometrical characteristics in coaxial laser cladding process". In: *Optics and Lasers in Engineering* 50 (2012), pp. 413–422. DOI: 10.1016/j.optlaseng.2011.10.014.

[33] J. Paulo Davim, Carlos Oliveira, and A. Cardoso. "Predicting the geometric form of clad in laser cladding by powder using multiple regression analysis (MRA)". In: *Materials and Design* 29.2 (2008), pp. 554–557. ISSN: 18734197. DOI: 10.1016/j.matdes.2007.01.023.

[34] V Ocelík et al. "Thick Co-based coating on cast iron by side laser cladding : Analysis of processing conditions and coating properties". In: *Surface & Coatings Technology* 201 (2007), pp. 5875–5883. DOI: 10.1016/j.surfcoat.2006.10.044.

[35] Yan-Lu Huang et al. "Three-dimensional analytical model on laser-powder interaction during laser cladding". In: *Journal of Laser Applications* 18.1 (2006), pp. 42–46. DOI: 10.2351/1.2164476.

[36] Yunchang Fu et al. "A theoretical model for laser and powder particles interaction during laser cladding". In: *Journal of Materials Processing Technology* 128.1-3 (2002), pp. 106–112. ISSN: 09240136. DOI: 10.1016/S0924-0136(02)00433-8.

[37] H. E. Cline and T. R. Anthony. "Heat treating and melting material with a scanning laser or electron beam". In: *Journal of Applied Physics* 48.9 (1977), pp. 3895–3900. ISSN: 00218979. DOI: 10.1063/1.324261.

[38] O. O. Diniz Neto and R. Vilar. "Physical–computational model to describe the interaction between a laser beam and a powder jet in laser surface processing". In: *Journal of Laser Applications* 14.1 (2002), pp. 46–51. DOI: 10.2351/1.1436485.

[39] Juansethi Ibarra-Medina, Michael Vogel, and Andrew J Pinkerton. "A CFD model of laser cladding: From deposition head to melt pool dynamics". In: *International Congress on Applications of Lasers & Electro-Optics* 2011.1 (2011), pp. 378–386. DOI: 10.2351/1.5062261.

[40] Gangxian Zhu et al. "Optics & Laser Technology Numerical simulation of metallic powder flow in a coaxial nozzle in laser direct metal deposition". In: *Optics and Laser Technology* 43.1 (2011), pp. 106–113. ISSN: 0030-3992. DOI: 10.1016/j.optlastec.2010.05.012.

[41] Gabriele Piscopo, Eleonora Atzeni, and Alessandro Salmi. "A Hybrid Modeling of the Physics-Driven Evolution of Material Addition and Track Generation in Laser Powder Directed Energy Deposition". In: *Materials (Basel)* 17.12 (2019). DOI: 10.3390/ma12172819.

[42] James C Haley, Julie M Schoenung, and Enrique J Lavernia. "Materials Science & Engineering A Modelling particle impact on the melt pool and wettability e ff ects in laser directed energy deposition additive manufacturing". In: *Materials Science & Engineering A* 761.June (2019), p. 138052. ISSN: 0921-5093. DOI: 10.1016/j.msea.2019.138052.

[43] M. Picasso et al. "A simple but realistic model for laser cladding". In: *Metallurgical and Materials Transactions B* 25.2 (1994), pp. 281–291. ISSN: 10735615. DOI: 10.1007/BF02665211.

[44] Wei Ya, B. Pathiraj, and Shaojie Liu. "2D modelling of clad geometry and resulting thermal cycles during laser cladding". In: *Journal of Materials Processing Technology* 230 (2016), pp. 217–232. ISSN: 09240136. DOI: 10.1016/j.jmatprotec.2015.11.012.

[45] Kamran Shah et al. "Numerical modelling of pulsed and continuous wave direct laser deposition of Ti-6Al-4V and Inconel 718". In: *International Journal of Advanced Manufacturing Technology* 95.1-4 (2018), pp. 847–860. ISSN: 14333015. DOI: 10.1007/s00170-017-1224-y.

[46] Zhe Zhang and Radovan Kovacevic. "A thermo-mechanical model for simulating the temperature and stress distribution during laser cladding process". In: *The International Journal of Advanced Manufacturing Technology* 102 (2019), pp. 457–472.

[47] Masoud Alimardani, Ehsan Toyserkani, and Jan P. Huissoon. "Three-dimensional numerical approach for geometrical prediction of multilayer

laser solid freeform fabrication process". In: *Journal of Laser Applications* 19.1 (2007), pp. 14–25. ISSN: 1042-346X. DOI: 10.2351/1.2402518.

[48] Youxiang Chew et al. "Thermo-mechanical model for simulating laser cladding induced residual stresses with single and multiple clad beads". In: *Journal of Materials Processing Technology* 224 (2015), pp. 89–101. ISSN: 09240136. DOI: 10.1016/j.jmatprotec.2015.04.031.

[49] T Mukherjee, W Zhang, and T Debroy. "An improved prediction of residual stresses and distortion in additive manufacturing". In: *Computational Materials Science* 126 (2017), pp. 360–372. ISSN: 0927-0256. DOI: 10.1016/j.commatsci.2016.10.003.

[50] F Martina et al. "Investigation of the benefits of plasma deposition for the additive layer manufacture of Ti – 6Al – 4V". In: *Journal of Materials Processing Tech.* 212.6 (2012), pp. 1377–1386. ISSN: 0924-0136. DOI: 10.1016/j.jmatprotec.2012.02.002.

[51] F Martina, S. W. Williams, and P Colegrove. "Design of an empirical process model and algorithm for the tungsten inert gas wire+arc additive manufacture of ti-6al-4v components". In: *24th International Solid Freeform Fabrication Symposium*. August. 2013, pp. 697–707.

[52] Sergio Ríos et al. "Analytical process model for wire + arc additive manufacturing". In: *Additive Manufacturing* 21.January (2018), pp. 651–657. ISSN: 2214-8604. DOI: 10.1016/j.addma.2018.04.003.

[53] Xiangman Zhou, Haiou Zhang, and Guilan Wang. "Three-Dimensional Numerical Simulation of Arc and Metal Transport for Stacking Deposition in Arc Welding Based Additive Manufacturing". In: *27th Annual International SOlid Freeform Fabrication Symposium*. 2016, pp. 268–285.

[54] Xingwang Bai et al. "Numerical Analysis of Heat Transfer and Fluid Flow in Multilayer Deposition of PAW-based Wire and Arc Additive Manufac-

turing". In: *International Journal of Heat and Mass Transfer* 124.September (2018), pp. 504–516. DOI: 10.1016/j.ijheatmasstransfer.2018.03.085.

[55] J Lundkvist. "CFD Simulation of Fluid Flow During Laser Metal Wire Deposition using OpenFOAM : 3D printing". PhD thesis. 2019.

[56] Filippo Montevecchi et al. "Finite element modelling of Wire-Arc-Additive-Manufacturing process". In: *Procedia CIRP* 55 (2016), pp. 109–114. ISSN: 2212-8271. DOI: 10.1016/j.procir.2016.08.024.

[57] Keval P Prajadhiama et al. "Development of Bead Modelling for Distortion Analysis Induced by Wire Arc Additive Manufacturing using FEM and Experiment". In: 05003 (2019), pp. 4–11.

[58] J Ding et al. "Thermo-mechanical analysis of Wire and Arc Additive Layer Manufacturing process on large multi-layer parts". In: *Computational Materials Science* 50.12 (2011), pp. 3315–3322. ISSN: 0927-0256. DOI: 10.1016/j.commatsci.2011.06.023.

[59] J Ding et al. "A computationally efficient finite element model of wire and arc additive manufacture". In: *International Journal of Advanced Manufacturing Technology* 70 (2014), pp. 227–236. DOI: 10.1007/s00170-013-5261-x.

[60] J Christian Nelson et al. "Model of the Selective Laser Sintering of Bisphenol-A Polycarbonate". In: (1993), pp. 2305–2317. DOI: 10.1021/ie00022a014.

[61] A Simchi. "Direct laser sintering of metal powders : Mechanism , kinetics and microstructural features". In: 428 (2006), pp. 148–158. DOI: 10.1016/j.msea.2006.04.117.

[62] Giovanni Strano et al. "Journal of Materials Processing Technology Surface roughness analysis , modelling and prediction in selective laser melt-

ing". In: *Journal of Materials Processing Tech.* 213.4 (2013), pp. 589–597. ISSN: 0924-0136. DOI: 10.1016/j.jmatprotec.2012.11.011.

[63] C. Y. Yap, C. K. Chua, and Z. L. Dong. "An effective analytical model of selective laser melting". In: *Virtual and Physical Prototyping* 11.1 (2016), pp. 21–26. DOI: 10.1080/17452759.2015.1133217.

[64] Jinqiang Ning et al. "Analytical modeling of 3D temperature distribution in selective laser melting of Ti-6Al-4V considering part boundary conditions". In: *Journal of Manufacturing Processes* 44.March (2019), pp. 319–326. ISSN: 1526-6125. DOI: 10.1016/j.jmapro.2019.06.013.

[65] I O P Conference Series and Materials Science. "Particle scale modelling of porosity formation during selective laser melting process using a coupled DEM – CFD approach Particle scale modelling of porosity formation during selective laser melting process using a coupled DEM – CFD approach". In: (2019). DOI: 10.1088/1757-899X/529/1/012001.

[66] Cheng-jui Li, Tsung-wen Tsai, and Chien-chou Tseng. "Numerical simulation for heat and mass transfer during selective laser melting of titanium alloys powder". In: *Physics Procedia* 83 (2016), pp. 1444–1449. ISSN: 1875-3892. DOI: 10.1016/j.phpro.2016.08.150.

[67] Bo Cheng et al. "Multi-Physics Modeling of Single Track Scanning in Selective Laser Melting: Powder Compaction Effect". In: (2018), pp. 1887–1902.

[68] Claire Bruna-rosso, Julia Mergheim, and Barbara Previtali. "Finite element modeling of residual stress and geometrical error formations in selective laser melting of metals". In: *Proceedings of the Institution of Mechanical Engineers, Part C:Journal of Mechanical Engineering Science* 0.0 (2020), pp. 1–17. DOI: 10.1177/0954406220943225.

[69] Panagiotis Michaleris. "Modeling Metal Deposition in Heat Transfer Analyses of Additive Manufacturing Processes". In: *Finite Elem. Anal. Des.* 86.C (Sept. 2014), pp. 51–60. ISSN: 0168-874X. DOI: 10.1016/j.finel.2014.04.003.

[70] Tiebing Chen and Yuwen Zhang. "NUMERICAL SIMULATION OF TWO-DIMENSIONAL MELTING AND RESOLIDIFICATION OF A TWO-COMPONENT METAL POWDER LAYER IN SELECTIVE LASER SINTERING PROCESS". In: *Numerical Heat Transfer, Part A: Applications* 46.7 (2004), pp. 633–649. DOI: 10.1080/10407789504177.

[71] L Dong et al. "Three-dimensional transient finite element analysis of the selective laser sintering process". In: 9 (2008), pp. 700–706. DOI: 10.1016/j.jmatprotec.2008.02.040.

[72] Dongming Hu and Radovan Kovacevic. "Sensing , modeling and control for laser-based additive manufacturing". In: 43 (2003), pp. 51–60.

[73] Xiaogang You et al. "Effect of solution heat treatment on the precipitation behavior and strengthening mechanisms of electron beam smelted Inconel 718 superalloy". In: *Materials Science & Engineering A* 689.2 (2017), pp. 257–268. ISSN: 0921-5093. DOI: 10.1016/j.msea.2017.01.093.

[74] Zhiqiang Fan and Frank Liou. "Numerical Modeling of the Additive Manufacturing (AM) Processes of Titanium Alloy". In: *Titanium Alloys*. Ed. by A.K.M. Nurul Amin. Rijeka: IntechOpen, 2012. Chap. 1. DOI: 10.5772/34848.

[75] Pengfei Tan et al. "A thermo-metallurgical-mechanical model for selective laser melting of Ti6Al4V". In: *Materials & Design* 168 (2019), p. 107642. ISSN: 0264-1275. DOI: 10.1016/j.matdes.2019.107642.

[76] Haider Ali, Hassan Ghadbeigi, and Kamran Mumtaz. "Residual stress development in selective laser-melted Ti6Al4V : a parametric thermal mod-

elling approach". In: *International Journal of Advanced Manufacturing Technology* (2018), pp. 2621–2633.

[77] Lars Erik Lindgren et al. "Simulation of additive manufacturing using coupled constitutive and microstructure models". In: *Additive Manufacturing* 12 (2016), pp. 144–158. ISSN: 22148604. DOI: 10.1016/j.addma.2016.05.005.

[78] Carolin Körner, Elham Attar, and Peter Heinl. "Mesoscopic simulation of selective beam melting processes". In: *Journal of Materials Processing Technology* 211.6 (2011), pp. 978–987. ISSN: 09240136. DOI: 10.1016/j.jmatprotec.2010.12.016.

[79] John A Goldak. *Computational welding mechanics*. Ed. by Mehdi Akhlaghi. New York: New York : Springer, 2005.

[80] Carlos Felippa, K C Park, and Charbel Farhat. "Partitioned analysis of coupled system". In: *Computer Methods in Applied Mechanics and Engineering* 190 (Mar. 2001), 3247–3270. DOI: 10.1016/S0045-7825(00)00391-1.

[81] Carlo Nonino. "Book review The Finite Element Method in Heat Transfer Analysis by R. W. Lewis, K. Morgan, H. R. Thomas, K. N. Seetharamu, John Wiley & Sons Ltd., Chichester, U.K. 1996. ISBN: 0 471 93424 0; 0 471 94362 2. No. of pages 279." In: *International Journal for Numerical Methods in Engineering* 44.1 (1999), pp. 147–148. DOI: 10.1002/(SICI)1097-0207(19990110)44:1<147::AID-NME494>3.0.CO;2-M.

[82] S.S. Rao. *The Finite Element Method in Engineering: Pergamon International Library of Science, Technology, Engineering and Social Studies*. Pergamon International Library of Science, Technology, Engin. Elsevier Science, 2013. ISBN: 9781483136929.

[83] René Borst et al. "Non-Linear Finite Element Analysis of Solids and Structures: Second Edition". In: *Non-Linear Finite Element Analysis of Solids and Structures: Second Edition* (July 2012). DOI: 10.1002/9781118375938.

[84] J Ronda and Graeme Oliver. "Consistent thermo-mechano-metallurgical model of welded steel with unified approach to derivation of phase evolution laws and transformation-induced plasticity". In: *Computer Methods in Applied Mechanics and Engineering* 189 (Sept. 2000), pp. 361–418. DOI: 10.1016/S0045-7825(99)00461-2.

[85] William A. Johnson and Robert F. Mehl. "Reaction Kinetics in Processes of Nucleation and Growth". In: *TransAime* 135 (Aug. 1939), pp. 396–415.

[86] M. Avrami. "Kinetics of phase change. i general theory". In: *The Journal of Chemical Physics* 7 (Dec. 1939), pp. 1103–1112.

[87] A.N. Kolmogrov. "On the statistical theory of the crystallization of metals". In: *Bull. Acad. Sci. USSR* 1 (Jan. 1937), pp. 355–359.

[88] D.P. Koistinen and R.E. Marburger. "A general equation prescribing the extent of the austenite-martensite transformation in pure iron-carbon alloys and plain carbon steels". In: *Acta Metallurgica* 7.1 (1959), pp. 59–60. DOI: 10.1016/0001-6160(59)90170-1.

[89] D Rosenthal. "The Theory of Moving Sources of Heat and its Application to Metal Treatments". In: *Transactions of ASME* 43.11 (1946), pp. 849–866.

[90] R.R Rykalin. "Energy Sources For Welding". In: *Welding in the World* 12.9/10 (1974), pp. 227–248.

[91] John Goldak, Aditya Chakravarti, and Malcolm Bibby. "A new finite element model for welding heat sources". In: *Metallurgical Transactions B* 15.2 (1984), pp. 299–305. ISSN: 1543-1916. DOI: 10.1007/BF02667333.

[92] V. PAVELIC. "Experimental and computed temperature histories in gas tungsten arc welding of thin plates". In: *Welding Journal Research Supplement* 48 (1969), pp. 296–305.

[93] S A Tsirkas, P Papanikos, and Th Kermanidis. "Numerical simulation of the laser welding process in butt-joint specimens". In: 134 (2003).

[94] Peiyun Xia et al. "Prediction of weld shape for fiber laser keyhole welding based on finite element analysis". In: *The International Journal of Advanced Manufacturing Technology* 75.1 (2014), pp. 363–372. ISSN: 1433-3015. DOI: 10.1007/s00170-014-6129-4.

[95] Tadashi Kasuya and Nobuyuki Shimoda. "Stefan problem for a finite liquid phase and its application to laser or electron beam welding". In: *Journal of Applied Physics* 82.8 (1997), pp. 3672–3678. ISSN: 0021-8979. DOI: 10.1063/1.365730.

[96] Asghar Hozoorbakhsh et al. "An Investigation of Heat Transfer and Fluid Flow on Laser Micro-welding Upon the Thin Stainless Steel Sheet (SUS304) Using Computational Fluid Dynamics (CFD)". In: *International Communications in Heat and Mass Transfer* 75 (May 2016). DOI: 10.1016/j.icheatmasstransfer.2016.05.008.

[97] Philippe Le Masson et al. "A complete model of keyhole and melt pool dynamics to analyze instabilities and collapse during laser welding". In: *Journal of Laser Applications* 26 (Nov. 2014). DOI: 10.2351/1.4886835.

[98] M Gatzen and Z. Tang. "CFD-based model for melt flow in laser beam welding of aluminium with coaxial magnetic field". In: *Physics Procedia* 5 (2010). Laser Assisted Net Shape Engineering 6, Proceedings of the LANE 2010, Part 2, pp. 317 –326. ISSN: 1875-3892. DOI: https://doi.org/10.1016/j.phpro.2010.08.058.

[99] Lars-Erik Lindgren, Henrik Runnemalm, and Mats Näsström. "Simulation of multipass welding of a thick plate". In: *International Journal for Numerical Methods in Engineering* 44 (Mar. 1999), pp. 1301 –1316. DOI: 10.1002/(SICI)1097-0207(19990330)44:9<1301::AID-NME479>3.0.CO;2-K.

[100] Gervasio Salerno et al. "Finite element modelling strategies of weld repair in pre-stressed thin components". In: *The Journal of Strain Analysis for Engineering Design* 51.8 (2016), pp. 582–597. DOI: 10.1177/0309324716666436.

[101] A. M. Kamara, S. Marimuthu, and L. Li. "Finite Element Modeling of Microstructure in Laser-Deposited Multiple Layer Inconel 718 Parts". In: *Materials and Manufacturing Processes* 29.10 (2014), pp. 1245–1252. DOI: 10.1080/10426914.2014.930963.

[102] Andreas Lundbäck and Lars-Erik Lindgren. "Modelling of metal deposition". In: *Finite Elements in Analysis and Design - FINITE ELEM ANAL DESIGN* 47 (Oct. 2011), pp. 1169–1177. DOI: 10.1016/j.finel.2011.05.005.

[103] Panagiotis Michaleris. "Modeling metal deposition in heat transfer analyses of additive manufacturing processes". In: *Finite Elements in Analysis and Design* 86 (2014), pp. 51–60. ISSN: 0168874X. DOI: 10.1016/j.finel.2014.04.003.

[104] Udo Hartel et al. "Finite element modeling for the structural analysis of Al-Cu laser beam welding". In: *Physics Procedia* 83 (2016), pp. 1404–1414. ISSN: 18753892. DOI: 10.1016/j.phpro.2016.08.147.

[105] R. Timothy Marler and Jasbir S. Arora. "The weighted sum method for multi-objective optimization: new insights". In: *Structural and Multidis-*

ciplinary Optimization 41.6 (2010), pp. 853–862. ISSN: 1615-1488. DOI: 10.1007/s00158-009-0460-7.

[106] Jorge Nocedal and Stephen J. Wright. *Numerical Optimization*. Jan. 2006. ISBN: 978-0-387-30303-1. DOI: 10.1007/978-0-387-40065-5.

[107] Amin S. Azar, Sigmund K. Ås, and Odd M. Akselsen. "Determination of welding heat source parameters from actual bead shape". In: *Computational Materials Science* 54.1 (2012), pp. 176–182. ISSN: 09270256. DOI: 10.1016/j.commatsci.2011.10.025.

[108] O R Myhr and Ø Grong. "Dimensionless maps for heat flow analyses in fusion welding". In: *Acta Metallurgica et Materialia* 38.3 (1990), pp. 449–460. ISSN: 0956-7151. DOI: https://doi.org/10.1016/0956-7151(90)90151-6.

[109] Guangming Fu et al. "Parameter determination of double-ellipsoidal heat source model and its application in the multi-pass welding process". In: *Ships and Offshore Structures* 10.2 (2015), pp. 204–217. ISSN: 17445302. DOI: 10.1080/17445302.2014.937059.

[110] S Rouquette, J Guo, and P Le Masson. "Estimation of the parameters of a Gaussian heat source by the Levenberg – Marquardt method : Application to the electron beam welding". In: *International Journal of Thermal Sciences* 46 (2007), pp. 128–138. DOI: 10.1016/j.ijthermalsci.2006.04.015.

[111] A. Belitzki et al. "Automated heat source calibration for the numerical simulation of laser beam welded components". In: *Production Engineering* 10.2 (2016), pp. 129–136. ISSN: 18637353. DOI: 10.1007/s11740-016-0664-9.

[112] Mato Perić et al. "Numerical prediction and experimental validation of temperature and residual stress distributions in buried-arc welded thick

plates". In: *International Journal of Energy Research* January (2019), pp. 3590–3600. ISSN: 1099114X. DOI: 10.1002/er.4506.

[113] Panagis Foteinopoulos, Alexios Papacharalampopoulos, and Panagiotis Stavropoulos. "On thermal modeling of Additive Manufacturing processes". In: *CIRP Journal of Manufacturing Science and Technology* 20 (2018), pp. 66–83. ISSN: 17555817. DOI: 10.1016/j.cirpj.2017.09.007.

[114] A. Ganser et al. "Numerical simulation of the thermal efficiency during laser deep penetration welding". In: *Physics Procedia*. 2016. DOI: 10.1016/j.phpro.2016.08.144.

[115] Gervasio Salerno et al. "An experimental and numerical investigation on the process efficiency of the focused-tungsten inert gas welding of Inconel 718 thick plates". In: *Journal of Engineering Manufacture* 233.3 (2019), pp. 823–833. DOI: 10.1177/0954405418775442.

[116] W. A. Ayoola, W. J. Suder, and S. W. Williams. "Parameters controlling weld bead profile in conduction laser welding". In: *Journal of Materials Processing Technology* (2017). ISSN: 09240136. DOI: 10.1016/j.jmatprotec.2017.06.026.

[117] M.F. Ashby and K.E. Easterling. "The transformation hardening of steel surfaces by laser beams—I. Hypo-eutectoid steels". In: *Acta Metallurgica* 32.11 (1984), pp. 1935 –1948. ISSN: 0001-6160. DOI: https://doi.org/10.1016/0001-6160(84)90175-5.

[118] Heng Pan et al. "The Investigation of Gravity-Driven Metal Powder Flow in Coaxial Nozzle for Laser-Aided Direct Metal Deposition Process". In: *Journal of Manufacturing Science and Engineering* 128.May 2006 (2006), p. 541. ISSN: 10871357. DOI: 10.1115/1.2162588.

[119] Y Liu et al. "Prediction of weld shape for fiber laser welding based on hybrid heat source model". In: *3rd International Conference on Material, Mechanical and Manufacturing Engineering*. 2015, pp. 1868–1873.

[120] Andrew J Pinkerton and Lin Li. "Modelling Powder Concentration Distribution From a Coaxial Deposition Nozzle for Laser-Based Rapid Tooling". In: *Journal of Manufacturing Science and Engineering* 126.1 (2004), pp. 33–41. ISSN: 1087-1357. DOI: 10.1115/1.1643748.

[121] Wei Ya, B Pathiraj, and A J Huis. "A study on attenuation of a Nd : YAG laser power by co-axial and off-axial nozzle powder stream during cladding". In: 453.2013 (2015). DOI: 10.2351/1.5062916.

[122] N. Pirch et al. "Influence of process strategy on distortion and residual stresses for the powder based laser metal deposition process". In: *Materialwissenschaft und Werkstofftechnik* 48.12 (2017), pp. 1304–1313. ISSN: 09335137. DOI: 10.1002/mawe.201700169.

[123] Torsten Petrat et al. "Build-up strategies for temperature control using laser metal deposition for additive manufacturing". In: *Welding in the World* 62 (2018), pp. 1073–1081.

[124] M. Naveed Ahsan et al. "Porous structures fabrication by continuous and pulsed laser metal deposition for biomedical applications; Modelling and experimental investigation". In: *Journal of Materials Processing Technology* 211.4 (2011), pp. 602–609. ISSN: 09240136. DOI: 10.1016/j.jmatprotec.2010.11.014.

[125] Yanxiang Li and Jian Ma. "Study on overlapping in the laser cladding process". In: *Surface and Coatings Technology* 90 (1997), pp. 1–5.

[126] Yong Cao et al. "Robotics and Computer-Integrated Manufacturing Overlapping model of beads and curve fitting of bead section for rapid manufacturing by robotic MAG welding process". In: *Robotics and Computer*

Integrated Manufacturing 27.3 (2011), pp. 641–645. ISSN: 0736-5845. DOI: 10.1016/j.rcim.2010.11.002.

[127] Donghong Ding et al. "A multi-bead overlapping model for robotic wire and arc additive manufacturing (WAAM)". In: *Robotics and Computer-Integrated Manufacturing* 31 (2015), pp. 101–110.

[128] S Suryakumar et al. "Computer-Aided Design Weld bead modeling and process optimization in Hybrid Layered Manufacturing". In: *Computer-Aided Design* 43.4 (2011), pp. 331–344. ISSN: 0010-4485. DOI: 10.1016/j.cad.2011.01.006.

[129] V Ocelík et al. "On the geometry of coating layers formed by overlap". In: *Surface & Coatings Technology* 242 (2014), pp. 54–61. ISSN: 0257-8972. DOI: 10.1016/j.surfcoat.2014.01.018.

[130] Shaoyi Wen and Yung C Shin. "Comprehensive predictive modeling and parametric analysis of multitrack direct laser deposition processes Comprehensive predictive modeling and parametric analysis of multitrack direct laser deposition processes". In: *Journal of Laser Applications* 23.2 (2011). DOI: 10.2351/1.3567962.

[131] Parisa Farahmand and Radovan Kovacevic. "An experimental – numerical investigation of heat distribution and stress fi eld in single- and multi-track laser cladding by a high-power direct diode laser". In: *Optics and Laser Technology* 63 (2014), pp. 154–168. ISSN: 0030-3992. DOI: 10.1016/j.optlastec.2014.04.016.

[132] Neil S. Bailey, Christopher Katinas, and Yung C. Shin. "Laser direct deposition of AISI H13 tool steel powder with numerical modeling of solid phase transformation, hardness, and residual stresses". In: *Journal of Materials Processing Technology* 247.April (2017), pp. 223–233. ISSN: 09240136. DOI: 10.1016/j.jmatprotec.2017.04.020.

[133] Ehsan Foroozmehr and Radovan Kovacevic. "Effect of path planning on the laser powder deposition process : thermal and structural evaluation". In: *International Journal of Advanced Manufacturing Technology* 51.5-8 (2010), pp. 659–669. DOI: 10.1007/s00170-010-2659-6.

[134] Navid Nazemi and Ruth Urbanic. "A numerical investigation for alternative toolpath deposition solutions for surface cladding of stainless steel P420 powder on AISI 1018 steel substrate". In: *International Journal of Advanced Manufacturing Technology* 96 (2018), pp. 4123–4143.

[135] X. He, G. Yu, and J. Mazumder. "Temperature and composition profile during double-track laser cladding of H13 tool steel". In: *Journal of Physics D: Applied Physics* 43.1 (2010). ISSN: 00223727. DOI: 10.1088/0022-3727/43/1/015502.

[136] Zhengtao Gan et al. "Numerical simulation of thermal behavior and multicomponent mass transfer in direct laser deposition of Co-base alloy on steel". In: *International Journal of Heat and Mass Transfer* 104 (2017), pp. 28–38. ISSN: 00179310. DOI: 10.1016/j.ijheatmasstransfer.2016.08.049.

[137] D V Bedenko et al. "International Journal of Heat and Mass Transfer Numerical simulation of transport phenomena , formation the bead and thermal behavior in application to industrial DMD technology". In: *International Journal of Heat and Mass Transfer* 95 (2016), pp. 902–912. ISSN: 0017-9310. DOI: 10.1016/j.ijheatmasstransfer.2015.12.046.

[138] Knut Partes. "Analytical model of the catchment efficiency in high speed laser cladding". In: *Surface and Coatings Technology* 204.3 (2009), pp. 366–371. ISSN: 02578972. DOI: 10.1016/j.surfcoat.2009.07.041.

[139] Andrew J. Pinkerton and Lin Li. "A verified model of the behaviour of the axial powder stream concentration from a coaxial laser cladding noz-

zle". In: *International Congress on Applications of Lasers & Electro-Optics* 2002.1 (2002), p. 165528. DOI: 10.2351/1.5066174.

[140] F. MERIAUDEAU et al. "Laser Cladding process and image processing". In: *Journal of laser in engineering* 6.33 (1997), pp. 161–187. ISSN: 0898-1507.

[141] P. M. Morse and H. Feshbach. *Methods of theoretical physics*. 1953.

[142] M Choi, R Greif, and M Salcudean. "A study of the heat transfer during arc welding with applications to pure metals or alloys and low or high boiling temperature materials." In: *Numerical Heat Transfer* 11.4 (1987), pp. 477–489. DOI: 10.1080/10407788708913566.

[143] R W Lewis et al. *The Finite Element Method in Heat Transfer Analysis*. John Wiley & Sons, 1996. ISBN: 9780471943624.

[144] Dean Deng and Hidekazu Murakawa. "Numerical simulation of temperature field and residual stress in multi-pass welds in stainless steel pipe and comparison with experimental measurements". In: *Computational Materials Science* 37.3 (2006), pp. 269–277. ISSN: 09270256. DOI: 10.1016/j.commatsci.2005.07.007.

[145] D Dye et al. "Modeling of the mechanical effects induced by the tungsten inert-gas welding of the IN718 superalloy". In: *Metallurgical and Materials Transactions A* 32.7 (2001), pp. 1713–1725. ISSN: 1073-5623. DOI: 10.1007/s11661-001-0149-z.

[146] W C Tseng and J N Aoh. "Experimental Validation of a Laser Heat Source Model for Laser Melting and Laser Cladding Processes". In: *The Open Mechanical Engineering Journal* 8 (2014), pp. 370–381.

[147] Tso Teng, Peng-Hsiang Chang, and Wen Tseng. "Effect of welding sequences on residual stresses". In: *Computers and Structures* 81 (Mar. 2003), pp. 273–286. DOI: 10.1016/S0045-7949(02)00447-9.

[148] M R Farahani. "International Journal of Pressure Vessels and Piping Effect of the weld groove shape and pass number on residual stresses in butt-welded pipes". In: *International Journal of Pressure Vessels and Piping* 86.11 (2009), pp. 723–731. ISSN: 0308-0161. DOI: 10.1016/j.ijpvp.2009.07.007.

[149] A. A. Deshpande et al. "Combined butt joint welding and post weld heat treatment simulation using SYSWELD and ABAQUS". In: *Proceedings of the Institution of Mechanical Engineers, Part L: Journal of Materials: Design and Applications* 225.1 (2011), pp. 1–10. ISSN: 14644207. DOI: 10.1177/14644207JMDA349.

[150] Conny Lampa et al. "An analytical thermodynamic model of laser welding". In: *Journal of Physics D: Applied Physics* 30 (Jan. 1999), p. 1293. DOI: 10.1088/0022-3727/30/9/004.

[151] J.J. Valencia and Quested P.N. "Thermophysical Properties". In: *ASM Handbook: Casting* 15.Ref 24 (2008), pp. 468–481. DOI: 10.1361/asmhba0005240.

[152] D Dye et al. "Modeling of the mechanical effects induced by the tungsten inert-gas welding of the IN718 superalloy". In: *Metallurgical and Materials Transactions A* 32.7 (2001), pp. 1713–1725. ISSN: 1073-5623. DOI: 10.1007/s11661-001-0149-z.

[153] Jonathan G Mullins and Jens Gunnars. "Effect of hardening model on the weld residual stress field in pipe girth welds". In: *International Conference on Structural Mechanics in Reactor Technology* SMiRT 20 (2009), pp. 1–10.

[154] *ABAQUS Analysis User's Manual Version 6.13*. USA: Dassault Systèmes Simulia Corp, 2013.

[155] ASTM International. "ASTM B214-16 Standard Test Method for Sieve Analysis of Metal Powders". In: *ASTM International* (2019), pp. 1–4. DOI: 10.1520/B0214-16.2.

[156] ASTM International. "ASTM C1070-01(2014) Standard Test Method for Determining Particle Size Distribution of Alumina or Quartz by Laser Light Scattering". In: *ASTM International* 01.Reapproved 2014 (2014), pp. 19–21. DOI: 10.1520/C1070-01R14.wavelength.

[157] Oerlikon. *DSMW-0002.6 – Nickel-Based Superalloy Powders for Laser Cladding*. Tech. rep. 2017, pp. 1–3. DOI: https://www.oerlikon.com/ecomaXL/files/metco/oerlikon_DSMW-0002.6_NiSuperalloys_LaserCladding.pdf.

[158] ASTM International. *ASTM E3-11 Standard Guide for Preparation of Metallographic Specimens*. Tech. rep. 2017, pp. 1–12.

[159] Rafael C Gonzalez, Richard E Woods, and Steven L Eddins. *Digital Image Processing*. ISBN: 9780982085400.

[160] J. R. Santisteban et al. "ENGIN-X: A third-generation neutron strain scanner". In: *Journal of Applied Crystallography* 39.6 (2006), pp. 812–825. ISSN: 00218898. DOI: 10.1107/S0021889806042245.

[161] A.C. Larson and R.B. Von Dreele. *General Structure Analysis System (GSAS)*. 2004.

[162] D Dye et al. "The determination of the residual strains and stresses in a tungsten inert gas welded sheet of IN718 superalloy using neutron diffraction". In: *The Journal of Strain Analysis for Engineering Design* 35.4 (2000), pp. 247–259. DOI: 10.1243/0309324001514396.

[163] T Coleman and Y Li. "An Interior Trust Region Approach for Nonlinear Minimization Subject to Bounds". In: *SIAM Journal on Optimization* 6.2 (1996), pp. 418–445. DOI: 10.1137/0806023.

[164] Richard H Byrd, Robert B Schnabel, and Gerald A Shultz. "Approximate solution of the trust region problem by minimization over two-dimensional subspaces". In: *Mathematical Programming* 40.1 (1988), pp. 247–263. ISSN: 1436-4646. DOI: 10.1007/BF01580735.

[165] Robert W Messler. "Chapter 6 - Welding as a Joining Process". In: *Joining of Materials and Structures: From Pragmatic Process to Enabling Technology*. Ed. by Robert W B T Joining of Materials Messler and Structures. Burlington: Butterworth-Heinemann, 2004, pp. 285–343. ISBN: 978-0-7506-7757-8. DOI: https://doi.org/10.1016/B978-075067757-8/50006-3.

[166] P Okon et al. "Laser welding of aluminium alloy 5083". In: *International Congress on Applications of Lasers & Electro-Optics* 2002.1 (2002), p. 158364. DOI: 10.2351/1.5065620.

[167] Greger Wiklund et al. "Geometrical aspects of hot cracks in laser-arc hybrid welding". In: *Journal of Laser Applications* 26.1 (2013), p. 12003. ISSN: 1042-346X. DOI: 10.2351/1.4827135.

[168] Moritz Oliver Gebhardt, Andrey Gumenyuk, and Michael Rethmeier. "Numerical Analysis of Hot Cracking in Laser-Hybrid Welded Tubes". In: *Advances in Materials Science and Engineering* 2013 (2013), pp. 1–8. ISSN: 1687-8434. DOI: 10.1155/2013/520786.

[169] Farhang Farrokhi, Benny Endelt, and Morten Kristiansen. "A numerical model for full and partial penetration hybrid laser welding of thick-section steels". In: *Optics and Laser Technology* 111.September 2018 (2019), pp. 671–686. ISSN: 0030-3992. DOI: 10.1016/j.optlastec.2018.08.059.

[170] Mark Anderson, Rahul Patwa, and Yung C Shin Ã. "Laser-assisted machining of Inconel 718 with an economic analysis". In: 46 (2006), pp. 1879–1891. DOI: https://doi.org/10.1016/j.ijmachtools.2005.11.005.

[171] R Ducharme, P Kapadia, and J Dowden. "A mathematical model of the defocusing of laser light above a workpiece in laser material processing". In: vol. 187. 1992. 2018, pp. 187–197. DOI: 10.2351/1.5058486.

[172] Peter kayode Farayibi. "Laser cladding of Ti-6Al- 4V with carbide and boride reinforcements using wire and powder feedstock." PhD thesis. University of Nottingham, 2014, p. 64.

[173] T. E. Abioye, J. Folkes, and A. T. Clare. "A parametric study of Inconel 625 wire laser deposition". In: *Journal of Materials Processing Technology* 213.12 (2013), pp. 2145–2151. ISSN: 09240136. DOI: 10.1016/j.jmatprotec.2013.06.007.

[174] Guangming Fu et al. "Parameter determination of double-ellipsoidal heat source model and its application in the multi-pass welding process". In: *Ships and Offshore Structures* 10.2 (2015), pp. 204–217. ISSN: 17445302. DOI: 10.1080/17445302.2014.937059.

[175] C SAINTE-CATHERINE et al. "STUDY OF DYNAMIC ABSORPTIVITY AT 10.6 µm (CO2) AND 1.06 µm (Nd-YAG) WAVELENGTHS AS A FUNCTION OF TEMPERATURE". In: *J. Phys. IV France* 01.C7 (1991), pp. C7–151–C7–157.

[176] D Bergström, J Powell, and A F H Kaplan. "The absorptance of steels to Nd:YLF and Nd:YAG laser light at room temperature". In: *Applied Surface Science* 253.11 (2007), pp. 5017–5028. ISSN: 0169-4332. DOI: https://doi.org/10.1016/j.apsusc.2006.11.018.

[177] BSI. "BSI Standards Publication EN 60584-1:2013 Thermocouples Part 1 : EMF Specifications and Tolerances". In: *British Standard* BS EN 6058.1 (2013), pp. 1–12.

[178] JT Nakos. *Uncertainty analysis of thermocouple measurements used in normal and abnormal thermal environment experiments at Sandia's Radi-*

ant Heat Facility and Lurance Canyon Burn Site. Tech. rep. 2004, pp. 1–86.

[179] Jorge J Moré and D C Sorensen. "Computing a Trust Region Step". In: *SIAM J. Sci. Stat. Comput.* 4.3 (1983), pp. 553–572. ISSN: 0196-5204. DOI: 10.1137/0904038.

[180] G X Xu et al. "Adaptive volumetric heat source models for laser beam and laser + pulsed GMAW hybrid welding processes". In: *The International Journal of Advanced Manufacturing Technology* 57.1 (2011), pp. 245–255. ISSN: 1433-3015. DOI: 10.1007/s00170-011-3274-x.

[181] B M Chaparro et al. "Material parameters identification : Gradient-based , genetic and hybrid optimization algorithms". In: *Computational Materials Science* 44.2 (2008), pp. 339–346. ISSN: 0927-0256. DOI: 10.1016/j.commatsci.2008.03.028.

[182] K. Dai and L. Shaw. "Thermal and stress modeling of multi-material laser processing". In: *Acta Materialia* 49.20 (2001), pp. 4171–4181. ISSN: 13596454. DOI: 10.1016/S1359-6454(01)00312-3.

[183] A.J. Pinkerton et al. "A Verified Model of Laser Direct Metal Deposition Using an Analytical Enthalpy Balance Method". In: *Proceedings of the 26th International Congress on Applications of Lasers and Electro-optics (ICALEO)* (2007).

[184] Jehnming Lin. "Simple model of powder catchment in coaxial laser cladding". In: *Optics and Laser Technology* 31.3 (1999), pp. 233–238. ISSN: 00303992. DOI: 10.1016/S0030-3992(99)00046-8.

[185] J. Lin and W. M. Steen. "Design characteristics and development of a nozzle for coaxial laser cladding". In: *Journal of Laser Applications* 10.2 (1998), pp. 55–63. ISSN: 1042-346X. DOI: 10.2351/1.521821.

[186] Xuan Liang et al. "A modified method for estimating inherent strains from detailed process simulation for fast residual distortion prediction of single-walled structures fabricated by directed energy deposition". In: *Additive Manufacturing* 23.August (2018), pp. 471–486. ISSN: 2214-8604. DOI: 10.1016/j.addma.2018.08.029.

[187] William Perret. "Welding Simulation of Complex Automotive Welded Assembly - Possibilities and Limits of the Application of Analytical Temperature Field Solutions". PhD thesis. Tech- nische Universität Berlin, Fakultät V - Verkehrs - und Maschinensysteme, 2013, pp. 1–169. ISBN: 9783981594409.

[188] Jehnming Lin. "Laser attenuation of the focused powder streams in coaxial laser cladding". In: 28.2000 (2015), pp. 27–33. DOI: 10.2351/1.521910.

[189] Yuze Huang, Mir Behrad Khamesee, and Ehsan Toyserkani. "A comprehensive analytical model for laser powder-fed additive manufacturing". In: *Additive Manufacturing* 12 (2016), pp. 90–99. ISSN: 22148604. DOI: 10.1016/j.addma.2016.07.001.

[190] H. Zhang. "Theoretical analysis of spreading and solidification of molten droplet during thermal spray deposition". In: *International Journal of Heat and Mass Transfer* 42.14 (1999), pp. 2499–2508. ISSN: 00179310. DOI: 10.1016/S0017-9310(98)00364-0.

[191] N. Pirch et al. "Temperature field and residual stress distribution for laser metal deposition". In: *Journal of Laser Applications* 30.3 (2018), p. 032503. DOI: 10.2351/1.5040634.

[192] O. Muránsky et al. "The effect of plasticity theory on predicted residual stress fields in numerical weld analyses". In: *Computational Materials Science* 54 (2012), pp. 125 –134. ISSN: 0927-0256. DOI: https://doi.org/10.1016/j.commatsci.2011.10.026.

[193] O. Muránsky et al. "The influence of constitutive material models on accumulated plastic strain in finite element weld analyses". In: *International Journal of Solids and Structures* 69-70 (2015), pp. 518–530. ISSN: 00207683. DOI: 10.1016/j.ijsolstr.2015.04.032.

[194] M Salcudean, M Choi, and R Greif. "A study of heat transfer during arc welding". In: *International Journal of Heat and Mass Transfer* 29.2 (1986), pp. 215–225. ISSN: 0017-9310. DOI: http://dx.doi.org/10.1016/0017-9310(86)90229-2.

[195] H Y Zhang et al. "Microstructure evolution of IN718 alloy during the delta process". In: *Procedia Engineering* 207 (2017), pp. 1099–1104. ISSN: 1877-7058. DOI: 10.1016/j.proeng.2017.10.1137.

[196] M.R. Daymond J.A. James, J.R. Santisteban, L. Edwards. "A Virtual Laboratory for Neutron and Synchrotron Strain Scanning". In: *Physica B* 350.Condensed Matter (2004), pp. 743–746.